Broadband Capture of Ocean Wave Energy by Rainbow Absorbing Arrays of Wave Energy Converters

THE UNIVERSITY of ADELAIDE

Submitted in fulfilment of the requirements for the degree of

Doctor of Philosophy

Amy-Rose Westcott

School of Computer and Mathematical Sciences

The University of Adelaide

March 2026

Contents

Abstract

Wave energy converters (WECs) are designed to harness the renewable power of ocean waves, but are not yet economically viable. The cost-competitive conversion of ocean wave energy at a commercial scale will require arrays of WECs to operate efficiently across a broad range of frequencies and directions, consistent with the distribution of wave energy feasible for power generation. Developing suitable array designs is an ongoing challenge, as WECs are typically efficient over narrow frequency ranges, and arrays are sensitive to wave direction. In this thesis, strategies for efficient, broadband absorption are developed by applying theories for rainbow absorption to an array of heaving buoy type WECs. Each WEC is attached to a linear spring–damper power take-off mechanism (PTO) to control the resonant properties for broadband absorption on a target frequency interval covering wave periods of 10–20 s. Linear potential-flow theory and semi-analytical methods are applied.

Starting with a two-dimensional (2D) domain, the WEC-resonances are graded to create an effective bandgap, with low transmission over the target interval, using a Bloch wave analysis. The grading generates spatially controlled energy amplifications that are captured by choosing the PTO damping to minimise reflected wave amplitudes. The reflection and transmission of the array are analysed in complex frequency space, where pole–zero pairs are connected to the resonant properties governing absorption, and the influence of higher-order passbands. An array of five WECs achieves near-perfect absorption ($\geq 99\%$). The broadband design is demonstrated in irregular sea states, and for incident wave packets in the time domain.

Strategies for broadband absorption are recreated in a three-dimensional (3D) domain, by arranging the WECs into stacks (periodic row of infinitely many, identical WECs), and grading the resonant frequencies of successive stacks via the PTOs. The array layout is chosen to support 2D wave propagation and achieve high efficiency with minimal stacks, such that the average absorption of six stacks exceeds 90% over a wide range of wave directions. The efficient, broadband absorption is demonstrated by comparing a graded array of 60 WECs in directionally spread, irregular sea states, to uniform arrays.

The broadband absorption generated by grading arrays is robust to a drag correction, which is incorporated into the 3D model to approximate non-linear effects from large, resonant WEC motions. Drag reduces the amplification of WEC motions as the incident wave amplitude increases, and consequently, efficiency. Finite arrays of 30 WECs capture a high proportion of the available incident energy relative to the array's width, outperforming uniform arrays over most of the target interval.

Overall, the findings motivate grading arrays to deliver efficient, broadband absorption that is robust to the wave direction using fixed PTO parameters, and without requiring accurate, short-term forecasts. The low transmission generated by graded arrays could have coastal protection applications, which would enhance the economic viability of WECs.

Declaration

I certify that this work contains no material which has been accepted for the award of any other degree or diploma in my name, in any university or other tertiary institution and, to the best of my knowledge and belief, contains no material previously published or written by another person, except where due reference has been made in the text. In addition, I certify that no part of this work will, in the future, be used in a submission in my name, for any other degree or diploma in any university or other tertiary institution without the prior approval of the University of Adelaide and where applicable, any partner institution responsible for the joint-award of this degree.

I acknowledge that copyright of published works contained within this thesis resides with the copyright holder(s) of those works. I also give permission for the digital version of my thesis to be made available on the web, via the University's digital research repository, the Library Search and also through web search engines, unless permission has been granted by the University to restrict access for a period of time.

I acknowledge the support I have received for my research through the provision of an Australian Government Research Training Program Scholarship.

Signed: Date: 07/03/2026

Statement

This thesis uses a combination of conventional and publication formatting. Chapters 1, 2 and 6 are written in the conventional style, while Chapters 3, 4 and 5 are written in manuscript style. Chapter 3 of this thesis is published as

Westcott, A.-R., Bennetts, L. G., Sergiienko, N. Y., and Cazzolato, B.S. (2024). Broadband near-perfect capture of water wave energy by an array of heaving buoy wave energy converters, *Journal of Fluid Mechanics* **998**: A5. doi:10.1017/jfm.2024.819

The following modifications have been made to the published version (CC BY 4.0) for consistent formatting within this thesis:

- the numbering and formatting of sections, figures and tables have been altered,
- typesetting, spelling and punctuation conventions have been edited,
- the size and location of figures and tables have been adapted to the thesis layout,
- the appendices and references have been incorporated into the back matter of the thesis.

In addition, and with thanks to the examiners of this thesis, typographical errors in Tables 3.1, 3.2 and 3.3, and Equations (A.3) and (A.6) have been corrected. The use of "$N = 5$ WECs" has been replaced with "five WECs" in Figure A.1 and § A.2 to avoid confusion. References to Appendix A.1 have been added on page 39, and a reference to Jiménez et al. (2017b) on page 50. A sentence explaining Equation (3.29) has been added on page 43, with earlier instances of $\xi^h_{(n)}$ replaced with ξ_n to clearly distinguish between the single body and array problems. In Appendix A.1, ξ_h has been corrected to ξ^h.

An extended abstract based on Chapter 4 is published as

Westcott, A.-R., Bennetts, L. G., Sergiienko, N. Y., Cazzolato, B. S. and Peter, M. A. (2025). Broadband absorption of wave energy by graded arrays of heaving buoys in 3D, In X. Zhang (ed.) *Proceedings of The 40th International Workshop of Water Waves and Floating Bodies*, Shanghai, China. http://www.iwwwfb.org/Abstracts/iwwwfb40/IWWWFB40_49.pdf

Acknowledgements

I could not have dreamt up a more perfect project. A heartfelt thanks to my supervisors, Prof Luke Bennetts, Dr Nataliia Sergiienko and Prof Ben Cazzolato, for your valued insight and guidance over the past few years that made this a delightful and fulfilling journey.

Prof Luke Bennetts, it has been an absolute privilege to learn from you and receive such exceptional supervision. An immense thank you for your support, generosity with your time and expertise, advice, approachability, consistency, and for going above and beyond in helping me navigate my PhD. Dr Nataliia Sergiienko, a huge thank you for your constant care, practical advice, and for always being there to help and support me, or reason things out. I learnt a great deal from your insightful questions. Prof Ben Cazzolato, a huge thank you for your enthusiasm, advice, for always having words of encouragement at the ready and examples to help me understand. It has been an honour and a joy to learn from each of you.

A special thank you to Prof M. A. Peter, Dr L. J. Yiew and Dr R. Alwan, for code that helped me cut around 5 years off this PhD, which was itself made possible by a UoA scholarship and ARC LP180101109 top-up scholarship. It was a privilege to collaborate with and learn from the amazing ARC team: Richard, Justin, Fanrui, Vicki, Kane, Wade, Nadav, Ian, Francois, and especially, Lidong, who offered much encouragement. I am very grateful to the Isaac Newton Institute for Mathematical Sciences and DAC, ICIAM, the Tuck Fellowship, and Luke, for travel funds that took me to Cambridge, Tokyo, Dunedin, and Shanghai, and gave me the opportunity to meet incredible people in this wonderful community.

My time at UoA would not have been the same without Harbans, Kai, Tayla, Nathan, Indu, Jie, Oska, Yawei, Noah, Philip, fabulous office 6.35 peers, Afnan, Tharindi and Rehab. Thanks to C. Parsons and Sarah for all the check-ins and encouragement, darling Gladiola, and to the Coxes, Hansfords and Ielasis for social outings with Michelin star sustenance. Nonnie, for always caring about the piggies, and Jesse and Robyn for your sustaining friendships.

I do not have enough, or sufficient, words to thank Stacey, Julsie and Shaunie for filling my emotional tank and providing fortitude! All the heart I have put into this is as a result of your unwavering love and support, which has always been a given. You have shared every up and down of this journey with me, and more, and I could not have done it without you. Like my faithful companions before them, my writing of this thesis was always accompanied by Mirry enforcing strict but unintelligible workplace etiquette, Roo chirping encouragement, Ethel warbling, and Silky and Blessing keeping my lymph moving through constant interventions.

I am grateful to have had the opportunity to commit to this PhD, during which, devastating wars and crises unfolded across the globe, amidst back-to-back years hitting record temperatures. To paraphrase Jane Goodall, I hope to remain encouraged by the fact that our individual actions matter, and even small choices will help shape the fabric of our society.

Abbreviations

2D	**T**wo-**D**imensional
3D	**T**hree-**D**imensional
CFD	**C**omputational **F**luid **D**ynamics
JONSWAP	**JO**int **N**orth **S**ea **WA**ve **P**roject
PTO	**P**ower **T**ake-**O**ff
PWE	**P**lane-**W**ave **E**xpansion
RAO	**R**esponse **A**mplitude **O**perator
WEC	**W**ave **E**nergy **C**onverter
WSA	**W**ide-**S**pacing **A**pproximation

List of Figures

List of Tables

Chapter 1

Introduction

1.1 Background and motivation

Energy-related carbon emissions reached a historic high in 2024, as record temperatures and extreme weather events amplified a record growth in electricity demand (IEA, 2025). Renewable energy technologies met 80% of the annual growth in demand, preventing an expanding reliance on fossil fuels that would have amounted to three times the emissions (IEA, 2025), at higher economic cost (IRENA, 2025). However, limiting global warming below 2°C relies on a drastic reduction in fossil fuel use in order to reach net-zero by 2050 (IPCC, 2023). Without urgent action, we risk parts of our planet becoming uninhabitable as we push the resilience of the ecosystems we depend on, closer, and more quickly, towards collapse (IPCC, 2023).

Wave energy converters (WECs) are devices that are designed to transform ocean wave energy into electrical power, and are positioned to play an important role in decarbonisation, and the diversification of renewable energy technologies (IRENA and OEE, 2023). The unmatched consistency, density and availability of ocean wave energy compared to, for example, solar or wind (Guo and Ringwood, 2021), could help ensure energy security, protecting against disruptions (e.g., wind droughts (Qu et al., 2025)), and increasing the reliability and flexibility of energy supply, while potentially reducing the growing reliance on storage technologies (IRENA, 2025; IRENA and OEE, 2023; Li et al., 2025; Satymov et al., 2024). Further, electricity transmission costs would benefit from proximity to demand, as around one third of the global population lives within 50 km of a coastline (Cosby et al., 2024; Li et al., 2025; Satymov et al., 2024). However, WECs are yet to reach economic viability, and despite a substantial body of research, design convergence has not occurred (Golbaz et al., 2022).

To become a competitive renewable energy technology, WECs will require strategies that enable them to operate efficiently across a broad range of ocean wave frequencies for cost-effectiveness (Ning and Ding, 2022; Pecher and Kofoed, 2017). With strategic placement, this transformation of destructive wave power into clean, renewable energy, could assist in the protection of coastlines (Boodoo et al., 2025). Coastal regions are particularly vulnerable to the impacts of climate change, which will have ecological, economic and geopolitical ramifications of global significance (IPCC, 2019, 2022). As some of the most densely populated regions on the globe, current adaptations against intensified storms, flooding, and accelerated

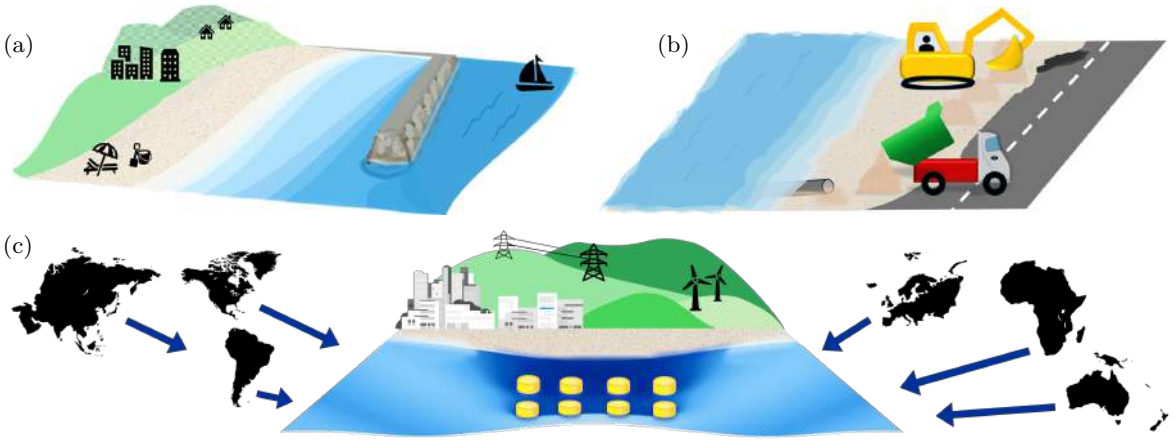

Figure 1.1: Hard defences, e.g., (a) breakwaters, prevent wave energy reaching coastlines, while nature-based solutions like (b) beach nourishment, improve coastal resilience. Damaging wave energy can potentially be transformed into electricity by (c) WECs, to facilitate sediment accretion.

sea level rise, face physical and economic barriers (Cosby et al., 2024; IPCC, 2019, 2022). *Hard* defences (e.g., breakwaters) disrupt natural processes and place pressure on already fragile ecosystems, undermining their ability for adaptation, and further requiring modification to remain effective as climate change progresses (Gittman et al., 2016; IPCC, 2019, 2022). *Nature-based* defences (e.g., beach nourishment) are less cost-intensive and improve the resilience of coastlines, but require ongoing maintenance and are inadequate in isolation (IPCC, 2022). Consequently, WECs could prove to be an attractive source of coastal defence in addition to renewable power (illustrated in Figure 1.1) as global warming progresses (Battisti et al., 2024), which would enhance their cost-effectiveness (Clemente et al., 2021).

1.2 Current state of wave energy

The prospect of capturing ocean wave energy at a meaningful scale has inspired over 50 years of research. However, wave energy technology is still in pre-commercial stages (Guo and Ringwood, 2021). To prove cost-effective, WECs must demonstrate efficiency, reliability and survivability appropriate to the nature of the resource, which is partially hindered by the variety of WEC concepts (various classifications outlined by Ning and Ding (2022)), each with their own challenges (Sheng, 2019), and the lack of government/policy assurances necessary to attract sufficient investment (IRENA and OEE, 2023). In 2017, oscillating bodies comprised an estimated 78% of developed prototypes (Ning and Ding, 2022). Of these, heaving buoy type WECs are prolific in the literature.

Like many other WECs, heaving buoys achieve maximum efficiency at resonance, where their natural frequency matches the ocean waves, creating amplified motions with the appropriate phase for optimum destructive interference (Falnes, 2007). The resonance can be controlled by

incorporating a stiffness mechanism into the power take-off system (PTO), which is responsible for converting ocean wave energy into electrical power. Larger WECs usually have lower natural frequencies, which are better suited to efficient capture in the powerful, low frequency waves, suitable for power generation (Coe et al., 2017; Fusco and Ringwood, 2010). However, CorPower Ocean (2024) have successfully demonstrated the down-tuning of their heaving buoy via a negative stiffness mechanism, which, in combination with a pretension cylinder, allows for a smaller, lighter WEC, decreasing costs (Coe et al., 2017; Todalshaug et al., 2016).

The frequency range over which high efficiency is sustained is termed the resonance bandwidth (Falnes, 2005). Although the WEC geometry can be optimised to increase efficiency and broaden the resonance bandwidth (e.g., Edwards et al., 2025; Edwards and Yue, 2022), heaving buoys are typically narrow-banded due to their physical characteristics (Falnes, 2007; Falnes and Hals, 2012). Here, a negative stiffness mechanism is again beneficial, and can broaden the resonance bandwidth of WECs while also providing inherent phase control, leading to a threefold increase in power capture to PTO force (Todalshaug et al., 2016). Similarly, non-linear stiffness mechanisms can broaden responses (Schubert et al., 2022), which has potential benefits for coastal protection (Jin, Zhang, Zheng, Lu, Xu and Greaves, 2024).

Wave climates conducive to power generation cover a broad range of frequencies and wave directions, with spatio-temporal variability experienced at a daily, seasonal and annual scale (Guo and Ringwood, 2021; Pecher and Kofoed, 2017). Frequencies suitable for power capture are generally considered to consist of wave periods lying between 5–20 s (Coe et al., 2021). Since most WECs have relatively narrow optimal operating conditions, variations between sea states, which may themselves be broadband and directionally spread, can significantly decrease power capture, even when the average incident wave power remains constant (Pecher and Kofoed, 2017). To reach the high efficiency power capture over broad frequency ranges (*broadband absorption*) required for cost-effectiveness, the PTO is altered to create resonant conditions, in a process known as *control* (Coe et al., 2017; Pecher and Kofoed, 2017).

Dynamic control strategies adapt the WEC properties according to the incoming wavefield, and include latching, declutching, reactive, and model predictive control, which effectively broaden the WEC's bandwidth (Ning and Ding, 2022; Pecher and Kofoed, 2017). While these advanced control methods employ different principles and types of PTO systems to enhance power capture, they generally require accurate wave forecasts and are sensitive to modelling errors (Pecher and Kofoed, 2017; Ringwood et al., 2023). In particular, direct-drive PTOs are noted for their ability to generate any desired PTO control force (Ning and Ding, 2022). However, generating very large forces can be more uneconomical than altering the physical WEC properties (Ringwood, 2025). Physical constraints on the WEC motions and PTO forces are needed to prevent structural fatigue, which may otherwise increase operational costs and maintenance requirements (Hals et al., 2010; Pecher and Kofoed, 2017; Ringwood, 2025;

Ringwood et al., 2023). Consequently, the PTO directly affects efficiency and reliability, which has the potential to reduce the cost of power generation, despite significantly contributing to the capital cost (Ning and Ding, 2022; Pecher and Kofoed, 2017).

The hydrodynamic and WEC–PTO interactions can exhibit complex, non-linear dynamics when controlled for maximum power (Battisti et al., 2024; Ning and Ding, 2022). High fidelity models accurately capture complex dynamics but are computationally demanding and can become intractable (Ning and Ding, 2022). Hydrodynamic interactions are linearised in the vast majority of the literature, assuming small WEC motions (relative to WEC dimensions) in waves of low steepness, subject to potential-flow theory (incompressible, inviscid, and irrotational) (Folley, 2016). Linear wave theory is widely considered to be acceptable in an operational regime, where the incident wave amplitudes are sufficiently small to justify linear wave–WEC interactions, or tolerate limited validity, due to the complexity incurred by higher-order models (Falnes and Kurniawan, 2020; Pecher and Kofoed, 2017; Penalba, Giorgi and Ringwood, 2017; Ringwood et al., 2023). Non-linearities arising from the PTO or mooring, for example, can be incorporated in time-domain models, however the PTO is approximated as a linear spring–damper in the frequency domain (Battisti et al., 2024; Folley, 2016).

Linear WEC dynamics in frequency domain models allow the behaviour in irregular sea states to be constructed from the response to regular waves through linear superposition (Folley, 2016). The time-domain solution can also be obtained through an inverse Fourier transform (Korde and Ringwood, 2016). Wave spectra are well-represented by a linear superposition of sinusoidal waves with randomly distributed phases, and different frequencies, amplitudes, and directions corresponding to the distribution of energy in non-steep waves (Cruz, 2008; Pecher and Kofoed, 2017). However, large WEC-amplitudes can occur at resonance, violating the assumption of linearity, and requiring restricted incident amplitudes to retain validity, and physical constraints on the WEC motions to prevent breaching (Hals et al., 2010).

So-called partially non-linear models have been developed with the aim of capturing key hydrodynamic non-linearities by incorporating second-order radiation–diffraction forces or non-linear contributions to the incident waves and buoyancy forces (e.g., Froude–Krylov forces) in a linear potential theory framework in the time domain (Penalba, Giorgi and Ringwood, 2017; Wolgamot and Fitzgerald, 2015). Although these models lack a rigorous mathematical basis, they are more computationally efficient than non-linear potential-flow models, and have been found to improve model accuracy and reduce motions when the associated non-linear forces are significant (Folley, 2016; Wolgamot and Fitzgerald, 2015). Similarly, viscous effects can be approximated by a drag correction in potential-flow models to improve model accuracy by reducing the large, amplified WEC motions that occur at resonance in linear models (Giorgi and Ringwood, 2017; Guo and Ringwood, 2021; Korde and Ringwood, 2016).

While it is becoming increasingly tractable to analyse the single body problem using fully non-linear potential-flow models, or even computational fluid dynamics (CFD) (Folley, 2016), these methods are still limited to a small number of devices due to computational requirements (Göteman, 2022). Early concept development remains reliant on linear theory, and is typical in control (Ringwood et al., 2023), optimisation (Göteman et al., 2020), and wave-to-wire models that cover the full extent of the energy conversion process, from hydrodynamic interactions to grid integration (e.g., Garcia-Rosa et al., 2022).

1.2.1 Arrays of WECs

To reach commercial viability and become cost-competitive with other renewable technologies, WECs will need to be deployed in arrays consisting of multiple devices, which will benefit from dramatically reduced costs through economies of scale (IRENA and OEE, 2023; Korde and Ringwood, 2016). Larger arrays (numbers of devices) possess the capacity for greater power generation relative to the array's footprint (ocean area and required infrastructure), and improve power intermittency (Göteman et al., 2015). The substantial upfront investment favours large arrays, due to the decreased cost of construction, installation, operations and maintenance per device (Ning and Ding, 2022; Penalba, Touzón, Lopez-Mendia and Nava, 2017). However, the profitability is likely to reach a threshold as the size of the array increases, due to diminishing returns on power capture per WEC, and practical restrictions on operations and maintenance activities (Teillant et al., 2012). Initial assessments suggest that such a threshold could occur when arrays exceed approximately 150 devices (Teillant et al., 2012).

Deployment sites are selected based on the mean power level and variability of the wave climate, which have a notable influence on capital and operational expenditure (Guo and Ringwood, 2021). Installation and operation costs vary with the distance from shore (associated with wave power), water depth, grid connection, ocean leasing and WEC technology, but are highly uncertain given the nascent nature of the industry, and will vary over the WEC's lifetime (Carballo and Iglesias, 2013; Satymov et al., 2024; Teillant et al., 2012). Beneficial array designs further depend on the WEC concept and appropriate operating conditions. For example, oscillating wave surge converters are deployed in nearshore, shallow waters, but heaving buoys are typically deployed further offshore (Ning and Ding, 2022).

Apart from a few exceptions (e.g., Göteman et al., 2015), recent literature is predominantly concerned with small arrays consisting of only a few devices (> 10 is considered large (Babarit, 2013)) (Teixeira-Duarte et al., 2022). Optimising arrays to maximise power capture is a recurring theme, in line with one of the foremost challenges to improve efficiency (Sheng, 2019). Given a particular array layout, Evans (1981b) and Falnes (1980) separately derived maxima for power absorption at a single frequency using linear theory, assuming perfect

control of the (unconstrained) amplitudes and phases of all the WECs is possible. However, determining the appropriate individualised PTOs required to attain the theoretical optimum velocities is complex, and are not achieved by tuning all the buoys to resonance in general (Falnes, 1980). The amplified WEC motions required to reach theoretical limits frequently violate the assumptions of linear theory, and must be constrained in practice to comply with physical and mechanical limitations, such as volume stroke, which places an upper bound on power capture, except in low incident amplitudes (Evans, 1981a,b; Todalshaug, 2013).

Ideally, an array should be optimised to maximise power at minimum cost over the lifespan of devices, given the deployment location, reliability, maintenance and operation, while subject to constraints on ocean area, WEC motions and power fluctuations, amongst others (Battisti et al., 2024; Göteman et al., 2020; Teixeira-Duarte et al., 2022). Given computational limitations and the complexity with which these factors interact with one another, the optimisation of arrays is often limited to a single objective (often to maximise power) and a small number (often one) of controlled variables corresponding to the aspect under consideration (Göteman et al., 2020). For example, the layout may be optimised while fixing the PTO to be optimal for the considered WEC in isolation (e.g., Child and Venugopal, 2010), or the layout optimised in conjunction with individualising the PTO for each WEC (e.g., David et al., 2022; Wilks et al., 2025). Crucially, the outcome is strongly tied to the objective and conditions under which optimisation is performed (Ning and Ding, 2022).

Linear theory is overwhelmingly applied in array optimisation due to the large number of evaluations which demand computationally efficient methods to compute hydrodynamic interactions (Göteman et al., 2020). Theoretically, constructive hydrodynamic interactions in an array will enhance power capture. Consequently, a popular objective is to maximise the q-factor, which quantifies constructive ($q > 1$) or destructive ($q < 1$) effects by relating the power captured by an array, to the power that would be captured by the same number of WECs in isolation, at a given frequency (Budal, 1977). Optimised arrays of fewer than ten devices (unconstrained amplitudes) are frequently shown to achieve $q > 1$, but are often highly sensitive to changes in wave direction and/or frequency (Babarit, 2013; McGuinness and Thomas, 2017; Ning and Ding, 2022). When averaged over direction, optimally-tuned arrays can at best achieve $q = 1$ (Wolgamot et al., 2012). Additionally, both destructive and constructive interactions will occur over typical incident frequencies (Budal, 1977; Cruz et al., 2010). Consequently, a constructive effect is unlikely in realistic sea states (McGuinness and Thomas, 2017), or when averaged over wave conditions (Ning and Ding, 2022).

Similarly, peak q-factors which rely on optimal control, determined for monochromatic waves, may be unachievable in irregular and directionally spread sea states (Babarit, 2013; Folley and Whittaker, 2009; Penalba, Touzón, Lopez-Mendia and Nava, 2017), and may require

WECs within the array to supply (as opposed to capture) power in constructive interactions (Wolgamot et al., 2012), demanding complex PTO mechanisms (Pecher and Kofoed, 2017). Constraining WEC motions according to the wave height and/or engineering factors further limits the potential for constructive interactions, and can increase destructive interference in small arrays while retaining their sensitivity to wave direction and frequency (Folley and Whittaker, 2009; McGuinness and Thomas, 2017; McIver, 1994; Zhong and Yeung, 2022). Consequently, it may be beneficial to minimise destructive effects through randomised, or large spacing (relative to a characteristic WEC dimension) instead, especially as the number of WECs increases (Babarit, 2013; McIver, 1994; Zhong and Yeung, 2022).

Although the layout is ideally designed to coincide with the expected range of wave directions for peak performance (Wolgamot et al., 2012), even a suitable deployment site will experience variability in terms of direction, frequency, and amplitude (Ning and Ding, 2022). Unlike isolated heaving buoys, directional variation can considerably reduce the efficiency of arrays (Pecher and Kofoed, 2017). The sensitivity of array design to frequency and wave direction must be considered (Cruz et al., 2010), as fixed array layouts will experience substantial variations in wave conditions over the lifetime of devices (Ning and Ding, 2022), with temporal variations expected to be amplified by climate change (Mahmoodi et al., 2025).

Generating power from ocean waves subject to temporal variability leads to power fluctuations which complexify grid integration (Said and Ringwood, 2021). Larger arrays tend to produce lower fluctuations, but layouts which enhance smoothing can be less efficient relative to the ocean area utilised, or length of sea-cabling, which are major contributors to the initial outlay (Engström et al., 2013; Göteman, 2022; Göteman et al., 2015). Although hydrodynamic interactions are important, analysing design suitability for large-scale energy systems (e.g., peaks in power exceeding the capability of electrical systems) may provide greater insight into economic designs than modelling fluid–structure interactions with higher-fidelity (Folley and Whittaker, 2009; Göteman et al., 2020).

Optimal layouts for power production (e.g., spacing, layouts with low power fluctuations) can conflict with economic goals (Ning and Ding, 2022), as compact arrays have a smaller footprint, which can decrease capital cost and energy losses through shorter sea-cables, fewer electrical subsystems, and distance to grid connection points (Battisti et al., 2024; Göteman et al., 2020). The multi-objective optimisation of economic measures in conjunction with power capture is becoming more common with advances in computational power and the development of sophisticated, global optimisation algorithms (Ning and Ding, 2022).

Meta-heuristic algorithms are often better equipped to handle the resulting multi-variate, non-convex, multi-modal optimisation problems (Giassi and Göteman, 2018; Göteman et al., 2020), and are adept at generating non-dominated solutions for multi-objective outcomes

(e.g., David et al., 2022). Since computational costs rise quickly and can become intractable (Göteman et al., 2020), semi-analytical methods are an efficient means to evaluate multiple configurations for bi-objective optimality (e.g., Göteman, 2022). The many unknowns and unresolved questions due to the relative technological immaturity have led to a host of design objectives in the literature, which in combination with different models, have limited generalised recommendations (Giassi and Göteman, 2018).

Dynamic control methods could potentially mitigate the limitations of static array layouts, which are unlikely to reconcile conflicting objectives, by adjusting the PTO for maximum power capture based on short-term wave prediction (Battisti et al., 2024; Guo and Ringwood, 2021). Global (centralised) control accounts for hydrodynamic interactions within an array, whereas independent (decentralised) control is based on the behaviour of isolated devices (Bacelli and Ringwood, 2013). Predicting excitation forces for each WEC is significantly more complex and computationally demanding in global control, even when assuming future wave conditions can be perfectly forecast (Ringwood et al., 2023). This has significant implications for some of the most advanced, and promising online methods, like model predictive control (Li et al., 2025), as hydrodynamic interactions must be resolved and the PTO optimised in real-time (Ringwood et al., 2023). Constraining maximum forces or WEC displacements generally reduces the gains obtained through global control (Bacelli and Ringwood, 2013).

The difference between control methods that do or do not consider interactions between WECs is overshadowed by the impact of optimising control and layout in isolation of one another (Garcia-Rosa et al., 2015). Control co-design seeks to address interdependence by integrating the search for optimal control into the optimisation of design parameters (e.g., WEC geometry and array layout), through control-informed optimisation (Peña-Sanchez et al., 2024; Ringwood et al., 2023). Different control principles lead to vastly different optimal layouts, which are strongly reliant on the chosen control (Garcia-Rosa et al., 2015; Ringwood, 2025).

The control strategy has a limited ability to compensate for sensitivity to wave direction, which is primarily governed by the array layout (Garcia-Rosa et al., 2015). Consequently, control co-design tends to produce single-row, straight line arrays, perpendicular to the direction of propagation, for maximum power capture in uni-directional waves, whereas multi-directional wave propagation leads to rectangular configurations (Ermakov et al., 2025; Peña-Sanchez et al., 2024). Regardless of the array layout, predictive control requires accurate wave forecasts to estimate future wave elevation or excitation force (Bacelli and Ringwood, 2013; Ringwood et al., 2023). Wave prediction algorithms typically construct the future wavefield from nearby measurements, or are based on the past history at a specific location (Fusco and Ringwood, 2010). Accurate prediction is challenging, and must cater for hydrodynamic interactions within arrays, and spatially irregular, multi-directional wave propagation, based

on buoy measurements that are subject to variability on multiple time scales, and expensive to maintain (Cruz, 2008; Fusco and Ringwood, 2010; Pecher and Kofoed, 2017).

Forecasting error can compound in models of arrays, which are also sensitive to hydrodynamic modelling simplifications (Ringwood, 2025; Veurink et al., 2023). Maximising energy capture in multi-directional, multi-frequency, variable sea states through dynamically controlling arrays is highly complex, even assuming linear theory, and is still largely limited to arrays with only a few WECs (Foteinis and Tsoutsos, 2017; Göteman et al., 2020). While advanced dynamic control strategies are widely viewed as the most promising route to efficient broadband capture, they too require economic designs that support high efficiency and are robust to wave direction. Like optimised layouts of large arrays (e.g., Tokić and Yue, 2021), control co-design appears to imply that regular, symmetric, and often rectangular arrays, enhance power capture in irregular sea states (e.g., Ermakov et al., 2025; Peña-Sanchez et al., 2024).

1.2.2 Periodicity, band structures, and graded arrays

The wave propagation supported by large arrays with regular spacing can be predicted using periodic arrays (infinitely many, repeating elements), which enables the problem to be simplified to a single WEC, subject to periodic boundary conditions (McIver, 2000). Analysing the scattering by a *diffraction grating* or *stack*, which consists of a single, periodic row of identical elements, has a long history in solid-state physics, acoustics and electromagnetics (Ashcroft and Mermin, 1976; Wilcox, 1984). Established theory exists to relate wave interference to ratios of the incident wavelength and spacing, which transforms the wavefield into a discrete directional spectrum (McIver, 2002), facilitating the manipulation of propagating modes for desired reflection and transmission properties using efficient computational methods (Petit, 1980; Twersky, 1962). Analysing the array effects (which do not exist for a single WEC) that arise in periodic arrays could help inform the design of WEC-arrays (Tokić and Yue, 2019).

Applying linear theory, a stack of three-dimensional (3D) heaving buoys shares theoretical maxima with two-dimensional (2D) WECs, and can capture at most 50% of the incident wave energy in heave (symmetric radiation) (Falnes, 1984; Todalshaug, 2013). Plane waves propagate away from a stack in the far field at *scattering angles* determined by constructive interference between the individual circular wavefields (Falnes and Budal, 1982). The number of real ($\in \mathbb{R}$) scattering angles depends on the inter-device spacing relative to the wavelength, and the wave direction. An inter-device spacing of less than half the wavelength returns a single pair of real scattering angles corresponding to propagating modes of transmission and reflection respectively, consistent with a 2D wavefield (Falnes and Budal, 1982).

To capture 100% of the incident energy at a prescribed frequency and arbitrary spacing, the number of rows (or independent modes of oscillation) must equal or exceed the number

of real scattering angles, which will grow as the inter-device spacing increases relative to the wavelength (Falnes, 1984). Power capture declines sharply at the emergence of new scattering angles[1], since the reflection and transmission properties are designed for destructive interference in a single direction (Tokić and Yue, 2019, 2021, 2023). The reflection and transmission properties of an array are illustrated in Figure 1.2 at selected wavelengths.

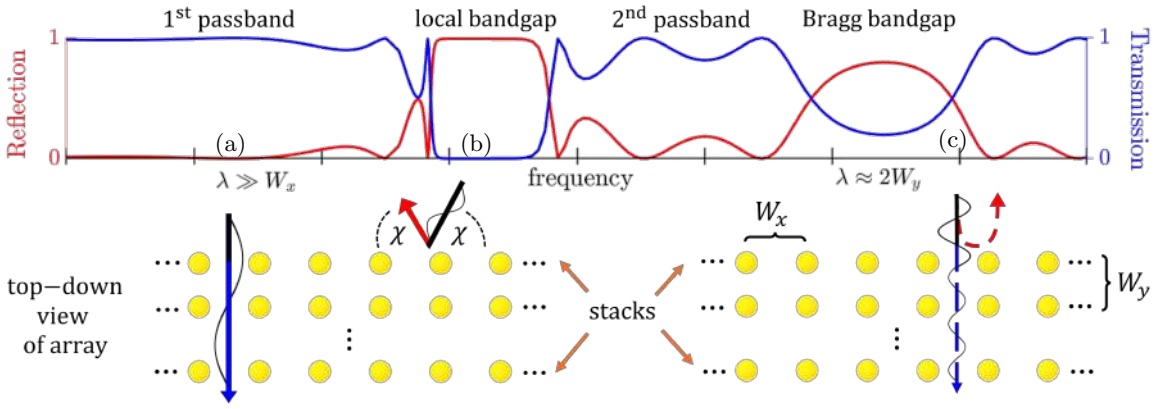

Figure 1.2: The proportion of the incident wave energy that is (a) transmitted (—), (b) reflected (—), or (c) partially reflected and transmitted by an array of non-absorbing (freely floating) WECs is shown as a function of the wavelength λ, and satisfies reflection + transmission = 1. The regular spacing W_x between WECs in a stack supports a single scattering angle χ (consistent with the incident wave direction) on the frequency range. The spacing W_y between stacks governs Bragg resonance.

Consequently, it is preferable to operate in a regime with a single pair of scattering angles. This only places mild restrictions on inter-device spacing, as the power in ocean waves is concentrated at long wavelengths (Fusco and Ringwood, 2010). Coherent interactions between incident and reflected waves occur when the spacing between rows is an integer multiple of half the wavelength (Bragg condition), leading to the phenomenon of Bragg resonance (Linton, 2011). The resulting band of strong reflection (low transmission) is referred to as a bandgap and delimits the frequency range where wave interference prohibits propagation, causing the wave amplitude to change with distance (McIver, 2000; Sheng et al., 2003). In contrast, passbands define frequency ranges which permit wave propagation through a periodic array.

Strongly reflective WECs are associated with wider bandgaps, and can cause bandgaps created by Bragg resonance (*Bragg bandgap*) to shift from the Bragg condition (Linton, 2011). The spacing between rows should be chosen to avoid Bragg resonance at targeted wavelengths for power generation, to prevent the substantial decline in power capture (Garnaud and Mei, 2010; Jin, Zhang, Zheng and Xu, 2024) that can occur with as few as two rows of strongly reflecting WECs (Tokić and Yue, 2019). It is expected that finite arrays would similarly prohibit transmission, especially as the number of WECs grows (Linton, 2011; McIver, 2000).

[1] Also referred to as Rayleigh resonances by Tokić and Yue (2019), and as Wood's anomalies, which lead to the redistribution of amplitudes over the scattering angles (Hessel and Oliner, 1965).

The resonant scattering by WECs in a periodic array gives rise to a *local* bandgap near the resonant frequency, where the array prohibits transmission (Raghavan and Phani, 2013). The manipulation of local bandgaps by the tuning of resonant sub-elements has seen widespread application outside of ocean wave energy capture to control wave propagation. The so-called *metamaterials* make use of resonances to engineer transmission properties using sub-wavelength structures (Li et al., 2016; Sheng et al., 2003). Mathematically, the Bloch–Floquet problem describes the change in phase and/or amplitude as the associated Bloch waves traverse one period (*unit cell*) in a periodic array (Linton and McIver, 2001). This information is contained in the eigenvalues, where the associated Bloch wavenumber determines the band structures (passbands and bandgaps), or dispersion characteristics, which are typically depicted by dispersion curves (Ashcroft and Mermin, 1976).

The local bandgap does not rely on periodicity, but a minimum number of resonators may be necessary to incur a bandgap (Raghavan and Phani, 2013; Sheng et al., 2003). Consequently, gradually varying (*grading*) the resonant properties within the array (e.g., through geometry or an external mechanism) modifies the associated local dispersion relations of neighbouring unit cells, creating spatially controlled frequency separation and broadband wave control over an extended, *effective* local bandgap (Soliman et al., 2025). Frequencies lying within the effective bandgap can propagate into the graded array up until a set distance, which is governed by the resonances (Bennetts et al., 2018), unlike periodic arrays where bandgaps only support exponentially decaying, evanescent waves (Romero-García et al., 2013).

The group velocity decreases to zero as frequencies approach the interface between passbands and bandgaps (*band edge*), causing localised amplifications as energy accumulates at the respective band edge, before being reflected back out of the array (Romero-García et al., 2013). At frequencies above these turning points, the wave cuts-off, prohibiting propagation (Bennetts et al., 2018). To permit a wide range of frequencies to propagate into the array, the cut-offs must be ordered from high to low in the direction of the incident waves, which is controlled through the resonances. The resulting *rainbow reflection* derives its name from optics, due to the spatial separation of frequency components in light spectra (Tsakmakidis et al., 2007). If the grading is sufficiently gradual, the behaviour of the wavefield at a particular location in the array can be inferred from the properties of the local unit cell (particular resonator), as if the array were uniform (Bennetts et al., 2018, 2019; Chaplain et al., 2020).

Efficient, broadband absorption is achieved by tuning an energy extracting mechanism to capture the reflected wave energy at the graded cut-off points in a process known as *rainbow trapping* (Chaplain et al., 2020; Romero-García, Theocharis, Richoux and Pagneux, 2016). The resonant oscillations of a periodic row of (non-absorbing) heaving buoys can generate zero transmission (full reflection) at a frequency near resonance (Tokić and Yue, 2019), which is a

necessary condition for 100% efficiency (Evans, 1981b). However, symmetric radiation cannot simultaneously cancel reflected waves (Falnes, 2005). Consequently, perfect absorption at a single frequency requires two rows of resonators: one to cancel transmission and the other, reflection (Jiménez et al., 2017b). An analogy can be drawn to employing a periodic row of non-absorbing oscillators as a reflector for enhanced power capture at particular frequencies in the water-wave context (e.g., Tokić and Yue, 2023). Similarly, positioning arrays in front of a vertical cliff face or breakwater, prevents transmission, leading to twice the power capture (Falnes and Hals, 2012), which can be likened to rigidly-backed systems in acoustics (e.g., Romero-García, Theocharis, Richoux, Merkel, Tournat and Pagneux, 2016).

Nonetheless, near-perfect broadband absorption has been obtained using mono-polar resonators in non-rigidly backed systems (allow transmission) in acoustics, by tuning the radiation losses of the array for critical coupling (complex zeros of reflection located on the real-axis (Romero-García, Theocharis, Richoux and Pagneux, 2016)) to coincide with zeros in transmission (Jiménez et al., 2017b). Excepting the backmost resonator (which is non-absorbing), each resonator is critically coupled to the exterior medium within the local bandgap induced by the successive, lower-frequency resonator, to create a rainbow trapping array (Jiménez et al., 2017a,b). The concept of grading arrays for rainbow trapping has found recent application in efficient, broadband and wide-angle absorption in solar cells (e.g., Feng et al., 2024), acoustics (e.g., Ryoo et al., 2024), and broadband, piezoelectric energy harvesting (e.g., Tang et al., 2025) amongst others (e.g., see Soliman et al., 2025).

Applications in the water-wave context were initiated by Bennetts et al. (2018) demonstrating spatially controlled amplifications of wave energy over a broad frequency range by grading a small array of non-absorbing, C-shaped cylinders. The rainbow reflection predicted by linear theory was later confirmed by experimental validation and CFD simulations, in spite of nonlinear wave breaking and viscous effects occurring around localised amplifications, which were overestimated by linear theory (Archer et al., 2020; Xu et al., 2024; Zhou and Song, 2025). Insight into energy amplifications and patterns in finite arrays can be gained from analysing how the eigenvalues of the transfer matrix for a unit cell (approximate the Bloch wavenumber for a stack (Porter and Porter, 2003)) evolve with grading (Bennetts et al., 2018, 2019).

Graded arrays demonstrate considerable potential for efficient, broadband absorption of ocean wave energy. Wilks et al. (2022) proposed the first rainbow absorbing WEC-array by grading surface-piercing, rigid, vertical barriers using a 2D, linear model of wave–structure interactions. Near-perfect, broadband absorption of 4–8 s ocean waves was obtained by augmenting the array with heaving pistons attached to linear dampers, and optimising the array's geometry (Wilks et al., 2022). This 'pan-flute' structure (successive barriers extend further throughout the water depth) can be achieved by integrating oscillating water columns into a

breakwater for broadband capture and coastal protection (Hu et al., 2025; Zhao et al., 2023). Graded designs have also inadvertently emerged in control co-design strategies when geometry is allowed to vary (e.g., Ermakov et al., 2025); for hinged, multi-float devices (e.g., Stansby et al., 2015); and when simultaneously optimising layout and PTOs (Wilks et al., 2025).

Bandgaps could further be utilised for coastal protection. For example, dikes composed of arrays of (non-absorbing) C-shaped resonators have been designed to attenuate periods associated with storm swell (10–20 s) over a range of wave directions, but permit transmission of frequencies associated with normal sea states, so that coastal protection is only activated in appropriate conditions (Dupont et al., 2017). Experimental validation demonstrated that the bandgaps remain effective with strong non-linearities, including viscous effects and wave breaking (Dupont et al., 2017). Moreover, graded arrays of non-absorbing C-shaped resonators have experimentally demonstrated broadband attenuation exceeding linear theory predictions, possibly as a result of non-linearities (Cao, Chen, Ning, Peng, Xu and Lin, 2025).

Similarly, generating Bragg resonance using bottom-fixed, submerged (non-resonant) bars has been explored as an alternative to breakwaters, with graded arrays again shown to broaden bandgaps (e.g., Xie et al., 2025; Xu et al., 2023). Utilising both local and Bragg bandgaps in periodic arrays of non-absorbing resonators produces substantial wave attenuation for coastal protection, with a greater number of devices and viscous dissipation often assisting this capability (Calvo et al., 2025; Lorenzo et al., 2023; Zhang et al., 2024). Recent interest in combining local and Bragg bandgaps into a super bandgap, or using local bandgaps to bridge or break Bragg bandgaps (e.g., Cenedese et al., 2021; Cleante et al., 2022; Guo et al., 2020), could offer a greater ability and flexibility to tailor arrays for coastal protection.

1.2.3 WEC-arrays in coastal protection

Over the last decade, an increasing number of studies have demonstrated the ability of WECs to provide coastal protection as a by-product of power capture, through significant, albeit wide ranging, reductions in transmission (10–50%), which are typically used to quantify coastal protection capability (Boodoo et al., 2025). The ability of WECs to protect against erosion (through modified sediment transport) incurred by flooding (Bergillos, Rodriguez-Delgado, Allen and Iglesias, 2019b), storm swells (Abanades et al., 2018, 2014), or longshore drift (Mendoza et al., 2014), among others, depends on the alongshore location (Abanades et al., 2015; Bergillos et al., 2018), inter-device spacing (Rodriguez-Delgado et al., 2019), WEC geometry (Bergillos, Rodriguez-Delgado, Allen and Iglesias, 2019a,b), layout of the array (Carballo and Iglesias, 2013), as well as the energy content of the sea state and wave direction (Bergillos, Rodriguez-Delgado and Iglesias, 2019; Boodoo et al., 2025)—alterations to which, can severely worsen erosion (Mortlock et al., 2017). In these coastal protection studies, the

WECs are typically modelled as obstacles with a set transmission percentage (estimated from numerical models or experiments), and their resonant properties and hydrodynamic interactions are neglected (Boodoo et al., 2025; Zanuttigh et al., 2015).

Models that incorporate hydrodynamic interactions between WECs support the possibility of low protection (transmission reduced by 10%) at the expense of efficient power capture (Battisti et al., 2024). Given that transmission is not the sole predictor of shoreline response, experimental results have indicated that sediment accretion requires a threshold reduction in transmission to be reached, failing which, offshore migration of sediment can occur (Cohen, 2025). The ability to adapt to real-time conditions through dynamic control, raises the possibility of altering the objective depending on the sea state, prioritising either power capture, or coastal protection, so as to fulfil the required function effectively (Battisti et al., 2024; Boodoo et al., 2025). Entirely separate modes of operation were further proposed by Cui et al. (2024), who optimised an array for coastal protection in the absence of power capture.

There is a general consensus that compact (closely-spaced), multi-row, nearshore arrays are best-suited to deliver coastal protection (Boodoo et al., 2025; Carballo and Iglesias, 2013). A nearshore location reduces installation and operating costs, but also power capture due to less energetic conditions, and potentially has a greater environmental impact (Cao, Shi, Zheng, Zhang and Pan, 2025; Carballo and Iglesias, 2013; Zanuttigh et al., 2015). However, offshore locations risk the regeneration of wave energy by wind or shoaling and diffraction around the array, thwarting any protection capability (Carballo and Iglesias, 2013; Mendoza et al., 2014). A separate coastal protection mode of operation may allow for less compact arrays, located further from the coastline (Cui et al., 2024). Although providing dual functionality will increase the economic viability of WECs (Clemente et al., 2021; Foteinis and Tsoutsos, 2017), achieving a reasonable degree of coastal protection could compromise efficient power capture (Battisti et al., 2024; Boodoo et al., 2025; Zanuttigh et al., 2015), which is typically the primary objective associated with the design of WEC-arrays in the literature.

1.3 Research problem

The question of how to design arrays for efficient power capture in broadband and directionally spread, variable ocean wave climates, is complex and still largely unresolved. This thesis aims to address the problem of generating strategies for efficient broadband absorption of ocean wave energy that are robust to wave direction, by grading the resonant properties of an array of heaving buoys for rainbow absorption, via the PTO mechanisms. The objectives are:

(i) To achieve rainbow absorption in a 2D model of an idealised WEC-array by grading the resonances for rainbow reflection, and choosing the PTO damping for near-perfect,

broadband absorption, which remains effective in irregular sea states, and robust to the release of non-absorbing modes of motion;

(ii) To extend the mathematical model to 3D and develop analogous strategies for an array composed of a finite number of stacks when accounting for wave direction, and contextualise the performance of graded finite arrays, obtained by truncating periodic rows, through comparisons with uniform arrays in irregular sea states;

(iii) To analyse how a drag correction impacts strategies by reducing resonant amplifications.

It is hypothesised that graded arrays could provide coastal protection in conjunction with high efficiency, broadband power capture in realistic wave climates, as a rainbow absorbing design creates a broad bandgap with little-to-no transmission, which aligns with the typical objective of coastal protection literature. Without physical, vertical barriers to prevent transmission, the array will rely on destructive interference to create bandgaps, which can be tailored to a particular wave climate. To provide both functions in a single mode of operation, wave periods of approximately 10–20 s are targeted, which comprise two thirds of usable ocean wave frequencies for power production (5–20 s; (Coe et al., 2017)), and are associated with storm swells responsible for erosion events (Dupont et al., 2017).

1.3.1 Significance and contribution

The primary contribution of this thesis is the development of strategies for broadband absorption which use fixed PTO parameters, avoiding the need for accurate, short-term forecasts and dynamic control methods, which are sensitive to model errors, and increase cost and system complexity. The theoretical approach aims to advance the understanding of how WEC-arrays could be designed for broadband capture to increase cost-effectiveness; provide insight into the factors governing the effectiveness of strategies for broadband absorption; and aid the development of a framework for constructing viable arrays using efficient computational methods.

Array designs that are relevant for coastal protection may enhance economic viability. The ability to protect coastlines while operating with broadband efficiency has significance for dual-purpose arrays, where dynamic control is currently required to alternate between power capture and coastal protection, as low power capture is required to appreciably reduce transmission (Battisti et al., 2024; Cui et al., 2024). The potential for bandgaps created by graded arrays to be maintained over a range of wave directions will also benefit coastal protection strategies, as an altered wave direction can worsen erosion (e.g., Mortlock et al., 2017).

1.3.2 Scope and thesis outline

To facilitate the use of computationally efficient, semi-analytical methods, heaving buoys are modelled as truncated cylinders (or squares in 2D), and are equipped with negative stiffness mechanisms[2] to access low ocean wave frequencies. The WEC dimensions, PTO parameters, and installation depth are inspired by CorPower Ocean's (2024) state-of-the-art C4 device. Unless otherwise specified, WECs are restricted to heave motion. This is considered a reasonable assumption for power capture as the PTO is designed to maximise coupling and power generation in heave, while remaining almost insensitive to surge and pitch motions.

Like other studies in the realm of concept development, linear potential-flow theory is applied, assuming the WECs undergo small amplitude oscillations relative to their dimensions, in waves of low steepness. Linear wave theory is generally assumed to be an acceptable approximation in typical operational conditions for wave energy conversion (Falnes and Kurniawan, 2020; Ringwood et al., 2023). However, WEC amplifications at resonance can severely restrict the steepness of acceptable incident waves for solutions to remain valid. Despite losing accuracy outside these bounds, analyses are typically conducted using linear theory, due to the complexity associated with applying higher-order wave models (Pecher and Kofoed, 2017).

Preliminary theory is outlined in Chapter 2 to introduce the concepts that are used to analyse the behaviour of a WEC-array. A 2D model is introduced in Chapter 3 to develop theoretical insight into how strategies for broadband absorption can be generated, and to understand the properties which govern their success. The heave restriction is relaxed to demonstrate the wider applicability of the strategies. Chapter 4 progresses to a 3D model. First, a computationally efficient model of a periodic array composed of diffraction gratings is used to determine a grading for high efficiency, broadband absorption over a wide range of incident wave directions. The array is later truncated, introducing edge effects with impact power capture and sensitivity to direction. Comparisons to uniform arrays are made to contextualise the performance of a finite, graded array.

A drag correction is incorporated into the 3D model in Chapter 5 to identify how drag alters the resonant motions of heaving buoys within a linear framework, and the impact that this has on rainbow absorption. The array properties that lead to efficient capture over broad frequency and directional bands are summarised in Chapter 6. The impact that WEC properties have on performance is discussed with the aim of guiding future work, which may seek to address idealisations or model different WEC concepts. Comments are made on the potential for graded arrays in coastal protection strategies, and future directions to investigate the effect on coastlines.

[2]The use of positive or negative stiffness depends on the WEC's natural frequency relative to the targeted wavelengths, and will not alter the methods and approach developed to grade arrays for broadband absorption.

Chapter 2

Preliminaries

This chapter introduces the models, methods, and key concepts used to analyse arrays of heaving buoys in two- and three-dimensions (2D and 3D, respectively), and to facilitate the development of strategies for broadband absorption. The underlying theory is widely applied to wave–structure interactions, and extends naturally between 2D and 3D. For specificity, a 3D perspective is assumed here, and links to 2D are outlined. The intuitive relationship between the 2D and 3D models is depicted in Figure 2.1, along with the key terminology. Derivations specific to the 2D and 3D models are given in Chapters 3 and 4, and the associated Appendices A and B, respectively, noting that notation is specific to each chapter.

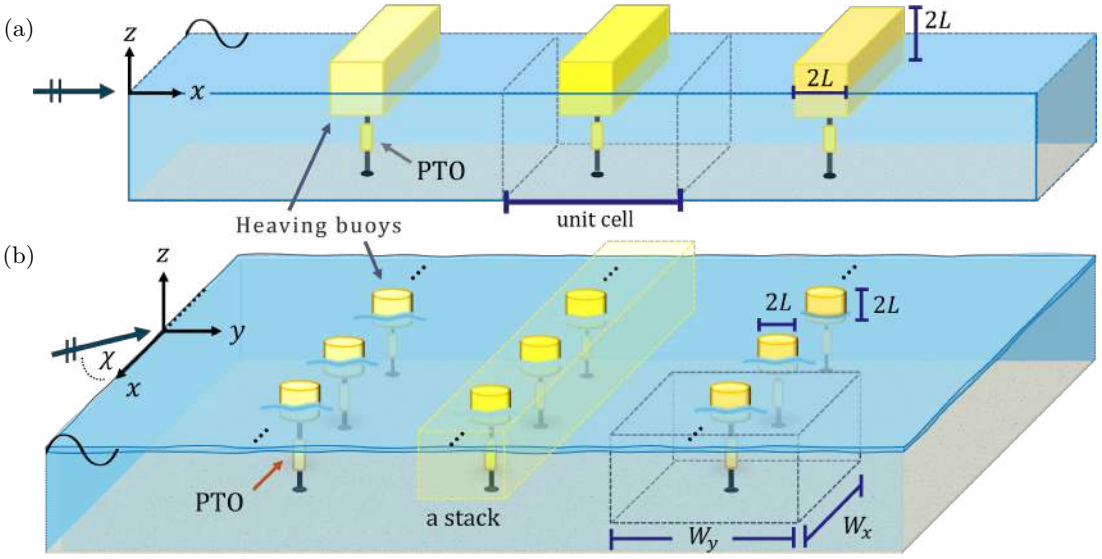

Figure 2.1: The arrays consists of a finite number of (a) WECs in 2D or (b) stacks in 3D which are graded for broadband absorption in Chapters 3 and 4, respectively. Each stack contains infinitely many, identical heaving buoys, attached to a PTO. The incident wave travels left-to-right (noting that the view of (b) is rotated by 90 degrees in the clockwise direction in comparison to (a)).

2.1 Modelling the resource

The ocean surface is often approximated as a linear superposition of infinitely many sinusoidal waves, composed of different frequencies, amplitudes, directions, and randomly distributed phases, in non-steep and non-breaking waves (Pecher and Kofoed, 2017). Assuming linearity, an irregular wavefield is decomposed into the individual frequency components (regular waves)

in the frequency domain via a Fourier transform (Korde and Ringwood, 2016). The Cartesian coordinate system (x, y, z) is applied to the 3D fluid domain Ω, which extends infinitely in the horizontal directions. The z-axis is directed out of the water, which is governed by potential-flow theory (incompressible, inviscid and irrotational). Applying conservation of mass, the scalar velocity potential Φ satisfies Laplace's equation (Falnes, 2005; Mei et al., 2005),

$$\nabla^2\Phi(x,y,z,t) = 0 \quad \text{on} \quad \Omega = \{(x,y,z) : x \in \mathbb{R}, y \in \mathbb{R}, -h \leq z \leq \eta(x,y,t)\}\,, \tag{2.1}$$

subject to no-normal flow at the finite depth (h), impermeable seabed,

$$\frac{\partial\Phi}{\partial z} = 0 \quad \text{at} \quad z = -h. \tag{2.2}$$

Conservation of momentum is applied at the air-water interface, defined by the free surface $z = \eta(x, y, t)$. Neglecting surface tension and the motion of air (due to its comparatively low density), the pressure is assumed to be constant and continuous across the interface, so that the free surface satisfies the dynamic condition described by Bernoulli's equation (Linton and McIver, 2001; Mei et al., 2005)

$$\frac{\partial\Phi}{\partial t} + \frac{1}{2}|\nabla\Phi|^2 + g\eta = 0 \quad \text{on} \quad z = \eta(x,y,t), \tag{2.3}$$

where $g = 9.81\,\mathrm{m\,s^{-2}}$ is gravitational acceleration. The free surface further satisfies a kinematic boundary condition to ensure that the vertical speed of fluid particles is equivalent to the free surface (particles do not cross the interface) (Linton and McIver, 2001)

$$\frac{\partial\eta}{\partial t} + \frac{\partial\Phi}{\partial x}\frac{\partial\eta}{\partial x} + \frac{\partial\Phi}{\partial y}\frac{\partial\eta}{\partial y} = \frac{\partial\Phi}{\partial z} \quad \text{on} \quad z = \eta(x,y,t). \tag{2.4}$$

The kinematic and dynamic free surface conditions are linearised about the undisturbed state $z = \eta(x, y, t) = 0$ assuming small wave amplitudes relative to the wavelength (non-steep), and combined to form the free surface condition (Linton and McIver, 2001; Mei et al., 2005)

$$\frac{\partial^2\Phi}{\partial t^2} + g\frac{\partial\Phi}{\partial z} = 0 \quad \text{on} \quad z = 0. \tag{2.5}$$

2.2 Wave–structure interactions

The wave–structure interactions in an array of WECs are constructed from the scattering[1] characteristics of a single, isolated device using multiple wave scattering theory. In periodic arrays, this forms the basis of the unit cell. Heaving buoys are modelled as floating, truncated cylinders with radius L and draught L, attached to a PTO mechanism (Figure 2.1). The fluid

[1]Defined as the combined diffraction and radiation in this thesis, unlike e.g., Linton and McIver (2001).

is assumed to undergo time-harmonic motion with amplitude A^{inc} at radian frequency ω,

$$\Phi = \Phi^{\mathrm{inc}} + \underbrace{\Phi^{\mathrm{diff}} + \Phi^{\mathrm{rad}}}_{\Phi^{\mathrm{scat}}} = \mathrm{Re}\left\{ \frac{gA^{\mathrm{inc}}}{\mathrm{i}\omega} \left(\phi^{\mathrm{inc}} + \phi^{\mathrm{diff}} + \zeta \phi^{\mathrm{rad}} \right) e^{-\mathrm{i}\omega t} \right\}, \tag{2.6}$$

where $\mathrm{i} = \sqrt{-1}$ is the imaginary number and ζ is the complex ($\in \mathbb{C}$) heave amplitude. Because of linearity, the velocity potential can be decomposed into incident ($^{\mathrm{inc}}$), diffracted ($^{\mathrm{diff}}$) and radiated ($^{\mathrm{rad}}$) components (noting that $gA^{\mathrm{inc}}/(\mathrm{i}\omega)$ is factored out of the right-hand side of Equation (2.6)). The solution to the diffraction problem is obtained by holding the WEC fixed in the incident waves, while the WEC undergoes forced, heave oscillations in the absence of an incident wave in the radiation problem, with normal velocity $\dot{\xi}(t) = \mathrm{Re}\left\{-\mathrm{i}\omega\zeta \mathrm{e}^{-\mathrm{i}\omega t}\right\}$. The respective boundary conditions on the wetted surface of the WEC (S_B) follow as

$$\frac{\partial \Phi^{\mathrm{diff}}}{\partial n} = -\frac{\partial \Phi^{\mathrm{inc}}}{\partial n} \quad \text{and} \quad \frac{\partial \Phi^{\mathrm{rad}}}{\partial n} = \dot{\xi}(t) \quad \text{on} \quad S_B, \tag{2.7a, b}$$

where $\dot{\xi}(t)$ is determined from the equation of motion (depends on the excitation force of the incident waves) (Linton and McIver, 2001). The diffraction and radiation potentials satisfy radiation conditions in the far field (outgoing at infinity) (Linton and McIver, 2001).

Wave–structure interactions are coupled through the forces exerted on the WEC by the surrounding fluid, which is incorporated through the equation of motion (Mei et al., 2005)

$$\mathfrak{M}\,\ddot{\xi} + B_{\mathrm{PTO}}\,\dot{\xi} + (\mathfrak{C} + C_{\mathrm{PTO}})\xi = -\rho \iint_{S_B} \frac{\partial \Phi}{\partial t} n \mathrm{d}S, \tag{2.8}$$

where $\rho = 1025\,\mathrm{kg\,m^{-3}}$ is the water density and $\xi(t) = \mathrm{Re}\left\{\zeta \mathrm{e}^{-\mathrm{i}\omega t}\right\}$ is the instantaneous heave. The WEC has mass $\mathfrak{M}$ (kg) with hydrostatic stiffness $\mathfrak{C}$ ($\mathrm{N\,m^{-1}}$), and the PTO mechanism is modelled as a linear spring–damper with stiffness C_{PTO} and damping B_{PTO}. The hydrodynamic forces on the WEC are found by integrating the pressure over the wetted surface with respect to the component of the unit normal vector to the WEC associated with heave (n), and decomposing it into diffracted and radiated components (Mei et al., 2005)

$$-\rho \iint_{S_B} \frac{\partial \Phi}{\partial t} n \mathrm{d}S = -\rho \iint_{S_B} \frac{\partial \Phi^{\mathrm{diff}}}{\partial t} n \mathrm{d}S - \rho \iint_{S_B} \frac{\partial \Phi^{\mathrm{rad}}}{\partial t} n \mathrm{d}S \quad \text{at} \quad z = -L. \tag{2.9}$$

The radiation forcing is separated into the components that are in phase with the acceleration and velocity of the WEC, respectively (Linton and McIver, 2001; Mei et al., 2005),

$$\begin{aligned} -\rho \iint_{S_B} \frac{\partial \Phi^{\mathrm{rad}}}{\partial t} n \mathrm{d}S &= -\left(\frac{\rho g}{\omega^2} \iint_{S_B} \mathrm{Re}\left\{ \phi^{\mathrm{rad}} \right\} n \mathrm{d}S \right) \ddot{\xi} - \left(\frac{\rho g}{\omega} \iint_{S_B} \mathrm{Im}\left\{ \phi^{\mathrm{rad}} \right\} n \mathrm{d}S \right) \dot{\xi} \\ &= -a(\omega)\ddot{\xi} - b(\omega)\dot{\xi}. \end{aligned} \tag{2.10}$$

The added mass $a(\omega)$ describes the increased inertia of the WEC given it is in water, while

the radiation damping $b(\omega)$ describes the energy lost to radiating waves. The diffraction component corresponds to the excitation force of the incident waves (Mei et al., 2005)

$$-\rho \iint_{S_B} \frac{\partial \Phi^{\text{diff}}}{\partial t} n \, \mathrm{d}S = \mathrm{Re}\left\{ F^{\text{exc}} \, \mathrm{e}^{-\mathrm{i}\omega t} \right\}. \tag{2.11}$$

2.3 A single WEC

The diffraction and radiation properties of an isolated WEC are encapsulated by a *diffraction transfer matrix* $\boldsymbol{B}$ (Appendix B.1) which describes how an incident wave will be scattered by a WEC. The eigenfunction expansion matching method (Linton and McIver, 2001) is applied to determine $\boldsymbol{B}$. The WEC is placed at the origin of the coordinate system, and divides the fluid domain into an interior region ($^{\text{I}}$) below the WEC, and an exterior ($^{\text{E}}$) region surrounding the WEC, which is demarcated by the sides of the WEC. In 2D, there are two external regions, defined by $-\infty < x \leq -L$ and $L \leq x < \infty$ in Cartesian coordinates. The interface between the internal and external regions occurs at the cylinder's radius $r = L$ in 3D, defined by a local cylindrical coordinate system (r, θ, z) with $x = r\cos(\theta)$ and $y = r\sin(\theta)$.

The complex-valued potential ϕ is found using separation of variables, and is expressed as an eigenfunction expansion in each region. The unknown coefficients of the expansions are obtained by matching the solutions across the interface(s) between interior and exterior regions by applying dynamic and kinematic boundary conditions (Linton and McIver, 2001),

$$\phi^{\text{E}} = \phi^{\text{I}} \qquad \text{on } z \in (-h, -L) \tag{2.12}$$

$$\frac{\partial \phi^{\text{E}}}{\partial r} = \begin{cases} \dfrac{\partial \phi^{\text{I}}}{\partial r} & \text{for} \quad z \in (-h, -L), \\ 0 & \text{for} \quad z \in (-L, 0), \end{cases} \tag{2.13}$$

to enforce continuity of pressure and horizontal velocity, respectively. Equations (2.12) and (2.13) are multiplied by test functions consistent with appropriate vertical eigenfunctions in the respective regions, and integrated over the corresponding water depth (Linton and McIver, 2001). The number of modes is truncated according to the desired level of accuracy.

Given an incident wavefield with amplitudes (in a Fourier–Bessel expansion; Chapter 4) contained in the vector $\boldsymbol{C}$, the diffraction transfer matrix $\boldsymbol{B}$ is defined such that $\boldsymbol{D} = \boldsymbol{B}\boldsymbol{C}$, where $\boldsymbol{D} = \boldsymbol{D}^{\text{diff}} + \zeta \boldsymbol{D}^{\text{rad}}$ is the vector of amplitudes for the scattered potential $\phi^{\text{scat}} = \phi^{\text{diff}} + \zeta\phi^{\text{rad}}$. Grouping the unknown diffraction coefficients in Equations (2.12) and (2.13) on the left, and the incident amplitudes on the right, the diffraction problem is symbolically written as (Martin, 2006)

$$\tilde{\boldsymbol{\Upsilon}} \begin{bmatrix} \boldsymbol{D}^{\text{diff}} \\ \boldsymbol{d}^{\text{diff}} \end{bmatrix} = \tilde{\boldsymbol{\Psi}} \begin{bmatrix} \boldsymbol{C} \\ \boldsymbol{C} \end{bmatrix}, \tag{2.14}$$

where $\boldsymbol{d}^{\text{diff}}$ are the unknown amplitudes beneath the WEC (Appendix B.1). The matrices $\tilde{\boldsymbol{\Psi}}$ and $\tilde{\boldsymbol{\Upsilon}}$ are derived from the incoming and outgoing waves, respectively, in combination with multiplication by the respective test functions (Appendices A.1 and B.1). The matrix defined by $\boldsymbol{B}_{\text{diff}} = \tilde{\boldsymbol{\Upsilon}}^{-1}\tilde{\boldsymbol{\Psi}}$ encapsulates the diffraction properties of the WEC.

Assuming unit amplitude oscillation ($\zeta = 1\,\text{m}$), a system of equations for the radiation problem is given by

$$\tilde{\boldsymbol{\Upsilon}} \begin{bmatrix} \boldsymbol{D}^{\text{rad}} \\ \boldsymbol{d}^{\text{rad}} \end{bmatrix} = \boldsymbol{v} \tag{2.15}$$

where $\boldsymbol{v}$ is the particular solution (from Equation (2.7b)) and $\boldsymbol{d}^{\text{rad}}$ are the unknown radiation amplitudes beneath the WEC. Expressing the excitation force in terms of the incident wave as $F^{\text{exc}} = \boldsymbol{f_e}\boldsymbol{C}$, the complex amplitudes associated with heave motion are written as

$$\boldsymbol{\zeta} = \left[-\omega^2(\mathfrak{M} + a(\omega)) - \mathrm{i}\omega\left(b(\omega) + B_{\text{PTO}}\right) + \left(\mathfrak{C} + C_{\text{PTO}}\right)\right]^{-1} \boldsymbol{f_e} \tag{2.16}$$

so that $\zeta \boldsymbol{D}^{\text{rad}} = \tilde{\boldsymbol{\Upsilon}}^{-1}\boldsymbol{v}\boldsymbol{\zeta}\boldsymbol{C}$. Consequently, the matrix defined by $\boldsymbol{B}_{\text{rad}} = \tilde{\boldsymbol{\Upsilon}}^{-1}\boldsymbol{v}\boldsymbol{\zeta}$ encapsulates the radiation properties of the WEC. The full solution is obtained through superposition, so that $\boldsymbol{B} = \boldsymbol{B}_{\text{diff}} + \boldsymbol{B}_{\text{rad}}$. The $\boldsymbol{B}$ for a 2D WEC is referred to as a scattering matrix, and contains the reflection and transmission properties of the WEC (Appendix A.1). While the $\boldsymbol{B}$ fulfils the same function, the term scattering matrix is reserved for a periodic row of WECs in 3D (§ 2.4.1), where the reflection and transmission have closer analogy to the 2D problem.

2.3.1 Power capture and efficiency

The resonant frequency of a WEC is given by non-trivial solutions to the equation of motion in the absence of forcing, and is tuned to a prescribed frequency ω_0 by setting

$$C_{\text{PTO}} = \omega_0^2\left(\mathfrak{M} + a(\omega)\right) - \mathfrak{C}. \tag{2.17}$$

The time-averaged power captured by a WEC is calculated from (Folley, 2016)

$$\mathcal{P} = \frac{1}{2} B_{\text{PTO}} |-\mathrm{i}\omega\zeta|^2, \tag{2.18}$$

where optimising the PTO damping for maximum power ($\mathcal{P}_{\max}$) at resonance yields

$$B^{\text{opt}}_{\text{PTO}}\Big|_{\omega=\omega_0} = \sqrt{b(\omega)^2 + \left(\omega\left(\mathfrak{M} + a(\omega)\right) - \left(\mathfrak{C} + C_{\text{PTO}}\right)/\omega\right)^2}\,\Big|_{\omega=\omega_0} = b(\omega_0). \tag{2.19}$$

The power captured is related to the ability of the WEC to radiate waves which destructively interfere with the incident wave (Falnes, 2005). Applying reciprocity relations (from Haskind's relations), the maximum power capture at resonance can be expressed in terms of the power

in a unit width of the incident wave crest as (Falnes, 2005; Mei et al., 2005)

$$\mathcal{P}_{\max} = |F^{\text{exc}}|^2 / \left[8b(\omega_0)\right] = \frac{1}{2k_0}\,\rho g\,|A^{\text{inc}}|^2\,\frac{\omega}{2k_0}\left(1+\frac{2k_0h}{\sinh(2k_0h)}\right). \tag{2.20}$$

The ratio of absorbed to available power defines the WEC's capture width (Mei et al., 2005),

$$CW = \frac{1}{k_0} = \frac{\lambda}{2\pi}, \tag{2.21}$$

and depends on the wavenumber k_0 (wavelength λ), which is the real root of the dispersion equation, obtained from the linearised free surface condition (Linton and McIver, 2001). The theoretical maximum for heave does not depend on the WEC dimensions (Mei et al., 2005). However, radiation damping decreases with decreasing wavenumber and WEC dimensions ($B^{\text{opt}}_{\text{PTO}} = b(\omega_0)$), implying that the smaller a WEC, or the lower the frequency, the larger the amplitudes required for maximum efficiency (Mei et al., 2005). This can be seen in Figure 2.2 (§ 2.3.2), where the optimal velocities of WECs tuned to $\omega_0 = 0.3\,\text{rad}\,\text{s}^{-1}$ and $\omega_0 = 0.65\,\text{rad}\,\text{s}^{-1}$, respectively, satisfy $|-\text{i}\omega_0\zeta| = |F^{\text{exc}}/2b(\omega_0)|$ at resonance (Falnes, 2005).

2.3.2 Drag correction

Large WEC amplitudes contradict the assumptions of linear theory. As the incident amplitude increases and frequencies approach resonance, non-linear effects like drag become increasingly relevant, and undermine the validity and accuracy of linear models (Folley, 2016; Giorgi and Ringwood, 2017). Drag effects can be separated into viscous drag, which arises from skin friction as the fluid viscosity acts on the surface of a body undergoing small-amplitude oscillations, and pressure drag, resulting from flow separation, turbulence and vortex shedding, which become prominent as the amplitude increases (Kaneko et al., 2014).

The drag experienced by a WEC is predominantly due to a pressure drag force opposing the motion of the body (Kaneko et al., 2014; Sarpkaya, 2010). The loss of kinetic energy through turbulence and/or vortices (Folley and Whittaker, 2010) can significantly reduce WEC amplitudes (Babarit et al., 2012; Folley, 2016; Giorgi and Ringwood, 2017), and is proportional to the dynamic pressure exerted on the base of the WEC (Clauss et al., 1992),

$$\begin{aligned} F_{\text{drag}}(t) &= \frac{1}{2}C_d\rho\left[\int_{S_B}\left|\frac{\partial\Phi}{\partial z}\right|\frac{\partial\Phi}{\partial z}\,\text{d}S\right]_{z=-L} \\ &= \frac{1}{2}C_d\rho\int_0^{2\pi}\int_0^{L}|\dot{\xi}(t)|\dot{\xi}(t)r\,\text{d}r\,\text{d}\theta \\ &= \frac{1}{2}C_d\rho\pi L^2|\dot{\xi}(t)|\dot{\xi}(t) \end{aligned} \tag{2.22}$$

where the absolute value is to ensure drag opposes the WEC motion (Sarpkaya, 2010). Equation (2.22) is commonly incorporated into idealised models of heaving WECs to serve as an empirical drag correction (Lei et al., 2023; Penalba, Giorgi and Ringwood, 2017).

The drag coefficient C_d relates the total drag experienced to the cross-sectional area of the WEC, and must be fitted to experimental or simulated data (Clauss et al., 1992; Douglas et al., 1986). There is considerable uncertainty associated with identifying an appropriate C_d, which depends on the wave conditions, geometry, experimental scaling and methodology employed (Giorgi and Ringwood, 2017; Molin, 2023; Penalba, Giorgi and Ringwood, 2017).

The drag term is appended to the linearised equation of motion in the time-domain

$$\mathfrak{M}\ddot{\xi} + B_{\mathrm{PTO}}\dot{\xi} + (\mathfrak{C} + C_{\mathrm{PTO}})\xi = -\rho \iint_{S_B} \frac{\partial \Phi}{\partial t}\, n \mathrm{d}S + F_{\mathrm{drag}}(t). \tag{2.23}$$

The velocity $\dot{\xi}(t)$ can feature multiple harmonics due to the non-linearity of Equation (2.22) (Mei et al., 2005). Higher harmonics are typically neglected on the assumption that the velocity at the forcing frequency dominates the response, although this has been criticised and should be verified *a posteriori* (Mei et al., 2005; Molin, 2023; Sarpkaya, 2010). For a WEC in regular waves (exciting force is at a single frequency), the time-averaged power will depend on the first harmonic due to orthogonality of the Fourier series (Elliott et al., 2015).

A drag force which is linearly proportional to the velocity at the driving frequency is defined as $F_{\mathrm{vis}}(t) = b_{\mathrm{vis}}\dot{\xi}(t)$, and derived by requiring the average work done over a period to be equivalent to the non-linear drag force (Korde and Ringwood, 2016; Mei et al., 2005)

$$\frac{1}{T}\int_0^T F_{\mathrm{vis}}\, \dot{\xi}(t)\, \mathrm{d}t = \frac{1}{T}\int_0^T F_{\mathrm{drag}}\, \dot{\xi}(t)\, \mathrm{d}t. \tag{2.24}$$

Writing $\dot{\xi}(t) = |-\mathrm{i}\omega\zeta| \cos(\omega t + \gamma)$, where γ is the phase, and defining $\sigma = \omega t + \gamma$,

$$\int_0^T F_{\mathrm{drag}}\, \dot{\xi}(t)\, \mathrm{d}t = \frac{1}{2}\rho\, C_d\, \pi L^2\, |-\mathrm{i}\omega\zeta|^3\, \frac{1}{\omega}\int_\gamma^{2\pi+\gamma} \left(|\cos(\sigma)| - |\cos(\sigma)| \sin^2(\sigma)\right) \mathrm{d}\sigma \tag{2.25a}$$

$$= \rho\, C_d \pi L^2\, |-\mathrm{i}\omega\zeta|^3\, \frac{4}{3\omega}. \tag{2.25b}$$

(Equation 2.25b is simplified when equated with Equation 2.26b.) Similarly,

$$\int_0^T F_{\mathrm{vis}}\, \dot{\xi}(t)\, \mathrm{d}t = b_{\mathrm{vis}}\, |-\mathrm{i}\omega\zeta|^2 \int_\gamma^{2\pi+\gamma} \cos^2(\sigma)\, \mathrm{d}\sigma \tag{2.26a}$$

$$= \frac{\pi}{\omega}\, b_{\mathrm{vis}}\, |-\mathrm{i}\omega\zeta|^2. \tag{2.26b}$$

Since $b_{\mathrm{vis}} = 4\rho\, C_d\, L^2\, |-\mathrm{i}\omega\zeta|/3$ depends on the unknown ζ, an iterative calculation is defined by

$$b_{\mathrm{vis}}^{(i-1)}\, \dot{\xi}^{(i)} = \frac{4}{3}\rho\, C_d L^2\, |-\mathrm{i}\omega\zeta^{(i-1)}|\, \mathrm{Re}\left\{-\mathrm{i}\omega\zeta^{(i)}\mathrm{e}^{-\mathrm{i}\omega t}\right\} \quad \text{for} \quad i = 1, 2, \ldots, I, \tag{2.27}$$

and justified to be quasi-linear on the basis that a linear system is returned at each iteration i (Molin, 2023), so that the Fourier transform of Equation (2.23) at a single frequency is

$$\left[-\omega^2(\mathfrak{M}+a(\omega))-\mathrm{i}\omega\left(b(\omega)+B_{\mathrm{PTO}}+b_{\mathrm{vis}}^{(i-1)}(\omega)\right)+\mathfrak{C}+C_{\mathrm{PTO}}\right]\zeta^{(i)}(\omega)=F^{\mathrm{exc}}(\omega). \quad (2.28)$$

for $i=1,2,\ldots,I$. An initial estimate, $b_{\mathrm{vis}}^{(0)}=\hat{b}_{\mathrm{vis}}$ is obtained by setting $b_{\mathrm{vis}}=0$ in Equation (2.28), and Algorithm 1 is implemented until a prescribed convergence criteria is met.

Algorithm 1: The iterative process to determine b_{vis} and ζ (Bacelli and Ringwood, 2013).

while $|b_{\mathrm{vis}}-\hat{b}_{\mathrm{vis}}|>0.1$, **let** $b_{\mathrm{vis}}=\hat{b}_{\mathrm{vis}}$;

Determine $\zeta=\left[-\omega^2(\mathfrak{M}+a(\omega))-\mathrm{i}\omega\left(b(\omega)+B_{\mathrm{PTO}}+b_{\mathrm{vis}}(\omega)\right)+\mathfrak{C}+C_{\mathrm{PTO}}\right]^{-1}F^{\mathrm{exc}}$;

Update $\hat{b}_{\mathrm{vis}}=\frac{4}{3}\rho\,C_d L^2\,|-\mathrm{i}\omega\zeta|$;

end

The drag correction reduces the WEC amplitudes around resonance, as illustrated in Figure 2.2. The absolute and proportional reduction is greater at lower frequencies where larger WEC motions are subject to higher drag, as b_{vis} depends on the WEC amplitudes.

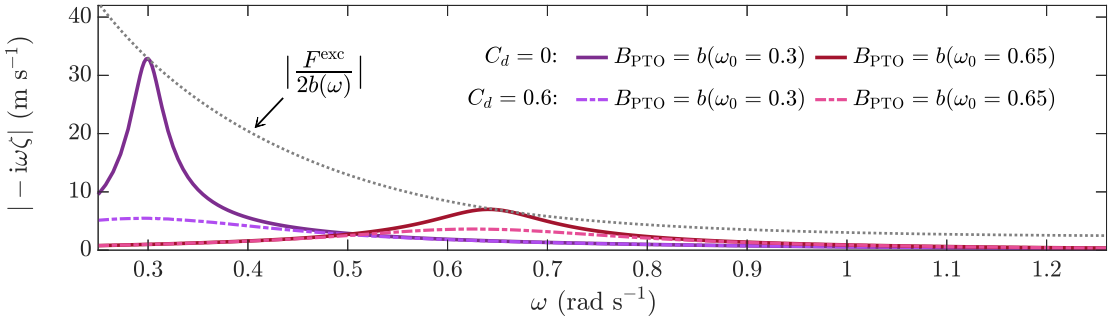

Figure 2.2: The velocities $|-\mathrm{i}\omega\zeta|$ of WECs tuned to $\omega_0=0.3\,\mathrm{rad\,s^{-1}}$ and $\omega_0=0.65\,\mathrm{rad\,s^{-1}}$ are plotted as a function of frequency when $C_d=0$ (—; no drag), and when $C_d=0.6$ (-·-; with drag). The optimal velocity at each ω when $C_d=0$ is given by $|F^{\mathrm{exc}}/2b(\omega)|$ (····), and is satisfied at resonance.

2.4 Multiple WECs

Multiple scattering theory is applied to model the hydrodynamic interactions in an array based on the scattering properties of the isolated WECs (i.e., no direct hydrodynamic coupling between WECs unlike the popular method described by Falnes (2005)). The solution for a finite array of WECs in 3D is first presented, and then extended to infinitely many WECs in a periodic row (*stack*). The scattering by stacks has strong analogies to a 2D model. The direct matrix method is applied (Kagemoto and Yue, 1986), which extends the approach by Simon (1982) to include evanescent modes. The semi-analytical method is exact in principle, but requires truncation in practice, which is selected according to the desired level of accuracy.

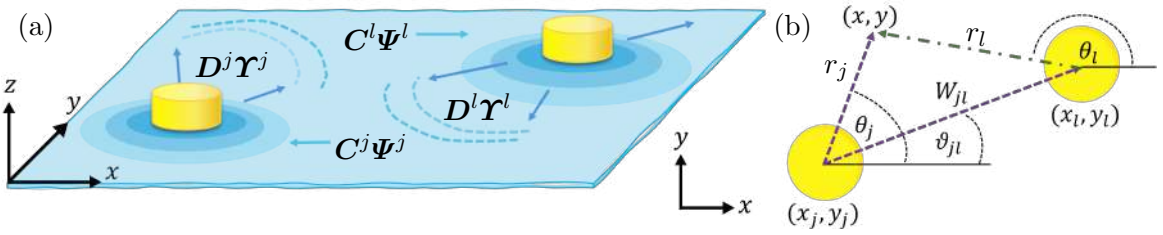

Figure 2.3: The (a) outgoing wavefield $\boldsymbol{D}^j\boldsymbol{\Upsilon}^j$ from WEC j is written as an incoming wavefield $\boldsymbol{C}^l\boldsymbol{\Psi}^l$ in the (b) local coordinates of WEC l using Graf's addition theorem, where (W_{jl}, ϑ_{jl}) specifies the location of WEC l in the local coordinates of WEC j.

The scattered wavefield about WEC j is written in terms of outgoing wave functions $\boldsymbol{\Upsilon}$ as $\phi^{\text{scat}} = \boldsymbol{D}^j\boldsymbol{\Upsilon}^j$ (matrix entries correspond to modes in the expansion). This is transformed into the local incoming wavefield on WEC l using a separation matrix $\boldsymbol{\sigma_{jl}}$ derived from Graf's addition theorem, as $\phi_l^{\text{inc}} = (\boldsymbol{A}^l + \boldsymbol{\sigma_{jl}}\boldsymbol{D}^j)\boldsymbol{\Psi}^l$, where $\boldsymbol{A}^l$ is the vector of ambient incident amplitudes, and $\boldsymbol{\Psi}$ is a regular wave function (Martin, 2006). The location of WEC l in terms of the coordinate system of WEC j is defined by (W_{jl}, ϑ_{jl}) and depicted in Figure 2.3.

A system of equations for the unknown coefficients is derived as (Kagemoto and Yue, 1986)

$$\begin{bmatrix} \boldsymbol{D}^1 \\ \boldsymbol{D}^2 \\ \vdots \\ \boldsymbol{D}^J \end{bmatrix} = \begin{bmatrix} \boldsymbol{B}^1 & 0 & \cdots & 0 \\ 0 & \boldsymbol{B}^2 & 0 & \cdots \\ \vdots & 0 & \ddots & 0 \\ 0 & \cdots & 0 & \boldsymbol{B}^J \end{bmatrix} \left(\begin{bmatrix} \boldsymbol{A}^1 \\ \boldsymbol{A}^2 \\ \vdots \\ \boldsymbol{A}^J \end{bmatrix} + \underbrace{\begin{bmatrix} \boldsymbol{\sigma_{11}} & \boldsymbol{\sigma_{12}} & \cdots & \boldsymbol{\sigma_{1J}} \\ \boldsymbol{\sigma_{21}} & \boldsymbol{\sigma_{22}} & \cdots & \boldsymbol{\sigma_{2J}} \\ \vdots & & \ddots & \vdots \\ \boldsymbol{\sigma_{J1}} & \boldsymbol{\sigma_{J2}} & \cdots & \boldsymbol{\sigma_{JJ}} \end{bmatrix}}_{\boldsymbol{\sigma}} \begin{bmatrix} \boldsymbol{D}^1 \\ \boldsymbol{D}^2 \\ \vdots \\ \boldsymbol{D}^J \end{bmatrix} \right) \tag{2.29a}$$

$$= [\boldsymbol{I} - \operatorname{diag}\left(\boldsymbol{B}^1 \cdots \boldsymbol{B}^J\right)\boldsymbol{\sigma}]^{-1} \operatorname{diag}\left(\boldsymbol{B}^1 \cdots \boldsymbol{B}^J\right) [\boldsymbol{A}^1 \cdots \boldsymbol{A}^J]^\top, \tag{2.29b}$$

where $\boldsymbol{I}$ is the identity matrix. To recover the amplitude of WEC j, the heave amplitude vector $\boldsymbol{\zeta}$ for an isolated WEC (Equation (2.16)) is multiplied by the incident wavefield,

$$\zeta^l = \boldsymbol{\zeta} \sum_{\substack{j=1 \\ j \neq l}}^{J} \boldsymbol{\sigma}_{jl}\boldsymbol{D}^j + \boldsymbol{\zeta}\boldsymbol{A}^l. \tag{2.30}$$

If the array consists of infinitely many identical WECs distributed periodically along the x-axis, with centre-to-centre spacing W_x (m), then $W_{jl} = |j - l|W_x$, for $j \neq l$, and

$$\vartheta_{j-l} = \begin{cases} \pi & \text{for} \quad j > l, \\ 0 & \text{for} \quad j < l. \end{cases}$$

An ambient incident wave propagating at an angle of χ rad with respect to the x-axis is shifted by the phase factor $\mathcal{Q}_j = \mathrm{e}^{\mathrm{i}k_0 j W_x \cos(\chi)}$ at WEC j, so that the amplitudes can be expressed

in terms of the zeroth unit cell (centred at the global origin) as $\boldsymbol{A}^j = \mathcal{Q}_j \boldsymbol{A}^0 = \mathcal{Q}_j \boldsymbol{A}$. The incident and scattered coefficients for any WEC l can similarly be phase shifted, so that the unknown incident field on WEC l can be written in terms of the zeroth cell as (Peter et al., 2006)

$$\boldsymbol{C} = \boldsymbol{A} + \sum_{\substack{j=-\infty \\ j\neq l}}^{\infty} \mathcal{Q}_{j-l} \boldsymbol{\sigma}_{jl} \boldsymbol{D}^j. \tag{2.31}$$

The infinite summation over $j \in \mathbb{Z} \setminus l$ is known as a lattice sum, or Schlömilch series (Linton, 1998), and can be efficiently pre-computed following Peter et al. (2006). The scattered coefficients for the zeroth cell are retrieved by solving (Martin, 2006)

$$\boldsymbol{D} = \boldsymbol{B}\boldsymbol{C} \tag{2.32a}$$

$$= \left[\boldsymbol{I} - \boldsymbol{B}\sum_{j\neq l} \mathcal{Q}_{j-l}\boldsymbol{\sigma}_{jl}\right]^{-1} \boldsymbol{B}\boldsymbol{A}. \tag{2.32b}$$

The velocity potential is the sum of the scattered wavefields of all WECs in terms of their local coordinate systems

$$\phi = \phi^{\text{amb}} + \sum_{j=-\infty}^{\infty} \mathcal{Q}_j \boldsymbol{D}^j \boldsymbol{\Upsilon}^j. \tag{2.33}$$

Constructive interference occurs between the scattered wavefields of the WECs, producing plane waves that propagate away from the stack in a finite number of directions (Falnes and Budal, 1982), described by the scattering angles χ_{mn}, satisfying (Peter and Meylan, 2010)

$$\chi_{mn} = \arccos\left(\frac{\psi_{mn}}{k_n}\right) \quad \text{where} \quad \psi_{mn} = k_n \cos(\chi) + \frac{2m\pi}{W_x}, \quad m \in \mathbb{Z}. \tag{2.34}$$

The number of real-valued scattering angles depends on the incident angle and the spacing W_x relative to the wavelength. The set $\mathcal{M}$ of real scattering angles corresponds to propagating modes, defined by integer values of m where $|\psi_m| < k_0$ (Peter and Meylan, 2010), namely

$$-1 < \cos(\chi) + \frac{2m\pi}{k_0 W_x} < 1 \quad \text{where} \quad k_0 = \frac{2m\pi}{W_x(\pm 1 - \cos(\chi))}, \quad m \in \mathbb{Z}, \tag{2.35}$$

defines the wavenumbers at which real scattering angles cut on, resulting in a redistribution of energy among the scattering angles (Tokić and Yue, 2019). Complex scattering angles correspond to evanescent modes that decay with distance (Mulholland and Heckl, 1994).

Therefore, the periodicity enables the wavefield to be defined by a discrete directional spectrum and represented as a plane-wave expansion (PWE; (Peter and Meylan, 2010))

$$\phi(r,\theta,z) = Z_0(z)\mathrm{e}^{\mathrm{i}k_0 r\cos(\theta-\chi)} + \sum_{n=0}^{\infty} Z_n(z) \sum_{m=-\infty}^{\infty} \mathcal{D}_{mn}^{\pm} \mathrm{e}^{\mathrm{i}k_n r\cos(\theta\mp\chi_{mn})} \quad \text{for } \pm y > L, \tag{2.36}$$

where $Z_n(z)$ are the vertical eigenfunctions and $\mathcal{D}^{\pm}_{mn}$ are the amplitudes of wave modes that propagate or decay in the $\pm$ y–direction (derived from $\boldsymbol{D}$; Appendix B.2). Propagating modes are given by $\chi_{m0} \in \mathbb{R}$, for $m \in \mathcal{M}$, and decaying modes by $\chi_{mn} \in \mathbb{C}$ for $n \geq 0, m \in \mathbb{Z}$. The incoming and outgoing waves before or after a stack are expressed in generalised form as

$$\phi(r,\theta,z) = \sum_{n=0}^{N} Z_n(z) \sum_{m=-p}^{q} \left(f^{+}_{mn} \mathrm{e}^{\mathrm{i}k_n r\cos(\theta-\chi_{mn})} + f^{-}_{mn} \mathrm{e}^{\mathrm{i}k_n r\cos(\theta+\chi_{mn})} \right), \tag{2.37}$$

where $f^{\pm}_{mn}$ are the amplitudes associated with the (real and complex) scattering angles m and vertical modes n, in the $\pm\, y$–direction, which are truncated in accordance with a prescribed accuracy. The number of scattering angles $M = p + q + 1$ includes both real and complex scattering angles. The term wide-spacing approximation (WSA) will refer to the neglect of evanescent modes in interactions between stacks/2D WECs. The equations in 2D are obtained by setting $\chi = \pi/2$ in Equation (2.37) (coordinate axes are rotated by $\pi/2$ in Chapter 3).

2.4.1 Scattering and transfer matrices

Reflection ($\boldsymbol{R}$) and transmission ($\boldsymbol{T}$) matrices are assembled from the scattered coefficients for incident waves travelling in the $\pm$ y–direction in the PWE for a stack (Peter and Meylan, 2010). Since scattering is symmetric about the x-axis, $\boldsymbol{R}^{\pm} = \boldsymbol{R}$ and $\boldsymbol{T}^{\pm} = \boldsymbol{T}$. The elements of the $(MN \times MN)$ matrices define the reflection and transmission characteristics for each combination of propagating and decaying modes, and are generated by treating each scattering angle and vertical mode as incident upon the stack (the same modes are incident on adjacent stacks). To illustrate this, $\boldsymbol{R}$ and $\boldsymbol{T}$ are partitioned into the $N \times N$ sub-matrices (denoted by a hat) obtained by treating each scattering angle $-p \leq m \leq q, m \in \mathbb{Z}$ as incident

$$\boldsymbol{T} = \overbrace{\begin{bmatrix} \hat{\boldsymbol{T}}^{-p}_{-p} & \cdots & \hat{\boldsymbol{T}}^{q}_{-p} \\ \vdots & \ddots & \vdots \\ \hat{\boldsymbol{T}}^{-p}_{q} & \cdots & \hat{\boldsymbol{T}}^{q}_{q} \end{bmatrix}}^{\text{inc: } \chi_{-q,0:N} \quad \cdots \quad \chi_{p,0:N}}, \quad \text{and } \boldsymbol{R} = \left.\begin{bmatrix} \hat{\boldsymbol{R}}^{-p}_{-p} & \cdots & \hat{\boldsymbol{R}}^{q}_{-p} \\ \vdots & \ddots & \vdots \\ \hat{\boldsymbol{R}}^{-p}_{q} & \cdots & \hat{\boldsymbol{R}}^{q}_{q} \end{bmatrix}\right\} \begin{matrix} \text{scat angle:} \\ \chi_{0:N,-p} \\ \vdots \\ \chi_{0:N,q} \end{matrix} \tag{2.38}$$

Denoting the vectors of wave amplitudes travelling in the $\pm$ y–direction, before and after a stack s by $\boldsymbol{f}^{\pm}_{s-1}$ and $\boldsymbol{f}^{\pm}_{s}$ respectively, a scattering matrix $\boldsymbol{\mathcal{S}}_s$ mapping the amplitudes of incoming waves to outgoing waves is assembled from $\boldsymbol{R}$ and $\boldsymbol{T}$ such that

$$\begin{bmatrix} \boldsymbol{f}^{-}_{s-1} \\ \boldsymbol{f}^{+}_{s} \end{bmatrix} = \boldsymbol{\mathcal{S}}_s \begin{bmatrix} \boldsymbol{f}^{+}_{s-1} \\ \boldsymbol{f}^{-}_{s} \end{bmatrix} \quad \text{where} \quad \boldsymbol{\mathcal{S}}_s = \begin{bmatrix} \boldsymbol{R}_s & \boldsymbol{T}_s \\ \boldsymbol{T}_s & \boldsymbol{R}_s \end{bmatrix}. \tag{2.39}$$

Similarly, a transfer matrix $\boldsymbol{P}_s$ for the stack maps wave amplitudes in the positive y–direction

$$\begin{bmatrix} \boldsymbol{f}_s^+ \\ \boldsymbol{f}_s^- \end{bmatrix} = \boldsymbol{P}_s \begin{bmatrix} \boldsymbol{f}_{s-1}^+ \\ \boldsymbol{f}_{s-1}^- \end{bmatrix} \quad \text{where} \quad \boldsymbol{P}_s = \begin{bmatrix} \boldsymbol{Q} & \boldsymbol{0} \\ \boldsymbol{0} & \boldsymbol{Q^{-1}} \end{bmatrix} \begin{bmatrix} \boldsymbol{T}_s - \boldsymbol{R}_s \text{inv}(\boldsymbol{T}_s)\boldsymbol{R}_s & \boldsymbol{R}_s \text{inv}(\boldsymbol{T}_s) \\ -\text{inv}(\boldsymbol{T}_s)\boldsymbol{R}_s & \text{inv}(\boldsymbol{T}_s) \end{bmatrix}, \quad (2.40)$$

and the diagonal matrix $\boldsymbol{Q}$, with elements $Q_{mn} = \mathrm{e}^{\mathrm{i}k_n W_y \sin(\chi_{mn})}$, encodes the phase change over a unit cell in the y–direction (wavefield is defined in local coordinates, before the stack).

The eigenvalues of $\boldsymbol{P}$ occur in complex conjugate pairs with unit magnitude, or real-valued, reciprocal pairs (Porter and Porter, 2003). In the WSA, the eigenvalues $\text{eig}(\boldsymbol{P}) = \exp(\pm \mathrm{i}\beta W_y)$ approximate the Bloch wavenumber β which describes the band structures governing propagation through a periodic array (Linton and McIver, 2001). The Bloch problem utilises Bloch–Floquet theory to reduce the problem to a single period (Porter and Porter, 2003), with the potential in adjacent unit cells related through periodic boundary conditions (McIver, 2000).

Real-valued Bloch wavenumbers define passbands where Bloch waves propagate across a unit cell with an appropriate phase change (Linton and McIver, 2001; Porter and Porter, 2003). Complex-valued Bloch wavenumbers define bandgaps in which the associated Bloch waves change in amplitude as they cross the unit cell (Linton and McIver, 2001). The transfer and scattering matrices for a unit cell in 3D accounts for the full stack (infinitely many WECs). The corresponding matrices in the 2D model (Equations 3.20 and 3.31, Chapter 3) are of the same form, but the scattering matrix is derived analogously to the diffraction transfer matrix in the 3D model (Appendix A.1).

2.4.2 Multiple stacks

The array consists of a finite number of stacks (or 2D WECs) S, with centre-to-centre distance W_y in the y–direction (assuming uniform W_y for simplicity). The wavefield between stacks $(s-1)$ and s is written in terms of incoming and outgoing amplitudes $\boldsymbol{f}_s^{\pm}$, for $s \geq 1$ noting phase factors must be considered as $\boldsymbol{f}_s^{\pm}$ are defined relative to the front of a stack to simplify notation. Scattering matrices are iteratively combined to capture interactions between stacks following Mulholland and Heckl (1994) to form a scattering matrix for the array.

Reflection and transmission matrices for the array consisting of stacks 1 to s, $s > 1$ are denoted $\boldsymbol{\mathcal{R}}_s^{\pm}$ and $\boldsymbol{\mathcal{T}}_s^{\pm}$ respectively, with $\boldsymbol{\mathcal{R}}_1^{\pm} = \boldsymbol{R}_1$ and $\boldsymbol{\mathcal{T}}_1^{\pm} = \boldsymbol{T}_1$, such that (Peter and Meylan, 2010)

$$\boldsymbol{\mathcal{R}}_s^+ \boldsymbol{f}_0^+ = \boldsymbol{R}_s^+ \boldsymbol{f}_0^+ + \boldsymbol{T}_s^+ \boldsymbol{f}_s^- \quad (2.41)$$

$$\boldsymbol{\mathcal{T}}_s^- \boldsymbol{f}_0^+ = \boldsymbol{\mathcal{T}}_{s-1}^- \boldsymbol{Q} \boldsymbol{f}_s^+, \quad (2.42)$$

where $\pm$ indicates reflection/transmission in front or behind the array. The amplitudes of the wavefield travelling between stacks 1 to s and stack $(s+1)$ are (Peter and Meylan, 2010)

$$\boldsymbol{f}_s^- = \boldsymbol{Q}\boldsymbol{\mathcal{R}}_{s-1}^+\boldsymbol{Q}\boldsymbol{f}_s^+ \tag{2.43}$$

$$\boldsymbol{f}_s^+ = \boldsymbol{T}_s^-\boldsymbol{f}_0^+ + \boldsymbol{R}_s^-\boldsymbol{f}_s^-. \tag{2.44}$$

An expression for $\boldsymbol{f}_s^+$ in terms of the known incident amplitude $\boldsymbol{f}_0^+$ of the ambient incident wave is obtained by substituting (2.43) into (2.44), so that $\boldsymbol{\mathcal{R}}_s^+$ and $\boldsymbol{\mathcal{T}}_s^-$ are given by

$$\boldsymbol{\mathcal{R}}_s^+\boldsymbol{f}_0^+ = \boldsymbol{R}_s^+\boldsymbol{f}_0^+ + \boldsymbol{T}_s^+\boldsymbol{Q}\boldsymbol{\mathcal{R}}_{s-1}^+\boldsymbol{Q}\left[\boldsymbol{I} - \boldsymbol{R}_s^-\boldsymbol{Q}\boldsymbol{\mathcal{R}}_{s-1}^+\boldsymbol{Q}\right]^{-1}\boldsymbol{T}_s^-\boldsymbol{f}_0^+ \tag{2.45}$$

$$\boldsymbol{\mathcal{T}}_s^-\boldsymbol{f}_0^+ = \boldsymbol{\mathcal{T}}_{s-1}^-\boldsymbol{Q}\left[\boldsymbol{I} - \boldsymbol{R}_s^-\boldsymbol{Q}\boldsymbol{\mathcal{R}}_{s-1}^+\boldsymbol{Q}\right]^{-1}\boldsymbol{T}_s^-\boldsymbol{f}_0^+. \tag{2.46}$$

Similarly, $\boldsymbol{\mathcal{R}}_s^-$ and $\boldsymbol{\mathcal{T}}_s^+$ are derived as

$$\boldsymbol{\mathcal{R}}_s^- = \boldsymbol{\mathcal{R}}_{s-1}^- + \boldsymbol{\mathcal{T}}_{s-1}^-\boldsymbol{Q}\boldsymbol{R}_s^-\left[\boldsymbol{I} - \boldsymbol{Q}\boldsymbol{\mathcal{R}}_{s-1}^+\boldsymbol{Q}\boldsymbol{R}_s^-\right]^{-1}\boldsymbol{\mathcal{T}}_{s-1}^+\boldsymbol{Q} \tag{2.47}$$

$$\boldsymbol{\mathcal{T}}_s^+ = \boldsymbol{T}_s^+\left[\boldsymbol{I} - \boldsymbol{Q}\boldsymbol{\mathcal{R}}_{s-1}^+\boldsymbol{Q}\boldsymbol{R}_s^-\right]^{-1}\boldsymbol{\mathcal{T}}_{s-1}^+\boldsymbol{Q}. \tag{2.48}$$

The wavefield scattered by the array is obtained from

$$\begin{bmatrix}\boldsymbol{f}_S^+\\ \boldsymbol{f}_0^-\end{bmatrix} = \boldsymbol{\mathcal{S}}\begin{bmatrix}\boldsymbol{f}_0^+\\ \boldsymbol{f}_S^-\end{bmatrix}, \text{ where } \boldsymbol{\mathcal{S}} = \begin{bmatrix}\boldsymbol{\mathcal{R}}_S^- & \boldsymbol{\mathcal{T}}_S^-\\ \boldsymbol{\mathcal{R}}_S^+ & \boldsymbol{\mathcal{T}}_S^+\end{bmatrix}. \tag{2.49}$$

When $b_{\text{vis}} = 0$, the elements of the reflection (R_{m0}) and transmission (T_{m0}) matrices of the array associated with propagating modes satisfy the energy conservation relation (McIver, 2000)

$$\sum_{m\in\mathcal{M}}\left(|R_{m0}|^2 + |T_{m0}|^2\right)\sin(\chi_{m0}) = \sin(\chi). \tag{2.50}$$

When the periodicity is less than half the wavelength, the wavefield is 2D in the far field (i.e., $m = 0$ and $\chi_{00} = \chi$), and consists of a single propagating mode of transmission (in the direction χ) and reflection (direction $-\chi$), regardless of the incident angle (Budal, 1977; Falnes, 1984). Consequently, Equation (2.50) simplifies to the 2D result $|R|^2 + |T|^2 = 1$ (Falnes and Budal, 1982; Newman, 1975), where $R \equiv R_{00}$ and $T \equiv T_{00}$.

The efficiency of a stack or 2D WEC (without drag) is quantified by the absorption

$$\alpha = 1 - |R|^2 - |T|^2, \tag{2.51}$$

which calculates the non-dimensionalised proportion of the incident wave energy power that is captured in terms of the power in the reflected and transmitted waves (Evans, 1976) (i.e., in terms of the wavefield). The absorption is determined by the radiation properties of the

device, which implicitly depends on the geometry and the modes of motion (Evans, 1976; Newman, 1975). Axisymmetric (symmetric about the axis of oscillation) WECs (2D or stack of WECs) can capture $\alpha = 0.5$ at optimum in a single mode, and $\alpha = 1$ by combining symmetric (heave) and antisymmetric (surge or pitch) modes of motion, as radiated waves must cancel both reflection and transmission (Falnes and Kurniawan, 2020; Todalshaug, 2013).

Equivalent results are obtained by relating the power capture (Equation (2.18)) of a WEC (2D, or in a unit cell of a stack) to the power available for conversion, which is characterised by the incident wave power across a unit cell width W_x (Mei et al., 2005), as the non-dimensionalised *capture width*

$$CW = \mathcal{P} / \left[\frac{\omega}{4k} \left(1 + \frac{2kh}{\sinh(2kh)} \right) |A^{\mathrm{inc}}|^2 \, W_x \, \sin(\chi) \right] = \alpha. \tag{2.52}$$

The efficiency is derived through far field expressions (Falnes and Kurniawan, 2020). (Since $0 \leq \alpha \leq 1$ is equivalent in 2D and 3D, the 2D term efficiency is also used for stacks in 3D here, as capture widths are seldom defined for arrays in the literature, and range widely depending on the characteristic length used to non-dimensionalise, i.e., CW can exceed 1.) In 3D, $\alpha = 1$ requires two independent modes of oscillation for axisymmetric WECs, either through two heave-restricted stacks, or one stack capable of multiple modes of motion (Falnes, 1984). Non-symmetric radiation can be accomplished using a WEC concept[2] with two modes of motion, or through grouping several WECs in a unit cell (Falnes and Budal, 1982).

These results can be generalised to a wider spacing W_x, where scattering modes will cut on at lower frequencies, provided the number of independent modes of oscillation or rows equals or exceeds the number of real scattering angles (Falnes, 1984). However, Equation (2.52) is not suitable for finite arrays (3D model), as $\chi \to 0$ is not necessarily accompanied by $\mathcal{P} \to 0$ (Evans, 1981b), and the concepts of reflection and transmission are not clearly defined. To quantify the proportion of power captured, a relative capture width is defined by

$$CW_{\mathrm{finite}} = \sum_{j=1}^{N_{\mathrm{WECs}}} \mathcal{P}^j / \left[\frac{\omega}{4k} \left(1 + \frac{2kh}{\sinh(2kh)} \right) |A^{\mathrm{inc}}|^2 \, N_{\mathrm{WECs/row}} \, W_x \right], \tag{2.53}$$

where N_{WECs} is the total number of WECs, and $N_{\mathrm{WECs/row}}$, the number of WECs per row. Equation (2.53) scales the capture width by the total frontage of the array (McIver, 1994).

The theoretical maxima assume unconstrained amplitudes that can be controlled for optimum wave cancellation which restricts validity to incident wave amplitudes at which physical limitations are respected (Falnes, 1984). When a drag correction is incorporated, Equation (2.51)

[2] Porter et al. (2021) demonstrate how theoretical capture widths of axisymmetric devices can be extended by encasing cylinders with paddles (controlled by individual PTOs) to create generalised modes of motion.

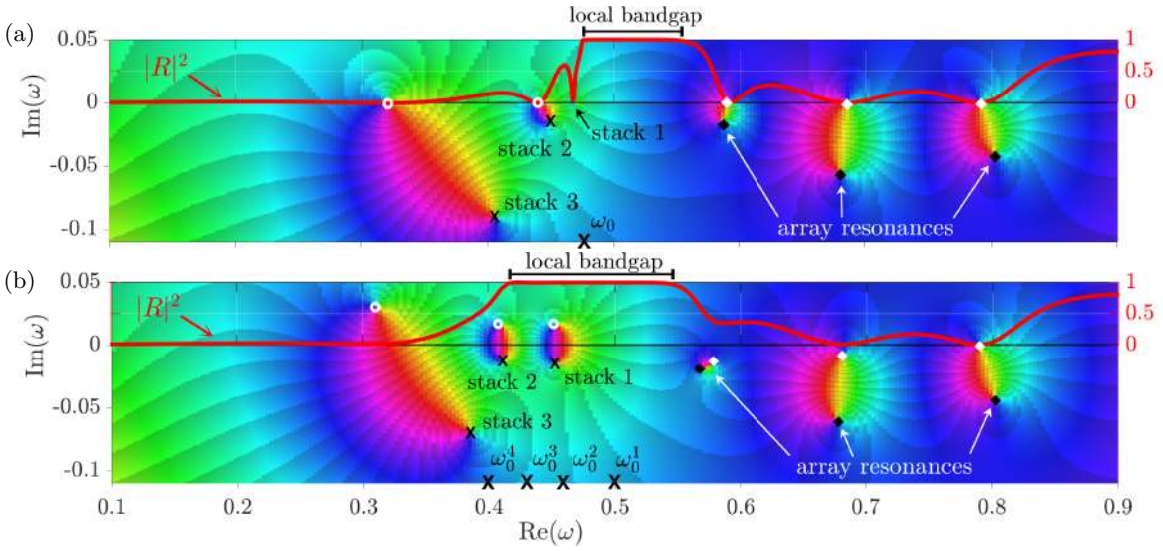

Figure 2.4: The phase portrait of the reflection coefficient for a (a) uniform and a (b) graded array. Poles are marked X, and zeros ∘. The resonant frequency ω_0 is marked on Re(ω), and the reflection $|R|^2$ for $\omega \in \mathbb{R}$ is overlaid. The location of array resonances is predominantly determined by W_y.

includes dissipative losses and is no longer indicative of power capture, which is instead calculated from the WEC motions (Equation (2.52)).

2.4.3 Complex plane: Phase portraits

The reflection and transmission coefficients encapsulate key properties of the array which can be accessed by extending the coefficients to complex frequencies, and visualising them in the complex plane by means of a phase portrait. To illustrate this, the phase portraits of reflection and transmission for energy conserving arrays (no drag/PTO damping) with four stacks are shown in Figures 2.4 and 2.5, respectively. The phase is colour-coded according to its location on the complex unit circle, and the corresponding hue on the colour wheel (Wegert, 2012).

Pole–zero pairs are produced by rapid phase changes at resonance (McIver, 1985), and are distinguished by the ordering of colours (poles are clockwise, zeros are anticlockwise) (Wegert, 2012). The properties of the complex resonances are encoded by the poles (marked X), so that the imaginary part is related to the radiation damping and the real part, to the resonant frequency (Romero-García, Theocharis, Richoux, Merkel, Tournat and Pagneux, 2016). The distance between a pole and zero is governed by the resonance bandwidth of the stack (2D WEC), with greater distances producing broader peaks/troughs in reflection/transmission at real frequencies (Romero-García, Theocharis, Richoux and Pagneux, 2016).

The location of pole–zero pairs in the complex plane govern the array behaviour, and can be manipulated via the PTO to alter the reflection and transmission of an array. In a uniform

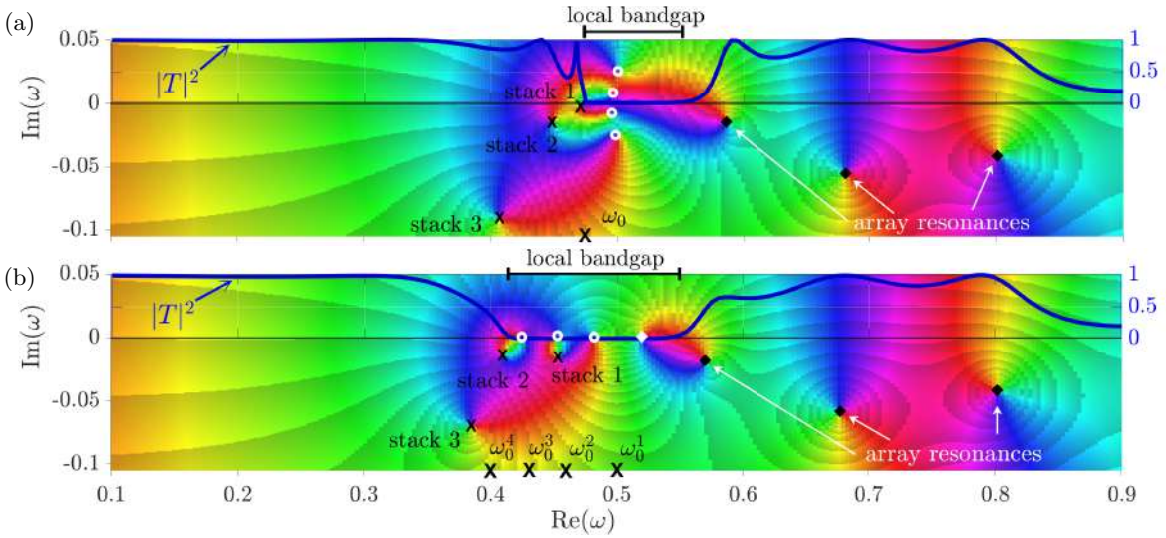

Figure 2.5: The phase portrait of the transmission coefficient for a (a) uniform and a (b) graded array. Poles are marked X, and zeros ∘. The associated resonant frequency is marked on Re(ω), and $|T|^2$ for $\omega \in \mathbb{R}$ is overlaid. The location of array resonances is predominantly determined by W_y.

array (all stacks) tuned to $\omega_0 = 0.475\,\mathrm{rad\,s^{-1}}$, the resonances accumulate below the local bandgap (Figures 2.4a and 2.5a). Zeros in reflection coincide with peak transmission, and zeros in transmission align near the start of the local bandgap. Array resonances (do not exist for a single stack) are generated through wave interference as waves are reflected back and forth between the array edges, and are primarily controlled by the spacing W_y.

Grading the resonant frequencies of stacks fundamentally alters the array's properties, as demonstrated in Figures 2.4b and 2.5b by tuning the stacks from right-to-left in an array to $\omega_0 = 0.4$, 0.43, 0.46 and $0.5\,\mathrm{rad\,s^{-1}}$, for a left-to-right incident wave. The grading distributes zeros in transmission over a wider frequency range which extends the local bandgap. Zeros in reflection are displaced to create full reflection. Array resonances restrict the extent of the local bandgap, but can be influenced by the PTO. Unlike a uniform array, the resonances occupy the local bandgap, where the grading creates near-zero transmission.

Near-perfect absorption is generated by tuning the PTO damping to place complex zeros in reflection near the real frequency axis, so that the extracted energy (or loss through drag) matches the inherent damping (Romero-García, Theocharis, Richoux and Pagneux, 2016). The PTO damping downshifts and deforms pole–zero pairs in the complex frequency plane (not shown), which can broaden the resonance bandwidth and thus absorption (Romero-García, Theocharis, Richoux, Merkel, Tournat and Pagneux, 2016). The wider the bandwidth, the more opportunity for strong interference between resonances (Romero-García, Theocharis, Richoux and Pagneux, 2016), which can affect the ability to control reflection and transmission. Greater separation in frequency space facilitates better control.

Statement of Authorship

Title of Paper	Broadband near-perfect capture of water wave energy by an array of heaving buoy wave energy converters
Publication Status	☑ Published ☐ Accepted for Publication ☐ Submitted for Publication ☐ Unpublished and Unsubmitted work written in manuscript style
Publication Details	Westcott, A.-R., Bennetts, L. G., Sergiienko, N. Y. & Cazzolato, B. S. (2024) Broadband near-perfect capture of water wave energy by an array of heaving buoy wave energy converters. *J. Fluid Mech.* 998, A5.

Principal Author

Name of Principal Author (Candidate)	Amy-Rose Westcott		
Contribution to the Paper	Conceptualisation; literature review; modelling; design and implementation of methodology; code writing; validation; development of strategies and generation of results; optimisation of strategies; analysis, interpretation and synthesis of results; production and formatting of figures; preparation and writing of initial draft; editing and revision of manuscript, before and after review; corresponding author.		
Overall percentage (%)	80%		
Certification:	This paper reports on original research I conducted during the period of my Higher Degree by Research candidature and is not subject to any obligations or contractual agreements with a third party that would constrain its inclusion in this thesis. I am the primary author of this paper.		
Signature		Date	16/12/2025

Co-Author Contributions

By signing the Statement of Authorship, each author certifies that:

i. the candidate's stated contribution to the publication is accurate (as detailed above);
ii. permission is granted for the candidate in include the publication in the thesis; and
iii. the sum of all co-author contributions is equal to 100% less the candidate's stated contribution.

Name of Co-Author	Luke Bennetts		
Contribution to the Paper	Conceptualisation; design of methodology; assisted with interpretation of results; supervision; feedback on initial draft; critical review and revision of manuscript.		
Signature		Date	10/12/2025

Name of Co-Author	Nataliia Sergiienko		
Contribution to the Paper	Conceptualisation; supervision; commentary and feedback on manuscript.		
Signature		Date	11/12/2025

Name of Co-Author	Benjamin Cazzolato		
Contribution to the Paper	Conceptualisation; supervision; commentary and feedback on manuscript.		
Signature		Date	14/12/2025

Chapter 3

Broadband near-perfect capture of water wave energy by an array of heaving buoy wave energy converters

Abstract

Arrays of heaving buoy type wave energy converters (WECs) are a promising contender to harness the renewable power of ocean waves on a commercial scale but require strategies to achieve efficient capture of wave energy over broad frequency bands for economic viability. A WEC-array design is proposed for absorption over a target frequency range in the two-dimensional water wave context by spatially grading the resonant properties of WECs via linear spring–damper power take-off mechanisms. The design is based on theories for rainbow reflection and rainbow absorption, which incorporate analyses based on Bloch wave modes and pole–zero pairs in complex frequency space. In contrast to previous applications of these theories, the influence of a higher-order passband and associated pole–zero pairs are shown to influence absorption at the high-frequency end of the target interval. The theories are used to inform initialisations for optimisation algorithms, and an optimised array of only five WECs is shown to give near-perfect absorption ($\geq 99\%$) over the target interval. Broadband absorption is demonstrated when surge and pitch motions are released, for irregular sea states, and for incident wave packets in the time domain, where the time-domain responses are decomposed into Bloch modes to connect with the underlying theory.

3.1 Introduction

Ocean waves offer an abundant and consistent source of renewable energy (Pecher and Kofoed, 2017). For over half a century, researchers have sought to harness this power using wave energy converters (WECs) (Cruz, 2008), although they are yet to reach economic viability (Gallutia et al., 2022). Heaving buoys with attached power take-off mechanisms (PTOs) are one of the most popular proposed/tested WEC concepts for commercial scale ocean-wave energy conversion (IRENA, 2020). Like most WECs, heaving buoys are tuned to resonate, such that maximum absorption is achieved through optimum wave interference at the resonant frequency (Falnes, 2005). But a naïve deployment of WECs in the inherently broadband,

seasonal, ocean-wave climate (Pecher and Kofoed, 2017) will not provide the broadband absorption needed to make them a competitive energy source, as they are efficient only in a narrow frequency range due to their physical characteristics (Falnes and Hals, 2012).

WECs are deployed in arrays (or "farms") to help meet energy demands and improve cost-effectiveness (Pecher and Kofoed, 2017). Wave interactions between the WECs in an array can either enhance or degrade the performance of the array in comparison with the same number of WECs operating independently (Gallutia et al., 2022; Göteman et al., 2020). Designing WEC-arrays to enhance power capture is an active research topic, with most studies based on numerical and mathematical models, of which the majority use linear potential-flow theory (Folley, 2016). Approaches include optimising WEC geometries/layouts (Babarit, 2013; Edwards and Yue, 2022; Göteman et al., 2020), employing control strategies via the PTO mechanism to maintain/create resonant conditions over broad frequency bands (Bacelli and Ringwood, 2013; Pecher and Kofoed, 2017), or a combination of optimising the WEC layout and a control strategy (Garcia-Rosa et al., 2015; Golbaz et al., 2022).

Theoretical progress has been made for uniform WEC-arrays, i.e., identical and equally spaced WECs with identical PTO parameters. Without absorption, the so-called Bloch waves supported by the array separate into passbands (where the Bloch waves propagate through the array) and bandgaps (where the Bloch waves are unable to propagate). Bandgaps are related to destructive wave interference between WECs in an array, which considerably reduces power capture, whereas frequencies on passbands just below the bandgap are related to constructive wave interference over the array that enhances power capture (Garnaud and Mei, 2010; Tokić and Yue, 2019). In general, bandgaps can be created by Bragg resonance, which is controlled by spacing of the WECs in the array (Tokić and Yue, 2019), or local resonances of individual WECs in the array. In the latter case, the bandgap structure has been shown experimentally to be robust to non-linear wave breaking caused by the local resonances (motivated by coastal protection and without absorption Dupont et al., 2017).

In order to be considered broadband, a WEC-array would need to achieve high efficiency over a broad power capture interval, most likely lying within wave periods between 5 and 20 s, which are feasible for ocean wave energy capture (Coe et al., 2021). The PTO parameters can be adjusted in time according to predicted sea states to achieve broadband absorption, but this approach requires accurate wave prediction capability (Fusco and Ringwood, 2010; Gallutia et al., 2022) and is sensitive to model errors (Cruz, 2008; Folley, 2016), while increasing cost, system complexity and maintenance requirements (Garnaud and Mei, 2009; Pecher and Kofoed, 2017). Designing WEC-arrays to be capable of broadband absorption with PTO parameters that are constant in time would improve economic viability (Pecher and Kofoed, 2017; Sergiienko et al., 2017).

Spatially graded arrays are a promising design strategy (Bennetts et al., 2018) to achieve broadband absorption (Porter, 2021; Wilks et al., 2022). Grading (without absorption) is used for spatially controlled amplification of wave energy within an array according to frequency, as wave energy at a certain frequency is gradually slowed and accumulates as it reaches the location in the array at which the local periodicity defines the transition from a passband to a bandgap (Bennetts et al., 2018). Predictions of this phenomenon from linear theory have been confirmed experimentally, in spite of non-linear wave breaking where the waves are amplified, which merely reduces the amplification factors (Archer et al., 2020). Without absorption (e.g. Archer et al., 2020; Bennetts et al., 2018; Xu et al., 2024), the graded array ultimately reflects the amplified wave energy (hence, the phenomenon is referred to as rainbow reflection), but with absorption the energy can potentially be captured (e.g. Chaplain et al., 2020). The resulting rainbow absorption has been demonstrated in acoustics (e.g. Jiménez et al., 2017b; Romero-García, Theocharis, Richoux and Pagneux, 2016), and elasticity (e.g. Chaplain et al., 2020).

Of particular relevance to the present study, Wilks et al. (2022) introduced the concept of rainbow absorption to ocean wave energy harvesting, using a two-dimensional (2D), linear model of wave–structure interactions. Closely following the approach of Jiménez et al. (2017b) in acoustics, Wilks et al. (2022) designed a water-wave rainbow reflection structure from an array of surface-piercing, rigid, vertical barriers by grading the width between barriers and their submergence. They then added heaving pistons with attached linear damping to create rainbow absorption, and optimised the graded geometry to achieve broadband absorption of 98.2% on an angular frequency interval of 0.8–1.6 $\mathrm{rad\,s^{-1}}$ (wave periods $\approx$ 4–8 s). The barrier submergence increases with distance along the array, reaching up to 80% of the water depth, such that the isolated barrier allows virtually no transmission for the wave frequencies of interest (B. Wilks, personal communication). The corresponding periodic arrays support a single passband at low frequencies, followed by a bandgap that extends to infinity in frequency (although interspersed with very narrow high-frequency passbands Wilks et al., 2024). Their approach is broadly similar to positioning a WEC-array near a rigid wall or breakwater (e.g. Konispoliatis and Mavrakos, 2020) to increase absorption by harnessing reflections (Falnes and Hals, 2012).

In this study, we show that it is possible to create rainbow absorption with a generic array of heaving buoy type WECs by grading the WEC-resonances using the PTOs while maintaining uniform WEC geometries and spacing, and without the need for a surrounding structure. We achieve near-perfect absorption (99% efficiency) over a broad, targeted frequency range of practical interest (angular frequencies 0.3–0.65 $\mathrm{rad\,s^{-1}}$ or wave periods $\approx$ 10–20 s) using a small number of WECs (typically five) with time-independent PTO parameters. The WECs do not act like rigid barriers, and destructive wave interactions within the array are necessary to

generate bandgaps. Over the frequency range considered, multiple passbands and bandgaps exist, which results in interplay between local resonance and Bragg resonance (Guo et al., 2020) not seen in previous cognate studies.

The governing equations and solutions methods used in the study are set out in § 3.2 and § 3.3, respectively. The model (based on 2D linear potential-flow theory) and methods (eigenfunction matching for individual WECs and transfer matrices for WEC interactions) are standard, but are presented for completeness and to establish key notations. The primary contribution of the article is to outline an approach to design an array that achieves near-perfect broadband absorption using bandgaps, zeros of reflection for complex-valued frequencies, and efficient optimisation algorithms. The approach is introduced in stages: by introducing Bloch waves for a uniform non-absorbing array and connecting the complex resonances of the finite array with the band structure (passbands and bandgaps) of the corresponding infinite array (§ 3.4); grading the PTO stiffness to achieve rainbow reflection, and then tuning the PTO damping to achieve complex zeros of reflection and, hence, rainbow absorption (§ 3.5); and using the knowledge gained to inform optimisation algorithms that generate near-perfect broadband absorption, which is subsequently extended to multiple degrees of freedom (surge and pitch released) and applied to irregular sea states (§ 3.6). The performance of one of the proposed arrays is demonstrated in the time domain for incident wave packets, for which a novel decomposition into the time-domain Bloch wave modes is used to connect with the underlying theory (§ 3.7). The relevance of the outlined approach to an equivalent three-dimensional (3D) model is discussed, along with other practical next steps (§ 3.8).

3.2 Preliminaries

Consider a two-dimensional water domain, Ω, in which locations are defined by a Cartesian coordinate system (x, z), where the x-axis is chosen to coincide with the undisturbed free surface, and the z-axis is directed out of the water. The water domain is bounded below by an impermeable seabed at $z = -h$, and above by a free surface, $z = \eta(x, t)$, where t is time. An array of N geometrically identical WECs (WEC 1, WEC 2, ..., WEC N) occupies the water domain. Each WEC involves a heaving buoy and a PTO mechanism, broadly representative of the bottom-referenced heaving buoy developed by CorPower Ocean (2024). For ease of computation, the buoys are square with side lengths $2L$, but should have rounded vertices in practice to prevent flow separation and vortices (Yeung and Jiang, 2014). The buoys are evenly spaced along the free surface with separation distance d, and the first buoy is centred at $x = 0$ (Figure 3.1).

Water motions are modelled using linear potential-flow theory (inviscid, incompressible and irrotational fluid with small amplitude relative to wavelength λ), such that the velocity field

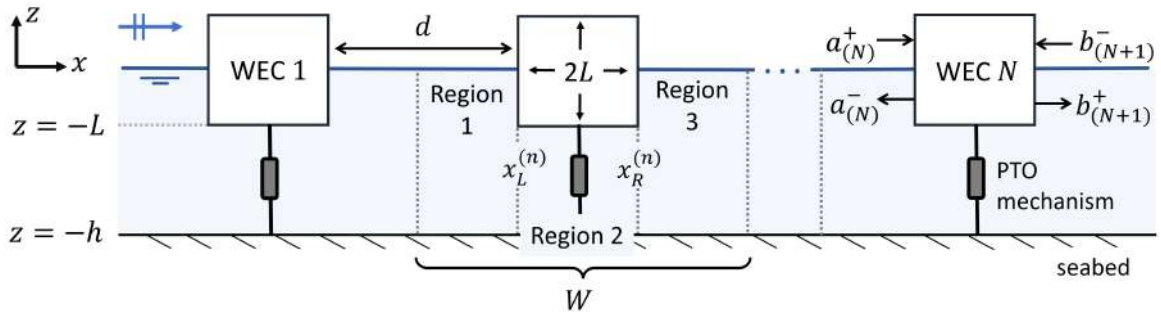

Figure 3.1: Schematic of the problem involving an array of N WECs forced by an incident wave from $x \to -\infty$ (blue arrow).

is the gradient of a scalar velocity potential, $\Phi(x, z, t)$ (Linton and McIver, 2001). The free surface is related to the velocity potential via the linearised dynamic condition

$$[\partial_t \Phi]_{z=0} = -g\,\eta, \tag{3.1}$$

where $g \approx 9.81\,\mathrm{m\,s^{-2}}$ is gravitational acceleration and $\partial_\bullet$ denotes the partial derivative with respect to the subscript (Linton and McIver, 2001). Under the assumption of time-harmonic motions at a prescribed angular frequency $\omega \in \mathbb{R} > 0$, the velocity potential and surface elevation can be written as

$$\Phi(x, z, t) = \mathrm{Re}\left\{\frac{gA}{\mathrm{i}\omega}\phi(x, z)\mathrm{e}^{-\mathrm{i}\omega t}\right\} \quad \text{and} \quad \eta(x, t) = \mathrm{Re}\left\{A\zeta(x)\mathrm{e}^{-\mathrm{i}\omega t}\right\} \tag{3.2a, b}$$

where $\phi \in \mathbb{C}$ and $\zeta \in \mathbb{C}$ are a reduced potential and surface elevation, respectively, A is the incident wave amplitude and $\mathrm{i} = \sqrt{-1}$ is the imaginary unit. The potential, ϕ, satisfies Laplace's equation

$$\nabla^2\phi = 0 \quad \text{throughout } \Omega, \tag{3.3}$$

and a no-normal flow condition at the seabed

$$\partial_z\phi = 0 \quad \text{on } z = -h. \tag{3.4}$$

At the free surface, the potential is related to the surface elevation, ζ, by dynamic and kinematic conditions, respectively,

$$\zeta = [\phi]_{z=0} \quad \text{and} \quad \zeta\omega^2/g = [\partial_z\phi]_{z=0}, \tag{3.5a, b}$$

which can be combined into the single boundary condition

$$\partial_z\phi = \frac{\omega^2}{g}\phi \quad \text{at } z = 0, \tag{3.6}$$

for the potential only. Radiation conditions are applied in the far-field (Linton and McIver, 2001).

The PTOs are modelled as linear spring–damper mechanisms, defined by stiffness and damping coefficients, respectively,

$$c_{(n)}^{\mathrm{PTO}} \quad \text{and} \quad b_{(n)}^{\mathrm{PTO}} \quad \text{for} \quad n = 1, 2, \dots N. \tag{3.7a, b}$$

The damping coefficients are non-negative but the stiffness coefficients can be positive or negative (Kurniawan and Zhang, 2018; Todalshaug et al., 2016). The complex amplitude of the vertical (heave) oscillations of WEC n is denoted by $\xi_n \mathrm{e}^{-\mathrm{i}\omega t}$ $(n = 1, 2, \dots, N)$. Linearised boundary conditions on the wetted surfaces of each WEC are given by

$$\partial_z \phi = \frac{\omega^2}{g} \xi_n \quad \text{for} \quad x_{\mathrm{L}}^{(n)} \leq x \leq x_{\mathrm{R}}^{(n)} \quad \text{and} \quad z = -L \tag{3.8}$$

$$\text{and} \quad \partial_x \phi = 0 \quad \text{for} \quad x = x_{\mathrm{L}}^{(n)}, \, x_{\mathrm{R}}^{(n)} \quad \text{and} \quad -L < z < 0, \tag{3.9}$$

for $n = 1, 2, \dots, N$, where $x_{\mathrm{L}}^{(n)}$ and $x_{\mathrm{R}}^{(n)}$ denote the left- and right-hand edges of WEC n, respectively (Figure 3.1).

For an incident plane wave with angular frequency ω, the heave amplitude ξ_n of WEC n, where $n = 1, 2, \dots, N$, is obtained from the equations of motion

$$\left[-\omega^2 \left(\mathcal{M} + a(\omega) \right) - \mathrm{i}\omega (b(\omega) + b_{(n)}^{\mathrm{PTO}}) + (c + c_{(n)}^{\mathrm{PTO}}) \right] \xi_n(\omega) = F_{(n)}(\omega), \tag{3.10}$$

given the excitation force $F_{(n)}(\omega)$ on WEC n, which depends on the wave amplitudes within an array (i.e., it accounts for WEC interactions; Appendix A.1). The heave excitation force arises from the hydrodynamic pressure exerted on the underside of a fixed WEC, while the added mass, $a(\omega)$, and radiation damping, $b(\omega)$, result from forced oscillations in heave (Appendix A.1), and are proportional to the acceleration and velocity of the isolated body, respectively (Linton and McIver, 2001; Mei et al., 2005). Assuming a suitable static force component of the PTO, the mass per unit breadth of a single WEC is $\mathcal{M} = 4100 L^2$ kg m^{-3}, and c is the hydrostatic stiffness (Mei et al., 2005).

The proportion of incident wave energy captured by the WEC-array, $\alpha(\omega)$, can be determined from the scattering coefficients of the array (reflection, $R \in \mathbb{C}$, and transmission, $T \in \mathbb{C}$, for the array of heaving WECs), using the relation

$$\alpha(\omega) = 1 - |R(\omega)|^2 - |T(\omega)|^2. \tag{3.11}$$

To achieve perfect absorption ($\alpha = 1$) at some $\omega_0 \in \mathbb{R}^+$, the WEC-array must prevent reflection and transmission of waves at ω_0, implying

$$|R(\omega_0)|^2 = 0 \quad \text{and} \quad |T(\omega_0)|^2 = 0. \tag{3.12a, b}$$

For a single WEC in isolation (i.e., an array with $N = 1$ WEC; heave amplitude later denoted $\xi^h_{(n)}$), the optimal PTO parameters for maximum power capture at a specified resonance frequency, $\omega = \omega_0$, can be derived as

$$c^{\mathrm{PTO}} = \omega_0^2 \left(\mathcal{M} + a(\omega_0)\right) - c \;\text{ and }\; b^{\mathrm{PTO}} = b(\omega_0), \tag{3.13a, b}$$

which gives $\alpha(\omega_0) = 0.5$ for a rigid, axisymmetric, heaving buoy (Evans, 1981b; Falnes, 2005). This can be interpreted as setting the stiffness coefficient to tune the natural WEC resonance to the chosen frequency and the damping coefficient such that the radiation cancels the maximum possible amount of diffracted energy.

Broadband absorption over the target frequency interval

$$\omega_\alpha \equiv [\omega_{lb}, \omega_{ub}] = [0.3, 0.65]\,\mathrm{rad\,s^{-1}} \tag{3.14}$$

is defined in terms of the mean absorption over the interval, $\hat{\alpha}$, such that

$$\hat{\alpha} = \frac{1}{\omega_{ub} - \omega_{lb}} \int_{\omega_{lb}}^{\omega_{ub}} \underbrace{\left(1 - |R(\omega)|^2 - |T(\omega)|^2\right)}_{\alpha(\omega)} \mathrm{d}\omega. \tag{3.15}$$

For the purposes of this study, near-perfect absorption is defined as $\alpha \geq 0.990$ at a single frequency and $\hat{\alpha} \geq 0.990$ over the target interval, which covers two thirds of usable ocean wave frequencies (Coe et al., 2021).

Parameter values broadly representative of CorPower Ocean's C4 device are applied to model the WEC-array (Alday et al., 2023). Each WEC has width $2L = 10\,\mathrm{m}$ (Babarit, 2013), and the water depth is $h = 50\,\mathrm{m}$ (Liu et al., 2023), as is typical of heaving buoy arrays. However, different dimensions and wavelengths could equivalently be employed. Negative stiffness coefficients are used to decrease the natural WEC-resonances in order to achieve resonance on the target interval. A negative stiffness mechanism can broaden the resonance bandwidth of the WECs, and has been successfully applied to tune the C4 devices for power capture over the target interval ω_α (Kurniawan and Zhang, 2018; Satymov et al., 2024; Todalshaug et al., 2016).

Without loss of generality, the array is forced by an incident plane wave of amplitude $A = 1\,\mathrm{m}$ from the left of the domain. Based on the corresponding wavelengths ($\lambda \in [142, 429]\,\mathrm{m}$), the steepness of the incident waves, ϵ, satisfies $0.0149 < \epsilon < 0.042$, where $\epsilon = kA \ll 1$ is required to operate in a linear regime (Ning and Ding, 2022).

3.3 Solution method

3.3.1 Single cell problem

Unit cell n is defined as the subregion $\Omega_{(n)}$ of length $W = 2L + d$, containing WEC n at its centre. The unit cell itself is partitioned into three regions, with interfaces defined by the left ($x_{\mathrm{L}}^{(n)}$) and right ($x_{\mathrm{R}}^{(n)}$) edges of WEC n (Figure 3.1). Without loss of generality, suppose WEC n is centred at $x = 0$ so that the unit cell is defined on $|x| \leq W/2$, with the left- and right-hand edges of the WEC given by $x_{\mathrm{L}}^{(n)} = -L$ and $x_{\mathrm{R}}^{(n)} = L$, respectively.

Separation of variables is used to solve for $\phi \equiv \phi_{(n)}$ on $\Omega_{(n)}$ (using the code of Yiew et al., 2016), which is expressed as an eigenfunction expansion in each region (Linton and McIver, 2001). Dynamic and kinematic boundary conditions (ensuring continuity of pressure and horizontal velocity) are applied at interfaces between the regions ($x = \pm L$) to determine the unknown coefficients of the expansions (Linton and McIver, 2001), which leads to a system of linear equations involving the amplitudes, denoted $a_m^{\pm}$ in Region 1 and $b_m^{\pm}$ in Region 3 ($m = 0, 1, \ldots$), as well as amplitudes in Region 2 that are not required for subsequent analysis (see Appendix A.1). Truncating each of the eigenfunction expansions at $m = M$ for a sufficiently large M ($M = 25$ is used in computations presented, see Appendix A.2), the wavefields on either side of WEC n are expressed as

$$\phi_{(n)}(x,z) \approx \begin{cases} \sum_{m=0}^{M} \left(a_m^{+}\mathrm{e}^{\mathrm{i}k_m(x+L)} + a_m^{-}\mathrm{e}^{-\mathrm{i}k_m(x+L)}\right) \dfrac{\cosh(k_m(z+h))}{\cosh(k_m h)} & x < -L, \\ \sum_{m=0}^{M} \left(b_m^{+}\mathrm{e}^{\mathrm{i}k_m(x-L)} + b_m^{-}\mathrm{e}^{-\mathrm{i}k_m(x-L)}\right) \dfrac{\cosh(k_m(z+h))}{\cosh(k_m h)} & x > L. \end{cases} \tag{3.16}$$

The wavenumbers k_m are roots k of the dispersion equation

$$gk\tanh(kh) = \omega^2, \tag{3.17}$$

where k_0 is the positive, real root and k_m ($m \geq 1$) are purely imaginary, in the upper half of the complex plane and ordered in increasing magnitude. Thus, amplitudes with superscripts $+/-$ are related to wave modes that propagate ($m = 0$) or decay ($m > 0$) rightwards/leftwards.

The scattering properties of WEC n (the heaving buoy plus PTO, see Appendix A.1) are defined by $(M+1)\times(M+1)$ reflection and transmission matrices, $\boldsymbol{R}_{(n)}$ and $\boldsymbol{T}_{(n)}$, respectively. These map the incoming waves on WEC n (a_m^{+} and b_m^{-}) to the outgoing waves (a_m^{-} and b_m^{+}). The relationships can be expressed in terms of a scattering matrix, $\boldsymbol{S}_{(n)}$, such that

$$\begin{bmatrix} \boldsymbol{a}^{-}{}_{(n)} \\ \boldsymbol{b}^{+}{}_{(n)} \end{bmatrix} = \begin{bmatrix} \boldsymbol{R}_{(n)} & \boldsymbol{T}_{(n)} \\ \boldsymbol{T}_{(n)} & \boldsymbol{R}_{(n)} \end{bmatrix} \begin{bmatrix} \boldsymbol{a}^{+}{}_{(n)} \\ \boldsymbol{b}^{-}{}_{(n)} \end{bmatrix}, \quad \text{where} \quad \boldsymbol{S}_{(n)} \equiv \begin{bmatrix} \boldsymbol{R}_{(n)} & \boldsymbol{T}_{(n)} \\ \boldsymbol{T}_{(n)} & \boldsymbol{R}_{(n)} \end{bmatrix} \tag{3.18}$$

and the $M+1$ column vectors

$$\boldsymbol{a}^{\pm}{}_{(n)} \equiv \begin{bmatrix} a^{\pm}_{n,0} \\ \vdots \\ a^{\pm}_{n,M} \end{bmatrix} \quad \text{and} \quad \boldsymbol{b}^{\pm}{}_{(n)} \equiv \begin{bmatrix} b^{\pm}_{n,0} \\ \vdots \\ b^{\pm}_{n,M} \end{bmatrix}, \tag{3.19a, b}$$

contain the amplitudes. In general, the PTO parameters differ between the WECs in the array, so that each of the WECs has a different reflection and transmission matrix.

3.3.2 WEC array

Let the scattering matrix for WEC p to WEC q be

$$\boldsymbol{S}_{(p,q)} \equiv \begin{bmatrix} \boldsymbol{R}^{-}_{(p,q)} & \boldsymbol{T}^{-}_{(p,q)} \\ \boldsymbol{T}^{+}_{(p,q)} & \boldsymbol{R}^{+}_{(p,q)} \end{bmatrix}, \tag{3.20}$$

which includes multiple scattering effects between the WECs. Its reflection and transmission matrices are given by (Bennetts and Squire, 2009)

$$\boldsymbol{R}^{-}_{(p,q)} = \boldsymbol{R}^{-}_{(p,q-1)} + \boldsymbol{T}^{+}_{(p,q-1)} \left[\boldsymbol{I} - \boldsymbol{R}^{-}_{(q)} \boldsymbol{R}^{+}_{(p,q-1)}\right]^{-1} \boldsymbol{R}^{-}_{(q)} \boldsymbol{T}^{-}_{(p,q-1)}, \tag{3.21}$$

$$\boldsymbol{T}^{-}_{(p,q)} = \boldsymbol{T}^{-}_{(p,q-1)} \left[\boldsymbol{I} - \boldsymbol{R}^{-}_{(q)} \boldsymbol{R}^{+}_{(p,q-1)}\right]^{-1} \boldsymbol{T}^{-}_{(q)}, \tag{3.22}$$

$$\boldsymbol{R}^{+}_{(p,q)} = \boldsymbol{R}^{+}_{(q)} + \boldsymbol{T}^{-}_{(q)} \left[\boldsymbol{I} - \boldsymbol{R}^{-}_{(q)} \boldsymbol{R}^{+}_{(p,q-1)}\right]^{-1} \boldsymbol{R}^{+}_{(p,q-1)} \boldsymbol{T}^{+}_{(q)}, \tag{3.23}$$

$$\text{and} \quad \boldsymbol{T}^{+}_{(p,q)} = \boldsymbol{T}^{+}_{(q)} \left[\boldsymbol{I} - \boldsymbol{R}^{-}_{(q)} \boldsymbol{R}^{+}_{(p,q-1)}\right]^{-1} \boldsymbol{T}^{+}_{(p,q-1)}, \tag{3.24}$$

where $\boldsymbol{I}$ is the $(M+1) \times (M+1)$ identity matrix. A recursive algorithm (Bennetts and Squire, 2009) is used to calculate the reflection and transmission matrices, $\boldsymbol{R}^{\pm}_{(1,n)}$ and $\boldsymbol{T}^{\pm}_{(1,n)}$, for $n = 2, 3, \ldots, N$, and initialised with $\boldsymbol{S}_{(1,1)} = \boldsymbol{S}_{(1)}$ (Equation (3.18)). Wave amplitudes within the array (to the right of WEC n for $n = 1, 2, \ldots, N-1$) are determined, based on the incident wave amplitude, using a combination of the left-to-right and right-to-left scattering matrices (Bennetts and Squire, 2009), such that

$$\boldsymbol{a}^{+}{}_{(n+1)} = \left[\boldsymbol{I} - \boldsymbol{R}^{+}_{(1,n-1)} \boldsymbol{R}^{-}_{(N,n)}\right]^{-1} \left[\boldsymbol{T}^{+}_{(1,n-1)} \boldsymbol{a}^{+}{}_{(1)} + \boldsymbol{R}^{+}_{(1,n-1)} \boldsymbol{T}^{-}_{(N,n)} \boldsymbol{b}^{-}{}_{(N)}\right], \tag{3.25}$$

$$\text{and} \quad \boldsymbol{b}^{-}{}_{(n)} = \left[\boldsymbol{I} - \boldsymbol{R}^{-}_{(N,n)} \boldsymbol{R}^{+}_{(1,n-1)}\right]^{-1} \left[\boldsymbol{R}^{-}_{(N,n)} \boldsymbol{T}^{+}_{(1,n-1)} \boldsymbol{a}^{+}{}_{(1)} + \boldsymbol{T}^{-}_{(N,n)} \boldsymbol{b}^{-}{}_{(N)}\right]. \tag{3.26}$$

3.3.3 Wide-spacing approximation

The wide-spacing approximation is used, in which evanescent modes ($m \geq 1$) are neglected in inter-device interactions (Linton and McIver, 2001). Consequently, only the reflection

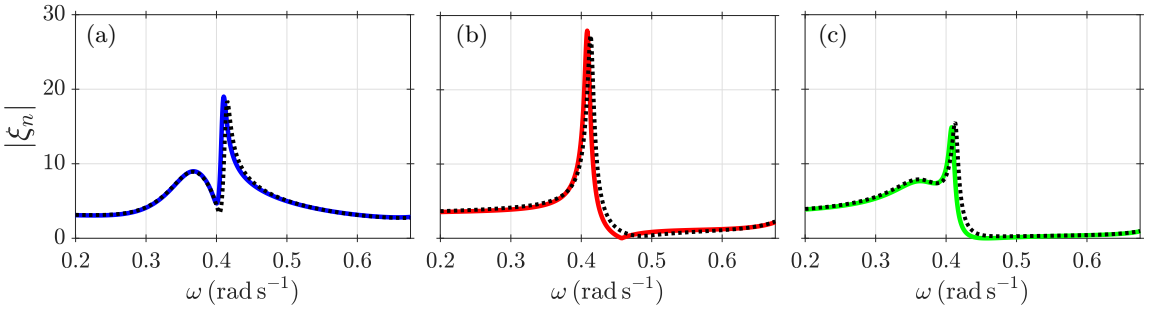

Figure 3.2: The amplitudes of three non-absorbing WECs ($\omega_0 = 0.44\,\mathrm{rad\,s^{-1}}$) in a uniform array obtained using the wide-spacing approximation (—) when $kd \in [0.0372, 0.2024]$ and $d/2L = 0.4$, compared with the amplitudes of (a) WEC 1, (b) WEC 2 and (c) WEC 3 obtained when including evanescent modes (····) in WEC-interaction calculations.

and transmission coefficients associated with propagating modes ($m = 0$) are retained in scatterings relations ($\boldsymbol{R}$ and $\boldsymbol{T}$ are reduced to scalars in Equations (3.18)–(3.26)), i.e., it is assumed that

$$\phi_{(n)} \sim \frac{\cosh(k_0(z+h))}{\cosh(k_0 h)} \times \begin{cases} a^+_{(n)} \mathrm{e}^{\mathrm{i}k_0\left(x-\Omega^{\mathrm{L}}_{(n)}\right)} + a^-_{(n)} \mathrm{e}^{-\mathrm{i}k_0\left(x-\Omega^{\mathrm{L}}_{(n)}\right)} & x \to \Omega^{\mathrm{L}}_{(n)}, \\ b^+_{(n)} \mathrm{e}^{\mathrm{i}k_0\left(x-\Omega^{\mathrm{R}}_{(n)}\right)} + b^-_{(n)} \mathrm{e}^{-\mathrm{i}k_0\left(x-\Omega^{\mathrm{R}}_{(n)}\right)} & x \to \Omega^{\mathrm{R}}_{(n)}, \end{cases} \tag{3.27}$$

where $\Omega^{\mathrm{L}}_{(n)} = (2n-3)W/2$ and $\Omega^{\mathrm{R}}_{(n)} = (2n-1)W/2$ specify the left- and right-hand edges of $\Omega_{(n)}$, respectively. Consequently, the far field ($x \to \pm\infty$) can be obtained using the 2×2 global scattering matrix, as

$$\phi \sim \frac{\cosh(k_0(z+h))}{\cosh(k_0 h)} \times \begin{cases} \mathrm{e}^{\mathrm{i}k_0 x} + R\mathrm{e}^{-\mathrm{i}k_0 x} & x \to -\infty \\ T\mathrm{e}^{\mathrm{i}k_0 x} & x \to \infty, \end{cases} \tag{3.28}$$

where R and T are the reflection and transmission coefficients for the array of heaving WECs, which can be used to calculate the absorption of the array (Equation (3.11)). In the absence of PTO damping, R and T satisfy the energy conservation identity $|R|^2 + |T|^2 = 1$.

Formally, the wide-spacing assumption requires $kd \gg 1$ and $d/2L \gg 1$ (Linton and McIver, 2001). For the problem considered, accurate solutions are obtained even when these conditions are violated, as demonstrated using the WEC amplitudes,

$$\xi_n = \left(a^+_{(n)} \mathrm{e}^{\mathrm{i}kd/2} + b^-_{(n+1)} \mathrm{e}^{\mathrm{i}kd/2}\right) \xi^h_{(n)}, \tag{3.29}$$

in Figure 3.2, where a spacing of $d = 4\,\mathrm{m}$ is applied to a uniform array of three WECs, tuned to resonate at $\omega \approx 0.44\,\mathrm{rad\,s^{-1}}$ (Equation (3.13)). (Additional justification is provided in Appendix A.2. Note that ξ_n is retrieved by multiplying the heave amplitude of the corresponding isolated WEC, $\xi^h_{(n)}$ (Appendix A.1), by the incident field which accounts for

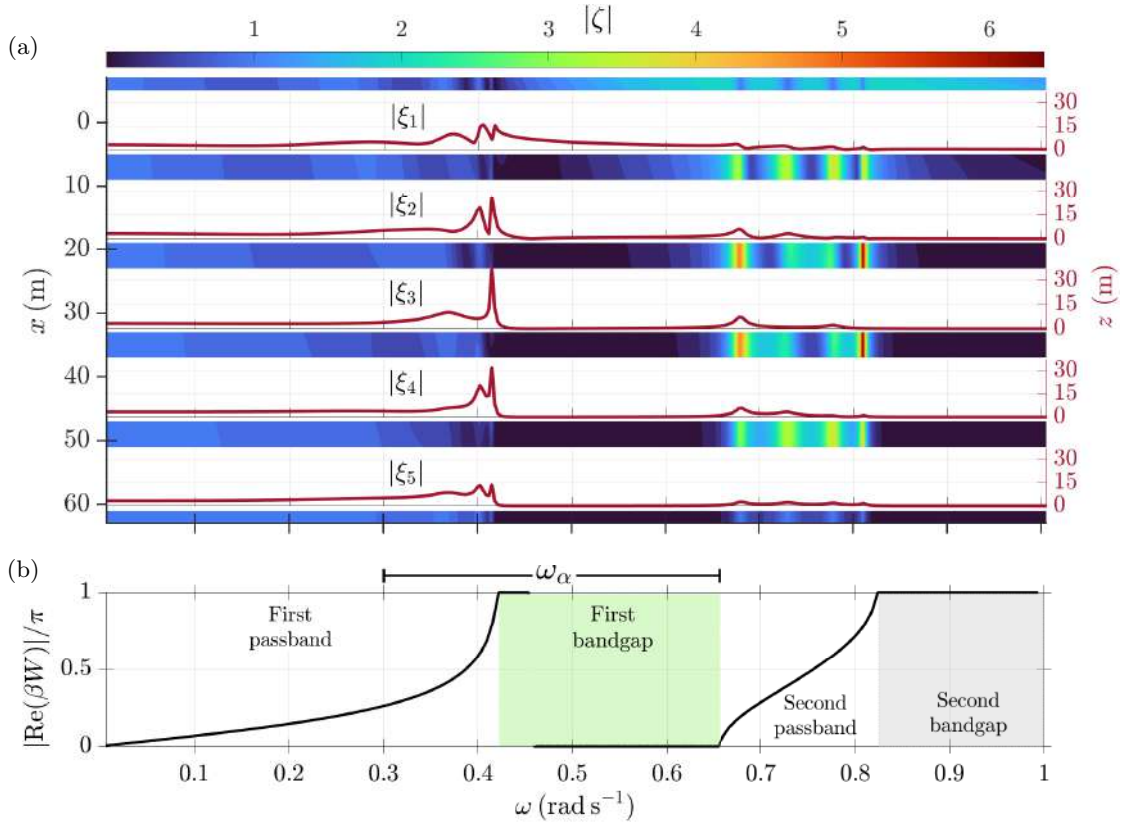

Figure 3.3: The modulus of the surface elevation $|\zeta|$ for a uniform array of five WECs ($\omega_0 = 0.44\,\mathrm{rad\,s^{-1}}$) is shown on the (a) ω–x axis, with the corresponding WEC amplitudes overlaid on ω–z axes. The local wavefield closely resembles the Bloch waves on the corresponding unit cell in (b) the dispersion diagram, with the array supporting propagation in passbands and preventing transmission in bandgaps.

interactions within the array.) This spacing is selected to separate resonances of individual WECs from resonances driven by the spacing of WECs in the array (§§ 3.4–3.5).

3.4 Uniform arrays, Bloch waves and complex resonances

3.4.1 A uniform array of non-absorbing WECs

Figure 3.3a shows the surface elevation over a range of frequencies (broader than the target power capture interval) for a uniform array of five non-absorbing ($b^{\mathrm{PTO}} = 0$), identically tuned WECs ($\omega_0 = 0.44\,\mathrm{rad\,s^{-1}} > \omega_{lb}$, as described in § 3.3.3), with spacing $d = 4\,\mathrm{m}$ ($W = 14\,\mathrm{m}$). For frequencies below approximately $\omega = \omega_0$, incident waves propagate through the array ($|\zeta| \in [0.88, 1]\,\mathrm{m}$ beyond WEC 5). Around the resonant frequency, $\omega = \omega_0$, there is a series of large resonant WEC responses ($|\xi_n|$ up to $36\,\mathrm{m}$). The resonances mark the transition to the array prohibiting wave propagation, up to approximately $\omega = 0.65\,\mathrm{rad\,s^{-1}}$ ($|\zeta| \approx 0\,\mathrm{m}$ and $|\xi_n| \approx 0\,\mathrm{m}$ beyond WEC 2). Between $\omega = 0.65\,\mathrm{rad\,s^{-1}} \equiv \omega_{ub}$ and $0.82\,\mathrm{rad\,s^{-1}}$, there

is an alternating pattern of narrow bands of moderately large ($|\xi_n|$ up to 7.5 m) and small (near zero) responses of the array to the incident waves. The array then transitions back to prohibiting wave propagation up to the highest frequency considered.

3.4.2 Bloch waves

The wavefield in a given cell can be decomposed into rightward and leftward Bloch wave modes, $\psi^{+}_{(n)}$ and $\psi^{-}_{(n)}$ ($n = 1, 2, \ldots, N$), respectively. They are such that

$$\psi^{\pm}_{(n)}(x,0) = \begin{cases} v^{\pm}_{(n)}\, \mathrm{e}^{\mathrm{i}k_0\left(x-\Omega^{\mathrm{L}}_{(n)}\right)} + v^{\mp}_{(n)}\, \mathrm{e}^{-\mathrm{i}k_0\left(x-\Omega^{\mathrm{L}}_{(n)}\right)}, & \text{for } x \leq x^{(n)}_{\mathrm{L}} \\ \mathrm{e}^{\pm \mathrm{i}\beta W}\left(v^{\pm}_{(n)}\mathrm{e}^{\mathrm{i}k_0\left(x-\Omega^{\mathrm{R}}_{(n)}\right)} + v^{\mp}_{(n)}\mathrm{e}^{-\mathrm{i}k_0\left(x-\Omega^{\mathrm{R}}_{(n)}\right)}\right) & \text{for } x \geq x^{(n)}_{\mathrm{R}}. \end{cases} \tag{3.30}$$

The Bloch wavenumber, $\beta_{(n)}$, and amplitudes, $v^{\pm}_{(n)}$, are calculated from the 2×2 transfer matrix, $\boldsymbol{P}_{(n)}$, which is defined such that (Porter and Porter, 2003)

$$\begin{bmatrix} b^{+}_{(n)} \\ b^{-}_{(n)} \end{bmatrix} = \boldsymbol{P}_{(n)} \begin{bmatrix} a^{+}_{(n)} \\ a^{-}_{(n)} \end{bmatrix} \quad \text{where} \quad \boldsymbol{P}_{(n)} = \frac{1}{T_{(n)}} \begin{bmatrix} T^2_{(n)} - R^2_{(n)} & R_{(n)} \\ -R_{(n)} & 1 \end{bmatrix}. \tag{3.31}$$

The transfer matrix is diagonalised as

$$\boldsymbol{P}_{(n)} = \begin{bmatrix} v^{+}_{(n)} & v^{-}_{(n)} \\ v^{-}_{(n)} & v^{+}_{(n)} \end{bmatrix} \begin{bmatrix} \mu_{(n)} & 0 \\ 0 & \mu^{-1}_{(n)} \end{bmatrix} \begin{bmatrix} v^{+}_{(n)} & v^{-}_{(n)} \\ v^{-}_{(n)} & v^{+}_{(n)} \end{bmatrix}^{-1}, \tag{3.32}$$

so that the Bloch wavenumber is calculated from the eigenvalue of the transfer matrix, $\beta_{(n)} = -\mathrm{i}\ln(\mu_{(n)})/W$, and the amplitudes are the entries of the eigenvectors. Note the symmetry of the rightward and leftward Bloch waves, which is due to the symmetry of the unit cells.

The band structure of the unit cell is visualised by plotting the real parts of the Bloch wavenumbers against frequency. For the uniform array, all unit cells are identical, and so the band structure of any unit cell is representative of the array. Passbands are defined by real-valued Bloch wavenumbers, and indicate frequency ranges over which Bloch waves propagate across the unit cell. Bandgaps are defined by complex-valued Bloch wavenumbers ($\mathrm{Re}(\beta_{(n)}) = 0$ or π), and indicate frequency intervals over which Bloch waves decay across the unit cell.

For the uniform array and frequency range considered in § 3.4.1, there are two passbands and two bandgaps (Figure 3.3b). The first passband corresponds to the low-frequency interval over which the incident waves propagate through the array, plus the narrow interval of resonances around ω_0. The first bandgap is connected with the resonances of the individual WECs and is often referred to as the local resonance bandgap. It starts just above the resonances of

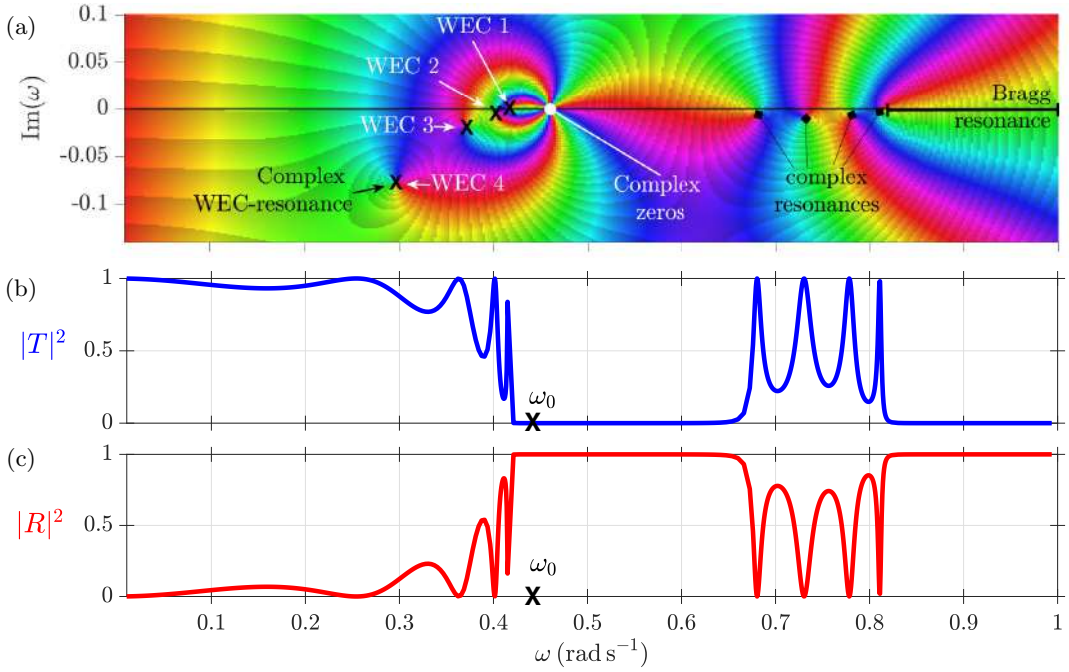

Figure 3.4: (a) The structure of transmission coefficient ($T \in \mathbb{C}$) as a function of $\omega \in \mathbb{C}$ for a uniform array of five WECs with $b^{\mathrm{PTO}} = 0$, visualised by colour-coding the phase ($\arg(T)$) to form a phase portrait (Wegert, 2012), where the magnitude of the phase is represented by hue. Poles (WEC-resonances; marked with an X) and zeros are identified by rapid phase changes and distinguished by the ordering of colours in the anticlockwise direction (Wegert, 2012). A white • marks the location where the complex zeros coalesce on $\mathrm{Im}(\omega) = 0$ at $\omega \approx 0.45\,\mathrm{rad\,s^{-1}}$, resulting in (b) $|T|^2 = 0$ and (c) $|R|^2 = 1$ for $\omega \in \mathbb{R}^+$, and the first bandgap in Figure 3.3b. Resonances in the complex plane produce a local maximum of $|T|^2$ and a local minimum of $|R|^2$ for $\omega \in \mathbb{R}^+$. The real-valued WEC-resonance is denoted ω_0.

the individual WECs, and corresponds to the lowest-frequency interval over which there is no propagation through the array, i.e., its upper bound is $\approx \omega_{ub}$. The second passband covers the interval of alternating narrow bands of large and small responses. Over this interval, waves propagate along the array but partially reflect at the ends of the array and constructively or destructively interfere following rereflections. The second bandgap is connected with the WEC spacing along the array and is referred to as the Bragg bandgap, as it is created by Bragg resonance. It extends to the highest frequencies considered, and also corresponds to an interval over which there is no propagation through the array.

3.4.3 Complex resonances

The modulus of the transmission coefficient squared for the array, $|T|^2$, i.e., the proportion of transmitted energy, also shows the band structure (Figure 3.4b). Almost full transmission ($|T|^2 \approx 1$) occurs in the first passband at frequencies up to $\omega \approx 0.3\,\mathrm{rad\,s^{-1}} \equiv \omega_{lb}$. There is a sequence of increasingly sharp, narrow peaks and troughs at the high-frequency end of the first passband, just below the resonant frequency, $\omega = \omega_0$. Transmission is zero in both

bandgaps and oscillates in the second passband that separates the bandgaps. The modulus of the reflection coefficient squared, $|R|^2$, shows the band structure in a complementary manner, i.e., near zero reflection or oscillations in the passbands and full reflection in the bandgaps, due to the energy conservation identity (Equation (3.11)) for the non-absorbing array ($\alpha \equiv 0$).

Transmission oscillations in the passbands are governed by the structure of the transmission coefficient in the complex frequency plane ($\omega \in \mathbb{C}$; Figure 3.4a). Each peak in transmission on the real frequency axis is associated with a pole in the transmission coefficient in the lower half of the complex plane, which are known as complex resonances (De Chowdhury et al., 2023; Meylan and Fitzgerald, 2018; Romero-García, Theocharis, Richoux and Pagneux, 2016). The closer the complex resonances are to the real frequency axis, the sharper the transmission peaks on the real axis are. Each complex resonance corresponding to a peak in the first passband is associated with a specific WEC in the array and labelled accordingly. The association indicates that the location of the complex resonance is sensitive to variations in the properties of the WEC (not shown), although all of complex resonances move to a certain degree when the properties of any WEC in the array or the array spacing vary. The resonance associated with WEC 5 is outside the axes limits.

The complex resonances associated with transmission peaks in the second passband are created by wave interference along the array (they have no analogue in the single body problem). Thus, their locations depend predominantly on the WEC spacing—for example, a larger spacing would push them to lower frequencies. There are four overlapping zeros in transmission on the real-frequency axis very close to the resonant frequency, $\omega = \omega_0$, and at the point where the Bloch wavenumber jumps between branches (shown by the discontinuity in $\mathrm{Re}(\beta)$, Figure 3.3b).

3.5 Grading the resonant properties of WECs

3.5.1 Rainbow reflection

Consider the uniform array of five non-absorbing WECs (as in § 3.4) but in which the stiffness coefficients are graded with distance along the array, so that the WEC-resonant frequencies increase from right to left (from WEC 5 to WEC 1). The grading has the effect of frequency upshifting the first bandgaps (in the unit cells, from right to left), as well as narrowing their frequency ranges, as they are bounded above by the second (Bragg) bandgaps, which are insensitive to the WEC-resonances (figures 3.5a–c). The grading is sufficiently gradual that the first bandgaps for adjacent unit cells overlap (the resonant frequency for WEC n lies in the bandgap associated with the WEC $(n+1)$). This creates a wide effective bandgap for the

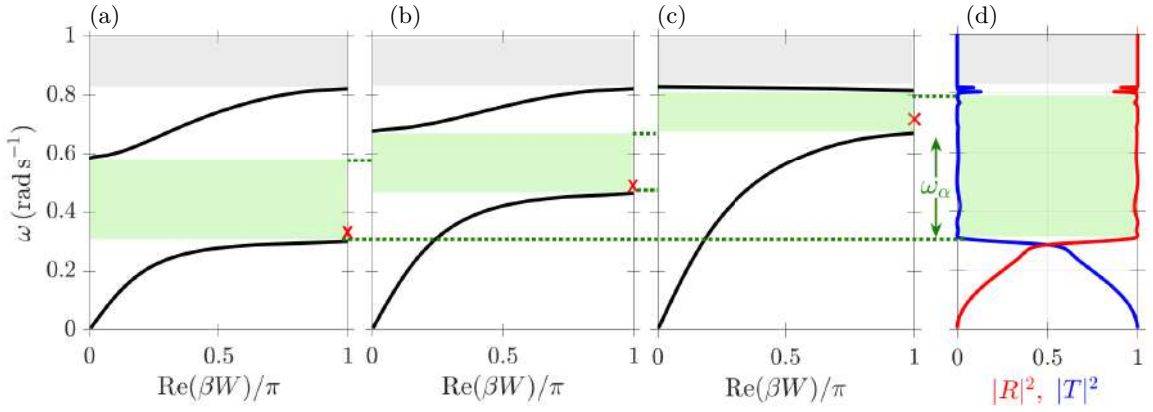

Figure 3.5: (a)–(c) Band diagrams of the Bloch waves for an array with $W = 14\,\mathrm{m}$ ($d = 4\,\mathrm{m}$ and $L = 5\,\mathrm{m}$), for increasing c^{PTO} values and $b^{\mathrm{PTO}} = 0$. Real-valued WEC-resonances $\omega_0 \in \mathbb{R}$ are marked by a red x, where (a) $\omega_0 = 0.31\,\mathrm{rad\,s^{-1}}$, (b) $\omega_0 = 0.48\,\mathrm{rad\,s^{-1}}$, (c) $\omega_0 = 0.72\,\mathrm{rad\,s^{-1}}$. Increasing c^{PTO} shifts the first bandgap (shaded green) to higher frequencies, and reduces the interval of the second passband. The second bandgap (grey) is caused by Bragg resonance. Grading the WEC-resonances in a finite array of five WECs (first, third and fifth WECs correspond to panels (c)–(a), respectively) forms (d) an effective bandgap on $\omega \in [0.3, 0.8]\,\mathrm{rad\,s^{-1}}$, where $|R|^2 \approx 1$ and $|T|^2 \approx 0$.

array that covers the target interval, i.e., array transmission is approximately zero ($|T|^2 \approx 0$ and $|R|^2 \approx 1$) for $\omega \in [0.3, 0.8]\,\mathrm{rad\,s^{-1}} \supset \omega_\alpha$. The effective bandgap manifests as separation of the complex zeros in the phase portrait of $T(\omega)$ along the real frequency axis over the target frequency range (Figure 3.6a).

The WEC-resonances are graded from high-to-low from left-to-right to create the rainbow reflection effect, such that incident waves at frequencies in the target range penetrate into the array, with penetration distances that depend on the wave frequency. (Grading low-to-high would prevent propagation into the array.) For a given $\omega \in \omega_\alpha$, an incident wave will propagate into the graded array until reaching a cut-off point, which is approximately where the local Bloch wave has zero group velocity, and occurs in the unit cell at which the frequency lies in the corresponding bandgap. Put simply, the Bloch wave propagates until it reaches a WEC with a comparable resonant frequency. The wave is amplified just before the cut-off point due to the slow-down of wave energy transport, which creates a near-resonant (i.e., finite) response.

The near-resonances are connected with complex resonances in the reflection coefficient in the lower-half complex frequency plane (black crosses in Figure 3.6b), which have real parts approximately covering the target interval. The near full reflection over the real frequency interval creates near symmetry in the real frequency axis of the reflection phase and reciprocity of the modulus, so that complex zeros of reflection occur at approximately the complex conjugates of the complex resonant frequencies (Figure 3.7a; Bennetts and Meylan, 2021). (Note the symmetry is weakest for the WEC 4 pole–zero pair, where full reflection is not

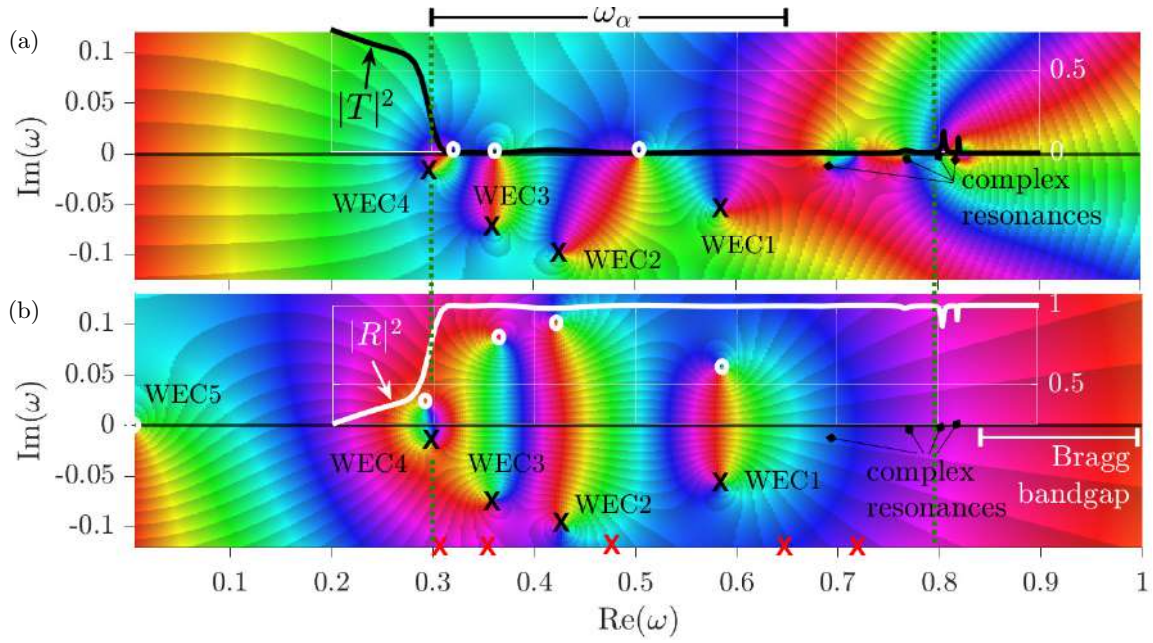

Figure 3.6: Phase portraits of (a) $T(\omega)$ and (b) $R(\omega)$ are shown as a function of $\omega \in \mathbb{C}$ for the graded array in Figure 3.5. Complex WEC-resonances (X) can be identified from (a) or (b). White circles (**o**) denote the complex zeros in R and T, and the corresponding $|R(\omega)|^2$ and $|T(\omega)|^2$ for $\omega \in \mathbb{R}$ are superimposed. Vertical dotted lines demarcate the effective bandgap induced by the grading (Figure 3.5), and red xs correspond to the real-valued WEC-resonance of each WEC. The complex resonances preceding the Bragg bandgap are marked by ♦ in (a), with the corresponding pole–zero pairs in (b) not visible at the current scale.

achieved.) Manipulating the properties of the pole–zero pairs in complex frequency space provides a novel means to analyse and control the array response based on the resonant properties of individual WECs. The PTO stiffness is used to influence the locations of real parts of the pole–zero pairs (Figure 3.7b). However, interactions between the phase structures supported by the pole–zero pairs (i.e., their bandwidths) prevent full control. The location of the pole–zero pair associated with WEC 1 is restricted towards high frequencies by pole–zero pairs related to complex resonances in the second passband.

3.5.2 Rainbow absorption

In complex frequency space, adding PTO damping to WEC n moves the corresponding complex zero of reflection towards the real axis and the pole away from it (Figure 3.7c). When the pole–zero pairs are sufficiently separated, a value of the PTO damping can be found such that the complex zero of reflection lies on the real frequency axis (Figure 3.7d). This approach is used as a basis to create rainbow absorption, i.e., high absorption over a wide frequency range, where the absorption peaks are spatially separated according to frequency.

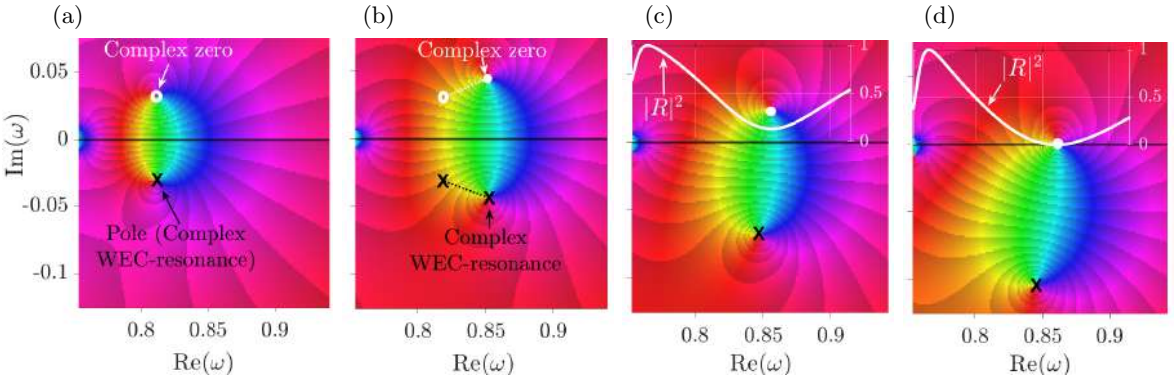

Figure 3.7: Phase portrait of $R(\omega)$, when $\omega \in \mathbb{C}$, for a single WEC in a graded array (of five WECs). When $b^{\mathrm{PTO}} = 0$, (a) the complex zero (white circle) is located above $\mathrm{Im}(\omega) = 0$, and the complex WEC-resonance (X) below $\mathrm{Im}(\omega) = 0$. Increasing c^{PTO} (b) moves the WEC-resonance to the right, tuning the WEC to a higher frequency. Positive b^{PTO} (c) moves the complex zero towards $\mathrm{Im}(\omega) = 0$. Perfect absorption (d) is achieved when $b_*^{\mathrm{PTO}} > 0$ places the complex zero on $\mathrm{Im}(\omega) = 0$. Simultaneously, a near-zero minimum of $|R|^2$ is obtained for $\omega \in \mathbb{R}$ (overlaid).

The rainbow absorption approach involves adding the WECs to the array one at a time, starting with the rightmost WEC (WEC 5 in this example) and moving leftwards, so that the number of WECs in the array increases with each iteration. The rightmost WEC is used only to create a zero in transmission close to the low-frequency end of the target frequency interval, rather than as an absorbing device (Figure 3.8a; (Jiménez et al., 2017b)). As each WEC is added to the array, its PTO stiffness is tuned to a chosen frequency (noting that pole–zero pair interactions mean the chosen frequency is not arbitrary) and then its damping is tuned to create a zero in reflection at a nearby (real) frequency. The tuning of the additional WEC PTO tends to slightly frequency-downshift the existing pole–zero pairs and displace the complex zeros from the real frequency axis. Thus, the PTOs of the existing WECs are simultaneously retuned increasingly far apart in the complex plane as the WEC-resonance frequency and corresponding resonance bandwidth increase (Romero-García, Theocharis, Richoux and Pagneux, 2016), which forces the reflection zeros to become spaced increasingly far apart.

The process is accomplished manually for WEC 4 down to WEC 2 (Figure 3.8b–d). However, it becomes increasingly challenging to separate the pole–zero pairs on the restricted interval (bounded above by the complex resonances associated with the second passband). The increasing distance between the pole–zero pair as frequency increases is responsible for increasing bandwidths around the zeros and the need for increasing separation between the zeros (e.g., Figure 3.8e). Only four near zeros of reflection ($|R|^2 \approx 0$) are found manually after WEC 1 is added. This solution is used as an initial guess in an optimisation algorithm (the sequential quadratic programming algorithm in the MATLAB function `fmincon`) with

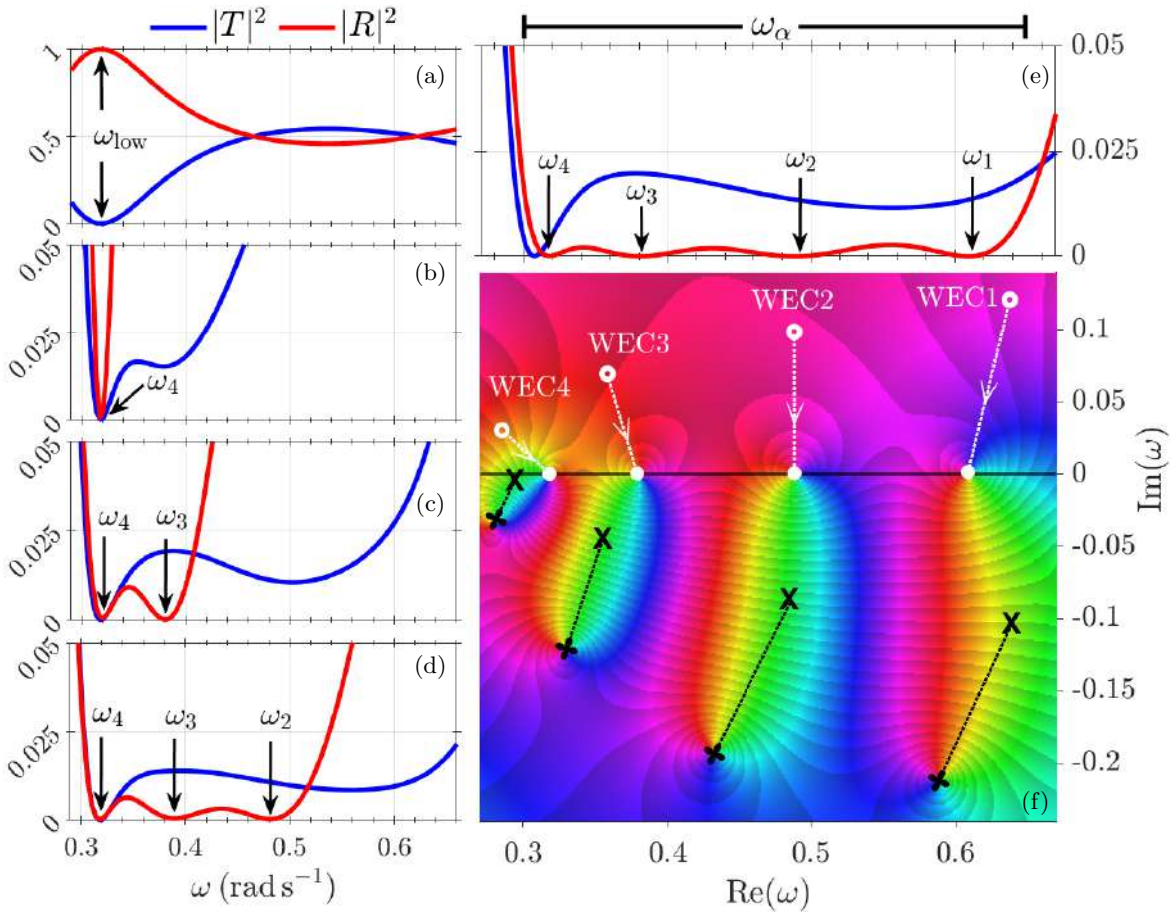

Figure 3.8: The transmission (—, blue) and reflection (—, red) of the array versus frequency as (a) WEC 5, (b) WEC 4, (c) WEC 3, (d) WEC 2 and (e) WEC 1 are added to the array (from right to left, with $W = 14\,\text{m}$) and tuned. The location of $|R|^2 \approx 0$ associated with each WEC is denoted ω_n, and corresponds to the location of complex zeros (white circles) of the absorbing WECs in the phase portrait of $R(\omega)$ for $\omega \in \mathbb{C}$ for the graded array shown in (f). The non-absorbing WEC 5 is denoted ω_{low}. Complex WEC-resonances are denoted X and open circles denote the zeros when $b_{(n)}^{\text{PTO}} = 0$ $(n = 1, 2, \ldots, N)$.

the objective

$$\text{minimise} \int_{\omega_{lb}}^{\omega_{ub}} |R(\omega)|^2 \mathrm{d}\omega \quad \text{with respect to } c_{(n)}^{\text{PTO}} \text{ and } b_{(n)}^{\text{PTO}} \ (n = 1, 2, \ldots, N), \tag{3.33}$$

to obtain four zeros in reflection (Figure 3.8e).

The above approach yields reflection zeros at $N - 1 = 4$ real frequencies, which corresponds to four complex zeros of reflection being translated to the real frequency axis by adding PTO damping (Figure 3.8f). The reflected energy remains small between the zeros ($|R|^2 < 0.003$), such that near-perfect broadband absorption of the incident wave energy is almost achieved over the target interval ($\hat{\alpha} = 0.984$). A small amount of transmitted energy away from its low-frequency zero prevents near-perfect absorption ($\int |T(\omega)|^2 \mathrm{d}\omega = 0.014$ on ω_α).

Table 3.1: PTO parameters and resulting WEC-resonance of each WEC in the graded array of five WECs shown in Figure 3.8.

WEC n	1	2	3	4	5
$\omega_0^{(n)}$ rad s^{-1}	0.789	0.655	0.482	0.353	0.299
$c_{(n)}^{\mathrm{PTO}}$ kN m^{-2}	−10.403	−36.752	−64.684	−81.028	−86.475
$b_{(n)}^{\mathrm{PTO}}$ kN m^{-2} s	29.582	50.276	40.221	24.137	0
$\hat{\alpha}_{(n)}$ on ω_α	0.255	0.422	0.255	0.068	0

3.6 Near-perfect broadband absorption

Both $|R|^2$ and $|T|^2$ should be minimised simultaneously over the target frequency interval ($\hat{\alpha}$ maximised) to achieve near-perfect, broadband power capture. Thus, optimisation is performed with the objective to

$$\text{minimise} \int_{\omega_{lb}}^{\omega_{ub}} \left\{|R(\omega)|^2 + |T(\omega)|^2\right\} \mathrm{d}\omega \quad \text{with respect to } c_{(n)}^{\mathrm{PTO}} \text{ and } b_{(n)}^{\mathrm{PTO}} \tag{3.34}$$

for $n = 1, \ldots, N$. The aim is to use the theory for rainbow absorption (§§ 3.4–3.5) to determine an initialisation strategy and constraints on the optimisation parameters that gives an efficient automated algorithm for near-perfect absorption.

3.6.1 Generic algorithm

To cover the target power capture interval, $\omega_\alpha = [\omega_{lb}, \omega_{ub}]$, the stiffness coefficients of the first and last WECs in the array ($c_{(1)}^{\mathrm{PTO}}$ and $c_{(N)}^{\mathrm{PTO}}$, respectively) are initialised so that the corresponding resonances ($\omega_0^{(1)}$ and $\omega_0^{(N)}$) coincide with the upper and lower bounds of the target interval (ω_{ub} and ω_{lb}). The WEC N resonance induces a zero in transmission at a frequency just above the lower bound (ω_{lb}, as in Figure 3.8a), and the stiffness coefficient of the penultimate WEC ($c_{(N-1)}^{\mathrm{PTO}}$) is initialised to place its resonance ($\omega_0^{(N-1)}$) at the frequency of the transmission zero. The remaining stiffness coefficients are initialised to space the resonances of WEC 2 to WEC $(N-2)$ evenly between $\omega_0^{(N-1)}$ and $\omega_0^{(1)}$, such that

$$\omega_0^{(N)} < \omega_0^{(N-1)} < \ldots < \omega_0^{(1)}. \tag{3.35}$$

The damping coefficients $b_{(1)}^{\mathrm{PTO}}$, $b_{(2)}^{\mathrm{PTO}}$, …, $b_{(N-1)}^{\mathrm{PTO}}$ are initialised at the optimal values for the corresponding WECs in isolation (Equation (3.13)). The final WEC is non-absorbing ($b_{(N)}^{\mathrm{PTO}} = 0$).

Table 3.2: Optimised PTO parameters for broadband absorption by the (generic) graded array of five WECs in Figure 3.9b.

WEC n	1	2	3	4	5
$\omega_0^{(n)}$ rad s^{-1}	0.722	0.563	0.433	0.340	0.310
$c_{(n)}^{\mathrm{PTO}}$ kN m^{-2}	−24.133	−52.264	−71.392	−82.453	−85.470
$b_{(n)}^{\mathrm{PTO}}$ kN m^{-2} s	39.046	39.393	28.008	14.390	0
$\hat{\alpha}_{(n)}$ on ω_α	0.443	0.372	0.154	0.030	0

To account for the leftward movement of WEC-resonances due to damping and WEC interactions on the restricted interval, the stiffness coefficients $c_{(n)}^{\mathrm{PTO}}$ $(n = 2, 3, \ldots, (N-1))$ are bounded below by their initial values and above by the initial value of the preceding WEC in the array (i.e., the initial value of $c_{(n-1)}^{\mathrm{PTO}}$). The upper bound for the stiffness coefficient of the first WEC ($c_{(1)}^{\mathrm{PTO}}$) is above the target interval and not an initial value. For arrays of $N < 7$ WECs, the upper bound is set to constrain $c_{(1)}^{\mathrm{PTO}}$ to a frequency interval length comparable to the constraints on $c_{(2)}^{\mathrm{PTO}}$, provided $\omega_0^{(1)} < 0.79\,\mathrm{rad\,s^{-1}}$ (i.e., the pole–zero pair remains on ω_α). When $N \geq 7$, the upper bound corresponds to $\omega_0^{(1)} = 0.72\,\mathrm{rad\,s^{-1}}$, which is approximately the minimum WEC-resonance required to maintain a bandgap at ω_{ub} (depending on pole–zero pair interactions). The damping coefficients $b_{(n)}^{\mathrm{PTO}}$ $(n = 1, 2, \ldots, (N-1))$ are constrained below such that they do not become negative (i.e., do not add energy to the system) and above such that they do not exceed twice the initial value, which does not limit the optimisation in practice (in tests conducted).

The generic algorithm creates near-perfect broadband absorption from an array of five WECs ($\hat{\alpha} = 0.990$), which slightly improves on the absorption given by the graded array of five WECs with zeros in reflection ($\hat{\alpha} = 0.984$; § 3.5.2). In comparison with the array with zeros in reflection (Table 3.1), the WEC-resonances are graded more gradually, over a narrower frequency range (Table 3.2). This slightly increases the absorption over the majority of the target power capture interval (Figure 3.9a). In complex-frequency space, the zeros in reflection are slightly displaced from the real frequency axis (Figure 3.9b) to balance reduced transmission. However, the absorption is lower than the array with zeros in reflection towards the ends of the target frequency interval, particularly at the high frequency end, which is influenced by the complex zeros corresponding to the second passband.

The grading of WEC-resonances partially controls the lower bound of the second passband. By grading the array more gradually to reduce transmission, this lower bound is downshifted, causing reflection and transmission to rise near ω_{ub} which decreases absorption. Increasing the number of WECs (e.g., to $N = 10$) improves the absorption at the high-frequency end of the target interval (and more generally across the interval, Figure 3.9a), by facilitating a

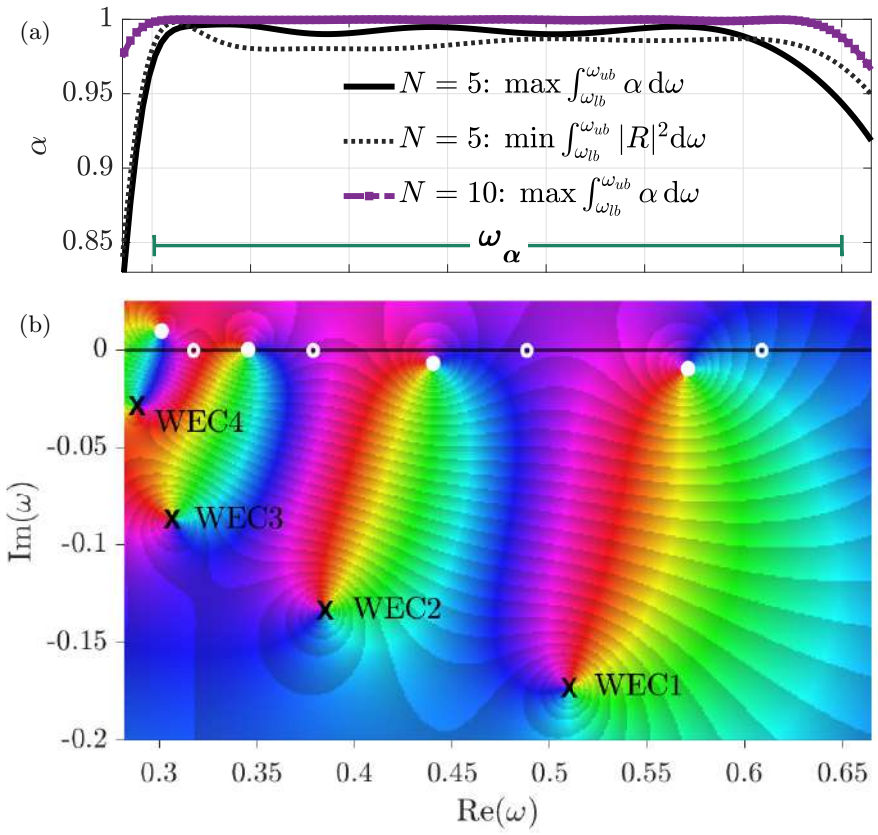

Figure 3.9: The absorption of the optimised, graded array (—) of five WECs is shown in (a) with the corresponding phase portrait of $R(\omega)$ for $\omega \in \mathbb{C}$ in (b). The absorption of the array in Figure 3.8f is overlaid (···) in (a), with the associated complex zeros in reflection marked by white **o**s in (b). Absorption improves over the majority of ω_α as a result of a more gradual grading in the generic solution (reduces $|T|^2$), which is facilitated by increasing the number of WECs to $N = 10$ in (a), using the array of $N = 10$ WECs in Figure 3.10b.

gradual grading across the entire target interval, which simultaneously reduces the width of the second passband, and the transmission over ω_α.

The generic algorithm becomes prohibitively expensive as the number of WECs increases. For $N = 6$, the algorithm takes 8 h on an Intel(R) Xeon(R) CPU E5-2699 v3 @ 2.30GHz with 251 GB RAM. Moreover, MATLAB exceeds the default tolerated number of function evaluations for $N \geq 7$. Consequently, an approach was developed for $N \geq 7$, in which approximate solutions were obtained using a coarse frequency resolution ($\omega = 0.01257\,\mathrm{rad\,s^{-1}}$) after the tolerated number of function evaluations, and then used as initial guesses in a second application of the algorithm with a higher frequency resolution ($\omega = 0.006283\,\mathrm{rad\,s^{-1}}$). In the second application, the stiffness coefficient constraints are updated to be bounded below by the initial guess, and above by the preceding WEC resonance. Here WEC 1 is constrained such that $\omega_0^{(1)} \in [0.72, 0.78]\,\mathrm{rad\,s^{-1}}$. The array of $N = 10$ WECs required three applications of the algorithm.

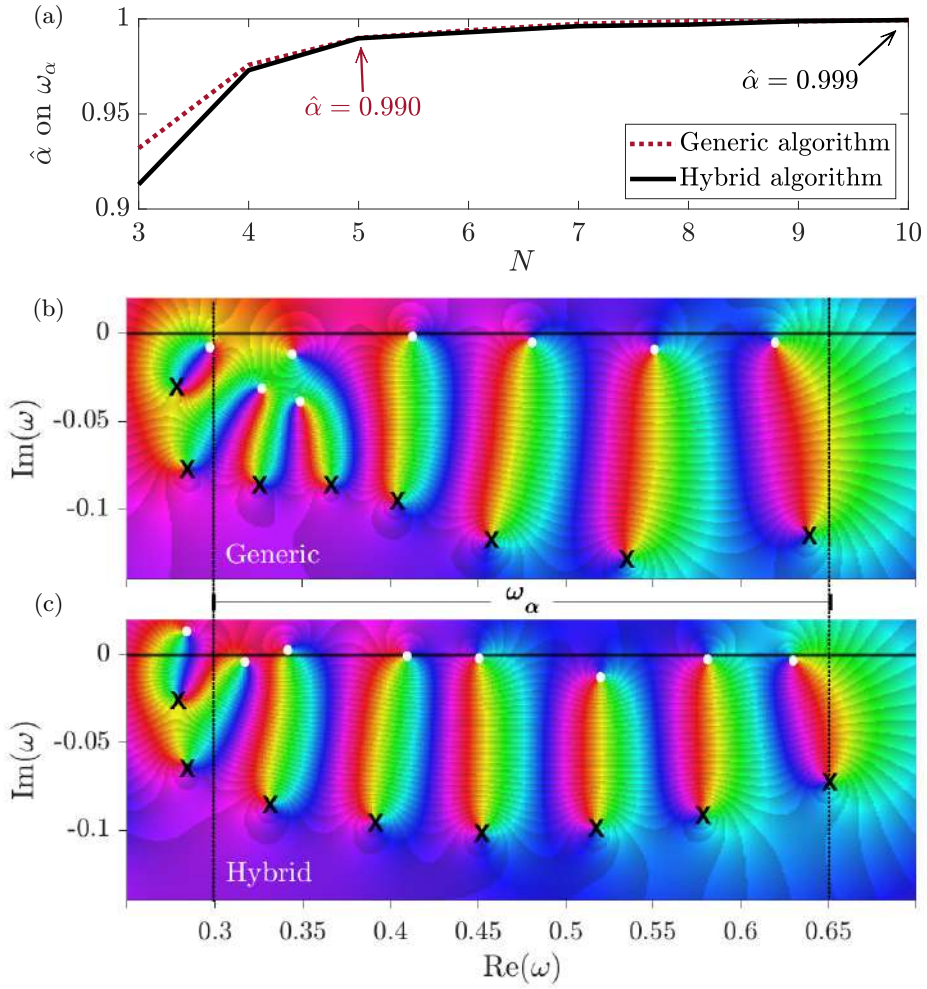

Figure 3.10: The average absorption on ω_α (a) increases with the number of WECs in both algorithms. Constraining the PTO parameters based on problem knowledge in the hybrid algorithm reduces run time and produces almost identical absorption (⋯) to the generic algorithm (—). However, the array properties differ, as demonstrated for an array of 10 WECs using the phase portraits of $R(\omega)$ for $\omega \in \mathbb{C}$ corresponding to the solution of the generic (b), and hybrid (c) algorithms, respectively. pole–zero pairs are more separated in (c) allowing for more near-zeros in reflection to be obtained compared with (b). In both algorithms, the pole–zero pair of an absorbing WEC is pushed beyond axes limits (WEC 10 lies below the axes limits).

3.6.2 Hybrid algorithm

The generic algorithm is adapted into a hybrid algorithm that incorporates more knowledge gained from the analysis of the graded array (§ 3.5.2) to accelerate the optimisation process. To cater for the leftward shift of the WEC-resonances and ensure absorption at ω_{ub}, WEC 1 is initialised and constrained such that its real-valued resonance lies above the power capture interval, with $c_{(1)}^{\mathrm{PTO}}$ constrained around $\omega \approx 0.75\,\mathrm{rad\,s^{-1}}$. Similarly, $c_{(N-1)}^{\mathrm{PTO}}$ is constrained to a narrow interval above ω_{lb}, around $\omega \approx 0.33\,\mathrm{rad\,s^{-1}}$. Further, the initial damping constants for the first and second last WECs in the array (WEC 1 and WEC $(N-1)$) are set lower

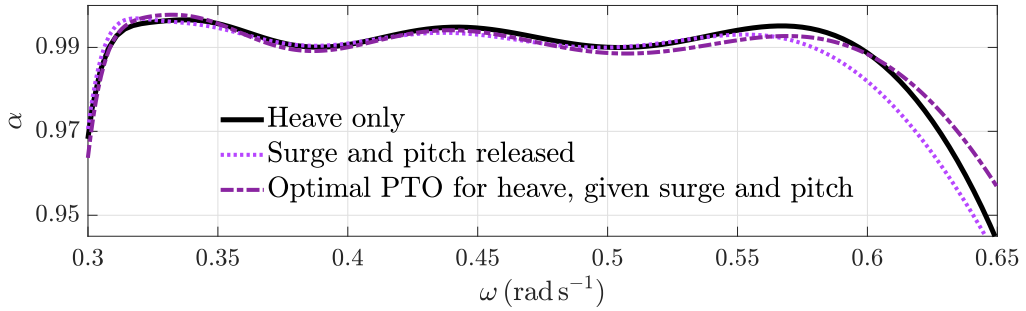

Figure 3.11: Releasing surge and pitch (⋯) in the optimal generic solution (—) for the array of $N = 5$ WECs in Table 3.2 reduces the average absorption by 0.0017 ($\hat{\alpha} = 0.988$). Re-optimising the solution to account for the uncontrolled surge and pitch motions (-·-) over the target interval results in an average absorption of $\hat{\alpha} = 0.990$.

than optimal values for the WECs in isolation to provide greater control over the location of pole–zero pairs of reflection and transmission in complex frequency space, i.e., consistent with observations in Table 3.1. The stiffness and damping coefficients, $c_{(n)}^{\mathrm{PTO}}$ $(n = 2, \ldots, (N-2))$ and $b_{(n)}^{\mathrm{PTO}}$ $(n = 1, 2, \ldots, N)$, respectively, are constrained analogously to the generic algorithm, with the exception of the upper bound for WEC 2, which is constrained above by the lower constraint bound of WEC 1.

The hybrid algorithm gives almost identical broadband absorption to the generic algorithm for $N \geq 5$ (Figure 3.10a). It does so at approximately half the runtime of the generic algorithm when $N = 6$. The algorithm was reapplied (as in § 3.6.1) for $N = 10$, with the constraints held fixed. The differences between the algorithms are manifest in the structure of the reflection coefficient in complex frequency space, for which the generic algorithm stacks the pole–zero pairs at low frequencies (Figure 3.10b), whereas the hybrid algorithm keeps them separated (Figure 3.10c). The increased separation allows for greater control over the location of pole–zero pairs, as evidenced by additional near-zeros in reflection in the hybrid solution. A pole–zero pair associated with an absorbing WEC is pushed beyond the axes limits in both algorithms as a result of interactions on the restricted interval.

3.6.3 Multiple degrees of freedom

Allowing the buoys to surge and pitch (as non-absorbing degrees of freedom), as well as heave (the absorbing degree of freedom), has little impact on the near-perfect, broadband absorption achieved by the optimised arrays. For example, the average absorption of the array of five WECs produced by the generic algorithm (Table 3.2) decreases only from $\hat{\alpha} = 0.990$ to $\hat{\alpha} = 0.988$ when the surge and pitch motions are released (Figure 3.11). Re-optimising the PTO parameters for heave motion for the problem including surge and pitch (starting from the optimised solution for heave only) brings the average absorption back to $\hat{\alpha} = 0.990$. The

Table 3.3: Optimised PTO parameters for the graded array of five WECs in Figure 3.11 when surge and pitch are released as uncontrolled degrees of freedom.

WEC n	1	2	3	4	5
$\omega_0^{(n)}\,\mathrm{rad\,s^{-1}}$	0.741	0.558	0.423	0.331	0.308
$c_{(n)}^{\mathrm{PTO}}\,\mathrm{kN\,m^{-2}}$	−20.111	−52.870	−72.269	−82.928	−85.160
$b_{(n)}^{\mathrm{PTO}}\,\mathrm{kN\,m^{-2}\,s}$	44.060	39.540	26.762	13.407	0
$\hat{\alpha}_{(n)}$ on ω_α	0.469	0.361	0.143	0.026	0

optimal PTO parameters for the multiple-degrees-of-freedom case (Table 3.3) differ from the single-degree-of-freedom case (Table 3.2) by only 5%, on average. Small differences for the absorption versus frequency are visible for the two optimised arrays (Figure 3.11).

3.6.4 Ocean wave spectra

The JONSWAP (JOint North Sea WAve Project (Hasselmann et al., 1973)) spectrum is commonly used to model realistic (irregular, random) sea states (Chakrabarti, 2005). The JONSWAP spectrum is defined by the spectral density function

$$S(\omega) = \frac{0.0081g^2}{\omega^5}\mathrm{e}^{-1.25(\omega_p/\omega)^4}\gamma^r \quad \text{where} \quad r = \mathrm{e}^{-(\omega-\omega_p)^2/2\sigma^2\omega_p^2} \tag{3.36}$$

and the spectral width is

$$\sigma = \begin{cases} 0.007 & \omega < \omega_p, \\ 0.009 & \omega \geq \omega_p. \end{cases} \tag{3.37}$$

The peak enhancement factor γ characterises the sharpness of the spectrum around the peak frequency $\omega_p = 2\pi/T_p$ (peak period T_p, with maximum energy in the spectrum). Smaller values are indicative of broader banded sea states, with $\gamma \leq 2.4$ generally suited to coastal regions (Mazzaretto et al., 2022).

Let the JONSWAP spectrum be approximated by a finite sum of monochromatic waves (Cruz, 2008), at frequencies $\omega_0 = 0.22\,\mathrm{rad\,s^{-1}}$, $\omega_1 = \omega_0 + \Delta\omega$, …, $\omega_{200} = \omega_0 + 200\Delta\omega = 1.26\,\mathrm{rad\,s^{-1}}$ ($\Delta\omega = 0.0052$), then the corresponding absorption of the spectrum is defined as

$$\alpha_s(\omega_i) = \sum_{i=0}^{200} \alpha(\omega_i)|A(\omega_i)|^2 \quad \text{where} \quad A(\omega_i) = \sqrt{2S(\omega_i)\Delta\omega}. \tag{3.38}$$

The proportion of the spectrum absorbed is

$$\hat{\alpha}_s = \frac{\int \alpha_s(\omega)\,\mathrm{d}\omega}{\int |A(\omega)|^2\,\mathrm{d}\omega}. \tag{3.39}$$

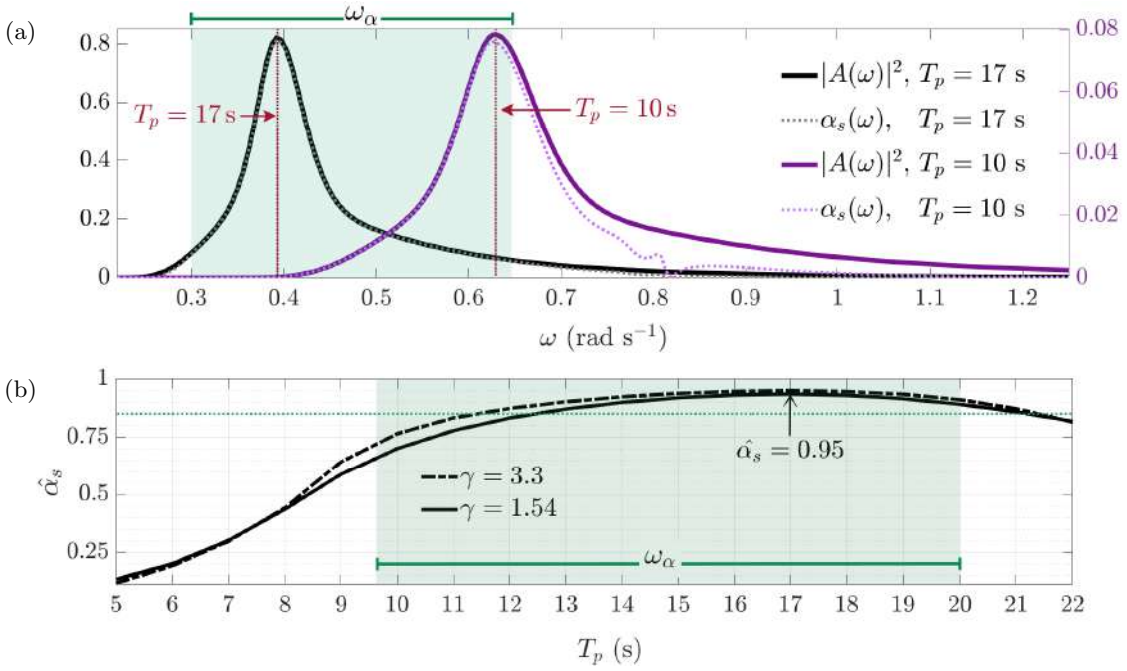

Figure 3.12: The absorption of spectra ($\gamma = 3.3$) with peak periods located in ω_α is shown in (a) for the graded array of five WECs in Table 3.2. The proportion of spectra captured by the array is shown as a function of peak period in (b) for a constant significant wave height of 1 m. Absorption decreases as the peak period shifts farther from the targeted interval and the energy of the spectrum is located outside the designed frequency range of the array. On average, $\hat{\alpha_s} > 0.85$ ($\cdots$) on ω_α for both $\gamma = 1.54$ and $\gamma = 3.3$.

The optimised array of five WECs (generic algorithm, Table 3.2) captures $\hat{\alpha}_s = 0.95$ of the incident energy in a JONSWAP spectrum with a narrow-banded sea state ($\gamma = 3.3$) and a peak period $T_p = 17\,\mathrm{s}$, as the spectral peak lies within the target power capture interval (Figure 3.12a). The array still captures over $\hat{\alpha}_s > 0.75$ of the incident energy when the spectral peak is moved close to the upper boundary of the target interval ($T_p = 10\,\mathrm{s}$, Figure 3.12a). The array captures over 85% of the incident energy for peak periods of approximately 11–20 s. For a broader sea state ($\gamma = 1.54$) this T_p-interval is shifted to 12–21 s, and the peak absorption is reduced slightly to $\hat{\alpha}_s = 0.936$ at $T_p = 17\,\mathrm{s}$.

3.7 Absorption of Bloch modes in time domain

An incident wave packet of unit amplitude in the time domain is specified via the Fourier transform of its ocean surface displacement, $\eta(x,t)$. The Fourier transform maps between the time and frequency domains and is expressed in terms of wavenumber, $k(\omega)$, as

$$F\{\eta(x,0)\} \equiv \hat{f}(k) = \frac{1}{\sigma\sqrt{2\pi}} \mathrm{e}^{-(k-k_0)^2/2\sigma^2}, \tag{3.40}$$

where k_0 is the prescribed central wavenumber and σ is the prescribed packet width (in wavenumber space). The response of the WECs and the free surface elevation are calculated from the frequency domain solutions, as, respectively,

$$\Xi_n(t) = \mathrm{Re}\left\{\frac{1}{\pi}\int_0^\infty \hat{f}(k)\,\xi_n(k)\,\mathrm{e}^{-\mathrm{i}\omega(k)t}\mathrm{d}k\right\} \quad \text{for} \quad n = 1, 2, \ldots, N, \tag{3.41}$$

and

$$\eta(x,t) = \mathrm{Re}\left\{\frac{1}{\pi}\int_0^\infty \hat{f}(k)\,\zeta(x:k)\,\mathrm{e}^{-\mathrm{i}\omega(k)t}\mathrm{d}k\right\}, \tag{3.42}$$

where the dependencies of frequency domain quantities on wavenumber are made explicit.

In the frequency domain, the wavefield in each unit cell is decomposed into the rightward and leftward Bloch modes, by writing

$$\phi_{(n)}(x,z:k) \approx w^+_{(n)}(k)\,\psi^+_{(n)}(x,z:k) + w^-_{(n)}(k)\,\psi^-_{(n)}(x,z:k) \quad \text{for} \quad n = 1, \ldots, N, \tag{3.43}$$

where the weights $w^\pm_{(n)}$ $(n = 1, \ldots, N)$ are calculated as

$$\begin{bmatrix} w^+_{(n)} \\ w^-_{(n)} \end{bmatrix} = \begin{bmatrix} v^+_{(n)} & v^-_{(n)} \\ v^-_{(n)} & v^+_{(n)} \end{bmatrix}^{-1} \begin{bmatrix} a^+_{(n)} \\ a^-_{(n)} \end{bmatrix}. \tag{3.44}$$

Similarly, the free surface elevation and heave amplitudes are decomposed as

$$\zeta(x:k) = w^+_{(n)}(k)\,\psi^+_{(n)}(x,0:k) + w^-_{(n)}(k)\,\psi^-_{(n)}(x,0:k) \quad \text{for} \quad \Omega^{\mathrm{L}}_{(1)} \le x \le \Omega^{\mathrm{R}}_{(N)}, \tag{3.45}$$

and

$$\xi_n(k) = w^+_{(n)}(k)\,\gamma^+_{(n)}(k) + w^-_{(n)}(k)\,\gamma^-_{(n)}(k) \quad \text{for} \quad n = 1, \ldots, N, \tag{3.46}$$

where

$$\gamma^\pm_{(n)} = \left(v^\pm_{(n)}\mathrm{e}^{\mathrm{i}k_0\left(x-\Omega^{\mathrm{L}}_{(n)}\right)} + \mathrm{e}^{\pm\mathrm{i}\beta W}\,v^\mp_{(n)}\mathrm{e}^{-\mathrm{i}k_0\left(x-\Omega^{\mathrm{R}}_{(n)}\right)}\right)\xi^h_{(n)}. \tag{3.47}$$

Equivalent decompositions of the surface elevation and heave displacements are made in the time domain, with

$$\eta(x,t) = \Psi^+_n(x,t) + \Psi^-_n(x,t) \quad \text{for} \quad \Omega^{\mathrm{L}}_{(n)} \le x \le \Omega^{\mathrm{R}}_{(n)}, \tag{3.48}$$

$$\text{and} \quad \Xi_n(t) = \Xi^+_n(t) + \Xi^-_n(t), \tag{3.49}$$

where

$$\Psi_n^{\pm}(x,t) = \mathrm{Re}\left\{\frac{1}{\pi}\int_0^{\infty} \hat{f}(k)\, w_{(n)}^{\pm}(k)\, \psi_{(n)}^{\pm}(x,0:k)\, \mathrm{e}^{-\mathrm{i}\omega(k)t}\mathrm{d}k\right\} \tag{3.50}$$

$$\text{and} \quad \Xi_n^{\pm}(t) = \mathrm{Re}\left\{\frac{1}{\pi}\int_0^{\infty} \hat{f}(k)\, w_{(n)}^{\pm}(k)\, \gamma_{(n)}^{\pm}\, \mathrm{e}^{-\mathrm{i}\omega(k)t}\mathrm{d}k\right\} \tag{3.51}$$

for $n = 1, 2, \ldots, N$. Note that the rightward and leftward Bloch modes are not continuous at the interfaces between the unit cells (only their sum is continuous).

As an example, consider the case of the optimised array of $N = 5$ WECs (Table 3.2), which gives near-perfect broadband absorption over the target interval ($\hat{\alpha} = 0.990$). The spatio-temporal responses to two separate incident wave packets are shown, where the packets are centred around a wavenumber at the resonant frequency of WEC 2 ($k_0 = 0.03441$, Figure 3.13) and WEC 4 ($k_0 = 0.01703$, Figure 3.14). Both have a packet width of $\sigma = 0.002673\,\mathrm{m}^{-1}$, so that the packet centred at WEC 2 covers the resonant frequencies of WECs 1–3, and the packet centred at WEC 4 covers WECs 2–5. The total responses are shown (figures 3.13a,b and 3.14a,b), as well as their decompositions into rightward and leftward Bloch mode (figures 3.13c,d and 3.14c,d, and figures 3.13e,f and 3.14e,f, respectively). The responses are shown for the non-absorbing array ($b_{(n)}^{\mathrm{PTO}} = 0$ for $n = 1, 2, \ldots, 5$, figures 3.13a,c,e and 3.14a,c,e), as well as the absorbing array (figures 3.13b,d,f and 3.14b,d,f). (The artificial periodicity introduced via the discrete implementation of the Fourier transform is ≈ 40 minutes, which is much greater than the ≈ 3 minute duration of the responses shown.)

For the non-absorbing array, the incident wave packets gradually reduce in amplitude as they propagate through the array due to a series of partial reflections by the WECs (figures 3.13a and 3.14a). There is a more abrupt cut-off after the WECs corresponding to the central wavenumbers of the incident packets (WEC 2 in Figure 3.13a and WEC 4 in Figure 3.14a), such that the amplitudes reduce to $\approx 20\%$ of their incident values. The overall reflection is indicated by the durations of the wave signals decreasing with distance into the array (up to the cut-offs). The incident and reflected packets are isolated from one another by the decomposition into Bloch modes, such that the incident wave packets propagate through the array in the form of rightward Bloch modes (figures 3.13c and 3.14c) and are reflected back out of the array in the form of leftward Bloch modes (figures 3.13e and 3.14e).

The incident wave packets propagate similar distances into the absorbing arrays (figures 3.13b and 3.14b), as their non-absorbing counterparts. However, there is almost no reflected wave packet generated, as indicated by similar durations of the wave signal along the array (up to the cut-offs), and the near-resonant WEC responses are reduced by 30–40% compared with the non-absorbing arrays. Thus, absorption is the cause of reductions in the amplitude of the incident packet. The decomposition into Bloch modes gives further evidence of the absence

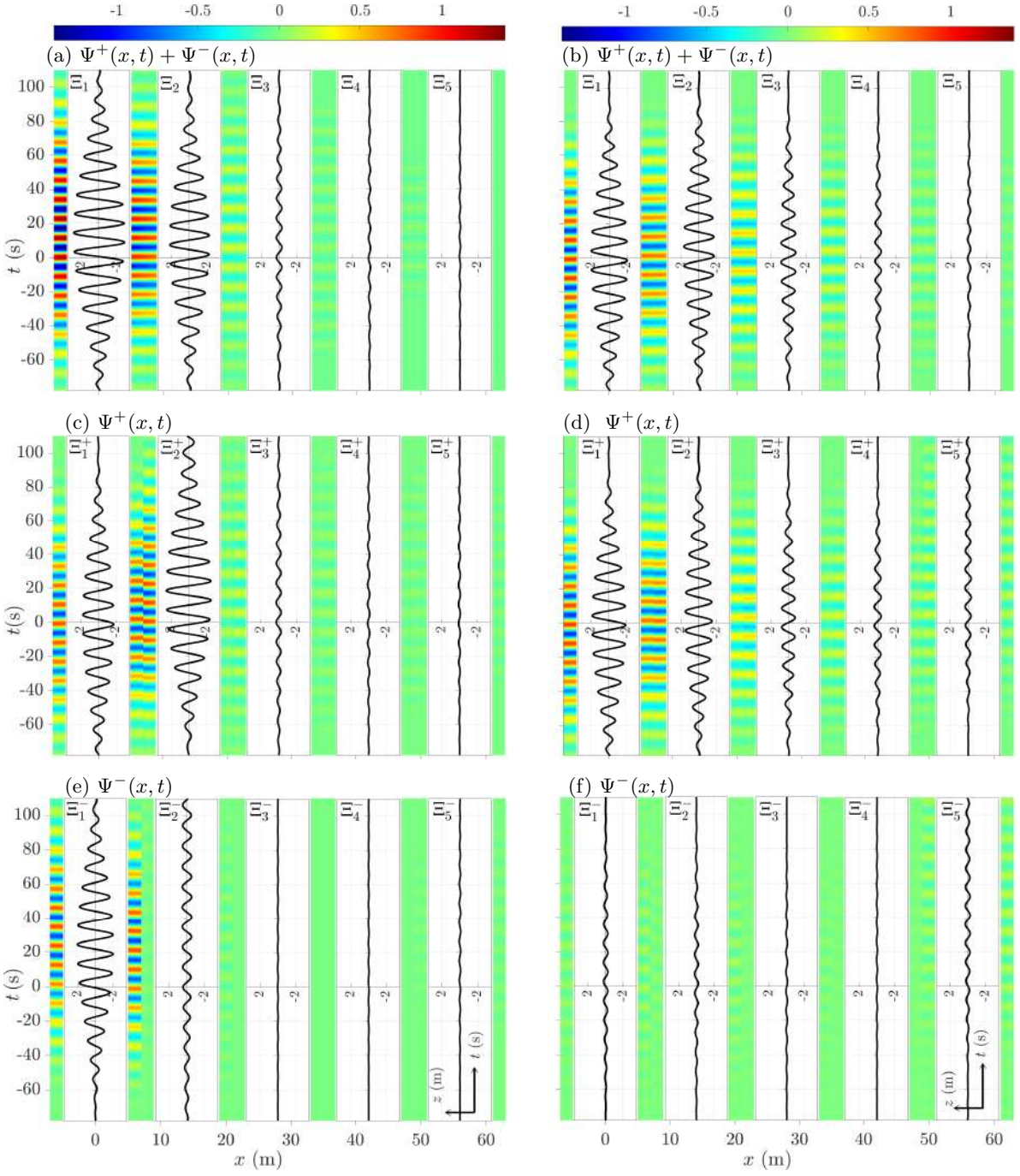

Figure 3.13: The spatio-temporal behaviour of the non-absorbing (column one) and absorbing arrays (column two), are shown in (a) and (b), respectively, when forced by a wave packet centred at $k_0 = 0.03441$. The total wavefields are decomposed into rightward Bloch modes in (c) and (d), and leftward Bloch modes in (e) and (f), respectively. The WEC displacements are overlaid on z–t axes at the x-location of WECs in the x–t domain. In the non-absorbing array, the rightward Bloch mode cuts off at WEC 2 (c). The leftward mode (e) then drives almost total reflection of frequencies above the cut-off. In the absorbing array, the total wavefield (b) and WEC displacements are dominated by the rightward Bloch mode (d), with little excitement of the leftward Bloch mode (f) through the absorption of incident energy.

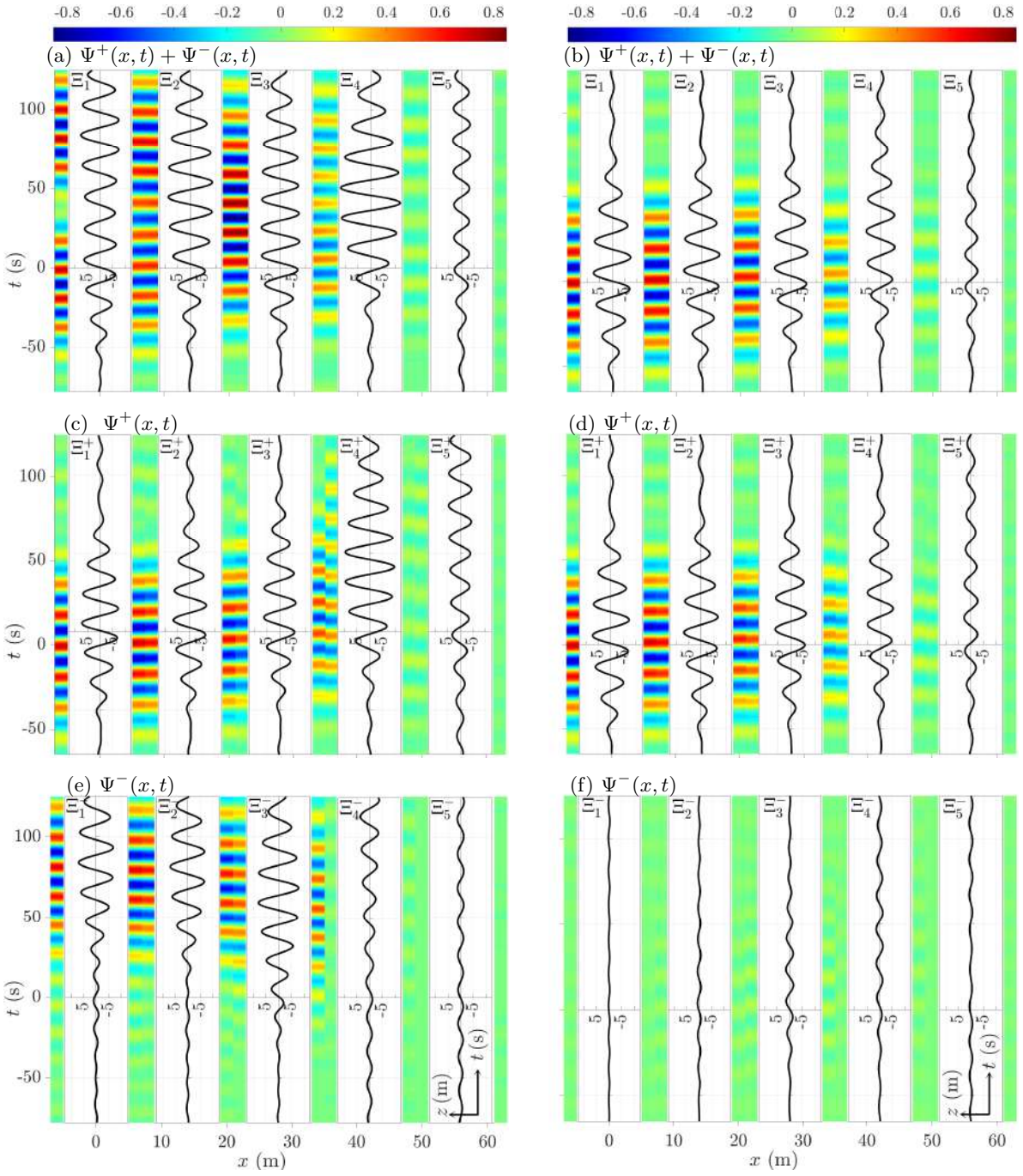

Figure 3.14: The spatio-temporal behaviour of the non-absorbing (column one) and absorbing arrays (column two) when forced by a wave packet centred at $k_0 = 0.01703$. The total wavefields are decomposed into rightward Bloch modes in (c) and (d), and leftward Bloch modes in (e) and (f), respectively. The WEC displacements are overlaid on z–t axes at the x-location of WECs in the x–t domain. The total wavefield (a) is dominated by the rightward Bloch mode (c) in the non-absorbing array before the cut off at WEC 4 is reached. The leftward mode (e) drives high reflection above the cut-off. With PTO damping, the total wavefield (b) and WEC displacements in the absorbing array are governed predominantly by the rightward Bloch mode (d), with little excitement of the leftward Bloch mode (f), and thus, near-zero reflection.

of reflection and dominance of absorption, with the rightward Bloch modes indistinguishable from the total wavefields (figures 3.13d and 3.14d) and virtually no leftward Bloch modes excited (figures 3.13f and 3.14f).

3.8 Conclusions and discussion

Arrays of heaving point-absorber WECs have been designed to achieve near-perfect, broadband wave energy absorption, using 2D linear potential-flow theory. The WECs consisted of floating buoys plus spring–damper PTOs, and used parameters inspired by CorPower Ocean's C4 device. Broadband absorption was demonstrated in both the frequency and time domains over a typical frequency interval for power capture (equivalent to a wave period interval $\approx$ 10–20 s) using time-independent PTO parameters. In particular, an array of only five heaving buoy type WECs was shown to capture 99% of the incident wave energy over the target interval. The array performance was analysed for irregular sea states, and near-perfect broadband absorption was also demonstrated when surge and pitch motions were released.

The approach to designing near-perfect broadband absorption was based on theories for graded arrays. From an underlying uniform array of non-absorbing WECs, the rainbow reflection effect was generated by grading the PTO stiffness coefficients to prohibit transmission of wave frequency bands at spatially controlled locations within the array, thus producing a wide effective bandgap over the targeted frequency range. The approach to this first stage was based on decomposing the local wavefields into Bloch wave modes, and requires the WEC-resonances to decrease in the direction of the incident wave. Rainbow absorption was then created by adding PTO damping to capture the reflected energy by manipulating the associated complex zeros over the targeted interval. This second stage used analysis of the reflection coefficient in complex-frequency space, and control of the pole–zero pair locations (via the PTO parameters) for zero reflection at discrete frequencies. A rainbow absorbing array of five WECs was presented, which gave high broadband absorption ($>$ 98% over the target frequency interval), although near-perfect absorption was prohibited by small amounts of transmission. The rainbow absorbing theory was used to inform algorithms that minimise the sum of the reflected and transmitted energies to generate near-perfect broadband absorption. An algorithm in which the initialisation incorporates knowledge about the manual process to move complex zeros to the real-frequency axis was found to create a far more efficient optimisation algorithm.

The high-frequency end of the target power capture interval is the most difficult to control as the cluster of pole–zero pairs close to the real frequency axis just above the target frequency interval (related to the second passband) force spikes in transmission and reflection, hence,

lowering absorption. Near-perfect absorption at the high-frequency end of the target power capture requires tuning a sufficient number of WECs to high frequencies, although this increases the difficulty of separating the complex zeros close to the real frequency axis without them interfering with one another. pole–zero pairs had to be forced towards the upper bound by adjusting the constraints and initialisations in the optimisation algorithms. This issue does not seem to have been encountered in previous designs of rainbow absorbing arrays (Jiménez et al., 2017b; Wilks et al., 2022), due to near total reflection above the target intervals, and more weakly coupled systems (Romero-García, Theocharis, Richoux and Pagneux, 2016).

The distance between WECs (i.e., the widths of the unit cells) can be used to control the separation of the pole–zero pairs corresponding to the first and second passbands, such that shorter WEC spacing gives greater separation. A spacing similar to the WEC dimensions ($d/L = 0.8$) was chosen to give a reasonable separation between the passbands/pole–zero pairs. A shorter spacing is unlikely to be feasible in applications. From a different perspective, using a longer WEC separation would have the benefit of compressing the second passband and bringing the second bandgap (due to Bragg resonance) to lower frequencies, such that it could be used to extend the target power capture interval to higher frequencies. Thus, the target interval would be covered by the first bandgap (due to local/WEC resonances) and the second bandgap (due to Bragg resonance). The combined bandgap (in the non-absorbing case) is similar to the super bandgap idea being developed in vibroacoustic systems (Cleante et al., 2022; Guo et al., 2020). However, the second bandgap/pole–zero pairs will occupy the target interval and cause absorption to drop over a frequency interval, such that near-perfect absorption would be more challenging to achieve.

The broadband extraction of wave energy demonstrated by WEC-arrays in this study could help protect coastlines against extreme events (e.g. Ozkan et al., 2022), by countering erosion at vulnerable coastlines as a by-product of power capture (Abanades et al., 2018), or in the design of WEC-arrays for coastal protection (e.g. Cui et al., 2024). In this guise, graded WEC-arrays would provide a broadband extension for coastal protection to the proposed uniform arrays of non-absorbing resonators that reflect (Dupont et al., 2017) or attenuate (Zhang et al., 2024) low-frequency bands of damaging wavelengths, or utilise local and Bragg resonant effects for attenuation over wider frequency ranges (Lorenzo et al., 2023).

The design for broadband absorption can be extended to different modes of motion, devices and operating principles, including multi-resonant devices which, as individual devices, are efficient over a relatively broad frequency range for fixed PTO parameters (e.g., Crowley et al., 2013; Evans and Porter, 2012), and oscillating wave surge converters which can achieve high capture factors (e.g., Huang and Porter, 2024; Noad and Porter, 2015; Renzi and Dias, 2012). In some instances, grading geometry may be more appropriate, as in Wilks et al.

(2022), which can be applied to oscillating water columns with multiple chambers (e.g., Zhao et al., 2023), or by altering flap length in arrays of oscillating wave surge converters (Noad and Porter, 2015).

The computational efficiency gained by using a 2D model facilitated the in-depth analysis of, in particular, complex-frequency space and the optimisation algorithms. However, the key components of the proposed approach to design highly efficient broadband arrays of WECs, namely Bloch waves and complex resonances, also exist in 3D models. Therefore, we envisage 3D models of WECs (e.g., Tokić and Yue, 2019, 2023), arranged into rows (otherwise known as gratings with associated Bloch waves (Bennetts and Squire, 2009; Peter and Meylan, 2010)), graded such that they produce rainbow reflection (similar to Bennetts et al. (2019)), and with PTOs tuned to achieve rainbow absorption.

Future research directions include incorporating factors such as physical constraints on the WEC operation and motion to develop practical designs for WEC-arrays (Bacelli and Ringwood, 2013; Wang et al., 2015), and non-linearities particularly relevant to more accurately modelling heaving buoys under operational conditions, for example, through viscous drag and non-linear Froude–Krylov forces in partially non-linear models (Giorgi and Ringwood, 2017; Penalba, Giorgi and Ringwood, 2017), or weakly non-linear approaches (e.g., Michele et al., 2018). Based on experimental results relating to band structures (Dupont et al., 2017; Lorenzo et al., 2023) and rainbow trapping (Archer et al., 2020) in arrays of non-absorbing resonators, it is likely that the demonstrated rainbow absorption will be robust to non-linear phenomena, but that the efficiency will be reduced.

In conclusion, we have shown that a handful of heaving point-absorber WECs can achieve near-perfect, broadband absorption, by grading their resonant properties using time-independent PTO parameters. The novel approach for tuning arrays of heaving buoys revolved around manipulating band structures local to each WEC in the array and taking an analytic continuation of the problem into complex-frequency space to connect the near-resonances generated as part of the rainbow reflection phenomenon to pole–zero pairs of the reflection coefficient. Near-perfect, broadband absorption was generated by choosing the PTO damping to move the complex zeros in reflection to the real frequency axis.

Statement of Authorship

Title of Paper	Broadband absorption of ocean wave energy using a graded array of heaving cylinders in 3D
Publication Status	☐ Published ☐ Accepted for Publication ☐ Submitted for Publication ☑ Unpublished and Unsubmitted work written in manuscript style
Publication Details	NA

Principal Author

Name of Principal Author (Candidate)	Amy-Rose Westcott		
Contribution to the Paper	Conceptualisation; literature review; modelling; design and implementation of methodology; writing of code; validation; development of strategies and generation of results; analysis, interpretation and synthesis of results; production and formatting of figures; preparation and writing of initial draft; editing and revision of manuscript.		
Overall percentage (%)	85%		
Certification:	This paper reports on original research I conducted during the period of my Higher Degree by Research candidature and is not subject to any obligations or contractual agreements with a third party that would constrain its inclusion in this thesis. I am the primary author of this paper.		
Signature		Date	16/12/2025

Co-Author Contributions

By signing the Statement of Authorship, each author certifies that:

i. the candidate's stated contribution to the publication is accurate (as detailed above);
ii. permission is granted for the candidate in include the publication in the thesis; and
iii. the sum of all co-author contributions is equal to 100% less the candidate's stated contribution.

Name of Co-Author	Luke Bennetts		
Contribution to the Paper	Conceptualisation; design of methodology; assisted with interpretation of results; supervision; feedback on initial draft, revision of manuscript.		
Signature		Date	10/12/2025

Name of Co-Author	Nataliia Sergiienko		
Contribution to the Paper	Conceptualisation; supervision; feedback.		
Signature		Date	11/12/2025

Name of Co-Author	Benjamin Cazzolato		
Contribution to the Paper	Conceptualisation; supervision; feedback.		
Signature		Date	14/12/2025

Chapter 4

Broadband absorption of ocean wave energy using a graded array of heaving cylinders in 3D

Abstract

The competitive generation of renewable power from ocean waves at a commercial scale will require arrays of wave energy converters (WECs) to be designed for efficient power capture over broad frequency bands. An array design is developed by arranging heaving buoy type WECs into stacks (periodic rows of infinitely many, identical WECs), and spatially grading the resonant properties of WECs in successive stacks via linear spring–damper power take-off mechanisms (PTOs). Applying linear potential-flow theory, analyses based on Bloch waves and pole–zero pairs in complex frequency space are used to inform the array layout and choice of PTO parameters, based on theories for rainbow reflection and rainbow absorption. The spacing within an array alters the resonant properties of stacks, the behaviour of higher-order passbands, and the associated pole–zero pairs, which has implications for the efficiency of an array. The theories are used to grade arrays (manually) for efficient, broadband absorption over a broad target frequency range, and an average absorption exceeding 90% is achieved over a wide range of wave directions. The strategies are applied to finite arrays, which demonstrate broadband absorption in directionally spread, irregular sea states, and are shown to outperform the absorption of uniform arrays across a wide range of peak periods.

4.1 Introduction

The renewable power of ocean waves is characterised by high energy density and availability, in proximity to almost half of the global population (Coe et al., 2021). Wave energy converters (WECs) are designed to harness this power, but are yet to reach commercial viability, despite the development of many different concepts (Guo and Ringwood, 2021). Heaving buoys are a popular type of WEC that convert power at maximum efficiency when tuned to resonate via an attached power take-off mechanism (PTO) for optimum wave interference (Falnes, 2005). However, like many other WECs, heaving buoys have a relatively narrow resonance bandwidth compared to ocean waves (Pecher and Kofoed, 2017), where wave periods between 5 and 20 s

are feasible for power capture (Coe et al., 2021), and will require strategies to remain efficient across operational conditions in order to become cost-effective.

WECs will need to be deployed in arrays that operate at high efficiency to reach economic viability through reducing the cost of power generated per ocean area, and the installation, operations and maintenance cost per WEC (Ning and Ding, 2022; Ringwood et al., 2023). The power captured by arrays is increased by optimising the WEC geometry (e.g., Edwards and Yue, 2022), layout (Göteman et al., 2020), or PTOs (Blanco et al., 2025; Sheng and Lewis, 2016), preferably in combination (e.g., Wilks et al., 2025) for a given sea state. However, given the inherent irregularity and variability of wave climates (Ning and Ding, 2022), and the sensitivity of arrays to directionality (Gallutia et al., 2022), it is likely that control strategies will be necessary to achieve the high efficiency over broad frequency bands (*broadband absorption*) required for cost-effectiveness (Coe et al., 2021; Pecher and Kofoed, 2017).

Developing control strategies to adjust the PTO parameters according to predicted sea states is an active research topic, with most models based on linear theory (Ringwood et al., 2023). The interdependence between the hydrodynamic interactions, array layout and control strategy makes dynamic control highly complex (Ringwood, 2025), which further requires sophisticated PTOs (Ning and Ding, 2022), accurate wave prediction, is sensitive to model errors, and increases overall cost (Pecher and Kofoed, 2017). Consequently, designing arrays to maintain high efficiency without requiring repeated adjustments based on short-term forecasting, is an appealing, and economic, prospect (Korde and Ringwood, 2016; Pecher and Kofoed, 2017).

Broadband capture of ocean wave energy has recently been demonstrated in 2D models governed by linear theory, by grading the resonant properties of WEC-arrays for rainbow absorption (Westcott et al., 2024; Wilks et al., 2022). The WEC resonances are graded to prevent the transmission of targeted wave frequencies by manipulating the underlying local band structures to create a rainbow reflecting array (Westcott et al., 2024; Wilks et al., 2022). The grading generates a frequency dependent series of near-resonant responses as the incident wave energy is selectively slowed according to frequency, and accumulates at locations in the array associated with cut-off points, which are defined by the local periodicity, and spatially controlled through the WEC resonances (Bennetts et al., 2018). The localised amplifications are captured via the PTO damping, which is chosen to minimise the amplitude of reflected waves for rainbow absorption (Westcott et al., 2024; Wilks et al., 2022).

The geometrically graded, surrounding structure of rigid vertical barriers devised by Wilks et al. (2022) aids the prevention of transmission (leading to 98.2% absorption of 4–8 s waves), and could be realised by integrating oscillating water columns into breakwaters (e.g., Hu et al., 2025; Zhao et al., 2023) for combined power capture and coastal protection. In contrast, arrays of heaving buoys prevent transmission by creating a series of overlapping, local bandgaps

through destructive interactions, which are generated by the graded resonances and controlled via PTO spring terms (Westcott et al., 2024). The spatially controlled amplifications are then captured for 99% absorption of 10–20 s waves (Westcott et al., 2024).

In this study, we extend the approach outlined by Westcott et al. (2024) to an array of heaving buoys in a 3D water domain, by arranging the WECs to form diffraction gratings, or *stacks* (Figure 4.1). The periodic distribution of WECs in each stack creates constructive interference in a finite number of directions which depend on the incident angle, frequency, and periodicity, so that the scattering properties of a stack can be described in terms of a discrete directional spectrum (Falnes and Budal, 1982; Peter and Meylan, 2010). The periodicity is chosen to be small relative to targeted wavelengths of practical interest (angular frequencies 0.3–0.65 rad s^{-1} or wave periods $\approx$ 10–20 s) to facilitate effective manipulation of reflected and transmitted propagating modes, analogously to a 2D model.

We demonstrate efficient broadband absorption ($\geq 94\%$) over the targeted frequency range by grading the resonant frequencies of successive stacks via the attached linear spring–damper PTOs, with time-independent parameters. The grading produces a wide-angle local bandgap, analogous to 2D graded arrays of resonators in acoustics (Bennetts et al., 2019), so that absorption is robust to the wave direction. The strategies transfer effectively to finite arrays which demonstrate efficient capture of broadly spread spectra. The choice of spacing within, and between, rows, is shown to have implications for controlling transmission, the number of rows required, and avoiding interference with array resonances on the target interval.

The model and methods applied in the study are introduced in § 4.2 and § 4.3. To develop a grading for an array, a Bloch wave analysis is used to link underlying band structures (passbands and bandgaps) to the reflection and transmission of the array, which are connected to the resonant properties of stacks in complex frequency space (§ 4.4.2). The spacing between WECs is chosen to create an array design that supports high efficiency, given the resonant properties of the array. The PTO springs are graded for rainbow reflection, and the PTO damping is chosen to generate near-zeros in reflection for rainbow absorption (§ 4.4.3). Strategies are transferred to finite arrays, where the efficient, broadband absorption of a graded array is demonstrated in directionally spread, irregular sea states, and compared to the absorption of uniform arrays (§ 4.4.4). Recommendations for practical next steps are given in § 4.5.

4.2 Preliminaries

Consider a 3D water domain, Ω, containing an array of WECs, where each WEC consists of a floating buoy and a linear spring–damper PTO that moors it to the seabed (Figure 4.1). The buoys are identical truncated vertical cylinders, with radius L, height $2L$ and draught

L. They are constrained to move in heave only. Let the Cartesian coordinate system (x, y, z) denote locations in the water domain, such that (x, y) is the horizontal coordinate and z is the vertical coordinate, which points upwards. The water domain is unbounded in the horizontal direction, $-\infty < x, y < \infty$, and bounded below by a flat impermeable seabed at $z = -h$. In the absence of WECs, the water is bounded above by a moving free surface, $z = \hat{\eta}(x, y, t)$, where t denotes time, and such that $\hat{\eta} \equiv 0$ in equilibrium.

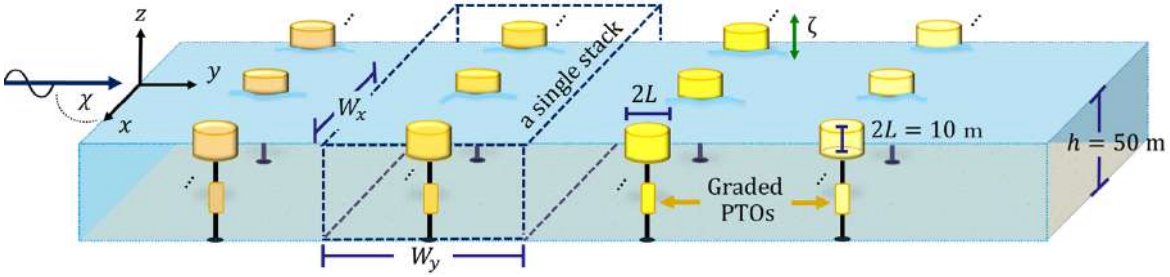

Figure 4.1: The graded array contains finitely many stacks, each consisting of infinitely many WECs (periodicity W_x). The incident wave travels left-to-right at an angle of χ rad to the x–axis.

The WECs are arranged into K *stacks*, where each stack contains an infinite number of identical WECs (identical PTOs, as well as buoys) in a straight line and with uniform spacing between adjacent WECs (Figure 4.1). Without loss of generality, let the stacks be aligned parallel to the x-axis and let W_x denote the centre-to-centre spacing between adjacent WECs in a stack. The spacing between adjacent stacks is also uniform and the centre-to-centre stack spacing is denoted W_y. The stacks are indexed $i \in \{1, 2, \ldots, K\}$ in ascending order along the the y-axis, and the WECs in each stack are indexed $j \in \mathbb{Z}$ in ascending order along the x-axis. Let one buoy in the first stack have its centre in the horizontal plane coincide with the origin $(x, y) = (0, 0)$, then the WEC-array occupies the water surface defined by the set

$$\Gamma = \{(x, y) : (x - j\,W_x)^2 + (y - i\,W_y + W_y)^2 \leq L^2 \text{ for } i \in [1, 2, \ldots, K] \text{ and } j \in \mathbb{Z}\}. \quad (4.1)$$

The heave motion of the j^{th} buoy in the i^{th} stack is denoted $\xi_{i,j}(t)$.

Motions of the coupled water and WEC-array system are excited by an ambient incident wavefield, propagating from $y \to -\infty$ (the left of the array in Figure 4.1). The water motions are modelled using linear potential-flow theory, such that the water velocity field is the gradient of a scalar velocity potential, $\Phi(x, y, z, t)$. Solutions are sought in the frequency domain, by imposing a time-harmonic condition via

$$\Phi(x, y, z, t) = \mathrm{Re}\left\{\frac{gA^{\text{inc}}}{\mathrm{i}\omega}\phi(x, y, z)\,\mathrm{e}^{-\mathrm{i}\omega t}\right\} \quad \text{and} \quad \xi_{i,j}(t) = \mathrm{Re}\left\{A^{\text{inc}}\,\zeta_{i,j}\,\mathrm{e}^{-\mathrm{i}\omega t}\right\} \quad (4.2)$$

for $i \in \{1, 2, \ldots, K\}$ and $j \in \mathbb{Z}$, where $\omega \in \mathbb{R}_+$ is a prescribed angular frequency, $g = 9.81\,\mathrm{m\,s^{-2}}$ is gravitational acceleration, $\mathrm{i} = \sqrt{-1}$ is the imaginary unit, and A^{inc} is the amplitude of the

ambient incident wave. The (reduced/time-independent) potential, $\phi(x, y, z) \in \mathbb{C}$, satisfies Laplace's equation throughout the water domain, that is

$$\nabla^2 \phi = 0 \quad \text{for} \quad (x, y, z) \in \Omega, \tag{4.3}$$

along with boundary conditions at the seabed and free surface (Mei et al., 2005), respectively,

$$\partial_z \phi = 0 \qquad \text{for} \quad (x, y) \in \mathbb{R}^2 \text{ and } z = -h \tag{4.4}$$

$$\text{and} \quad \partial_z \phi = \frac{\omega^2}{g} \phi \quad \text{for} \quad (x, y) \in \mathbb{R}^2 \backslash \Gamma \text{ and } z = 0. \tag{4.5}$$

It also satisfies conditions on the linearised wetted surfaces of the buoys that equate normal velocities of the water and the buoys, and radiation conditions in the far field, $|y| \to \infty$ (defined in § 4.3.1). The (reduced/time-independent) heave motions, $\zeta_{i.j} \in \mathbb{C}$, satisfy equations of motion (defined in § 4.3.1).

4.3 Solution method

4.3.1 Individual WECs: The diffraction transfer matrix

Consider an individual WEC (with no other WECs surrounding it) and suppose the centre of the WEC in the horizontal plane coincides with the origin, $(x, y) = (0, 0)$. As such, it is convenient to map to cylindrical polar coordinates by writing the velocity potential as $\phi(x, y, z) = \varphi(r, \theta, z)$ where $r > 0$ is the radial coordinate and $\theta \in (-\pi, \pi]$ is the azimuthal coordinate, such that $x = r \cos(\theta)$ and $y = r \sin(\theta)$. The velocity potential is decomposed as

$$\varphi(r, \theta, z) = \varphi^{\text{inc}}(r, \theta, z) + \varphi^{\text{scat}}(r, \theta, z), \tag{4.6}$$

where φ^{inc} and $\varphi^{\text{scat}} \in \mathbb{C}$ are the velocity potentials for the incident and scattered wavefields, respectively. Both of the velocity potentials satisfy Laplace's equation in the water domain, and the free surface and seabed boundary conditions (Equations (4.3)–(4.5)).

The incident wavefield, φ^{inc}, is taken in the general form

$$\varphi^{\text{inc}}(r, \theta, z) = \sum_{n=0}^{\infty} \sum_{\mu=-\infty}^{\infty} C_{n\mu} \, I_\mu(\kappa_n \, r) \, \mathrm{e}^{\mathrm{i} \, \mu \, \theta} \, Z_n(z), \tag{4.7}$$

where $C_{n\mu} \in \mathbb{C}$ are arbitrary amplitudes, I_μ are modified Bessel functions of the first kind (order μ), and Z_n are the vertical eigenfunctions

$$Z_n(z) = \frac{\cosh(k_n \, (z + h))}{\cosh(k_n \, h)}. \tag{4.8}$$

The wavenumbers k_n are the real ($n = 0$) and positive, imaginary ($n \geq 1$) roots k of the dispersion equation

$$\omega^2 = g\, k\, \tanh(k\, h). \tag{4.9}$$

The κ_n are defined such that $\kappa_n = -\mathrm{i}k_n$ ($n \in \mathbb{Z} \geq 0$).

The scattered wavefield satisfies the Sommerfeld radiation condition

$$\sqrt{r}\left(\partial_r\, \varphi^{\mathrm{scat}} - \mathrm{i}\, k_0\, \varphi^{\mathrm{scat}}\right) \to 0 \quad \text{as} \quad r \to \infty. \tag{4.10}$$

Thus, it can be expressed as

$$\varphi^{\mathrm{scat}}(r, \theta, z) = \sum_{n=0}^{\infty} \sum_{\mu=-\infty}^{\infty} D_{n\mu}\, K_\mu(\kappa_n\, r)\, \mathrm{e}^{\mathrm{i}\,\mu\,\theta}\, Z_n(z), \tag{4.11}$$

where $D_{n\mu} \in \mathbb{C}$ are amplitudes to be calculated, and K_μ are modified Bessel functions of the second kind (order μ). The amplitudes $D_{n\mu}$ are decomposed as

$$D_{n\mu} = D_{n\mu}^{\mathrm{diff}} + \zeta\, D_{n\mu}^{\mathrm{rad}} \quad \text{for} \quad n \in \mathbb{Z} \geq 0 \quad \text{and} \quad \mu \in \mathbb{Z}, \tag{4.12}$$

where $\zeta \in \mathbb{C}$ is the as yet unknown heave amplitude of the buoy. The amplitudes $D_{n\mu}^{\mathrm{diff}}$ are found by solving a diffraction problem in which the buoy is held stationary, and the amplitudes $D_{n\mu}^{\mathrm{rad}}$ are found by solving a radiation problem in which the buoy is forced to move with unit amplitude heave motion, without an incident wavefield (Appendix B.1). The associated boundary conditions on the wetted surface of the buoy S_B, are given by, respectively,

$$\frac{\partial \varphi^{\mathrm{diff}}}{\partial n} = -\frac{\partial \varphi^{\mathrm{inc}}}{\partial n} \quad \text{and} \quad \frac{\partial \varphi^{\mathrm{rad}}}{\partial n} = \frac{\omega^2}{g} \quad \text{on} \quad S_B. \tag{4.13a, b}$$

The heave amplitude, ζ, is obtained from the equation of motion

$$\left[-\omega^2(\mathfrak{M} + a(\omega)) - \mathrm{i}\omega\,(b(\omega) + B_{\mathrm{PTO}}) + (\mathfrak{C} + C_{\mathrm{PTO}})\right] \zeta(\omega) = F^{\mathrm{exc}}(\omega). \tag{4.14}$$

On the left-hand side of Equation (4.14), $\mathfrak{M} \equiv \rho\pi L^3$ is the mass of the buoy and $\mathfrak{C} = \rho g \pi L^2\, \mathrm{N\,m^{-1}}$ is its hydrostatic stiffness, where $\rho = 1025\, \mathrm{kg\,m^{-3}}$ is the water density. The frequency dependent coefficients, $a(\omega)$ and $b(\omega)$, are the added mass and radiation damping, respectively, which are calculated from the radiation potential, φ^{rad} (see Appendix B.1). The coefficients C_{PTO} and B_{PTO} are, respectively, the spring and damping coefficients of the PTO. The right-hand side of Equation (4.14), $F^{\mathrm{exc}}(\omega)$, is the excitation force, which is calculated using the incident amplitudes, $C_{n\mu}$, in the diffraction problem (Appendix B.1).

A diffraction transfer operator is used to define the relation between the incident amplitudes, $C_{n\mu}$, and scattered amplitudes, $D_{n\mu}$. Truncating the infinite summations at $n = N_0$ and

$\mu = \pm U$ (chosen sufficiently large to achieve a desired level of accuracy), reduces the diffraction transfer operator to a $(N_0+1)(2U+1)$-square matrix, $\boldsymbol{B}$, such that

$$\boldsymbol{D} = \boldsymbol{B}\,\boldsymbol{C}, \tag{4.15}$$

where the entries of the vectors $\boldsymbol{D}$ and $\boldsymbol{C}$ are

$$[\boldsymbol{C}]_{(n-1)\,(2\,U+1)+\mu} = C_{n\mu} \quad \text{and} \quad [\boldsymbol{D}]_{(n-1)\,(2\,U+1)+\mu} = D_{n\mu}, \tag{4.16}$$

for $n = 0, 1, \ldots, N_0$ and $\mu = -U, (-U+1), \ldots, U$. The elements of $\boldsymbol{B}$ are defined in Appendix B.1.

4.3.2 Individual stacks: Plane-wave expansion, scattering matrices and Bloch waves

Consider an individual stack, in which the WECs are indexed $j \in \mathbb{Z}$, and the horizontal centre of the buoy j is located at $(x, y) = (j\,W_x, 0)$. Each WEC in the stack has an associated local polar coordinate system (r_j, θ_j) for $j \in \mathbb{Z}$, such that $x = j\,W_x + r_j\,\cos(\theta_j)$ and $y = r_j\,\sin(\theta_j)$. In the local region around WEC j ($r_j < W_x - L$), the velocity potential can be expressed as

$$\phi(x, y, z) = \varphi_j^{\text{inc}}(r_j, \theta_j, z) + \varphi_j^{\text{scat}}(r_j, \theta_j, z), \tag{4.17}$$

where

$$\varphi_j^{\text{inc}}(r_j, \theta_j, z) = \sum_{n=0}^{\infty} \sum_{\mu=-\infty}^{\infty} C_{n\mu}^{j} I_\mu(\kappa_n\,r_j)\,\mathrm{e}^{\mathrm{i}\,\mu\,\theta_j}\,Z_n(z) \tag{4.18a}$$

$$\text{and} \quad \varphi_j^{\text{scat}}(r_j, \theta_j, z) = \sum_{n=0}^{\infty} \sum_{\mu=-\infty}^{\infty} D_{n\mu}^{j} K_\mu(\kappa_n\,r_j)\,\mathrm{e}^{\mathrm{i}\,\mu\,\theta_j}\,Z_n(z) \tag{4.18b}$$

are the velocity potentials corresponding to the local incident and scattered fields, respectively.

The stack is excited by an ambient incident wavefield, with velocity potential ϕ^{amb}. In the local coordinates of WEC j, the velocity potential is expressed as

$$\phi^{\text{amb}}(x, y, z) \equiv \varphi_j^{\text{amb}}(r_j, \theta_j, z) = \sum_{n=0}^{\infty} \sum_{\mu=-\infty}^{\infty} A_{n\mu}^{j}\,I_\mu(\kappa_n\,r_j)\,\mathrm{e}^{\mathrm{i}\,\mu\,\theta_j}\,Z_n(z), \tag{4.19}$$

where the amplitudes $A_{n\mu}^{j}$ are considered known. The incident wavefield for WEC j is expressed as a superposition of the ambient wavefield and the scattered wavefields of all other WECs ($l \neq j$), such that the velocity potential of the local incident field is

$$\varphi_j^{\text{inc}}(r_j, \theta_j, z) = \varphi_j^{\text{amb}}(r_j, \theta_j, z) + \sum_{\substack{l=-\infty \\ l\neq j}}^{\infty} \varphi_{l\to j}^{\text{scat}}(r_j, \theta_j, z), \tag{4.20}$$

where $\varphi^{\text{scat}}_{l\to j}$ is the velocity potential for the field scattered field by WEC l, expressed in the local coordinates of WEC j. Using Graf's addition theorem (Martin, 2006), $\varphi^{\text{scat}}_{l\to j}$ has the representation

$$\varphi^{\text{scat}}_{l\to j}(r_j,\theta_j,z)=\sum_{n=0}^{\infty}\sum_{\mu=-\infty}^{\infty}\left[\sum_{\tau=-\infty}^{\infty}D^l_{n\tau}(-1)^{\mu}K_{\tau-\mu}(\kappa_n W_{lj})\mathrm{e}^{\mathrm{i}\,(\tau-\mu)\vartheta_{l-j}}\right]I_{\mu}(\kappa_n r_j)\,\mathrm{e}^{\mathrm{i}\,\mu\theta_j}\,Z_n(z), \tag{4.21}$$

where $(r_j,\theta_j)=(W_{lj},\vartheta_{lj})$ is the origin of the local coordinate system of WEC l in the local coordinates of WEC j, and $r_j<W_{lj}$. Substituting (4.19) and (4.21) into (4.20) and comparing with (4.18a), gives

$$C^j_{n\mu}=A^j_{n\mu}+\sum_{\substack{l=-\infty\\ l\neq j}}^{\infty}\sum_{\tau=-\infty}^{\infty}D^l_{n\tau}(-1)^{\mu}K_{\tau-\mu}(\kappa_n W_{lj})\,\mathrm{e}^{\mathrm{i}\,(\tau-\mu)\,\vartheta_{l-j}} \tag{4.22}$$

for $n\in\mathbb{Z}\geq 0$, $\mu\in\mathbb{Z}$ and $l\in\mathbb{Z}$.

Suppose that the ambient incident wavefield is such that

$$A^j_{n\mu}=\mathcal{Q}_j\,A_{n\mu}\quad\text{where}\quad\mathcal{Q}_j=\mathrm{e}^{\mathrm{i}\,k_0\,j\,W_x\,\cos(\chi)}, \tag{4.23}$$

in which the $A_{n\mu}\equiv A^0_{n\mu}$ are known and $\chi\in(0,\pi)$ denotes the incident angle with respect to the x-axis. (This is the case for a plane ambient incident wave, for example.) Due to the periodicity of the geometry in the x–direction, $C^j_{n\mu}$ and $D^j_{n\mu}$ inherit similar quasi-periodic properties, such that

$$C^j_{n\mu}=\mathcal{Q}_j\,C_{n\mu}\quad\text{and}\quad D^j_{n\mu}=\mathcal{Q}_j\,D_{n\mu}, \tag{4.24}$$

where $C_{n\mu}\equiv C^0_{n\mu}$ and $D_{n\mu}\equiv D^0_{n\mu}$ are to be found. They are intentionally written to match the notation for incident and scattered amplitudes in the individual WEC problem (§ 4.3.1), to emphasise that they are related by the diffraction transfer matrix, such that $\boldsymbol{D}=\boldsymbol{B}\,\boldsymbol{C}$.

A relation between the $A_{n\mu}$, $C_{n\mu}$ and $D_{n\mu}$ is found by substituting the quasi-periodicities (4.23)–(4.24) into Equation (4.22), to give

$$C_{n\mu}=A_{n\mu}+\sum_{\tau=-\infty}^{\infty}\sigma^n_{\tau-\mu}\,D_{n\tau}\quad\text{for}\quad n\in\mathbb{Z}\geq 0\quad\text{and}\quad\mu\in\mathbb{Z}, \tag{4.25}$$

where $\sigma^n_{\tau-\mu}$ is a lattice sum known as a Schlömilch series, defined as

$$\sigma^n_{\tau-\mu}=(-1)^{\mu}\sum_{j=1}^{\infty}\left(\mathcal{Q}_{-j}+(-1)^{\tau-\mu}\,\mathcal{Q}_j\right)\,K_{\tau-\mu}(\kappa_n\,j\,W_x) \tag{4.26}$$

and for which an efficient computation method exists (Linton, 1998; Peter et al., 2006).

Truncating the infinite sums over vertical and Fourier modes, as in § 4.3.1, Equation (4.25) is expressed as

$$\boldsymbol{C} = \boldsymbol{A} + \boldsymbol{\sigma}\boldsymbol{D} \quad \text{where the vector} \quad [\boldsymbol{A}]_{(n-1)\,(2\,U+1)+\mu} = A_{n\mu}, \tag{4.27}$$

and $\boldsymbol{\sigma}$ is defined in Appendix B.2. It follows that

$$\boldsymbol{D} = \boldsymbol{B}(\boldsymbol{A} + \boldsymbol{\sigma}\boldsymbol{D}) \quad \Rightarrow \quad \boldsymbol{D} = [\boldsymbol{I} - \boldsymbol{B}\boldsymbol{\sigma}]^{-1}\,\boldsymbol{B}\boldsymbol{A}. \tag{4.28}$$

Equation (4.28) gives the local incident amplitudes, and hence the local scattered amplitudes, in terms of the ambient incident amplitudes. The heave amplitude, $\zeta \equiv \zeta^0$, which is such that $\zeta^j = \mathcal{Q}_j\,\zeta$, is computed from Equation (4.14) with an exciting force as given in Appendix B.1.

For $|y| > L$, the wavefield can be expressed in terms of a plane-wave expansion (see Appendix B.2; Peter and Meylan, 2010), such that the velocity potential is

$$\begin{aligned}\phi(x,y,z) = \sum_{n=0}^{\infty}\sum_{m=-\infty}^{\infty} \Big\{ & F^{\pm}_{mn}\,\mathrm{e}^{\mathrm{i}k_n\,\{x\,\cos(\chi_{mn})\pm y\,\sin(\chi_{mn})\}} \\ & + G^{\mp}_{mn}\,\mathrm{e}^{\mathrm{i}k_n\,\{x\,\cos(\chi_{mn})\mp y\,\sin(\chi_{mn})\}}\Big\}\,Z_n(z),\end{aligned} \tag{4.29}$$

for $\pm y > L$, where $F^{\pm}_{mn}$ and $G^{\pm}_{mn}$ are, respectively, the amplitudes of waves incoming to and outgoing from the stack in the $\pm y$-direction. The χ_{mn} are the scattering angles

$$\chi_{mn} = \arccos\left(\frac{\psi_{mn}}{k_n}\right) \quad \text{where} \quad \psi_{mn} = k_n\,\cos(\chi) + \frac{2\,m\,\pi}{W_x}, \tag{4.30}$$

defined such that $\mathrm{e}^{\mathrm{i}\,k_n\,W_x\,\cos(\chi_{mn})} = \mathrm{e}^{\mathrm{i}\,k_0\,W_x\,\cos(\chi)}$ for all m and n, and where the complex branch of arccos is defined by (Peter et al., 2006)

$$\arccos(\varsigma) = \begin{cases} \mathrm{i}\,\mathrm{arccosh}(\varsigma), & \varsigma > 1, \\ \pi - \mathrm{i}\,\mathrm{arccosh}(-\varsigma) & \varsigma < -1, \end{cases} \tag{4.31}$$

with $\mathrm{arccosh}(\varsigma) = \log(\varsigma + \sqrt{\varsigma^2 - 1})$ for $\varsigma > 1$. There is a finite set, $\mathcal{M}$, where

$$\mathcal{M} = \{m \in \mathbb{Z} : |\psi_{m0}| < k_0\}, \tag{4.32}$$

such that the scattering angles $\chi_{m0} \in \mathbb{R}$, and, thus, the corresponding plane waves in Equation (4.29), are propagating. All other scattering angles are complex-valued ($\chi_{mn} \notin \mathbb{R}$ for $n = 0$ and $m \notin \mathcal{M}$ or $n > 0$), such that they decay exponentially away from the stack (those with G-amplitudes) or grow exponentially away from the stack (those with F-amplitudes).

The amplitudes of the incoming and outgoing plane waves, $F^{\pm}_{mn}$ and $G^{\pm}_{mn}$ respectively, are related via scattering coefficients, R^{ij}_{mn} for reflection and T^{ij}_{mn} for transmission, such that

$$G^{\pm}_{ij} = \sum_{n=0}^{\infty} \sum_{m=-\infty}^{\infty} \left\{ R^{ij}_{mn} F^{\mp}_{ij} + T^{ij}_{mn} F^{\pm}_{ij} \right\} \quad \text{for} \quad j, n \in \mathbb{Z} > 0 \quad \text{and} \quad i, m \in \mathbb{Z}, \tag{4.33}$$

where the symmetry of the stack with respect to the x-axis has been used. Truncating the infinite summations to $j, n = N_1 \leq N_0$ vertical modes and $M = p + q + 1$ scattering angles ($p, q \geq 0$) such that $i, m = -p, ..., q$ can include a finite number of complex scattering angles, the scattering relations (4.33) are expressed in terms of reflection and transmission matrices, $\boldsymbol{R}$ and $\boldsymbol{T}$, respectively, such that

$$\begin{pmatrix} \boldsymbol{G}^{-} \\ \boldsymbol{G}^{+} \end{pmatrix} = \begin{bmatrix} \boldsymbol{R} & \boldsymbol{T} \\ \boldsymbol{T} & \boldsymbol{R} \end{bmatrix} \begin{pmatrix} \boldsymbol{F}^{+} \\ \boldsymbol{F}^{-} \end{pmatrix}. \tag{4.34}$$

The vectors $\boldsymbol{F}$ and $\boldsymbol{G}$, have entries

$$[\boldsymbol{F}^{\pm}]_{(m-1)\,(N_1+1)+n} = F^{\pm}_{mn}, \quad [\boldsymbol{G}^{\pm}]_{(m-1)\,(N_1+1)+n} = G^{\pm}_{mn}. \tag{4.35}$$

The entries of the $M \times (N_1 + 1)$-square matrices $\boldsymbol{R}$ and $\boldsymbol{T}$ are given in Appendix B.2.

Consider the stack as existing in a unit cell Ω_{unit}, where

$$\Omega_{\text{unit}} = \{(x, y, z) \in \Omega : -W_y/2 < y < W_y/2\}, \tag{4.36}$$

i.e., Ω_{unit} is a strip of the water domain of width W_y in the y-direction and with stack along its centreline. The unit cell has an associated transfer matrix, $\boldsymbol{P}$, which maps plane-wave amplitudes from the left-hand side of the unit cell ($y = -W_y/2$) to the right-hand side ($y = W_y/2$), such that

$$\begin{pmatrix} \boldsymbol{G}^{+} \\ \boldsymbol{F}^{-} \end{pmatrix} = \boldsymbol{P} \begin{pmatrix} \boldsymbol{F}^{+} \\ \boldsymbol{G}^{-} \end{pmatrix} \quad \text{where} \quad \boldsymbol{P} = \begin{bmatrix} \boldsymbol{T} - \boldsymbol{R}\boldsymbol{T}^{-1}\boldsymbol{R} & \boldsymbol{R}\boldsymbol{T}^{-1} \\ -\boldsymbol{T}^{-1}\boldsymbol{R} & \boldsymbol{T}^{-1} \end{bmatrix}. \tag{4.37}$$

The eigenspace of the transfer matrix defines the modes supported by the unit cell. In particular, the eigenvalues define wavenumbers, $\pm\beta_n$, for the modes, via the relation

$$\text{eig}(\boldsymbol{P}) = \{\exp(\pm \mathrm{i}\beta_n W_y) : n \in [0, 1, \ldots, M N_1]\}, \tag{4.38}$$

where the $\pm$ pairs indicate the symmetry of the unit cell with respect to the y-axis. The β-wavenumbers and associated modes define so-called Bloch waves that exist in the doubly-periodic medium that would be formed from repeating the unit cell, such that it occupies the entire water domain, Ω.

4.3.3 Full array: Multiple stacks

The plane-wave expansion associated with stack $i \in \{1, 2, \ldots, K\}$ in the array has velocity potential $\phi \equiv \phi_i$, such that

$$\phi_i(x, y_i, z) = \sum_{n=0}^{\infty} \sum_{m=-\infty}^{\infty} \Big\{ F_{mn}^{i\pm} \, \mathrm{e}^{\mathrm{i}k_n \{x \cos(\chi_{mn}) \pm y_i \sin(\chi_{mn})\}} + G_{mn}^{i\mp} \, \mathrm{e}^{\mathrm{i}k_n \{x \cos(\chi_{mn}) \mp y_i \sin(\chi_{mn})\}} \Big\} Z_n(z), \tag{4.39}$$

where $y_i \equiv y - i\,W_y + W_y$. Expression (4.39) holds in the strips $L < \pm y_i < W_y - L$ that separate stack i from the adjacent stacks (with suitable modifications for the outermost stacks, $i = 1$ and K; see below). Upon truncation (at $n = N_1$ and $m = -p, \ldots, q$), the amplitudes $F_{mn}^{i\pm}$ and $G_{mn}^{i\pm}$ are related by reflection and transmission matrices, $\boldsymbol{R}_i$ and $\boldsymbol{T}_i$, such that

$$\begin{pmatrix} \boldsymbol{G}_i^- \\ \boldsymbol{G}_i^+ \end{pmatrix} = \begin{bmatrix} \boldsymbol{R}_i & \boldsymbol{T}_i \\ \boldsymbol{T}_i & \boldsymbol{R}_i \end{bmatrix} \begin{pmatrix} \boldsymbol{F}_i^+ \\ \boldsymbol{F}_i^- \end{pmatrix} \tag{4.40}$$

where the reflection and transmission matrices are evaluated for the PTO parameters applied to stack i (in the local coordinates).

Here, a propagating ambient incident field, travelling at an angle $\chi \in (0, \pi)$ with respect to the positive x-axis, is prescribed by setting $F_{00}^{1+} = 1$ and $F_{mn}^{1+} = 0$ for n or $m \neq 0$ and $F_{mn}^{K-} = 0$ for all n and m. Reflection and transmission matrices for the entire array, $\boldsymbol{\mathcal{R}}^{\pm}$ and $\boldsymbol{\mathcal{T}}^{\pm}$, are used to relate the amplitudes of the ambient incident field (F_{mn}^{1+} and F_{mn}^{K-}) and the amplitudes of the plane waves scattered to the far field (G_{mn}^{1-} to $y \to -\infty$ and G_{mn}^{K+} to $y \to \infty$), such that

$$\begin{pmatrix} \boldsymbol{G}_1^- \\ \boldsymbol{G}_K^+ \end{pmatrix} = \begin{bmatrix} \boldsymbol{\mathcal{R}}^- & \boldsymbol{\mathcal{T}}^- \\ \boldsymbol{\mathcal{T}}^+ & \boldsymbol{\mathcal{R}}^+ \end{bmatrix} \begin{pmatrix} \boldsymbol{F}_1^+ \\ \boldsymbol{F}_K^- \end{pmatrix}, \tag{4.41}$$

where the superscripts $\pm$ are required as the array is not x-symmetric, in general (unlike the individual stacks).

The reflection and transmission matrices for the array are calculated using an efficient recursive algorithm (Bennetts and Squire, 2009; Peter and Meylan, 2010) to combine the scattering relations for the individual stacks (4.40) for $i \in \{1, 2, \ldots, K\}$ with relations that equate the outgoing plane waves from stack i with the incoming waves for stack $i + 1$ and vice-versa, that is

$$\boldsymbol{F}_{i+1}^+ = \boldsymbol{Q}\boldsymbol{G}_i^+ \quad \text{and} \quad \boldsymbol{Q}^{-1}\boldsymbol{F}_i^- = \boldsymbol{G}_{i+1}^- \quad \text{for} \quad i \in \{1, 2, \ldots, (K-1)\}, \tag{4.42}$$

where $\boldsymbol{Q}$ is a diagonal phase-change matrix, with entries

$$[\boldsymbol{Q}]_{(m-1)(N_1+1)+n} = \mathrm{e}^{\mathrm{i}k_n W_y \sin(\chi_{mn})}. \tag{4.43}$$

A subsequent recursive algorithm (Bennetts and Squire, 2009) is applied to calculate the amplitudes of the wavefield between stacks $i = 1, 2, \ldots, K$

$$\boldsymbol{F}^+_{i+1} = \left[\boldsymbol{I} - \boldsymbol{\mathcal{R}}^+_{(1,\,i-1)}\boldsymbol{Q}\,\boldsymbol{\mathcal{R}}^-_{(K,\,i)}\boldsymbol{Q}\right]^{-1}\left[\boldsymbol{\mathcal{T}}^+_{(1,\,i-1)}\boldsymbol{F}^+_1 + \boldsymbol{\mathcal{R}}^+_{(1,\,i-1)}\boldsymbol{Q}\,\boldsymbol{\mathcal{T}}^-_{(K,\,i)}\boldsymbol{F}^-_K\right] \tag{4.44}$$

$$\boldsymbol{G}^-_{i+1} = \left[\boldsymbol{I} - \boldsymbol{\mathcal{R}}^-_{(K,\,i)}\boldsymbol{Q}\,\boldsymbol{\mathcal{R}}^+_{(1,\,i-1)}\boldsymbol{Q}\right]^{-1}\left[\boldsymbol{\mathcal{R}}^-_{(K,\,i)}\boldsymbol{Q}\,\boldsymbol{\mathcal{T}}^+_{(1,\,i-1)}\boldsymbol{F}^+_1 + \boldsymbol{\mathcal{T}}^-_{(K,\,i)}\boldsymbol{F}^-_K\right], \tag{4.45}$$

where $\boldsymbol{\mathcal{R}}^{\pm}_{(i,\,j)}$ and $\boldsymbol{\mathcal{T}}^{\pm}_{(i,\,j)}$ denotes the combined reflection and transmission matrices, respectively, for stacks i to j, with $i, j = 1, 2, \ldots, K$. The amplitude of the zeroth WEC in stack i, for $i = 1, 2, \ldots, K$, is retrieved from

$$\zeta_i = \boldsymbol{\zeta}_i\boldsymbol{\sigma}\boldsymbol{D}_i + \boldsymbol{\zeta}_i(\boldsymbol{F}^+_i + \boldsymbol{F}^-_i), \tag{4.46}$$

where the scattered amplitudes for stack i are obtained from $\boldsymbol{D}_i = \boldsymbol{B}(\boldsymbol{F}^+_i + \boldsymbol{F}^-_i)$, and $\boldsymbol{\zeta_i}$ is defined in Appendix B.1.

The proportion of the ambient incident wavefield energy absorbed by the array, α, is calculated as

$$\alpha = \sin(\chi) - \sum_{m\in\mathcal{M}}\left(|R_{m0}|^2 + |T_{m0}|^2\right)\sin(\chi_{m0}), \tag{4.47}$$

where R_{m0} and T_{m0} are, respectively, the propagating elements of the reflection and transmission matrices for the array, i.e., α is the proportion of energy not reflected and transmitted by the array. In the case where there is not PTO damping ($B_{\mathrm{PTO}} = 0$), $\alpha = 0$ and Equation (4.47) reduces to an energy conservation relation (McIver, 2000).

4.4 Numerical results

4.4.1 Parameter ranges and implications

The water depth is set to $h = 50\,\mathrm{m}$, and the WEC diameter is fixed as $2L = 10\,\mathrm{m}$ to resemble the parameter regime of CorPower Ocean's (2024) C4 device. The WEC separations, W_x and W_y, are such that the distance between the nearest points of adjacent buoys is between 1.5 to 3 times the WEC diameter, similar to Sharp and DuPont (2018). The PTO spring constant is set to achieve WEC resonances over the target range $\omega \in [0.3, 0.65]\,\mathrm{rad\,s^{-1}}$, which requires negative stiffness values, as successfully demonstrated for the C4 WEC (Todalshaug et al., 2016). The PTO damping is unrestricted and values are chosen to capture large proportions of incident wave energy (see § 4.4.3).

The incident wavelengths over the frequency range of interest ($\omega \in [0.3, 0.65]\,\mathrm{rad\,s^{-1}}$) are $\lambda \approx$142–428 m. Incident directions are considered in the range $\pi/6 \leq \chi \leq \pi/2$, which is equivalent to $\pi/6 \leq \chi \leq 5\pi/6$ by symmetry. The incident amplitude is arbitrary, as a linear model

is used, and $A^{\text{inc}} = 1\,\text{m}$ is set for convenience. As $\lambda/2 > W_x$ for $\omega \in [0.3, 0.65]\,\text{rad}\,\text{s}^{-1}$, there is a single propagating scattering angle (the incident wave direction, χ) over the frequency range of interest (Falnes and Budal, 1982). Additional scattering angles cut-on, for instance, at $\omega \approx 1.43\,\text{rad}\,\text{s}^{-1}$ for normal incidence ($\chi = \pi/2\,\text{rad}$) and at $\omega \approx 1.03$ at $\chi = \pi/8\,\text{rad}$ when $W_x = 30\,\text{m}$. However, complex scattering angles are included in calculations to capture resonant interactions between stacks accurately. Where there is no chance of ambiguity, the reflection and transmission coefficients of the sole propagating mode (Equation (4.47)) are denoted $|R|^2$ and $|T|^2$, respectively.

There is a maximum of one propagating Bloch wave over the frequency range of interest, associated with the Bloch wavenumber that tends to $k_0 \sin(\chi)$ at low frequencies, which is designated as $\beta = \beta_0$. For a given unit cell, its passbands are the frequency intervals on which the Bloch wavenumber is real-valued, $\beta_0 \in \mathbb{R}_+$, i.e., the unit cell supports the propagation of the Bloch wave for the passband frequencies. Bandgaps are the frequencies intervals on which the Bloch wavenumber is complex-valued, $\beta_0 \in \mathbb{R}_+ + \text{i}\,\mathbb{R}_+$, i.e., the Bloch wave decays across the unit cell for bandgap frequencies. As $\lambda > 2W_y \geq 2W_y \sin(\chi)$ for $\omega \in [0.3, 0.65]\,\text{rad}\,\text{s}^{-1}$, bandgaps are achieved on the target frequency interval via local resonance only. Bragg bandgaps (centred around $k_0 = \pi/(W_y \sin(\chi))$) occur at higher frequencies, for instance, for $\omega \in (0.85, 0.95)\,\text{rad}\,\text{s}^{-1}$ at normal incidence ($\chi = \pi/2\,\text{rad}$) when $W_x = 30\,\text{m}$ and $W_y = 40\,\text{m}$ (Figure 4.2).

4.4.2 Preliminary results

4.4.2.1 Band structures for individual stacks

Figure 4.2 shows a surface plot (dispersion diagram) of the (a) real and (b) imaginary parts of the Bloch wavenumber for a stack tuned to $\omega_0 = 0.475\,\text{rad}\,\text{s}^{-1}$ (the middle of the target frequency range) for incident angles between $\chi = \pi/8\,\text{rad}$ (near grazing incidence) and $\chi = \pi/2\,\text{rad}$ (normal incidence). For all incident angles, a passband ($\text{Im}\{\beta\} = 0$) exists at low frequencies, such that the Bloch wave propagates across the unit cell. A *local bandgap* begins close to the resonant frequency, ω_0, for all incident angles. In the low-frequency part of the local bandgap, $\text{Re}(\beta\, W_y) = \pi$, whilst $\text{Im}(\beta\, W_y)$ increases monotonically and unboundedly, up to $\omega \approx 0.5\,\text{rad}\,\text{s}^{-1}$ for all incident angles.

As the frequency increases above $\omega \approx 0.5\,\text{rad}\,\text{s}^{-1}$, the Bloch wavenumber switches to a branch where $\text{Re}(\beta\, W_y) = 0$, and where $\text{Im}(\beta\, W_y)$ decreases monotonically (the corresponding eigenvalue of the transfer matrix has moved from the negative real axis to the positive real axis). This marks a transition from a "locally resonant" regime (resonances of the individual WECs) to a Bragg regime, where the wavelength across the unit cell dominates. Hence, the incident angle has a greater influence over the band surface, but at different rates for different incident

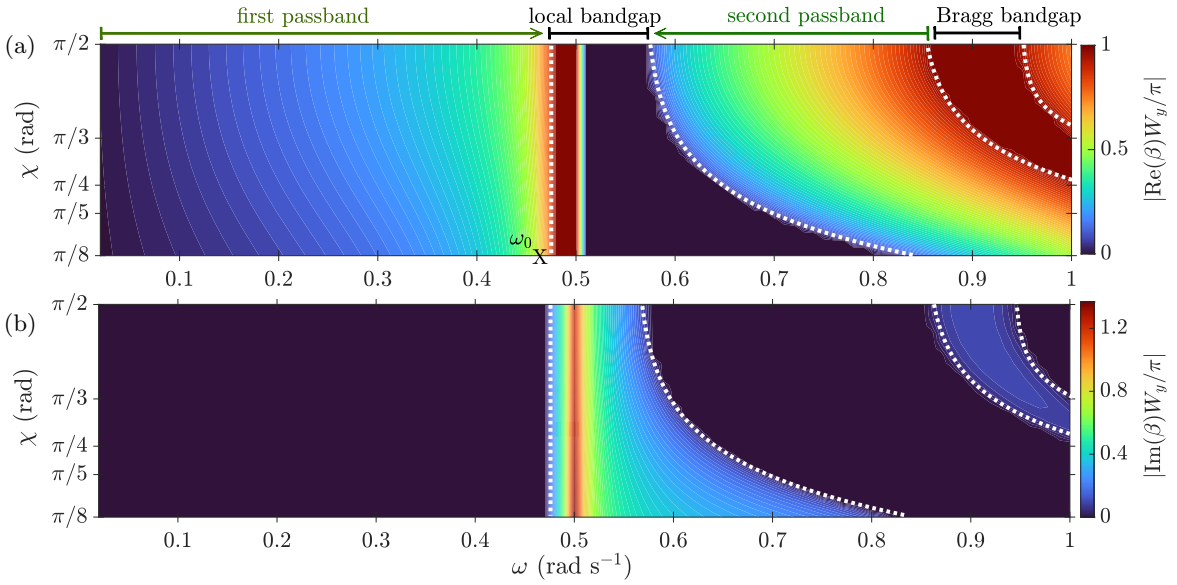

Figure 4.2: Dispersion curves (as surface plots) of the (a) real and (b) imaginary parts of the Bloch wavenumber for a stack tuned to $\omega_0 = 0.475\,\mathrm{rad\,s^{-1}}$ (marked X), and for incident angles $\pi/8 \leq \chi \leq \pi/2$, when $W_x = 30\,\mathrm{m}$ and $W_y = 40\,\mathrm{m}$. (Note that non-smooth interfaces between passbands and bandgaps result from a coarse resolution.)

angles, such that $\mathrm{Im}(\beta\, W_y)$ reaches zero (the transition to the second passband) at higher frequencies as the incident angle decreases (away from normal incidence), thus widening the local bandgaps.

Similarly, the second passband widens at an increasing rate as the incident angle decreases. The Bragg bandgap determines the upper bound of the second passband, and moves up in frequency as the incident angle decreases. In the Bragg bandgap, $\mathrm{Re}(\beta\, W_y) = \pi$ and $\mathrm{Im}(\beta\, W_y)$ increases monotonically up to the centre of the bandgap, before monotonically decreasing to $\mathrm{Im}(\beta\, W_y) = 0$. The band structures in Figure 4.2 are representative of the behaviour for all resonant frequencies lying within the target interval ($\omega_0 \in [0.3, 0.65]\,\mathrm{rad\,s^{-1}}$), however, the location of the local bandgap shifts up or down depending on the resonant frequency, which extends or contracts the second passband accordingly.

4.4.2.2 Broadband reflection by non-absorbing uniform arrays

The reflection ($|R|^2$) properties of a uniform, non-absorbing array (and also the transmission $|T|^2 = 1 - |R|^2$) are directly connected to the band structures for a unit cell. This relationship is illustrated in Figure 4.3 using normally incident waves to an array of five stacks, where all stacks are tuned to $\omega_0 = 0.3\,\mathrm{rad\,s^{-1}}$. Passbands permit propagation through the array, resulting in oscillatory reflection and transmission coefficients due to wave interference along the array. Bandgaps prevent propagation through the array, generating high reflection and low transmission through destructive interference.

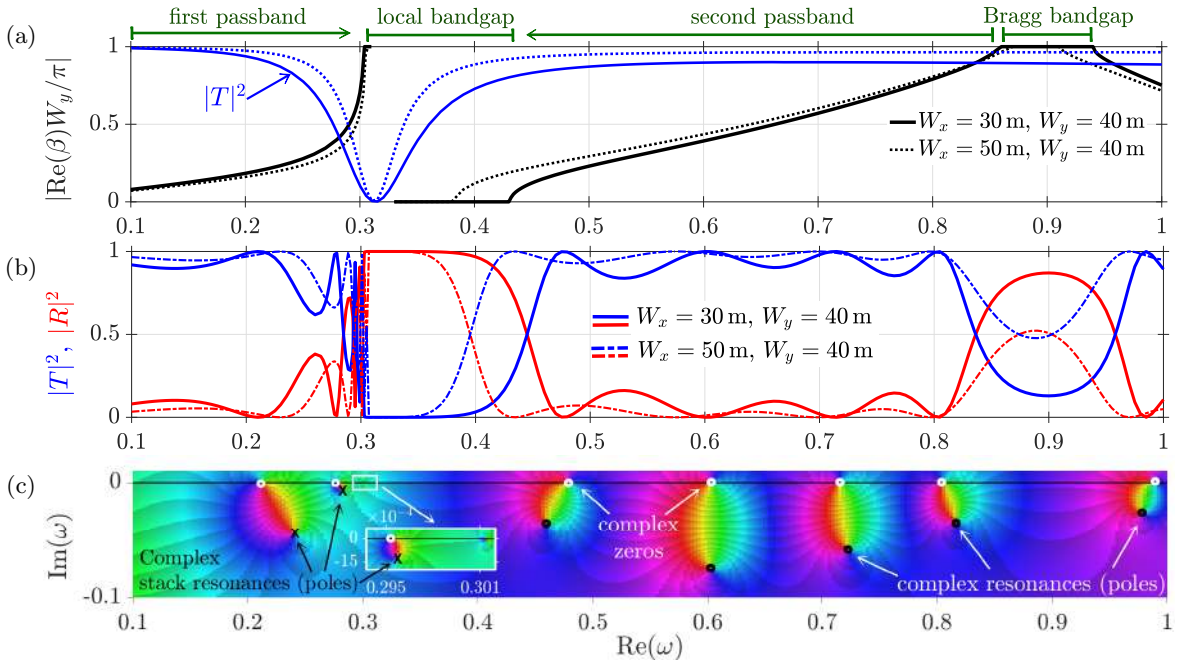

Figure 4.3: Panel (a) shows the dispersion curves (black lines) and transmission $|T|^2$ (blue lines) for a stack tuned to $\omega_0 = 0.3\,\mathrm{rad\,s^{-1}}$ with $W_x = 30\,\mathrm{m}$ (—) or $W_x = 50\,\mathrm{m}$ (····) at $\chi = \pi/2\,\mathrm{rad}$ with $W_y = 40\,\mathrm{m}$. The transmission $|T|^2$ and reflection ($|R|^2$) for a uniform array of five stacks is shown in (b), where $|T|^2 \approx 0$ and $|R|^2 \approx 1$ in the local bandgaps. The peaks and troughs in $|T|^2$ and $|R|^2$, respectively, within passbands are governed by pole–zero pairs in complex frequency space $\omega \in \mathbb{C}$, which are visualised using a phase portrait (Wegert, 2012) of the reflection coefficient $R(\omega)$ in (c) when $W_x = 30\,\mathrm{m}$. The hue represents the magnitude of the colour-coded phase $\arg(R)$, and poles/zeros are identified by rapid phase changes (Wegert, 2012).

The width of the local bandgap is influenced by the choice of spacing W_x, as shown in Figure 4.3a. Smaller W_x produce stronger reflection/scattering, which widens the local bandgap and the resonance bandwidth of individual stacks, and leads to higher reflection in the Bragg bandgap (Figure 4.3b). Compared to a 1D array (Westcott et al., 2024), stacks have a narrower resonance bandwidth and are weaker reflectors, particularly as W_x increases relative to the WEC diameter (Bennetts and Squire, 2009).

The reflection and transmission in the second passband are governed by array resonances that arise from interference between waves reflected back and forth between the stacks in the y–direction (i.e., do not exist for a single stack). These manifest as pole–zero pairs in the complex plane, and are shown using the phase portrait (Wegert, 2012) of the reflection coefficient as a function of $\omega \in \mathbb{C}$ in Figure 4.3c. The pole–zero pairs generate zeros in reflection and peaks in transmission for $\omega \in \mathbb{R}$ (Figure 4.3b). The distance between the pole and zero determines the associated resonance bandwidth (Romero-García, Theocharis, Richoux and Pagneux, 2016).

The locations of the array resonances are determined by the resonant properties of the stacks and W_y. Strongly reflective stacks have a greater ability to move array resonances up in frequency, reducing the width of the second passband. For example, decreasing $W_x = 50\,\mathrm{m}$ to

$W_x = 30\,\mathrm{m}$ shifts the start of the second passband from $\omega = 0.38\,\mathrm{rad\,s^{-1}}$ to $\omega = 0.43\,\mathrm{rad\,s^{-1}}$ (Figure 4.3a). The Bragg bandgap moves up in frequency as W_y decreases, with $W_y \leq 50\,\mathrm{m}$ required to keep the Bragg bandgap sufficiently far above the target interval to prevent strong interference between stack and array resonances.

4.4.2.3 Rainbow reflection for non-absorbing graded arrays

Rainbow reflection is generated by grading the resonant frequencies of successive stacks via the PTO spring constants from high to low ($\omega \approx 0.65 \rightarrow \omega \approx 0.3\,\mathrm{rad\,s^{-1}}$) in the direction of the incident wave, such that the resonance of stack i lies in the local bandgap of stack $(i+1)$. Figure 4.4 shows the band diagrams for selected stacks in a graded array of five stacks at normal incidence, for the PTO spring constants given in Table 4.1 with $B^i_{\mathrm{PTO}} = 0$ for $i = 1, 2, \ldots, 5$. A spacing of $W_x = W_y = 25\,\mathrm{m}$ is applied to compress the second passband for a clear demonstration of the approach. The overlapping of local bandgaps on the corresponding unit cells associated with adjacent stacks creates a wide effective bandgap over $\omega \in [0.3, 0.65]\,\mathrm{rad\,s^{-1}}$, where $|T|^2 \approx 0$ and $|R|^2 \approx 1$ in the graded array (Figure 4.4d).

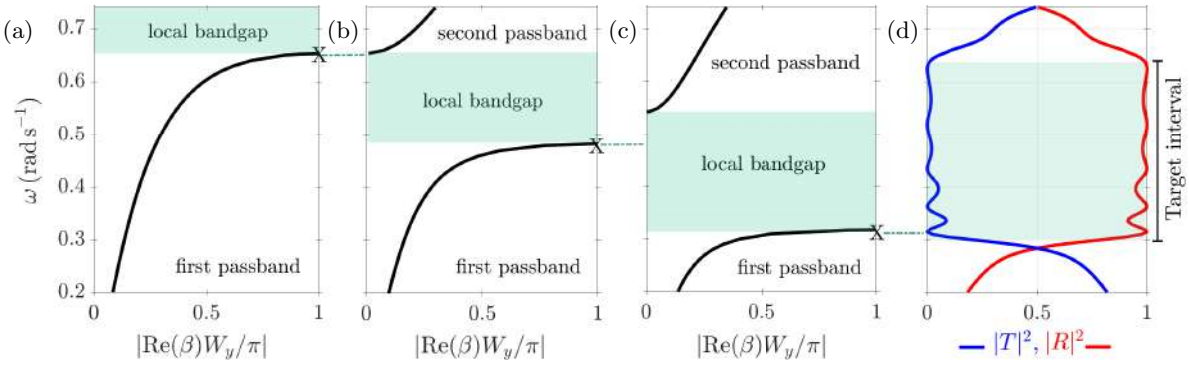

Figure 4.4: The band diagrams for stacks tuned to (a) $\omega_0 = 0.65\,\mathrm{rad\,s^{-1}}$, (b) $\omega_0 = 0.475\,\mathrm{rad\,s^{-1}}$, and (c) $\omega_0 = 0.31\,\mathrm{rad\,s^{-1}}$, are shown for $W_x = W_y = 25\,\mathrm{m}$ at $\chi = \pi/2\,\mathrm{rad}$. The resonance (marked X) induces a local bandgap (shaded green). A graded array of five stacks (first, third and fifth stacks: (a)–(c)) creates (d) an effective bandgap on $\omega \in [0.3, 0.65]\,\mathrm{rad\,s^{-1}}$, where $|T|^2 \approx 0$ and $|R|^2 \approx 1$.

Qualitatively, the band structures are identical to a 2D model (Westcott et al., 2024). However, the grading of PTO parameters depends on the resonant properties and chosen spacing in 3D, which differ substantially from the 2D model. In particular, a severe grading and close spacing is required in 2D to control the resonant properties for low transmission over the target interval, as the WECs are strongly reflecting (Westcott et al., 2024). In contrast, stacks are relatively weak reflectors and require a gradual grading for low transmission in 3D.

Apart from at $\omega \approx 0.62\,\mathrm{rad\,s^{-1}}$, the zeros in transmission and peaks in reflection on the target interval (Figure 4.4d) are generated by the graded stack resonances, and are governed by pole–zero pairs in complex frequency space. The pole–zero pairs are visualised in Figure 4.5

Table 4.1: The resonant frequency ω_0 and PTO parameters of each stack in a graded array of five stacks with $W_x = W_y = 25\,\mathrm{m}$ in Figure 4.6.

stack i	**1**	**2**	**3**	**4**	**5**
ω_0^i rad s^{-1}	0.617	0.500	0.410	0.324	0.296
C_{PTO}^i kN m^{-1}	−533	−618	−674	−717	−729
B_{PTO}^i kN s m^{-1}	111	60.3	48.3	30.2	11.1

using phase portraits of the reflection and transmission coefficients in complex frequency space (Wegert, 2012). Poles correspond to stack resonances, and are located in the lower half of the complex plane. The associated zeros in reflection are displaced from the real frequency axis ($\mathrm{Im}(\omega) = 0$; Figure 4.5a), while zeros in transmission lie on $\mathrm{Im}(\omega) = 0$, and are staggered across the target interval at locations associated with the local bandgaps on the corresponding unit cells. The incident wave energy is amplified near the stack with a comparable resonant frequency (not shown; e.g., see Bennetts et al. (2019)), which defines the transition to a local bandgap, before being reflected out of the array. Consequently, the wave energy is selectively slowed according to frequency as the group velocity of the associated Bloch wave decreases to zero, and low frequencies penetrate further into the array than high frequencies.

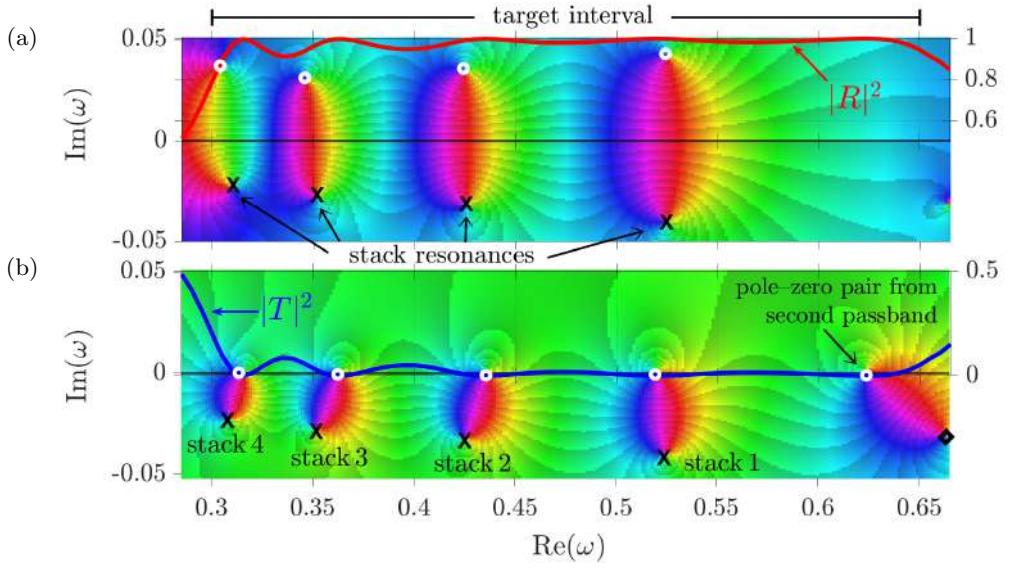

Figure 4.5: Phase portraits of the reflection (a) $R(\omega)$ and transmission (b) $T(\omega)$ coefficients of the array (Table 4.1) are shown as a function of complex frequency ($\omega \in \mathbb{C}$), with $|R|^2$ and $|T|^2$ for $\omega \in \mathbb{R}$ overlaid. Stack resonances (poles) are marked X, and zeros are depicted by ∘. The pole–zero pair for stack 5 lies below the axes limits.

To maintain low transmission (defined as $< 10\%$, to be $< 1\%$ of the incident energy) over the target interval, a gradual grading is required at low frequencies where stacks have narrower resonance bandwidths, with the severity of the grading increasing with frequency as the resonance bandwidths broaden. The choice of W_y permits a pole–zero pair originating from

the second passband to encroach on the target interval (right-hand side of Figure 4.5b), which restricts the extent of the local bandgap, and down-shifts the stack resonances in frequency (interference between pole–zero pairs). Weaker interactions in 3D compared to 2D (e.g., see Westcott et al. (2024)) produce less interference at the upper bound of the target interval, and permit wider spacings between stacks. For a fixed spacing in the y–direction such that $W_y \leq 50\,\mathrm{m}$, the minimum number of stacks required to achieve an effective bandgap over the target interval depends on W_x, due to the associated transmission properties (Section 4.4.2).

4.4.3 Broadband absorption

Rainbow absorption is created by extracting the amplified energy in the rainbow reflecting array using the PTO damper. The PTO damping for each stack in the graded array of five stacks (Figure 4.5) is chosen to create a near-zero in reflection and corresponding peak in absorption, starting with the penultimate stack (low frequency) and working towards the front of the array (Figure 4.6a–d). The fourth stack is less able to sustain low reflection as a result of a narrow resonance bandwidth, which causes a rapid rise in reflection around $\omega = 0.3\,\mathrm{rad\,s^{-1}}$. To counteract this, relatively low damping (compared to other stacks) is applied to the fifth stack (unlike in 2D (Westcott et al., 2024)) to reduce reflection and achieve $|R|^2 \approx |T|^2 \approx 0$ in combination with the fourth stack at $\omega \approx 0.3\,\mathrm{rad\,s^{-1}}$. The graded array achieves an average absorption of $\hat{\alpha} = \frac{1}{0.35}\int_{0.3}^{0.65} \alpha\,\mathrm{d}\omega = 94.1\%$ using the PTO parameters in Table 4.1.

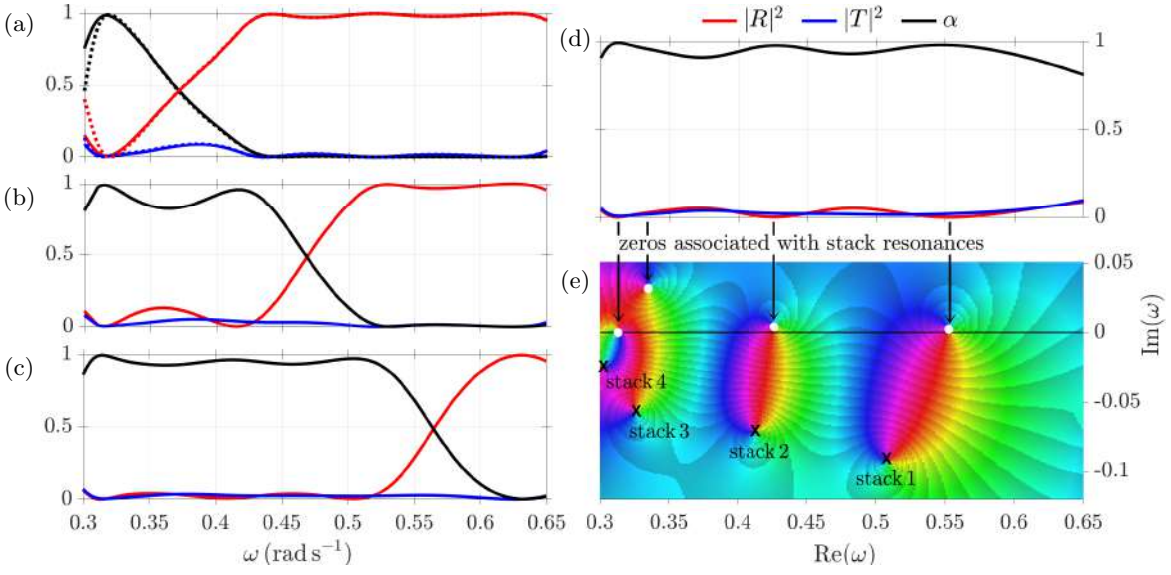

Figure 4.6: The PTO damping for the (a) fifth and fourth, (b) third, (c) second and (d) first stack in a graded array of five stacks (Table 4.1) is chosen to create zeros in reflection ($|R|^2$; —), producing peaks in absorption α (—). Dotted lines in (a) give the α, $|R|^2$, and transmission ($|T|^2$; —) when only $B^4_{\mathrm{PTO}} \neq 0$. Each $|R(\omega)|^2 \approx 0$, $\omega \in \mathbb{R}$, translates zeros in the complex plane towards $\mathrm{Im}(\omega) \approx 0$, which are shown in the (e) phase portrait of the reflection coefficient $R(\omega)$, for $\omega \in \mathbb{C}$. The zero for stack 3 is displaced from $\mathrm{Im}(\omega) \approx 0$.

Table 4.2: The resonant frequency ω_0 and PTO parameters of each stack in the graded array of six stacks with $W_x = 30\,\mathrm{m}$ and $W_y = 40\,\mathrm{m}$.

stack i	**1**	**2**	**3**	**4**	**5**	**6**
ω_0^i rad s^{-1}	0.611	0.567	0.511	0.418	0.342	0.300
C_{PTO}^i kN m^{-1}	-538	-572	-611	-670	-709	-728
B_{PTO}^i kN s m^{-1}	111	52.3	60.3	56.3	40.2	13.7

Near-zeros in reflection for real frequencies translate the complex zeros of reflection associated with stack resonances towards $\mathrm{Im}(\omega) = 0$ in the complex frequency plane (Figure 4.6e). The complex zero associated with stack 3 is displaced from $\mathrm{Im}(\omega) \approx 0$ due to interactions between closely spaced pole–zero pairs in frequency space that result from the gradual grading of stack resonances required to maintain low transmission and reflection at low frequencies. Reflection and transmission rise at the upper bound of the target interval ($|R|^2 < 0.089$ and $|T|^2 < 0.099$ on $\omega \in [0.3, 0.65]\,\mathrm{rad\,s^{-1}}$) as a result of interference between the stack and array resonances (a pole–zero pair from the second passband is located at $\omega = 0.66\,\mathrm{rad\,s^{-1}}$), which limits control over the location of pole–zero pairs through the PTO parameters (Westcott et al., 2024).

To reduce transmission and reflection, additional stacks are necessary to achieve a sufficiently gradual grading on the target interval. A good combination of high absorption, practical spacing, and rapid convergence is obtained by grading an array of six stacks when $W_x = 30\,\mathrm{m}$ and $W_y = 40\,\mathrm{m}$ using the PTO parameters in Table 4.2. The graded array has an average absorption of 94.89% at $\chi = \pi/2\,\mathrm{rad}$ and maintains $|T|^2 < 0.085$ and $|R|^2 < 0.078$ on $\omega \in [0.3, 0.65]\,\mathrm{rad\,s^{-1}}$. The efficient broadband absorption that is generated at normal incidence is maintained over a wide range of incident wave directions, as the stack resonances, which control the local band structures, are unaffected by the incident wave angle.

Figure 4.7 illustrates how the stack resonances control the spatial separation, and subsequent capture, of incident frequencies, at three different incident angles. Incident frequencies of $\omega = 0.52, 0.43$ and $0.35\,\mathrm{rad\,s^{-1}}$ are chosen to slightly exceed the resonance frequencies of stacks 3, 4 and 5, respectively (i.e., they lie in the associated bandgap), to demonstrate how the local band structures associated with the corresponding unit cell control propagation. The incident wave propagates until reaching the spatial location in the array at which the stack resonance on the associated unit cell is lower than the incident frequency, resulting in an abrupt and substantial decrease in transmission. The WEC motions are amplified at this location, due to the accumulation of incident energy, which is captured by the PTO damping in the rainbow absorbing array.

The absorption of the graded array of six stacks over the target interval is shown in Figure 4.8a, for incident angles covering a range of $\chi = \pi/3\,\mathrm{rad}$. As the incident angle decreases ($\chi \rightarrow$

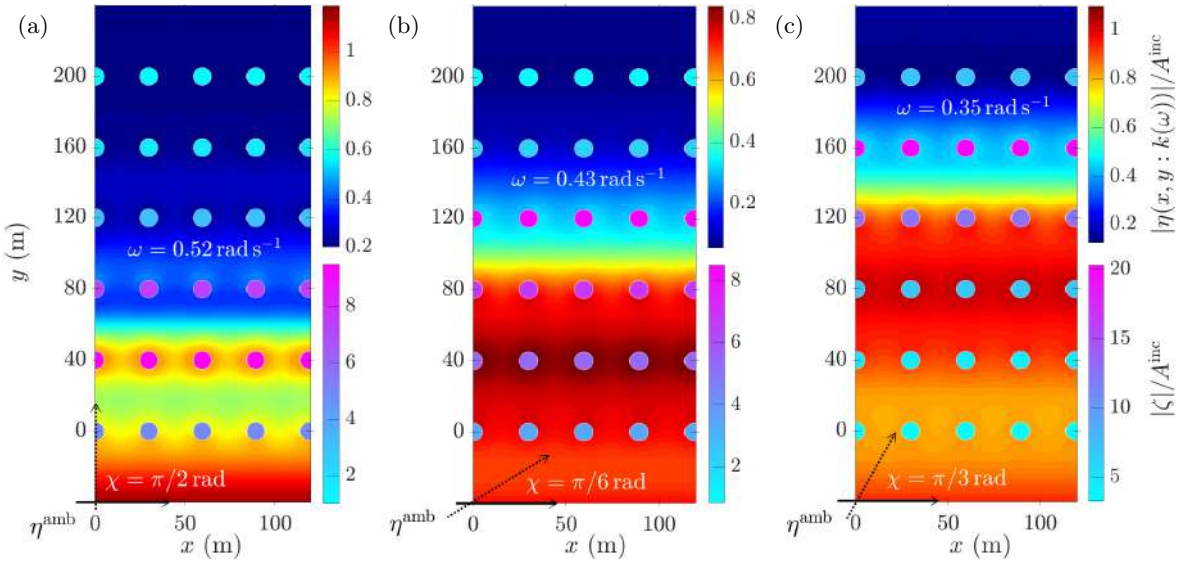

Figure 4.7: The surface elevation η (upper colourbar) and WEC amplitudes ζ (lower colourbar) in the graded array of six stacks (Table 4.2) are shown for ambient incident waves η^{amb} with (a) $\omega = 0.52\,\mathrm{rad\,s^{-1}}$ at $\chi = \pi/2\,\mathrm{rad}$, (b) $\omega = 0.43\,\mathrm{rad\,s^{-1}}$ at $\chi = \pi/6\,\mathrm{rad}$, and (c) $\omega = 0.35\,\mathrm{rad\,s^{-1}}$ at $\chi = \pi/3\,\mathrm{rad}$. Incident waves propagate (bottom-to-top) until reaching a resonant stack, which gives rise to a bandgap with $|T|^2 \approx 0$.

$\pi/6$), transmission (Figure 4.8b) decreases over the targeted interval (local bandgaps widen in frequency space and increasingly overlap), causing absorption to increase across the target interval, with the average absorption peaking at $\hat{\alpha} \approx 0.955$ when $\chi \approx \pi/3\,\mathrm{rad}$. However, near-zeros in reflection (Figure 4.8c) are gradually displaced from $|R|^2 \approx 0$ (fixed PTO parameters) as χ decreases past $\chi \approx \pi/3\,\mathrm{rad}$, causing absorption to decline on the upper half of the target interval, and between the peaks in absorption associated with near-zeros of reflection.

The initial increase in absorption followed by a gradual decline as the incident wave angle decreases, is observed at different combinations of W_x and W_y, as shown in Figure 4.9, and is particularly noticeable at $W_x = W_y = 50\,\mathrm{m}$. Since larger periodicities (e.g., $W_x = 50\,\mathrm{m}$ versus $W_x = 30\,\mathrm{m}$) support greater transmission, the reduction in transmission as the incident angle decreases from $\chi = \pi/2\,\mathrm{rad}$ to $\chi = \pi/6\,\mathrm{rad}$, outweighs the gradual displacement of near-zeros in reflection, and results in higher absorption at $\chi = \pi/6\,\mathrm{rad}$ compared to $\chi = \pi/2\,\mathrm{rad}$. Generally, a greater number of stacks (Figure 4.9b) counteract this trend, provided there are sufficiently many stacks to create low transmission over the target interval at normal incidence, so that absorption monotonically declines as the incident angle decreases. The various array layouts maintain high absorption for $\pi/6 \leq \chi \leq 5\pi/6$ (by symmetry), with the average absorption exceeding 90% for all but five stacks (where $\hat{\alpha} = 0.878$ at $\chi = \pi/6\,\mathrm{rad}$).

For fixed W_x and W_y, the average absorption increases with the number of stacks (Figure 4.9a versus Figure 4.9b). The (unoptimised) average absorption of the graded array of ten stacks, with a practically feasible spacing of $W_x = 30\,\mathrm{m}$ and $W_y = 40\,\mathrm{m}$, reaches 98% at normal

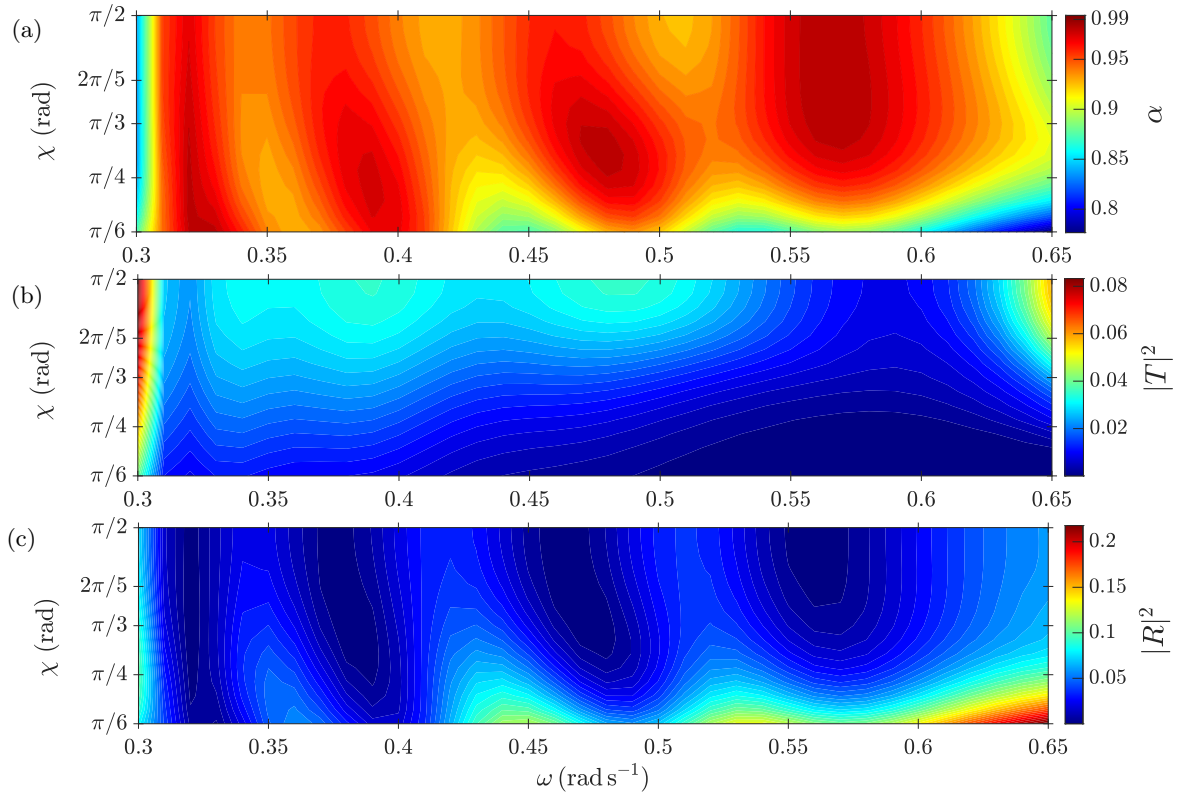

Figure 4.8: The (a) absorption of the array of six stacks ($W_x = 30\,\text{m}$ and $W_y = 40\,\text{m}$; Table 4.2) exceeds 90% over the majority of the target interval $\omega \in [0.3, 0.65]\,\text{rad}\,\text{s}^{-1}$, for $\pi/6 \leq \chi \leq \pi/2$. As the incident angle decreases ($\chi \to \pi/6$), (b) transmission decreases ($|T|^2 \to 0$), and (c) near-zeros in reflection ($|R|^2 \approx 0$) are gradually lost.

incidence (Figure 4.9b; $\chi = \pi/2\,\text{rad}$), which is less than 2% lower than an optimised 1D array of ten WECs (Westcott et al., 2024). The slight difference in absorption is attributed to stacks being weaker reflectors than 2D WECs. The absorption of the ten stacks is shown in Figure 4.9c, and exceeds 95% for the majority of $\omega \in [0.3, 0.65]\,\text{rad}\,\text{s}^{-1}$ and $\pi/6 \leq \chi \leq \pi/2$.

Stacks with closely spaced WECs are stronger reflectors and sustain low transmission over a wider frequency range as a result of broader resonance bandwidths. The separation distances between WECs should remain between three and eight times the WEC radius, as a closer spacing is unlikely to be feasible in practice, while wider spacing decreases efficiency. The maximum spacing is restricted by the second passband, which must occupy some minimum width in frequency space. The ability to decrease this width via the grading depends on W_x (fixed WEC properties), and requires strongly reflective stacks (small W_x). The upper bound of the second passband is controlled by Bragg resonance, and is driven down in frequency as W_y increases. Consequently, the resonances associated with the second passband move down in frequency, which raises transmission near the upper bound of the target interval and causes absorption to drop. If both W_x and W_y are increased, the resonances can become interspersed between the stack resonances, and potentially allow transmission to rise on the

targeted interval (Appendix B.3).

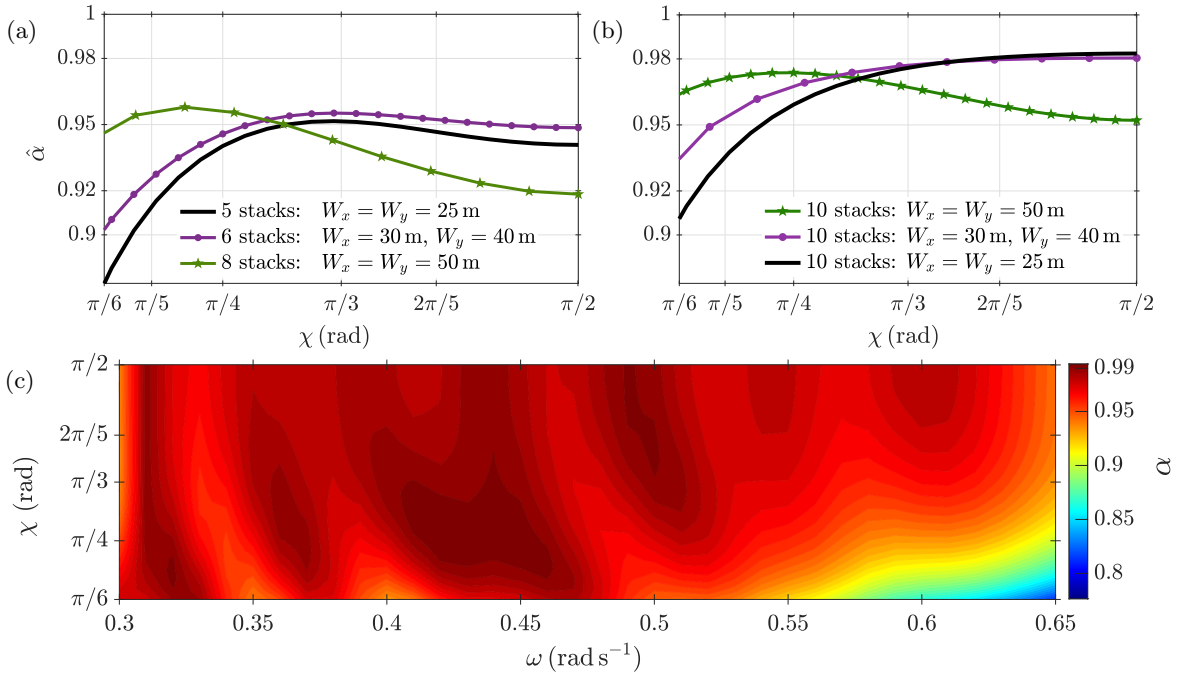

Figure 4.9: The average absorptions $\hat{\alpha}$ of graded arrays over $\omega \in [0.3, 0.65]$ rad s^{-1} are shown versus the incident wave angle χ, for different choices of W_x and W_y, in (a), and for ten stacks in (b). The absorption of an array of ten stacks with $W_x = 30$ m and $W_y = 40$ m is shown in (c) for $\omega \in [0.3, 0.65]$ rad s^{-1} and $\pi/6 \leq \chi \leq \pi/2$.

In general, higher transmission at larger W_x and W_y distances can be counteracted by increasing the number of stacks. For example, ten stacks achieve $\hat{\alpha} = 0.952$ at $W_x = W_y = 50$ m ($\chi = \pi/2$ rad; Figure 4.9b). However, similar to 1D arrays, the precise control of reflection and transmission zeros is limited by strong interactions between an increasing number of stacks on a fixed frequency interval (Westcott et al., 2024). Similarly to Westcott et al. (2024), the PTO parameters could be optimised for better absorption, however, the minimal gains to be made come at high computational expense.

4.4.4 Finite arrays

Strategies for broadband absorption extend effectively to finite arrays where the infinite number of WECs in each stack is truncated to form a row containing a finite number of WECs. In the finite array, the scattered coefficients of each WEC are obtained by replacing the lattice sums in Equation (4.26) with $(N_0 + 1) \times (2U + 1)$-square separation matrices $\boldsymbol{\sigma_{jl}} = (-1)^{\mu} K_{\tau-\mu}(\kappa_n W_{jl}) \mathrm{e}^{\mathrm{i}(\tau-\mu)\vartheta_{j-l}}$, where $(W_{jl}, \vartheta_{j-l})$ specifies the location of WEC l in the local coordinate system of WEC j (Martin, 2006). For an array with J WECs, the scattered coefficients are calculated from

$$[\boldsymbol{D}^1 \;\; \boldsymbol{D}^2 \cdots \boldsymbol{D}^J]^{\top} = [\boldsymbol{I} - \boldsymbol{\mathcal{B}}]^{-1} [\boldsymbol{B}^1 \boldsymbol{A}^1 \;\; \boldsymbol{B}^2 \boldsymbol{A}^2 \;\; \cdots \boldsymbol{B}^J \boldsymbol{A}^J]^{\top}, \tag{4.48}$$

where the matrix $\boldsymbol{\mathcal{B}}$ has elements $[\boldsymbol{\mathcal{B}}]_{jl} = \boldsymbol{B^j \sigma_{jl}}$. The vector of incident amplitudes for WEC j has elements defined by $[\boldsymbol{A^j}]_{n\mu} = \exp\left(\mathrm{i}k_0 W_{j0}\cos(\vartheta_j - \chi)\right)A_{n\mu}$, where (W_{j0}, ϑ_{j0}) specifies the position of WEC j in global coordinates (Kagemoto and Yue, 1986).

As few as five WECs per row are sufficient to generate the rainbow absorption behaviour of the graded infinite array (not shown), with good correspondence observed as the number of WECs per row is increased. The WEC amplitudes in a finite array of $J = 60$ WECs with six rows ($K = 6$; 10 WECs per row) are shown in Figure 4.10. The rows are graded using the PTO parameters in Table 4.2, with $W_x = 30$ and $W_y = 40\,\mathrm{m}$. Boundary effects are observed at edge WECs, and are most prominent near resonance, which typically experience amplified motions compared to the corresponding infinite array. The amplitudes of the interior WECs 4–7 closely resemble the WEC amplitudes in the infinite array. Increasingly many interior WECs resemble the behaviour of the infinite array as the number of WECs per row increases.

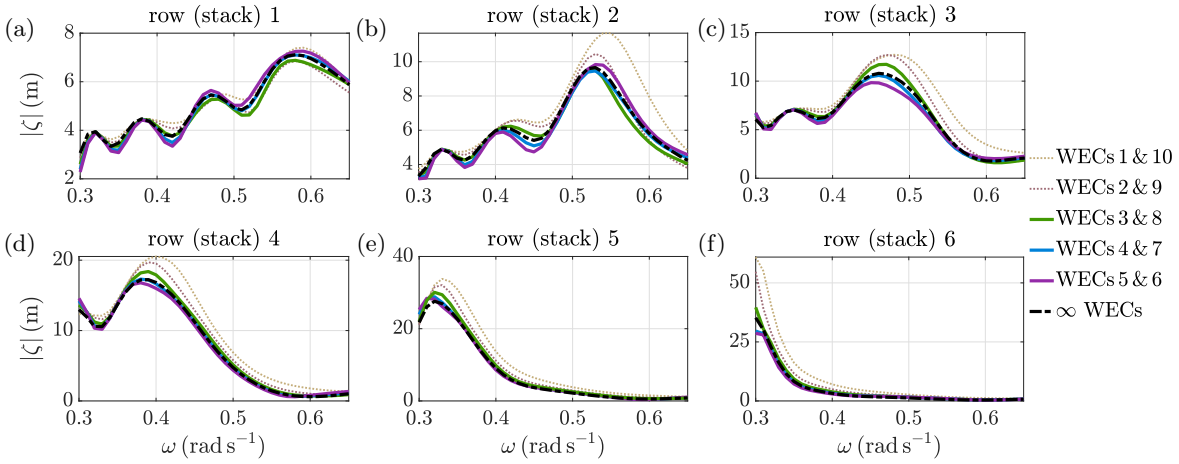

Figure 4.10: The WEC amplitudes ($|\zeta|$; —) in a graded array of 60 WECs with $W_x = 30$ and $W_y = 40\,\mathrm{m}$ are shown for $\omega \in [0.3, 0.65]\,\mathrm{rad\,s^{-1}}$ at $\chi = \pi/2\,\mathrm{rad}$. The PTO parameters of stack i in Table 4.2 are applied to all WECs (numbered 1 to 10 from left-to-right) in row i of the finite array, with $i = 1, 2, \ldots, 6$. The $|\zeta|$ of interior WECs tends towards the $|\zeta|$ in the infinite array (- -), with boundary effects visible at edge WECs (light coloured ····).

To relate the performance of a finite array to the infinite array, a relative capture width CW_{finite}, is defined as the power captured by the array as a proportion of the power available in the wavefront across the width of the array (JW_x/K) (McIver, 1994),

$$CW_{\text{finite}} = \left[\frac{1}{2}\sum_{j=1}^{J} B^j_{\text{PTO}}\,\omega^2\,|\zeta^j|^2\right] \Big/ \left[\frac{\omega}{4k_0}\left(1 + \frac{2k_0 h}{\sinh(2k_0 h)}\right)|A^{\text{inc}}|^2\,J\,W_x/K\right], \tag{4.49}$$

where K is the number of rows, and $\chi = \pi/2\,\mathrm{rad}$ is fixed (Gong et al., 2024; He et al., 2022). Since the relative capture width is non-dimensionalised relative to the array's cross-sectional width (including $W_x/2$ on either side), the efficiency measure can exceed one as the finite array can capture energy from the sides of the array, unlike the infinite array, where $0 \leq \alpha \leq 1$.

Efficiencies exceeding one are primarily attributed to boundary effects in the finite array, where the resulting amplification of WEC motions increase the numerator in Equation (4.49). At normal incidence, the boundary effects are generally limited to three edge WECs (either side of the array). Consequently, the proportion of power capture attributed to edge effects gradually decreases as the number of WECs per row increases.

Figure 4.11a shows the relative capture width of the finite array of 60 WECs (Figure 4.10) when excluding the two WECs at the edges of each row which experience boundary effects. The locations of peaks in the relative capture width are consistent with the absorption of the infinite array, but vary in magnitude over the target interval. Correspondence to the infinite array improves as the number of WECs per row increases, and is particularly good when based on the behaviour of interior WECs. For example, the relative capture width for 35 WECs per row is qualitatively identical to the infinite array, but with higher efficiency, which tends towards the absorption of the infinite array as edge WECs are excluded. There is little change in the relative capture width of interior WECs beyond 20 WECs per row.

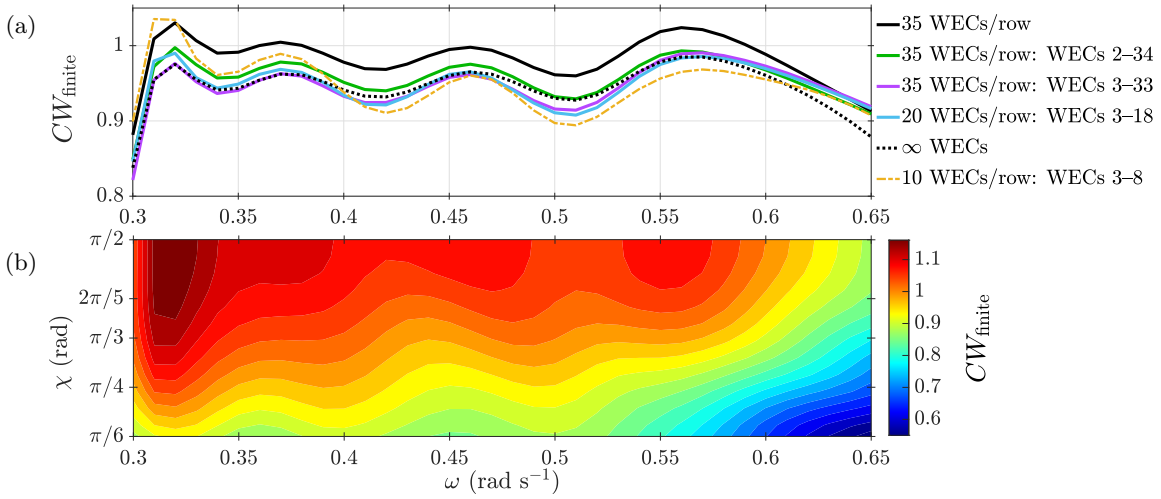

Figure 4.11: The relative capture width (a) CW_{finite} of graded, finite arrays (Table 4.2) are shown for $\omega \in [0.3, 0.65]\,\text{rad}\,\text{s}^{-1}$, with the absorption of the corresponding infinite array overlaid. The CW_{finite} is also shown when excluding edge WECs on either side of each row to eliminate boundary effects. The (b) CW_{finite} of the graded array of 60 WECs (Figure 4.10; Table 4.2) for $\omega \in [0.3, 0.65]\,\text{rad}\,\text{s}^{-1}$ is highest at $\chi = \pi/2\,\text{rad}$, and gradually declines as $\chi \to \pi/6$, particularly at higher frequencies.

Like the infinite array, the relative capture width of the graded array of 60 WECs remains high over the target interval $\omega \in [0.3, 0.65]\,\text{rad}\,\text{s}^{-1}$ at normal incidence, and gradually decreases as $\chi \to \pi/6$, particularly at higher frequencies (Figure 4.11b). The finite array preserves the underlying band structures, which are robust to changes in the incident wave direction, despite boundary effects impacting an increasing number of WECs within each row as the incident angle decreases. For incident angles $\pi/6 \leq \chi \leq \pi/2$, the finite array achieves over 90% efficiency on the majority of the target interval (Figure 4.11b).

The surface elevation and WEC amplitudes in the finite array are shown in Figure 4.12, corresponding to two of the incident wave frequencies and directions given in Figure 4.7. Boundary effects are evident near resonance, and have a reasonably minor impact on the wavefield. The finite array permits slightly higher transmission across the width of the array, particularly as $\chi \to \pi/6$. For example, the surface elevation in the finite array is $|\eta(x, y : k)| \approx 0.23\,\mathrm{m}$ when $\omega = 0.52\,\mathrm{rad\,s^{-1}}$ at $\chi = \pi/2\,\mathrm{rad}$, and $0.17\,\mathrm{m} \leq |\eta(x, y : k)| \leq 0.25\,\mathrm{m}$ when $\omega = 0.35\,\mathrm{rad\,s^{-1}}$ at $\chi = \pi/3\,\mathrm{rad}$, for $-75\,\mathrm{m} < x < 75\,\mathrm{m}$ and at $y = 220\,\mathrm{m}$, compared to $|\eta(x, y : k)| \approx 0.17\,\mathrm{m}$ and $|\eta(x, y : k)| \approx 0.14\,\mathrm{m}$, respectively, in the infinite array.

4.4.4.1 Ocean wave spectra

To illustrate the broadband (frequency and direction) efficiency of the graded finite array, using fixed PTO parameters, consider a multi-directional, irregular sea state defined by

$$S(\omega, \theta) = S_{\mathrm{f}}(\omega) D(\theta), \tag{4.50}$$

with amplitude $A(\omega, \theta) = \sqrt{2S(\omega, \theta)\Delta\omega\Delta\theta}$ (Chakrabarti, 2005). The spectral density function is chosen to be the JONSWAP (JOint North Sea WAve Project; Hasselmann et al., 1973) spectrum (Chakrabarti, 2005)

$$S_{\mathrm{f}}(\omega) = \frac{0.0081 g^2}{\omega^5} \mathrm{e}^{-1.25(\omega_{\mathrm{p}}/\omega)^4} \gamma^r \quad \text{where} \quad r = \mathrm{e}^{-(\omega-\omega_{\mathrm{p}})^2/(2\sigma^2\omega_{\mathrm{p}}^2)} \tag{4.51}$$

with peak frequency $\omega_{\mathrm{p}} = 2\pi/T_{\mathrm{p}}$ (period T_{p}; maximum energy in the spectrum) and spectral width

$$\sigma = \begin{cases} 0.007 & \omega < \omega_{\mathrm{p}}, \\ 0.009 & \omega \geq \omega_{\mathrm{p}}. \end{cases} \tag{4.52}$$

The sharpness of the spectrum is characterised by the peak enhancement factor γ. Globally, $\gamma = 1.54$ is typical of broadband sea states, particularly in coastal regions, while $\gamma = 3.3$ (narrower spectra) is typically used in the wave energy literature (Mazzaretto et al., 2022). The directional spreading function is modelled as a cosine-2ς distribution (Chakrabarti, 2005)

$$D(\theta) = \frac{\Gamma(\varsigma + 1)}{\sqrt{\pi}\,\Gamma(\varsigma + 1/2)} \cos^{2\varsigma}(\theta - \chi) \quad \text{for } 0 \leq |\theta - \chi| < \pi/2, \tag{4.53}$$

which is characterised by a spreading parameter ς, where $\varsigma = 1$ defines broadly spread sea states, and $\varsigma = 4$, more narrowly spread sea states. The principle direction χ is set to normal incidence ($\chi = \pi/2\,\mathrm{rad}$). The proportion of the incident spectrum absorbed by the array is defined as α_{spec}, such that

$$0 \leq \alpha_{\mathrm{spec}} = \frac{\iint CW_{\mathrm{finite}}(\omega, \theta)\,|A(\omega, \theta)|^2\,\mathrm{d}\omega\,\mathrm{d}\theta}{\iint |A(\omega, \theta)|^2\,\mathrm{d}\omega\,\mathrm{d}\theta} \lessapprox 1. \tag{4.54}$$

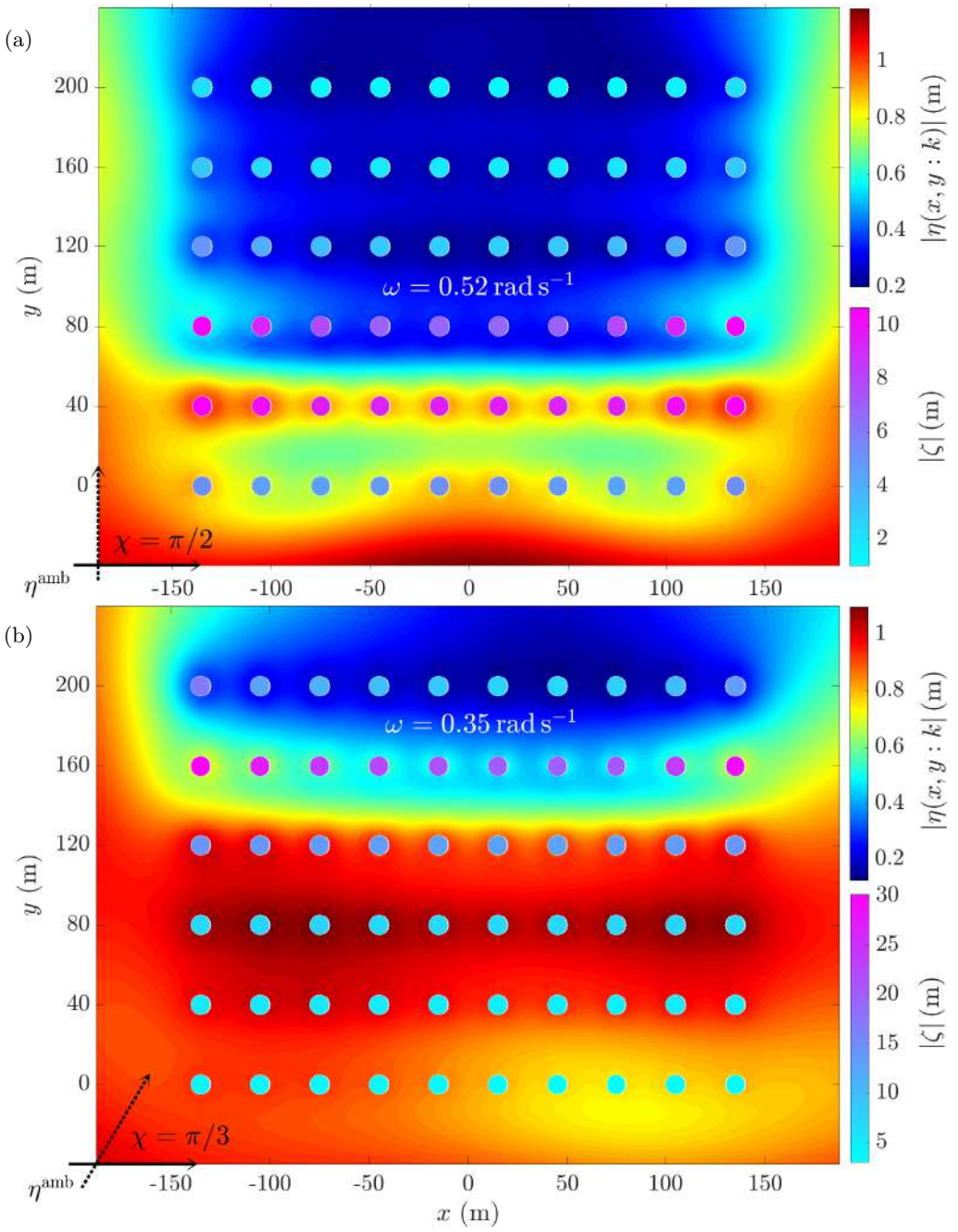

Figure 4.12: The surface elevation η (upper colourbar) and WEC amplitudes ζ (lower colourbar) in the finite array of 60 WECs (Table 4.2) are shown when (a) $\omega = 0.52\,\mathrm{rad\,s^{-1}}$ at $\chi = \pi/2\,\mathrm{rad}$, and when (b) $\omega = 0.35\,\mathrm{rad\,s^{-1}}$ at $\chi = \pi/3\,\mathrm{rad}$. Boundary effects are visible at the edge WECs in each row near resonance, and impact an increasing number of WECs as χ moves away from $\chi = \pi/2\,\mathrm{rad}$.

The double integrals on the right-hand side of Equation (4.54) are approximated using the trapezoidal rule, where the spectrum $S(\omega, \theta)$ is approximated by a finite sum of monochromatic waves (Cruz, 2008), at frequencies $\omega_0 = 0.2\,\mathrm{rad\,s^{-1}}$, $\omega_1 = \omega_0 + \Delta\omega$, ..., $\omega_{106} = \omega_0 + 106\Delta\omega = 1.26\,\mathrm{rad\,s^{-1}}$ ($\Delta\omega = 0.01$) and $\theta_0 = \pi/10\,\mathrm{rad}$, $\theta_1 = \theta_0 + \Delta\theta$, ..., $\theta_{14} = \theta_0 + 14\Delta\theta = \pi/2\,\mathrm{rad}$ ($\Delta\theta = 0.0898$).

The proportion of relatively narrow ($\gamma = 3.3$ and $\varsigma = 4$) and broad spectra ($\gamma = 1.54$ and $\varsigma = 1$) absorbed by the graded array of 60 WECs is shown in Figure 4.13 for $T_\mathrm{p} \in [5, 22]$ s, which covers feasible frequencies for power generation (Coe et al., 2021). The proportion of a spectrum captured depends on where T_p lies within the designed frequency range ($T_\mathrm{p} \in [10.3, 20.9]$ s) of the graded array. For example, 95% of a broad spectrum with $T_\mathrm{p} = 17$ s (shown in Figure 4.13b) is captured, as the majority of the spectrum lies within the target interval ($T_\mathrm{p} \in (9.6, 21)$ s). In comparison, 72% of the narrow spectrum with $T_\mathrm{p} = 10$ s shown in Figure 4.13a is captured, as a large proportion of the spectrum lies above the target interval. The average absorption is 86.8% when $\gamma = 1.54$ and $\varsigma = 1$, and 94% when $\gamma = 3.3$ with $\varsigma = 4$, for T_p lying within the target interval. Generally, α_spec increases for narrower spectra, particularly as γ increases.

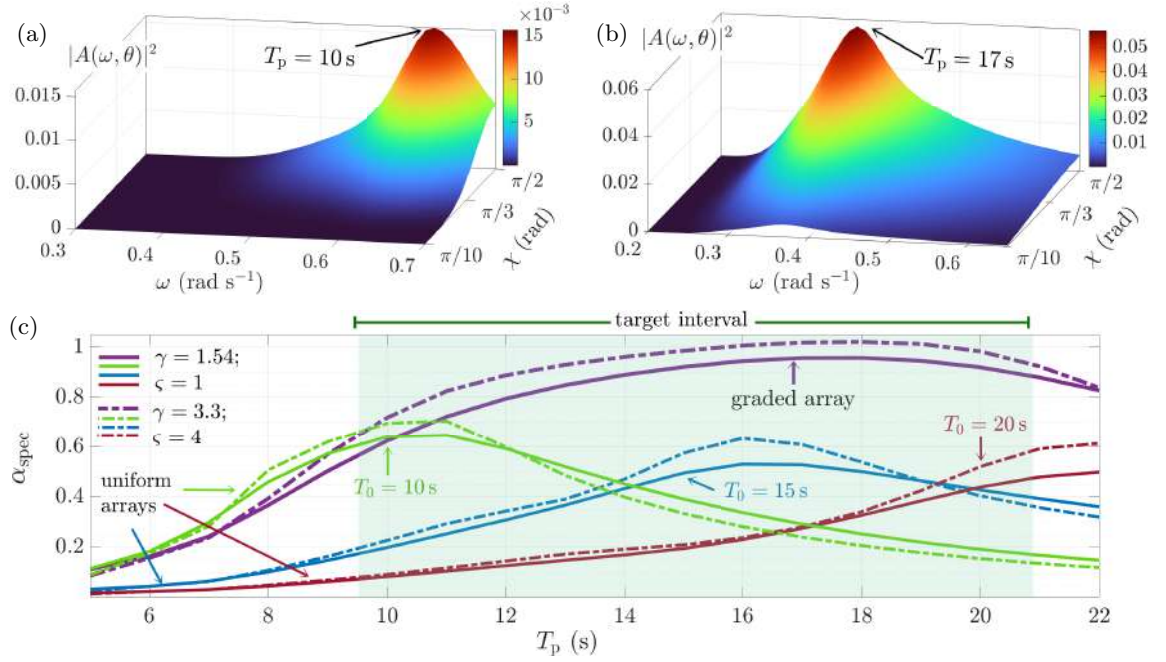

Figure 4.13: Incident spectra with a significant wave height of $H_\mathrm{s} = 1$ m, defined by (a) $\gamma = 3.3$, $\varsigma = 4$ (- - -) and $T_\mathrm{p} = 10$ s, and (b) $\gamma = 1.54$, $\varsigma = 1$ (—) and $T_\mathrm{p} = 17$ s, are shown to illustrate the energy in incident spectra relative to the target interval (shaded green) of the graded array. The proportion of the spectra absorbed (α_spec) by the graded array (purple) of 60 WECs (Table 4.2) with $W_x = 30$ and $W_y = 40$ m is shown in (c), where the α_spec for uniform arrays tuned to $T_0 = 10$ s (green), $T_0 = 15$ s (blue) and $T_0 = 20$ s (red) are shown for comparison.

To contextualise the proportion of the spectra absorbed, the absorptions of three different uniform arrays are shown in Figure 4.13c, to represent arrays designed for a particular wave climate. The arrays are tuned to resonate (fixed PTOs) at $T_0 = 10, 15$, and 20 s, respectively, corresponding to incoming spectra with $T_\mathrm{p} = 10, 15$, and 20 s, respectively. The absorptions of the uniform arrays peak at spectra with slightly higher T_p than the respective spectra to which they are tuned, and decline elsewhere (away from resonance). In general, the peak absorption is considerably lower than the graded array, where the broadband design ensures

efficient capture over a much larger proportion of frequencies within a spectrum.

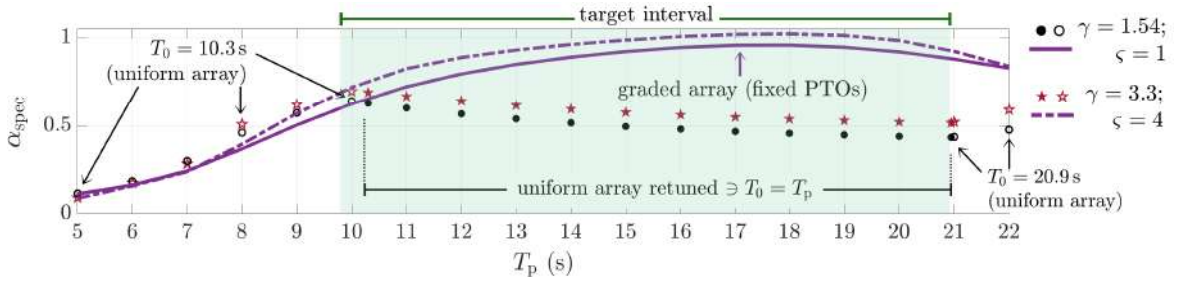

Figure 4.14: The α_{spec} of narrow ($\gamma = 3.3, \varsigma = 4$; ---) and broad ($\gamma = 1.54, \varsigma = 1$; —) spectra by the graded array (fixed PTOs; Table 4.2) is shown for $T_\mathrm{p} \in [5, 22]\,s$. The α_{spec} of the narrow (★) and broad (•) spectra by a uniform array is shown for comparison at each T_p. The uniform array is re-tuned (resonance T_0) to every T_p within the target interval (i.e. $T_0 = T_\mathrm{p} \in [10.3, 20.9]\,\mathrm{s}$), and held fixed at $T_0 = 10.3$ for $T_\mathrm{p} \in [5, 10]$, and $T_0 = 20.9$ for $T_\mathrm{p} = 21, 22\,\mathrm{s}$ (∘, open ★).

Similarly, Figure 4.14 shows the absorption of a uniform array which is re-tuned (dynamic PTOs) to be resonant at every peak period (i.e., absorption of a spectrum when $T_0 = T_\mathrm{p}$) on the target interval. The PTOs of the uniform array are held fixed outside the designed frequency range of the graded array, to enable a fair comparison (alternatively, the graded array should be re-graded over comparable periods). Again, the graded array (fixed PTOs) significantly outperforms the uniform array over the target interval, with the exception of at the upper bound ($T_\mathrm{p} < 10.3\,\mathrm{s}$), which lies at the limit of the designed frequency range of the graded array ($T_\mathrm{p} = 10.3\,\mathrm{s}$ coincides with the highest resonant frequency in the graded array). On average, the graded array captures 33.45% more of the broad spectra, and 33.01% more of the narrow spectra, over the target interval, than a dynamically re-tuned uniform array.

4.5 Discussion and conclusions

Arrays of heaving buoys were designed for the broadband absorption of ocean wave energy by grading their resonant properties through attached PTOs in a 3D model governed by linear potential-flow theory. The WECs were arranged into stacks (each of which contained infinitely many WECs) with a small periodicity length relative to the target wavelengths, to transform the wavefield into a discrete directional spectrum that supports a single propagating mode of transmission and reflection. An effective bandgap was generated over the target interval for low transmission, by grading the PTO spring constants of WECs in successive stacks from high-to-low in the direction of the incident wave (normal incidence), to create a rainbow reflecting array. The PTO damping was tuned to capture the reflected wave energy for rainbow absorption, by manipulating the location of the complex zero in reflection for each stack in the complex frequency plane.

Restrictions on the spacing between WECs were proposed to control reflection and transmission over the target interval for high efficiency with a relatively small number of stacks. The spacing is connected to the resonance bandwidth of stacks, and influences the ability to control the location of pole–zero pairs in complex frequency space. The resonant properties of the individual WECs influence the choice of spacing. Increasing the number of stacks can compensate for higher transmission resulting from wider spacings within stacks (W_x) or narrower resonance bandwidths, provided the spacing between stacks (W_y) is sufficiently small to prevent Bragg resonance from encroaching on the target interval. Arrays of five and six stacks achieved an average absorption of 10–20 s waves exceeding 94% at normal incidence (98% with ten stacks), and over 90% for a wide range of wave directions.

To develop practical array designs, the stacks were truncated to form rows with a finite number of WECs. Finite arrays with 60 WECs (ten WECs per row) were shown to execute the strategies for broadband absorption. The rainbow absorbing design enables the finite array to achieve efficient, broadband absorption over broad directional bands, without retuning the WECs, which produces high efficiency in realistic sea states. The graded array outperforms uniform arrays tuned to the peak period of incident spectra covering the designed frequency range of the graded array, as the broadband design ensures the capture of a much higher proportion of both narrow and broadly spread spectra.

The low transmission generated by the graded array could provide coastal protection benefits in addition to power capture. Graded arrays have garnered recent attention for their ability to generate broadband attenuation for coastal protection, and include graded arrays of non-absorbing submerged bars (Xie et al., 2025; Xu et al., 2023), bottom-mounted cylinders (Zhou and Song, 2025), resonant C-shaped cylinders (Bennetts et al., 2018; Cao, Chen, Ning, Peng, Xu and Lin, 2025) and floating plates with attached resonators (Liu et al., 2025). Consequently, WEC-arrays capable of providing the required attenuation while also generating power, are an attractive prospect. Since the grading is implemented via the PTO mechanisms in the WEC-array, rather than a surrounding structure, the array can be retuned if desired. This offers the additional flexibility to alternate between protecting coastlines or generating power, as proposed by Battisti et al. (2024) and Cui et al. (2024).

For linear theory to remain valid, the strategies presented are restricted to incident waves with small amplitudes, where the amplified WEC motions do not exceed the WEC draught, and break the water surface. Future research directions include approximating non-linearities like drag, which will reduce WEC motions and therefore efficiency, and introducing physical constraints on WEC motions to remain within practical limitations as the incident amplitude increases. Based on recent demonstrations of non-absorbing graded arrays (e.g., Archer et al., 2020; Cao, Chen, Ning, Peng, Xu and Lin, 2025; Zhou and Song, 2025), it is likely that the

broadband control will remain effective when subject to non-linear effects, but absorption will decline.

In conclusion, we have shown that arrays of heaving buoys can be designed for efficient broadband absorption, without optimisation, by grading their resonant properties for rainbow absorption. Array designs were presented that capture over 90% of the incident energy from two thirds of usable ocean wave frequencies, and for incident wave directions ranging up to 60 degrees from normal incidence, using fixed PTO parameters. The key properties of the rainbow absorbing design extend effectively to finite arrays with a reasonably small number of WECs per row. The practical design for finite arrays demonstrates highly efficient power capture in realistic sea states that are broadly spread in both frequency and direction.

Chapter 5

A rainbow absorbing array of heaving buoys subject to a drag correction

Abstract

Grading arrays of heaving buoy type wave energy converters (WECs) is a promising strategy to achieve the efficient capture of ocean wave energy over broad frequency ranges required for economic viability. The broadband control of wave energy is achieved by spatially grading the resonant frequencies of the WECs via linear spring–damper power take-off mechanisms, in a model governed by linear theory. However, the localised amplifications that are created and captured for high efficiency, produce large WEC motions that violate the assumptions of linear theory. A linearised drag correction derived from Morison's equation is incorporated in the frequency domain to approximate the non-linear effects that arise from large motions in regular waves. The impact of drag on the underlying band structures in a rainbow absorbing array are examined as the incident amplitude increases, using a periodic arrangement of WECs. The broadband behaviour remains intact, but the proportion of the incident wave energy that is captured by the array decreases as the amplifications of WEC motions are reduced by drag. Relatively small finite arrays capture all available incident energy across the width of the array on average, when the incident amplitude is restricted to prevent WECs from breaching the water surface. The broadband absorption is robust to the wave direction, and outperforms uniform arrays on the target frequency interval.

5.1 Introduction

The commercial-scale conversion of ocean wave energy into electrical power by arrays of wave energy converters (WECs) could significantly contribute to the growing global demand for renewable energy (IRENA and OEE, 2023; Ringwood et al., 2023). However, designing arrays to operate at high efficiency is challenging, as ocean waves suitable for power capture cover a broad range of frequencies and directions, which are subject to spatio-temporal variability on multiple time scales (Ning and Ding, 2022). For a given sea state, optimising the array layout (Göteman et al., 2020), WEC geometry (e.g., Edwards and Yue, 2022), and/or power take-off parameters (PTOs) (e.g., Garcia-Rosa et al., 2015) enhances power capture.

The high efficiency over broad frequency bands (*broadband absorption*) required for cost-effectiveness can theoretically be achieved by dynamically retuning the PTOs according to the sea state (Coe et al., 2021; Pecher and Kofoed, 2017). However, dynamic control does not necessarily address sensitivity to wave direction (Gallutia et al., 2022; Garcia-Rosa et al., 2015), requires accurate wave prediction, is sensitive to model error, and is technically challenging from a PTO design perspective (Ning and Ding, 2022; Pecher and Kofoed, 2017).

Alternatively, rainbow absorbing arrays can achieve broadband absorption using fixed PTO parameters by grading the resonant properties of the array for spatially controlled amplifications of wave energy over broad frequency bands (Westcott et al., 2024; Wilks et al., 2022). The graded resonances create an effective bandgap over the target frequency range, characterised by low transmission and a series of near-resonant responses that are captured by the PTO damping, which is chosen to minimise reflected wave amplitudes (Westcott et al., 2024; Wilks et al., 2022). Assuming linear theory, arrays of heaving buoys, modelled as truncated cylinders, have demonstrated over 90% absorption (proportion of incident energy captured) of 10–20 s waves over a wide range of wave directions (Westcott et al., 2025).

Large WEC motions relative to the WEC dimensions and incident amplitude occur at resonance, and are increased by localised amplifications from the rainbow absorbing design (Chapter 4), which violate the assumption of linearity. In reality, flow separation and vortex shedding become dominant as the WEC amplitude increases, producing a pressure drag force opposing the WEC motion (Kaneko et al., 2014). These non-linear effects significantly reduce the large WEC motions predicted by linear theory (Babarit et al., 2012; Folley, 2016; Giorgi and Ringwood, 2017). In practice, WEC motions are further physically constrained to comply with amplitude restrictions (Falnes and Kurniawan, 2020) and prevent WECs from breaching the water surface as the incident amplitude increases (Li et al., 2012).

Computational fluid dynamics (CFD) models capture viscous effects with high-fidelity but are computationally infeasible for the large-scale modelling of arrays (Göteman et al., 2020). Consequently, viscous losses are typically approximated in linear potential-flow models by incorporating an additional damping term into the linearised equation of motion (Wolgamot and Fitzgerald, 2015). The drag experienced by a WEC is primarily due to pressure drag from flow separation, rather than viscous drag (Sarpkaya, 2010) that arises from shear stress and is more relevant at small-amplitude oscillations (Kaneko et al., 2014). The pressure drag component of Morison's equation (Morison et al., 1950) is the most prevalent heuristic drag correction used in combination with idealised wave theories (Lei et al., 2023; Sarpkaya, 2010), and is commonly applied to linear models of heaving WECs to account for viscous effects (Penalba, Giorgi and Ringwood, 2017). To circumvent the computational expense of time-domain models, a quasi-linear drag correction based on Morison's equation can be iteratively

derived (Korde and Ringwood, 2016) and applied in the frequency domain for regular waves (Molin, 2023).

There is high uncertainty surrounding appropriate drag coefficients for WECs as a result of different methodologies employed to identify coefficients across studies, isolating drag from other un-modelled non-linear effects, and identifying a single value which is representative of a variety of wave conditions (Babarit et al., 2012; Giorgi and Ringwood, 2017; Molin, 2023; Penalba, Giorgi and Ringwood, 2017). Consequently, the drag coefficient can be a significant source of error (Babarit et al., 2012). Drag coefficients also depend on the WEC geometry, which should ideally be optimised to minimise drag (Guo and Ringwood, 2021). Hemispherical WEC shapes, for example, can capture over 50% more power than truncated shapes due to the minimal drag supporting larger motions, but can be difficult to construct compared to simply rounding the corners of a flat-bottomed base, which otherwise leads to high drag (Gu et al., 2018; Stansby et al., 2015; Tom and Yeung, 2013; Yeung and Jiang, 2014).

Despite the associated uncertainties, a drag correction can improve model accuracy (Guo and Ringwood, 2021), leading to an improved understanding of how drag may impact the power capture predicted by linear models, particularly in the early stages of concept development (Lei et al., 2023; Sarpkaya, 2010). Since a drag correction alters the resonant response of WECs, which control the underlying band structures in a rainbow absorbing array, it is important to analyse the impact on strategies for broadband absorption. In this study, we demonstrate that graded arrays of heaving buoys subject to a drag correction based on Morison's equation, achieve efficient broadband absorption of 10–20 s waves (angular frequencies $\omega \in [0.3, 0.65]\,\mathrm{rad\,s^{-1}}$) using static PTO parameters.

After setting out the model and methods in § 5.2, drag is incorporated in an array composed of periodic rows of WECs to determine the effect on the reflection and transmission properties, which are critical to efficient rainbow absorption (§ 5.3). Given the uncertainty associated with drag coefficients, two values are applied to analyse the effect on the array design. Comparisons to a uniform tuning are used to illustrate how the ability to considerably extend the local bandgap by grading an array is gradually lost as the impact of drag increases. The altered WEC motions determine the efficiency that is achieved. Lastly, strategies are transferred to a finite array in § 5.4, where the incident amplitude is restricted to retain model validity, and solutions are contextualised against a typical uniform tuning applied in the literature.

5.2 Preliminaries

The array of heaving buoy type WECs is modelled in a three-dimensional (3D) water domain Ω as depicted in Figure 5.1, in which locations are defined by a Cartesian coordinate system.

The domain extends infinitely in the (x, y) horizontal directions and is bounded below by an impermeable seabed at constant, finite depth $z = -h$. The z-axis is directed out of the water, and $z = \eta(x, y, t) = 0$ coincides with the undisturbed free surface.

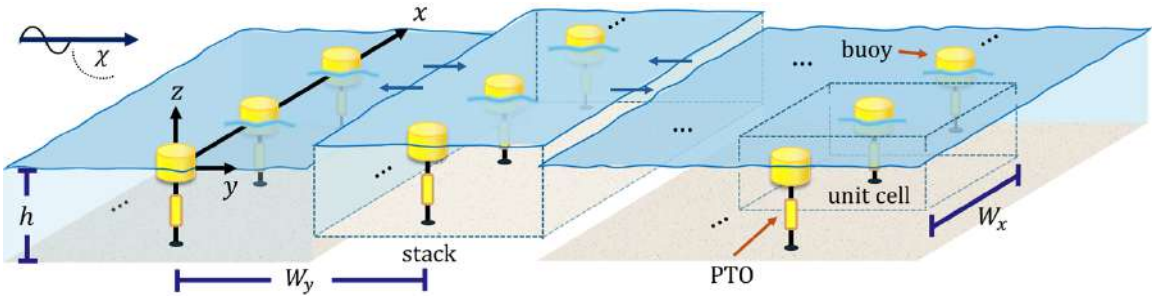

Figure 5.1: The array consists of a finite number of stacks with centre-to-centre spacing W_y (m) in the y–direction. Each stack contains infinitely many, identical WECs, distributed periodically in the x–direction with centre-to-centre spacing W_x (m). The ambient incident wave propagates left-to-right at an angle of χ rad with respect to the x-axis.

The WECs are modelled as truncated cylinders with radius L and draught L (height $2L$), attached to a linear spring–damper PTO, which is modelled using stiffness and damping terms, C_{PTO} and B_{PTO}, respectively. The array consists of a finite number of stacks, with a constant centre-to-centre spacing W_y in the y–direction. Each stack is composed of a periodic row of identical WECs in the x–direction with constant spacing W_x. The centre of WEC j in stack s is located at $(jW_x, (s-1)W_y)$ in the (x, y) plane, where $j \in \mathbb{Z}$, and $s = 1, 2, \ldots, S$. The dimensions $L = 5\,\text{m}$ and $h = 50\,\text{m}$ are selected to be broadly consistent with CorPower Ocean's (2024) state-of-the-art C4 device.

Linear potential-flow theory is applied, assuming small amplitudes relative to the wavelengths. The potential Φ satisfies Laplace's equation (Linton and McIver, 2001; Mei et al., 2005)

$$\nabla^2\Phi(x, y, z, t) = 0 \quad \text{on} \quad \Omega = \{(x, y, z) : x \in \mathbb{R}, y \in \mathbb{R}, -h \leq z \leq \eta(x, y, t)\}\,, \tag{5.1}$$

subject to a linearised free surface condition and no-normal flow at the seabed, respectively

$$\frac{\partial^2\Phi}{\partial t^2} + g\frac{\partial\Phi}{\partial z} = 0 \quad \text{at} \quad z = 0, \tag{5.2}$$

$$\frac{\partial\Phi}{\partial z} = 0 \quad \text{at} \quad z = -h. \tag{5.3}$$

The potential is decomposed into incident ($^{\text{inc}}$), diffracted ($^{\text{diff}}$) and radiated ($^{\text{rad}}$) components

$$\Phi = \Phi^{\text{inc}} + \Phi^{\text{diff}} + \Phi^{\text{rad}}, \quad \text{where} \quad \Phi^{\text{scat}} = \Phi^{\text{diff}} + \Phi^{\text{rad}} \tag{5.4}$$

is defined as the scattered potential, which satisfies radiation conditions in the far field (Kagemoto and Yue, 1986). In the diffraction problem, the WEC is held fixed in the incident waves,

while in the radiation problem, the WEC undergoes forced, heave oscillations in the absence of an incident wave (Linton and McIver, 2001). The respective boundary conditions on the wetted surface S^i_{Bj} of WEC j in stack i are (Linton and McIver, 2001)

$$\frac{\partial \Phi^{\text{diff}}}{\partial n} = -\frac{\partial \Phi^{\text{inc}}}{\partial n} \quad \text{and} \quad \frac{\partial \Phi^{\text{rad}}}{\partial n} = \dot{\xi}^j_i(t) \quad \text{on} \quad S^i_{Bj}, \tag{5.5a, b}$$

where $\dot{\xi}^j_i(t) = \text{Re}\left\{-\text{i}\omega\zeta^j_i \text{e}^{-\text{i}\omega t}\right\}$ is the WEC velocity (dot denotes times derivative), which is determined using the equation of motion (omitting ^j_i for ease of notation) (Mei et al., 2005),

$$\mathfrak{M}\,\ddot{\xi} + B_{\text{PTO}}\,\dot{\xi} + (\mathfrak{C} + C_{\text{PTO}})\,\xi = -\rho \iint_{S_B} \frac{\partial \Phi}{\partial t} n \,\text{d}S + F_{\text{drag}}(t), \tag{5.6}$$

where $\mathfrak{M}$ (kg) is the mass of the WEC, and $\mathfrak{C}$ (N m^{-1}) is the hydrostatic stiffness. The drag force $F_{\text{drag}}(t)$ acting on each WEC is modelled using Morison's equation, which implies that drag is proportional to the dynamic pressure exerted on the base of the cylinder by the local wavefield (Clauss et al., 1992),

$$F_{\text{drag}}(t) = -\frac{1}{2} C_d \rho \int_{S_B} \left|\frac{\partial \Phi}{\partial z}\right| \frac{\partial \Phi}{\partial z} \text{d}S \quad \text{at} \quad z = -L \tag{5.7a}$$

$$= -\frac{1}{2} C_d \rho \pi L^2 |\dot{\xi}(t)| \dot{\xi}(t). \tag{5.7b}$$

The absolute value ensures drag opposes the WEC motion given the quadratic dependence on velocity associated with the loss of kinetic energy (Clauss et al., 1992; Folley and Whittaker, 2010; Sarpkaya, 2010). The drag coefficient C_d relates the total drag to the WEC's cross-sectional area, projected onto a plane normal to the motion (Clauss et al., 1992; Douglas et al., 1986). Drag coefficients are fitted to experimental or CFD data, or based on tabulated ratios of the Keulegan–Carpenter and Reynolds numbers (Giorgi and Ringwood, 2017; Penalba, Giorgi and Ringwood, 2017), the frontal area of the body (Douglas et al., 1986), or the sharpness of corners (Molin, 2023). Reported values for truncated cylinders range from $C_d = 0.6$ to $C_d = 2$, and depend on the methodology used to identify C_d, the model to which C_d is calibrated, the WEC geometry (Babarit et al., 2012; Douglas et al., 1986; Giorgi and Ringwood, 2017; Molin, 2023) and whether the flow is steady or oscillatory (Journée and Massie, 2001).

The generalisation of Morison's equation for oscillating bodies models drag as the dynamic pressure force from the normal component of the relative velocity between the WEC and the unperturbed water particle velocity ($u(t) = \partial \Phi^{\text{amb}}_z$) at a fixed point (r_0, θ_0, z_0) which is considered representative of the cross-sectional area (Clauss et al., 1992),

$$F_{\text{drag}}(t) = -\frac{1}{2}\,\rho\, C_d\, \pi L^2\, |\dot{\xi}(t) - u(t)| \left(\dot{\xi}(t) - u(t)\right). \tag{5.8}$$

Typically, $(r_0, \theta_0, z_0) = (0, 0, z_0)$, with z_0 selected at some submergence depth of the WEC

(e.g., the WEC's draught (George and Cho, 2024)). This assumes that a body with a small characteristic dimension relative to the wavelength ($2L < \lambda/6$) produces negligible scattering, and the incident wave remains unperturbed by the body, so that any local variation can be neglected across small dimensions (Clauss et al., 1992; Molin, 2023). Although this assumption is unlikely to be satisfied by WECs, where resonant scattering perturbs the local wavefield significantly and will alter drag effects (Mérigaud et al., 2024), the local wavefield cannot be accommodated in a linear theory framework, as the wave particle velocity underneath the WEC satisfies the kinematic condition (Equation (2.7b)), implying no drag occurs.

For generality, let $v(t) = \mathrm{Re}\left\{V\mathrm{e}^{-\mathrm{i}\omega t}\right\} = |V|\cos(\omega t + \gamma)$ symbolise the velocity ($V = |-\mathrm{i}\omega\zeta|$), or relative velocity ($V = |-\mathrm{i}\omega\zeta - U|$), where γ is the corresponding phase, so that

$$F_{\mathrm{drag}}(t) = -\frac{1}{2}\rho\, C_d\, \pi L^2 \left|v(t)\right| v(t). \tag{5.9}$$

The velocity $\dot{\xi}(t) = \mathrm{Re}\left\{-\mathrm{i}\omega\zeta(\omega)\mathrm{e}^{-\mathrm{i}\omega t}\right\}$ can feature multiple harmonics due to the non-linearity introduced by the quadratic drag correction (Mei et al., 2005). However, the time-averaged power dissipated will depend on the first harmonic at the driving frequency due to orthogonality of the Fourier series, when driven by a sinusoidal input (Elliott et al., 2015). Consequently, it is typically assumed that the velocity at the driving frequency dominates the response so that higher harmonics can be neglected (Mei et al., 2005; Molin, 2023).

Assuming excitation by a regular wave, a linearised drag force $F_{\mathrm{vis}}(t) = b_{\mathrm{vis}}\, v(t)$ is defined such that the average work done over a period is equivalent to the non-linear drag force (Korde and Ringwood, 2016; Mei et al., 2005)

$$\frac{1}{T}\int_0^T F_{\mathrm{vis}}\, v(t)\,\mathrm{d}t = \frac{1}{T}\int_0^T F_{\mathrm{drag}}\, v(t)\,\mathrm{d}t \tag{5.10}$$

$$\frac{1}{2}\, b_{\mathrm{vis}}\, |V|^2 = \frac{1}{2T}\,\rho\, C_d\, \pi L^2\, |V|^3\, \frac{8}{3\omega}. \tag{5.11}$$

The drag correction b_{vis} depends on the unknown $\dot{\xi}(t)$. To transform Equation (5.6) to the frequency domain, the coefficients should be independent of $\xi(t)$ to obtain a linear differential equation with constant coefficients at a specified frequency (Falnes, 2005). Consequently, a quasi-linear drag correction is defined as the solution to an iterative procedure, which is then transformed to the frequency domain, as it returns a linear system at each iteration i (Molin, 2023),

$$b_{\mathrm{vis}}^{(i-1)}\, v^{(i)}(t) = \frac{4}{3}\rho\, C_d\, L^2\, |V^{(i-1)}|\, \mathrm{Re}\left\{V^{(i)}\mathrm{e}^{-\mathrm{i}\omega t}\right\}, \quad \text{for } i = 1, 2, \ldots I, \tag{5.12}$$

where I depends on the frequency and convergence criteria. Note that, solutions for regular waves should not be superimposed to obtain the response in irregular waves, as b_{vis} is not truly linear.

5.2.1 Individual stacks in the frequency domain

Solutions are sought in the frequency domain, following Chapter 4, where water motions are modelled using linear potential-flow theory. Given an incident wave with amplitude A^{inc} at a prescribed angular frequency ω, the time-harmonic motions are defined by

$$\Phi(x,y,z,t) = \text{Re}\left\{\frac{gA^{\text{inc}}}{\text{i}\omega}\left(\phi^{\text{inc}}(r,\theta,z) + \phi^{\text{diff}}(r,\theta,z) + \zeta\phi^{\text{rad}}(r,\theta,z)\right)e^{-\text{i}\omega t}\right\}, \tag{5.13}$$

where $g = 9.81\,\text{m}\,\text{s}^{-2}$ is gravitational acceleration, $\text{i} = \sqrt{-1}$ is the imaginary number and $\zeta \in \mathbb{C}$ is the heave amplitude. The solution for each stack (Figure 5.1) is obtained in isolation and later combined using multiple wave scattering theory to retrieve the full wavefield. An ambient incident wave propagating at $\chi \in (0,\pi)$ radians with respect to the positive x-axis is defined as

$$\phi^{\text{amb}}(r,\theta,z) = Z_0(z)\,\text{e}^{\text{i}\,k_0\,r\cos(\theta-\chi)} = Z_0(z)\sum_{\mu=-\infty}^{\infty} A_{0\mu}\,I_\mu(\kappa_0 r)\,\text{e}^{\text{i}\mu\theta} \tag{5.14}$$

where $A_{0\mu} = (-1)^\mu\,\text{e}^{-\text{i}\mu\chi}$, and $Z_0(z)$ is the associated vertical eigenfunction

$$Z_n(z)\big|_{n=0} = \left.\frac{\cosh(k_n(z+h))}{\cosh(k_n h)}\right|_{n=0}. \tag{5.15}$$

The wavenumbers k_n are the real ($n = 0$; $k_0 \in \mathbb{R}^+$ is the propagating mode), and positive imaginary ($n \geq 1$; evanescent modes) roots to the dispersion equation (derived from Equation (5.2))

$$\omega^2 = gk\tanh(kh). \tag{5.16}$$

The wavenumbers κ_n are defined as $\kappa_n = -\text{i}k_n$ for $n \in \mathbb{Z} \geq 0$.

A local cylindrical coordinate system (r_j,θ_j,z) is defined at the centre of each WEC in the stack, with the zeroth WEC placed at the origin of the global coordinate system where $x = r\cos(\theta)$ and $y = r\sin(\theta)$. Due to the periodicity, it suffices to consider the solution to the boundary value problem on a unit cell containing WEC j at its centre. Applying separation of variables and expressing ϕ_j as an eigenfunction expansion in cylindrical coordinates (Linton and McIver, 2001),

$$\phi_j(r_j,\theta_j,z) = \phi_j^{\text{inc}}(r_j,\theta_j,z) + \phi_j^{\text{scat}}(r_j,\theta_j,z) \tag{5.17a}$$

$$= \sum_{n=0}^{\infty} Z_n(z)\sum_{\mu=-\infty}^{\infty}\left(C_{n\mu}^j I_\mu(\kappa_n r_j) + D_{n\mu}^j K_\mu(\kappa_n r_j)\right)\text{e}^{\text{i}\mu\theta_j} \tag{5.17b}$$

where I_μ and K_μ are modified Bessel functions of the first and second kind, respectively, and of order μ. The unknown scattered coefficients $D_{n\mu}^j = D_{n\mu}^{\text{diff}} + \zeta_j D_{n\mu}^{\text{rad}}$ are obtained by

solving the diffraction and radiation problems subject to the respective boundary conditions (Equation (5.5)), where $D_{n\mu}^{\mathrm{rad}}$ is obtained for unit amplitude heave motion. The complex-valued heave amplitude ζ_j of WEC j, $j \in \mathbb{Z}$, is determined from the equation of motion

$$\left[-\omega^2(\mathfrak{M} + a(\omega)) - \mathrm{i}\omega\left(b(\omega) + B_{\mathrm{PTO}} + b_{\mathrm{vis}}(\omega)\right) + \mathfrak{C} + C_{\mathrm{PTO}}\right]\zeta_j(\omega) = F_j^{\mathrm{exc}}(\omega). \tag{5.18}$$

The excitation force F_j^{exc} accounts for interactions in the array, and is decomposed as $F^{\mathrm{exc}} = \boldsymbol{f_e}\boldsymbol{C}^j$, where $\boldsymbol{f_e}$ is a known vector, arising from the hydrodynamic pressure in the diffraction problem of the isolated WEC (Appendix B.1), and $\left[\boldsymbol{C}^j\right]_{n\mu} = C_{n\mu}^j$ are to be determined.

The left-hand side of Equation (5.18) depends on the hydrodynamic forcing from the radiated wavefield of an isolated WEC with mass $\mathfrak{M} = \rho\pi L^3\,\mathrm{kg}$ and hydrostatic stiffness $\mathfrak{C} = \rho g\pi L^2\,\mathrm{N\,m^{-1}}$. The added mass $a(\omega)$ and radiation damping $b(\omega)$ arise in response to forced oscillations in heave (Appendix B.1), and are proportional to the acceleration and velocity of the body, respectively (Linton and McIver, 2001). The quasi-linear drag correction b_{vis} is obtained through iteration in the full array problem (§ 5.2.2).

The incident potential ϕ_j^{inc} is a superposition of the ambient incident wavefield and the scattered wavefields of the WECs in the stack ($l \in \mathbb{Z}, l \neq j$) (Peter and Meylan, 2010)

$$\phi_j^{\mathrm{inc}}(r_j, \theta_j, z) = \phi^{\mathrm{amb}}(r_j, \theta_j, z) + \sum_{\substack{l=-\infty \\ l\neq j}}^{\infty} \phi_{l\to j}^{\mathrm{scat}}(r_j, \theta_j, z). \tag{5.19}$$

WEC l is located at $(r_j, \theta_j) = (W_{jl}, \vartheta_{jl})$ in the local coordinates of WEC j ($j \neq l$), where $W_{jl} = |j - l|W_x$ and

$$\vartheta_{j-l} = \begin{cases} \pi & \text{for} \quad j > l, \\ 0 & \text{for} \quad j < l. \end{cases}$$

The scattered field of WEC l can be expressed as the incident field on WEC j, provided $r_l < W_x$, using Graf's addition theorem (Martin, 2006),

$$K_\tau(\kappa_n r_l)\mathrm{e}^{\mathrm{i}\mu\theta_l} = \sum_{\mu=-\infty}^{\infty} K_{\tau-\mu}(\kappa_n W_{jl})\mathrm{e}^{\mathrm{i}(\tau-\mu)\vartheta_{j-l}} I_\mu(\kappa_n r_j)\mathrm{e}^{\mathrm{i}\mu(\pi+\theta_j)}, \quad l \neq j. \tag{5.20}$$

Consequently, the incident coefficients in Equation (5.17b) are given by

$$C_{n\mu}^j = A_{n\mu}^j + \sum_{\substack{l=-\infty \\ l\neq j}}^{\infty} \sum_{\tau=-\infty}^{\infty} D_{n\tau}^l (-1)^\mu K_{\tau-\mu}(\kappa_n W_{jl})\mathrm{e}^{\mathrm{i}(\tau-\mu)\vartheta_{j-l}} \tag{5.21}$$

where $A_{n\mu}^j = 0$ for $n > 0$, and $A_{n\mu}^0 \equiv A_{n\mu}$ is known. The $A_{n\mu}^j$ are obtained through a phase shift defined by $\mathcal{Q}_j = \mathrm{e}^{\mathrm{i}kjW_x\cos(\chi)}$ as $A_{n\mu}^j = \mathcal{Q}_j A_{n\mu}$. Similarly, $D_{n\mu}^j$ and $C_{n\mu}^j$ can be expressed in terms of $C_{n\mu} \equiv C_{n\mu}^0$ and $D_{n\mu} \equiv D_{n\mu}^0$ due to the periodicity as $C_{n\mu}^j = \mathcal{Q}_j C_{n\mu}$

and $D^j_{n\mu} = \mathcal{Q}_j D_{n\mu}$. Consequently, the summation over $l \in \mathbb{Z} \setminus j$ in Equation (5.21) is pre-computed following Peter et al. (2006) and Linton (1998) by defining

$$\sigma^n_\nu = (-1)^\mu \sum_{\substack{l=-\infty \\ l\neq j}}^{\infty} \mathcal{Q}_{l-j} K_\nu(\kappa_n |j-l| W_x) \mathrm{e}^{\mathrm{i}\nu\vartheta_{j-l}} = (-1)^\mu \sum_{l=1}^{\infty} \left(\mathcal{Q}_l + (-1)^\nu \mathcal{Q}_{-l}\right) K_\nu(\kappa_n l W_x). \tag{5.22}$$

To solve the system of equations, the infinite summations are truncated according to the desired level of accuracy, such that $n = 0, 1, \ldots, (N_0 - 1)$ and $\mu = -U, \ldots, U$. The scattering properties of the WEC are encoded by a $N_0 \times (2U+1)$-square diffraction transfer matrix $\boldsymbol{B}$ (Appendix B.1), so that the unknown scattered coefficients are given by

$$\boldsymbol{D} = \boldsymbol{B}\boldsymbol{C} \tag{5.23a}$$

$$= \boldsymbol{B}(\boldsymbol{A} + \boldsymbol{\sigma}\boldsymbol{D}) \tag{5.23b}$$

$$= \left[\boldsymbol{I} - \boldsymbol{B}\boldsymbol{\sigma}\right]^{-1} \boldsymbol{B}\boldsymbol{A}, \tag{5.23c}$$

where the $N_0(2U+1) \times N_0(2U+1)$ matrices $\boldsymbol{\sigma}$, $\boldsymbol{D}$ and $\boldsymbol{C}$ have elements

$$[\boldsymbol{\sigma}]_{n\nu} = \sigma^n_\nu, \quad [\boldsymbol{D}]_{n\mu} = D_{n\mu} \quad \text{and} \quad [\boldsymbol{C}]_{n\mu} = C_{n\mu}. \tag{5.24}$$

The full solution around a stack is obtained by summing the scattered wavefields of all WECs in the stack in terms of the local coordinate systems (Peter et al., 2006),

$$\phi(r,\theta,z) = \phi^{\mathrm{amb}}(r,\theta,z) + \sum_{n=0}^{\infty} Z_n(z) \sum_{j=-\infty}^{\infty} \mathcal{Q}_j \sum_{\mu=-\infty}^{\infty} D_{n\mu} K_\mu(\kappa_n r_j) \mathrm{e}^{\mathrm{i}\mu\theta_j}. \tag{5.25}$$

Constructive interference between the circular, scattered wavefields of the WECs transforms the far field into a discrete directional spectrum, in which plane waves propagate away from the stack in a finite number of directions (Falnes and Budal, 1982) determined by the scattering angles χ_m, which satisfy (Peter and Meylan, 2010)

$$\chi_m = \arccos\left(\frac{\psi_m}{k_0}\right) \quad \text{where} \quad \psi_m = k_0 \cos(\chi) + \frac{2m\pi}{W_x}, \quad m \in \mathbb{Z}. \tag{5.26}$$

The set $\mathcal{M}$ of real scattering angles corresponds to propagating modes and is defined by integer values of m such that $|\psi_m| < k_0$, namely

$$-1 < \cos(\chi) + \frac{2m\pi}{k_0 W_x} < 1, \quad m \in \mathcal{M}. \tag{5.27}$$

Complex scattering angles correspond to evanescent modes that decay with distance from the stack when $|\psi_m| > k_0$ (Mulholland and Heckl, 1994), in which case the complex branch of

arccos is defined by (Peter et al., 2006)

$$\arccos(\varsigma) = \begin{cases} \mathrm{i}\,\mathrm{arccosh}(\varsigma), & \varsigma > 1, \\ \pi - \mathrm{i}\,\mathrm{arccosh}(-\varsigma) & \varsigma < -1 \end{cases} \tag{5.28}$$

with $\mathrm{arccosh}(\varsigma) = \log(\varsigma + \sqrt{\varsigma^2 - 1})$ for $\varsigma > 1$. A plane-wave expansion (PWE) is derived following Peter et al. (2006) by replacing the modified Bessel functions with an integral representation, extended to include decaying vertical modes, such that

$$\phi(r,\theta,z) = \begin{cases} Z_0(z)\mathrm{e}^{\mathrm{i}k_0 r\cos(\theta-\chi)} + \displaystyle\sum_{n=0}^{\infty} Z_n(z) \sum_{m=-\infty}^{\infty} R_{mn}\,\mathrm{e}^{\mathrm{i}k_n r\cos(\theta+\chi_{mn})} & y < -L \\ \displaystyle\sum_{n=0}^{\infty} Z_n(z) \sum_{m=-\infty}^{\infty} T_{mn}\,\mathrm{e}^{\mathrm{i}k_n r\cos(\theta-\chi_{mn})} & y > L \end{cases} \tag{5.29}$$

where $\chi_{mn} = \arccos(\psi_m/k_n)$ and the amplitudes of the reflected and transmitted wave modes propagating or decaying in the $\mp\, y$–direction, respectively, are

$$R_{mn} = \frac{\mathrm{i}\pi}{k_n W_x} \frac{1}{\sin(\chi_{mn})} \sum_{\mu=-\infty}^{\infty} D_{n\mu}\,\mathrm{e}^{-\mathrm{i}\mu\chi_{mn}} \tag{5.30}$$

$$T_{mn} = \delta_n + \frac{\mathrm{i}\pi}{k_n W_x} \frac{1}{\sin(\chi_{mn})} \sum_{\mu=-\infty}^{\infty} D_{n\mu}\,\mathrm{e}^{\mathrm{i}\mu\chi_{mn}}, \tag{5.31}$$

where $\delta_n = 1$ for $n = 0$, and zero otherwise. Truncating the infinite number of scattering angles to $-p \le m \le q$, where $m \in \mathbb{Z}$ and $p, q \ge 0$, such that $M = p + q + 1$ includes both real and complex scattering angles, and the number of vertical modes to $n = N_1 \le N_0$, the reflection and transmission coefficients in the PWE are used to assemble a scattering matrix which relates the amplitudes of incoming waves to outgoing waves (Peter and Meylan, 2010),

$$\boldsymbol{\mathcal{S}} = \begin{bmatrix} \boldsymbol{R} & \boldsymbol{T} \\ \boldsymbol{T} & \boldsymbol{R} \end{bmatrix} \text{ such that } \begin{bmatrix} \boldsymbol{f}_1^+ \\ \boldsymbol{f}_0^- \end{bmatrix} = \boldsymbol{\mathcal{S}} \begin{bmatrix} \boldsymbol{f}_0^+ \\ \boldsymbol{f}_1^- \end{bmatrix}. \tag{5.32}$$

The $(MN_1 \times MN_1)$ reflection ($\boldsymbol{R}^{\pm} = \boldsymbol{R}$) and transmission ($\boldsymbol{T}^{\pm} = \boldsymbol{T}$) matrices have elements defined by Equations (5.30) and (5.31).

The incoming and outgoing amplitudes $\boldsymbol{f}_s^{\pm}$ are associated with wave modes that propagate or decay in the $\pm\, y$–direction in the generalised PWE for the wavefield, such that

$$\phi(r,\theta,z) = \sum_{n=0}^{N_1-1} Z_n(z) \sum_{m=-p}^{q} \left(f_{mn}^{+}\mathrm{e}^{\mathrm{i}k_n r\cos(\theta-\chi_{mn})} + f_{mn}^{-}\mathrm{e}^{\mathrm{i}k_n r\cos(\theta+\chi_{mn})} \right) \text{ for } y < -L \tag{5.33}$$

corresponding to $\boldsymbol{f}_0^{\pm}$ ($s = 1$ behind the stack; $y > L$). Propagating modes are associated

with $\chi_{m0} \in \mathbb{R}$, and decaying modes with $\chi_{mn} \in \mathbb{C}$ for $n \geq 0$. On the target frequency band, $\omega \in [0.3, 0.65]\,\mathrm{rad\,s^{-1}}$, all stacks considered have a single, real scattering angle, which is consistent with the incident angle, and corresponds to one propagating direction. However, decaying modes are included to capture interactions between resonant stacks accurately.

5.2.2 Combining multiple stacks into an array

The reflection and transmission matrices for each stack are iteratively combined following Mulholland and Heckl (1994) to form the reflection ($\boldsymbol{\mathcal{R}}^{\pm}_{(1,s)}$) and transmission ($\boldsymbol{\mathcal{T}}^{\pm}_{(1,s)}$) matrices encapsulating the scattering of stacks 1 to s, for $s = 2, \ldots, S$, defined by

$$\boldsymbol{\mathcal{R}}^{+}_{(1,s)} = \boldsymbol{R}^{+}_{s} + \boldsymbol{T}^{+}_{s}\boldsymbol{Q}\,\boldsymbol{\mathcal{R}}^{+}_{(1,s-1)}\boldsymbol{Q}\left[\boldsymbol{I} - \boldsymbol{R}^{-}_{s}\,\boldsymbol{Q}\,\boldsymbol{\mathcal{R}}^{+}_{(1,s-1)}\,\boldsymbol{Q}\right]^{-1}\boldsymbol{T}^{-}_{s} \tag{5.34}$$

$$\boldsymbol{\mathcal{T}}^{-}_{(1,s)} = \boldsymbol{\mathcal{T}}^{-}_{(1,s-1)}\boldsymbol{Q}\left[\boldsymbol{I} - \boldsymbol{R}^{-}_{s}\boldsymbol{Q}\,\boldsymbol{\mathcal{R}}^{+}_{(1,s-1)}\boldsymbol{Q}\right]^{-1}\boldsymbol{T}^{-}_{s} \tag{5.35}$$

$$\boldsymbol{\mathcal{R}}^{-}_{(1,s)} = \boldsymbol{\mathcal{R}}^{-}_{(1,s-1)} + \boldsymbol{\mathcal{T}}^{-}_{(1,s-1)}\boldsymbol{Q}\,\boldsymbol{R}^{-}_{s}\left[\boldsymbol{I} - \boldsymbol{Q}\,\boldsymbol{\mathcal{R}}^{+}_{(1,s-1)}\boldsymbol{Q}\,\boldsymbol{R}^{-}_{s}\right]^{-1}\boldsymbol{\mathcal{T}}^{+}_{(,1s-1)}\boldsymbol{Q} \tag{5.36}$$

$$\boldsymbol{\mathcal{T}}^{+}_{(1,s)} = \boldsymbol{T}^{+}_{s}\left[\boldsymbol{I} - \boldsymbol{Q}\,\boldsymbol{\mathcal{R}}^{+}_{(1,s-1)}\boldsymbol{Q}\,\boldsymbol{R}^{-}_{s}\right]^{-1}\boldsymbol{\mathcal{T}}^{+}_{(1,s-1)}\boldsymbol{Q} \tag{5.37}$$

where $\boldsymbol{\mathcal{R}}^{\pm}_{(1,1)} = \boldsymbol{R}_1$ and $\boldsymbol{\mathcal{T}}^{\pm}_{(1,1)} = \boldsymbol{T}_1$. The diagonal matrix $\boldsymbol{Q}$ has elements $Q_{mn} = \mathrm{e}^{\mathrm{i}k_n W_y \sin(\chi_{mn})}$ which encode the phase change over a unit cell in the y–direction. The scattering matrix of the array is defined by

$$\boldsymbol{\mathcal{S}} = \begin{bmatrix} \boldsymbol{\mathcal{R}}^{-}_{(1,S)} & \boldsymbol{\mathcal{T}}^{-}_{(1,S)} \\ \boldsymbol{\mathcal{R}}^{+}_{(1,S)} & \boldsymbol{\mathcal{T}}^{+}_{(1,S)} \end{bmatrix} \text{ such that } \begin{bmatrix} \boldsymbol{f}^{+}_{S} \\ \boldsymbol{f}^{-}_{0} \end{bmatrix} = \boldsymbol{\mathcal{S}} \begin{bmatrix} \boldsymbol{f}^{+}_{0} \\ \boldsymbol{f}^{-}_{S} \end{bmatrix}. \tag{5.38}$$

The amplitudes of the wavefield between stacks are (Bennetts and Squire, 2009)

$$\boldsymbol{f}^{+}_{s} = \left[\boldsymbol{I} - \boldsymbol{\mathcal{R}}^{+}_{(1,s-1)}\boldsymbol{Q}\,\boldsymbol{\mathcal{R}}^{-}_{(S,s)}\boldsymbol{Q}\right]^{-1}\left[\boldsymbol{\mathcal{T}}^{+}_{(1,s-1)}\boldsymbol{f}^{+}_{0} + \boldsymbol{\mathcal{R}}^{+}_{(1,s-1)}\boldsymbol{Q}\,\boldsymbol{\mathcal{T}}^{-}_{(S,s)}\boldsymbol{f}^{-}_{S}\right] \tag{5.39}$$

$$\boldsymbol{f}^{-}_{s} = \left[\boldsymbol{I} - \boldsymbol{\mathcal{R}}^{-}_{(S,s)}\,\boldsymbol{Q}\boldsymbol{\mathcal{R}}^{+}_{(1,s-1)}\boldsymbol{Q}\right]^{-1}\left[\boldsymbol{\mathcal{R}}^{-}_{(S,s)}\boldsymbol{Q}\,\boldsymbol{\mathcal{T}}^{+}_{(1,s-1)}\boldsymbol{f}^{+}_{0} + \boldsymbol{\mathcal{T}}^{-}_{(S,s)}\boldsymbol{f}^{-}_{S}\right], \tag{5.40}$$

with $\boldsymbol{f}^{\pm}_{(s-1)}$ denoting the wavefield before stack s, and $\boldsymbol{f}^{\pm}_{s}$, the wavefield after, for $s = 1, 2, \ldots, S$. The scattered amplitudes for stack s are obtained from $\boldsymbol{D}_s = \boldsymbol{B}(\boldsymbol{f}^{+}_{s-1} + \boldsymbol{Q}\boldsymbol{f}^{-}_{s})$, with the amplitude of WEC j in stack s retrieved from

$$\zeta^{j}_{s} = \boldsymbol{\zeta}^{j}_{s}\boldsymbol{\sigma}\boldsymbol{D}_s + \boldsymbol{\zeta}^{j}_{s}(\boldsymbol{f}^{+}_{s-1} + \boldsymbol{Q}\boldsymbol{f}^{-}_{s}), \tag{5.41}$$

and calculated iteratively due to the drag correction b_{vis}. The vector of heave amplitudes $\boldsymbol{\zeta}^{j}_{s}$ is obtained from Equation (5.18) for an unspecified incident wave $\boldsymbol{f_e}$ (Appendix B.1). An initial estimate $\hat{b}^{s}_{\mathrm{vis}}$ is generated using Equation (5.18) with $b^{s}_{\mathrm{vis}} = 0$ for ζ^{j}_{s} in each stack, for $s = 1, 2, \ldots, S$. Algorithm 2 is implemented until a prescribed convergence criterion is met.

Algorithm 2: The iterative process described by Bacelli and Ringwood (2013) is adapted to determine b^s_{vis} and ζ_s of the zeroth WEC in each stack s, $s = 1, \ldots, S$ within the array.

while $|b^s_{\text{vis}} - \hat{b}^s_{\text{vis}}| > 0.1$, **let** $b_{\text{vis}} = \hat{b}_{\text{vis}}$;

Determine $\boldsymbol{\zeta}_s = \left[-\omega^2(\mathfrak{M} + a(\omega)) - \mathrm{i}\omega\left(b(\omega) + B^s_{\text{PTO}} + b^s_{\text{vis}}(\omega)\right) + \mathfrak{C} + C^s_{\text{PTO}}\right]^{-1} \boldsymbol{f_e}$;

Calculate $\boldsymbol{D}_s = [\boldsymbol{I} - \boldsymbol{B\sigma}]^{-1}\boldsymbol{B}(\boldsymbol{f}^+_{s-1} + \boldsymbol{Q}\boldsymbol{f}^-_s)$;

Retrieve the buoy amplitudes $\zeta_s = \boldsymbol{\zeta}_s\boldsymbol{\sigma}\boldsymbol{D}_s + \boldsymbol{\zeta}_s(\boldsymbol{f}^+_{s-1} + \boldsymbol{Q}\boldsymbol{f}^-_s)$;

Update $\hat{b}^s_{\text{vis}} = 4C_d\,\rho\,L^2\,|-\mathrm{i}\omega\zeta_s|/3$;

end

The wave particle velocity in the vertical direction at WEC j in stack s (omitting s superscript for ease of notation) is defined in terms of the external potential (defined for $r \geq L$),

$$\left.\frac{\partial \Phi^{\text{inc}}}{\partial z}\right|_{(r_0,\theta_0,z_0)} = \mathrm{Re}\left\{\frac{g}{\mathrm{i}\omega}\sum_{n=0}^{\infty} k_n \frac{\sinh(k_n(z_0+h))}{\cosh(k_n h)} \sum_{\mu=-\infty}^{\infty} C^j_{n\mu} I_\mu(\kappa_n r_0)\mathrm{e}^{\mathrm{i}\mu\theta_0}\mathrm{e}^{-\mathrm{i}\omega t}\right\} \tag{5.42a}$$

$$= \mathrm{Re}\left\{U(\omega)\mathrm{e}^{-\mathrm{i}\omega t}\right\} = u(t), \tag{5.42b}$$

as per the assumption that the incident field is unperturbed by the scattering of WEC j (otherwise the kinematic condition enforces zero drag). The drag correction based on the relative velocity $b^s_{\text{vis}} = \frac{4}{3}\rho\, C_d\, L^2\,|-\mathrm{i}\omega\zeta_s - U|$ is similarly obtained through Algorithm 2, with C_d adjusted for the altered model, and the excitation force amended to

$$F^{\text{exc}}_s(\omega) = \left[\boldsymbol{f_e} + b^s_{\text{vis}}(\omega)\frac{g\boldsymbol{k}\sinh(\boldsymbol{k}(h-z_0))}{\mathrm{i}\omega\cosh(\boldsymbol{k}h)}\right]\boldsymbol{C}, \tag{5.43}$$

where $\boldsymbol{C}$ is resolved through multiple scattering (incident field on WEC j, given the interactions within the array). At $z_0 = 0$, Equation (5.42b) is equivalent to the time derivative of the surface elevation (using Equation (5.16)). Breaching events are defined as any crossing of the free surface (measured at the centre of each WEC $(r_j, \theta_j, z) = (0, 0, 0)$) for $t \in [0, 2\pi/\omega]$ as

$$\text{breaching occurs if } \begin{cases} \mathrm{Re}\left\{\zeta e^{-\mathrm{i}\omega t}\right\} < \mathrm{Re}\left\{\eta e^{-\mathrm{i}\omega t}\right\} - L, \text{ when } \mathrm{Re}\left\{\zeta e^{-\mathrm{i}\omega t}\right\} < 0 \\ \mathrm{Re}\left\{\zeta e^{-\mathrm{i}\omega t}\right\} > \mathrm{Re}\left\{\eta e^{-\mathrm{i}\omega t}\right\} + L, \text{ when } \mathrm{Re}\left\{\zeta e^{-\mathrm{i}\omega t}\right\} \geq 0. \end{cases} \tag{5.44}$$

The non-dimensionalised absorption (proportion of power captured) is obtained by summing the power extracted by the WECs in the zeroth cells of all stacks in the array and expressing it as a proportion of the power available across a unit cell width of the incident wave crest

$$\alpha = \left[\frac{1}{2}\sum_{s=1}^{S} B^s_{\text{PTO}}\,\omega^2\,|\zeta_s|^2\right] \Big/ \left[\frac{\omega}{4k_0}\left(1 + \frac{2k_0 h}{\sinh(2k_0 h)}\right)|A^{\text{inc}}|^2\, W_x\, \sin(\chi)\right]. \tag{5.45}$$

Equation (5.45) is equivalent to $\alpha_0 = 1 - |R|^2 - |T|^2$ when $C_d = 0$, where R and T are the

propagating modes of the reflection and transmission in Equation (5.38). However, $\alpha_0 = 1 - |R|^2 - |T|^2$ includes dissipative losses when $C_d \neq 0$ (i.e., it is non-conservative when $B_{\mathrm{PTO}} = 0$), and no longer represents efficiency (power capture).

In a finite array with J WECs, the scattered coefficients of each WEC are obtained from

$$[\boldsymbol{D}^1 \;\; \boldsymbol{D}^2 \;\; \cdots \;\; \boldsymbol{D}^J\,]^\top = [\,\boldsymbol{I} - \boldsymbol{\mathcal{B}}\,]^{-1}\,[\,\boldsymbol{B}^1\boldsymbol{A}^1 \;\; \boldsymbol{B}^2\boldsymbol{A}^2 \;\; \cdots \;\; \boldsymbol{B}^J\boldsymbol{A}^J\,]^\top, \tag{5.46}$$

given the incident amplitudes defined by $\left[\boldsymbol{A}^j\right]_{n\mu} = \exp\left(\mathrm{i}k_0 W_{0j}\cos(\vartheta_{0j} - \chi)\right)A_{n\mu}$, where (W_{0j}, ϑ_{0j}) specifies the position of WEC j in global coordinates (Kagemoto and Yue, 1986). The matrix $\boldsymbol{\mathcal{B}}$ has elements $[\boldsymbol{\mathcal{B}}]_{jl} = \boldsymbol{B}^j\boldsymbol{\sigma_{jl}}$, where $\boldsymbol{\sigma_{jl}} = (-1)^\tau K_{\mu-\tau}(\kappa_n W_{jl})\mathrm{e}^{\mathrm{i}(\mu-\tau)\vartheta_{j-l}}$ is the $N_0 \times (2U+1)$-square separation matrix (Martin, 2006), and $\boldsymbol{I}$ is the identity matrix. A drag correction for each WEC is determined by applying Algorithm 2 to all WECs simultaneously.

5.2.3 Drag coefficients

A drag coefficient of $C_d = 0.6$, which is likely to be appropriate for a WEC in turbulent flow (Douglas et al., 1986), is applied in addition to an experimentally obtained $C_d = 2$ for a truncated cylinder of similar diameter (Molin, 2023). The experimental data reported by Molin (2023) is further used to fit $C_d^{\mathrm{rel}} = 2.3$ to the drag correction derived from Equation (5.8) (relative velocity), to demonstrate the equivalence of results. Experimental drag coefficients are often derived from physical models scaled by Froude similarity. Since gravitational acceleration and viscosity are constant across scales, a sufficiently large geometric scale is required to maintain kinematic similarity with a Reynolds number $Re = u2L/\nu \gtrsim 10^5$, where ν is the kinematic viscosity, for the ratio of viscous to gravity forces to be consistent with the turbulent flow (drag from pressure rather than friction) typical of WEC prototypes (Clauss et al., 1992; Molin, 2023; Schmitt and Elsäßer, 2017; Sheng et al., 2014). Small geometric scales inadvertently increase drag coefficients (Gu et al., 2018) if the Reynolds number is too low (Chakrabarti, 2005; Journée and Massie, 2001).

At field scale, C_d generally decreases as the flow transitions from laminar to turbulent, converging to $C_d = 0.6$ at $Re \gtrsim 10^5$ (Clauss et al., 1992; Molin, 2023; Sarpkaya, 2010). Numerical wave tanks have the advantage of simulating field scale, or scaling viscosity to satisfy Froude and Reynolds scaling (e.g., Windt et al., 2021). However, truncated cylinders with sharp corners create vortices (Tom and Yeung, 2013; Yeung and Jiang, 2014), leading to high drag coefficients (e.g., $C_d = 2$) that are virtually independent of the Reynolds number, as a result of flow separation (Molin, 2023; Schmitt and Elsäßer, 2017). In practice, the corners of truncated cylinders are rounded for drag reduction (Stansby et al., 2015), which reduces C_d (Molin, 2023), with even minor rounding in physical models reducing drag (e.g., Palm et al., 2016). Consequently, the experimental $C_d = 2$ could mean that drag has an outsized effect

on results, as a truncated cylinder experiences higher drag than rounded geometries, which are more typical of heaving buoys (Tom and Yeung, 2013; Yeung and Jiang, 2014).

5.3 Infinite arrays

5.3.1 Reflection, transmission and WEC amplitudes

The graded array in Table 5.1 is designed to create low transmission over the target interval to support efficient, broadband absorption, as demonstrated in Chapter 4 when $C_d = 0$. The incorporation of the drag correction into the model ($C_d \neq 0$) alters the WEC motions around resonance. The amplification of WEC motions relative to the incident wave amplitude rapidly decline as the incident amplitude increases, and the zero in transmission and peak in reflection associated with each stack resonance are lost. Consequently, the reflection and transmission of the graded array are altered, as shown in Figure 5.2 when $B^s_{\mathrm{PTO}} = 0$ for $s = 1, \ldots, 6$, and using $C_d = 2$ to emphasise the altered properties (Figure C.1 shows $C_d = 0.6$).

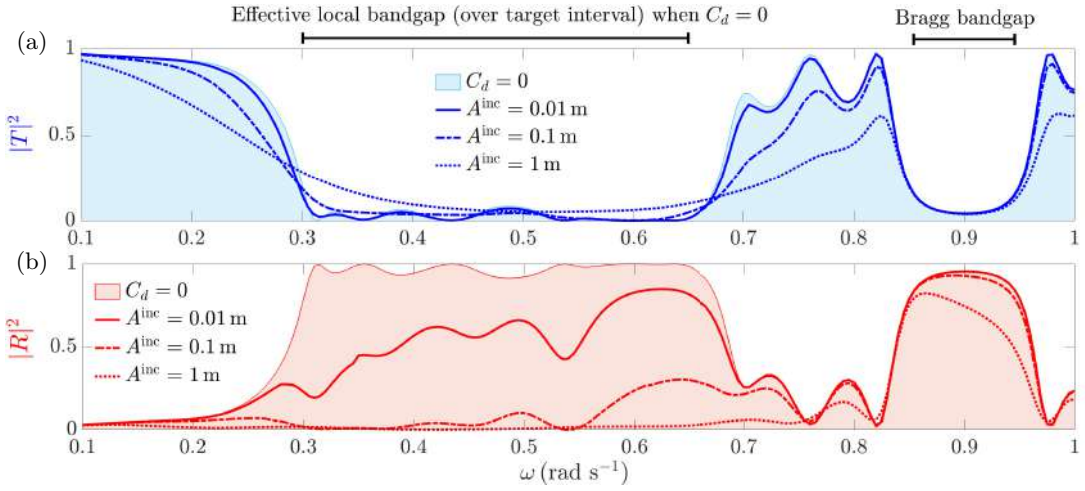

Figure 5.2: The (a) transmission $|T|^2$ (blue) and (b) reflection $|R|^2$ (red) for the graded array of six stacks in Table 5.1 (when $B^s_{\mathrm{PTO}} = 0\ \forall s$) is shown when $C_d = 0$ (shaded) and when $C_d = 2$ (lines), for $A^{\mathrm{inc}} = 0.01$ (—), 0.1(- - -) and 1 (···) m.

Low transmission is maintained in the local bandgap when $C_d \neq 0$. As the incident amplitude increases, the large WEC motions required to radiate waves that cancel the incoming wavefield cannot be realised (particularly at low frequencies), and the limits of the bandgap become less clearly defined. A substantial proportion of the wave energy that would be reflected as a result of the grading is dissipated by drag within the array, causing the reflection coefficient to flatten as the incident amplitude increases. The effect of drag is less pronounced (more similar to $C_d = 0$) away from resonance, at low incident amplitudes, and at higher frequencies. This is evident in the Bragg bandgap, which arises from the periodicity rather than WEC motions, but is affected by the altered reflection properties of the WECs (Linton, 2011).

Table 5.1: The resonant frequency ω_0 and PTO parameters of the six stacks in an array with $W_x = 30\,\text{m}$ and $W_y = 40\,\text{m}$. In the uniform array, stacks are tuned identically and B^s_{PTO} is optimal for a stack in isolation. In the graded array, B^s_{PTO} are selected such that $|R(\omega_0)|^2 \approx 0$ when $C_d = 0$.

	Graded array					
stack s	1	2	3	4	5	6
ω_0^s rad s^{-1}	0.611	0.567	0.511	0.418	0.342	0.299
C^s_{PTO} kN m^{-1}	−538	−572	−611	−670	−709	−728
B^s_{PTO} kN s m^{-1}	111	52.3	60.3	56.3	40.2	13.7
	Uniform array (all stacks) tuned to ω_0					
ω_0^s rad s^{-1}	0.650		0.475		0.300	
C^s_{PTO} kN m^{-1}	−506		−635		−727	
B^s_{PTO} kN s m^{-1}	63.9		50.1		47.8	

The grading of the array becomes less critical to achieving low transmission over the target interval as drag effects increase. This is illustrated in Figure 5.3 by contrasting the transmission of the graded array with a uniform array tuned to $\omega_0 = 0.475\,\text{rad}\,\text{s}^{-1}$, for an incident wave with $A^{\text{inc}} = 1\,\text{m}$ at $C_d = 0.6$ and $C_d = 2$. Incorporating drag broadens the local bandgap (responsible for $|T|^2 \approx 0$) of a uniform array appreciably. The extended, *effective* local bandgap obtained by grading becomes less notable, and limited to approximately a third of the target interval when $C_d = 2$. In comparison, the effective bandgap is over four times wider than the uniform array's bandgap when $C_d = 0$ (shaded). The graded array maintains a wider local bandgap than a uniform array over the entire range of C_d and A^{inc}.

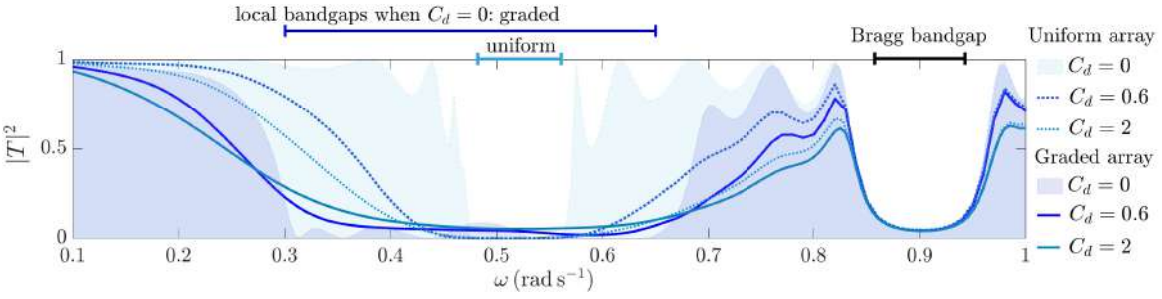

Figure 5.3: The transmission of a graded and uniform array (six stacks, $W_x = 30\,\text{m}$ and $W_y = 40\,\text{m}$), is shown when $C_d = 0$ (shaded), $C_d = 0.6$ and $C_d = 2$ (lines) for $A^{\text{inc}} = 1\,\text{m}$.

The changes to reflection and transmission behaviour arise from the WEC amplitudes, which are shown, with and without drag, in Figure 5.4. When $C_d = 0$, amplified WEC motions in a uniform array at resonance induce a relatively narrow bandgap, where motions drop to zero. Array resonances arise from the spacing between rows (W_y) causing amplified motions for $\omega \in (0.56, 0.8]\,\text{rad}\,\text{s}^{-1}$ (peaks in transmission above $\omega \approx 0.55\,\text{rad}\,\text{s}^{-1}$). In contrast, the graded array produces a series of resonant peaks across the effective bandgap (to be harnessed

for efficient power capture), and restricts array resonances to lie above the target frequency range, while also altering their properties (e.g., narrows their resonance bandwidth).

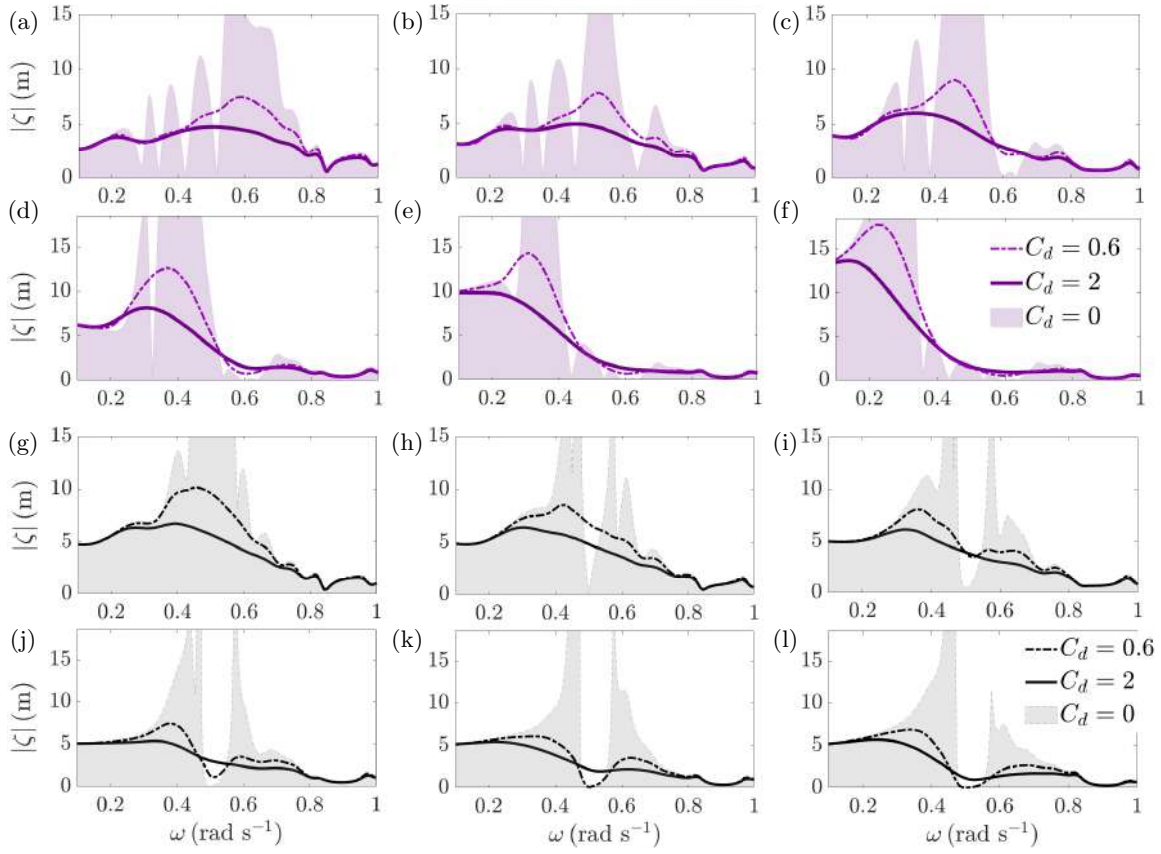

Figure 5.4: The WEC amplitudes $|\zeta|$ of the zeroth WEC in each stack of a graded (a)–(f) and uniform array (g)–(l) of six stacks ($W_x = 30\,\mathrm{m}$ and $W_y = 40\,\mathrm{m}$), is shown when $C_d = 0$ (shaded), $C_d = 0.6$ (- · -) and $C_d = 2$ (——).

The distinct behaviours of graded and uniform arrays are gradually eroded as the impact of drag increases (at higher C_d and/or A^{inc}). The graded array maintains higher amplitudes at low frequencies, which are responsible for the increased width of the local bandgap. However, the broadened, but dramatically reduced WEC motions on the interval are less distinguishable from the uniform array, where peaks associated with each of the passbands merge, with only minimal evidence of the bandgap. The Bragg bandgaps are identical (same periodicity).

5.3.2 Absorption

Figure 5.5a shows the broadband absorption of the graded array (Table 5.1) when $C_d = 0.6$, which declines as the incident amplitude A^{inc} increases. The average absorption $\hat{\alpha}$ over the target interval $\omega \in [0.3, 0.65]\,\mathrm{rad\,s^{-1}}$ remains high (relative to the $\hat{\alpha}$ at $\chi = \pi/2\,\mathrm{rad}$) across a wide range of incident wave directions (Figure 5.5b). The efficiency is determined by the amplifications of WEC motions at resonance, which depend on A^{inc} due to the non-linearity

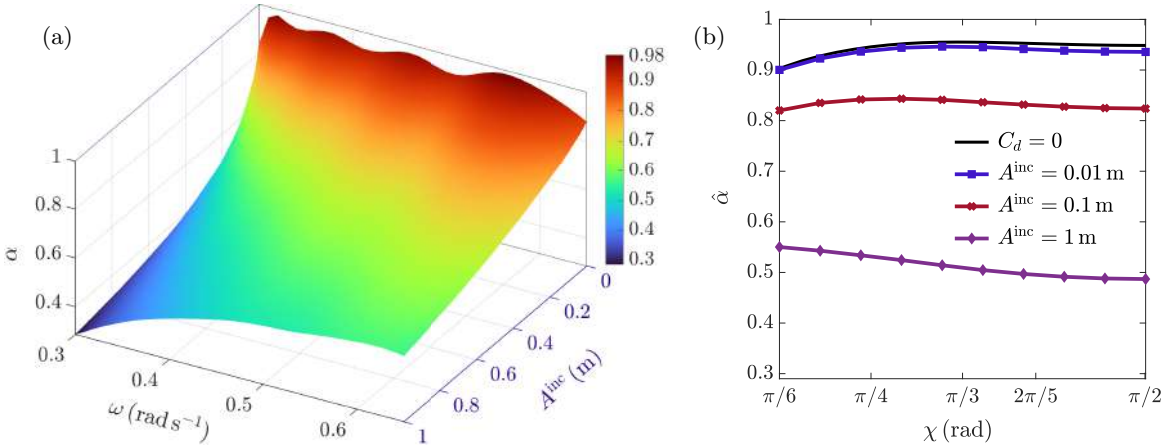

Figure 5.5: The absorption (a) α of the graded array (Table 5.1) is shown as a function of the incident amplitude $A^{\text{inc}}\,(\text{m})$ on the target interval $\omega \in [0.3, 0.65]\,\text{rad}\,\text{s}^{-1}$ when $C_d = 0.6$. The average absorption over the target interval, $\hat{\alpha}$, is plotted in (b) as a function of the incident wave angle $\chi\,(\text{rad})$.

of the drag correction, and are shown in Figures 5.6a–f as the non-dimensional response amplitude operators (RAO $= |\zeta|/A^{\text{inc}}$) of the zeroth WECs in stacks 1–6.

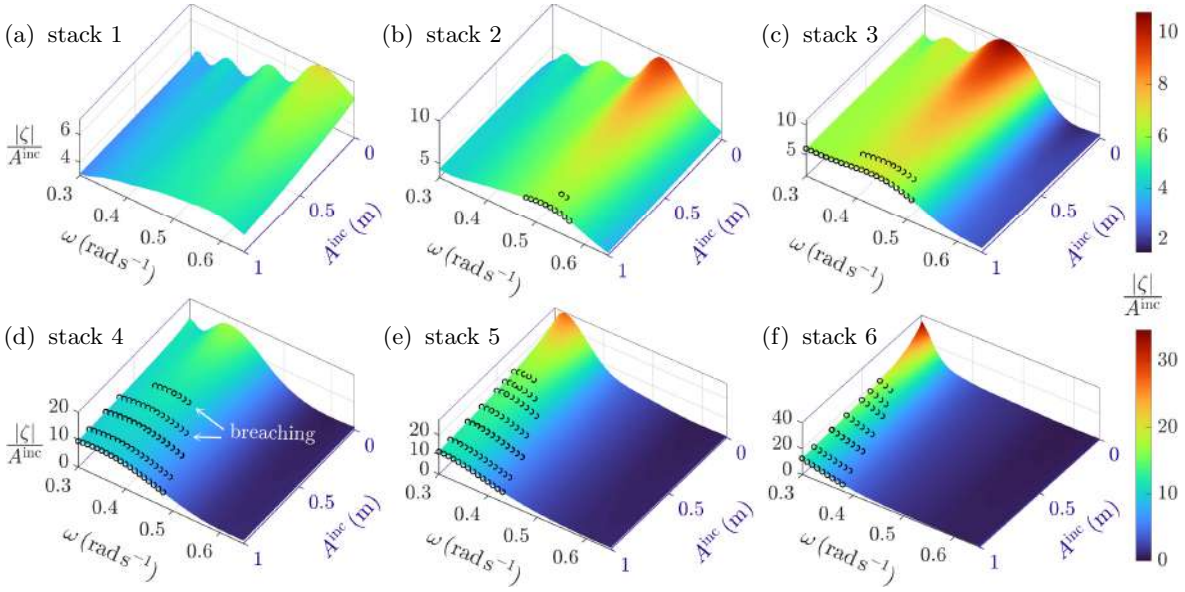

Figure 5.6: The RAOs ($|\zeta|/A^{\text{inc}}$) of the zeroth WEC in stacks 1-6 (a)–(f) of the graded array (Table 5.1) are shown as a function of the incident wave amplitude $A^{\text{inc}}\,(\text{m})$ for $\omega \in [0.3, 0.65]\,\text{rad}\,\text{s}^{-1}$ when $C_d = 0.6$. Breaching is indicated by $\circ$. No breaching occurs for $A^{\text{inc}} \leq 0.25\,\text{m}$.

High efficiency absorption requires large amplifications of the WEC motions relative to A^{inc}. The WEC motions become larger as A^{inc} increases, leading to higher drag which causes the RAOs around resonance to gradually decline, thereby lowering absorption. The RAOs remain relatively consistent away from resonance, and decline more slowly as A^{inc} increases for stacks with higher resonant frequencies. Consequently, high absorption is better retained at high frequencies as A^{inc} increases, where drag has less effect. The RAOs and absorption

decline more rapidly as A^{inc} increases when $C_d = 2$ (not shown), so that the solutions for $A^{\text{inc}} \in [0.01, 0.25]$ m when $C_d = 2$ are similar to $A^{\text{inc}} \in [0.01, 1]$ m with $C_d = 0.6$.

The average absorption is sensitive to C_d, as illustrated in Figure 5.7, and initially declines more rapidly as A^{inc} increases for higher C_d values. For example, almost half of the decline in absorption over $A^{\text{inc}} \in [0.01, 1]$ m when $C_d = 0.6$ occurs over $A^{\text{inc}} \in [0.01, 0.1]$ m when $C_d = 2$. The average absorption at $C_d = 2$ is shown to be virtually unchanged by altering the drag correction (Equation (5.7b)) to incorporate the relative velocity of each WEC (Equation (5.8)), given an appropriate, recalibrated $C_d^{\text{rel}} = 2.3$ is applied to the relative motion (§ 5.2.3).

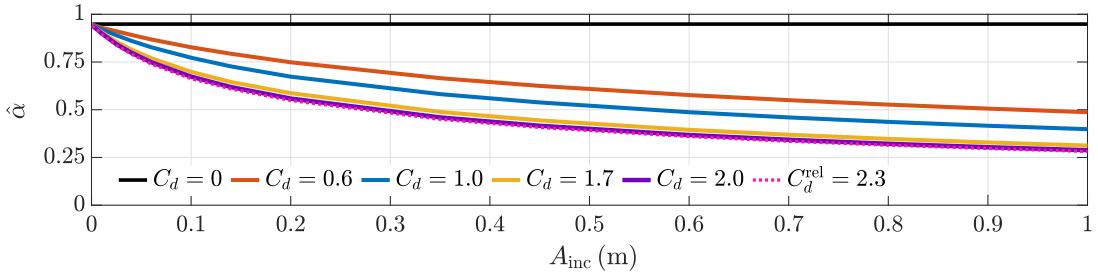

Figure 5.7: The average absorption $\hat{\alpha}$ of the graded array (Table 5.1) on $\omega \in [0.3, 0.65]\,\text{rad}\,\text{s}^{-1}$ decreases as the incident amplitude A^{inc} increases as a result of drag. Larger drag coefficients C_d accelerate the decline. Drag proportional to the relative velocity (C_d^{rel}) produces virtually equivalent $\hat{\alpha}$.

To contextualise the efficient, broadband absorption of the graded array, the absorption of uniform arrays (stacks tuned identically) is compared to the graded array in Figure 5.8 at selected incident wave amplitudes. The PTO parameters for the uniform arrays (Table 5.1) are optimal for a stack in isolation, and three different resonant frequencies ($\omega_0 = 0.3, 0.475$ and $0.65\,\text{rad}\,\text{s}^{-1}$, respectively) are selected to compare the performance across the target interval. The graded array achieves higher absorption across the target frequency interval, with the exception of $\omega \in [0.3, 0.32]\,\text{rad}\,\text{s}^{-1}$, where the uniform array tuned to $\omega_0 = 0.3\,\text{rad}\,\text{s}^{-1}$ reaches higher absorption from a combination of higher amplitudes and PTO damping.

Like the graded array, the amplifications of WEC motions at resonance in the uniform arrays decline as the incident amplitude increases and drag increasingly penalises larger motions, resulting in declining absorption, but broadened responses. Drag has relatively small influence away from resonance. Uniform arrays with a suitable combination of spacing and resonant frequency are able to utilise array resonances (from the spacing between rows) for a second peak in absorption (at $\omega \approx 0.45$ and $0.6\,\text{rad}\,\text{s}^{-1}$ in Figures 5.8b and c, respectively). However, the semi-constant absorption of uniform arrays tuned to $\omega_0 = 0.3$ and $0.475\,\text{rad}\,\text{s}^{-1}$ at $C_d = 2$ and $A^{\text{inc}} = 1$ m raises concerns as to the model validity, as WEC motions are amplified across the entire interval due to arguably excessive broadening from drag.

The drag correction penalises the graded array to a greater extent than a uniform array, as it is designed to sustain resonant conditions across the entire target interval, and does not

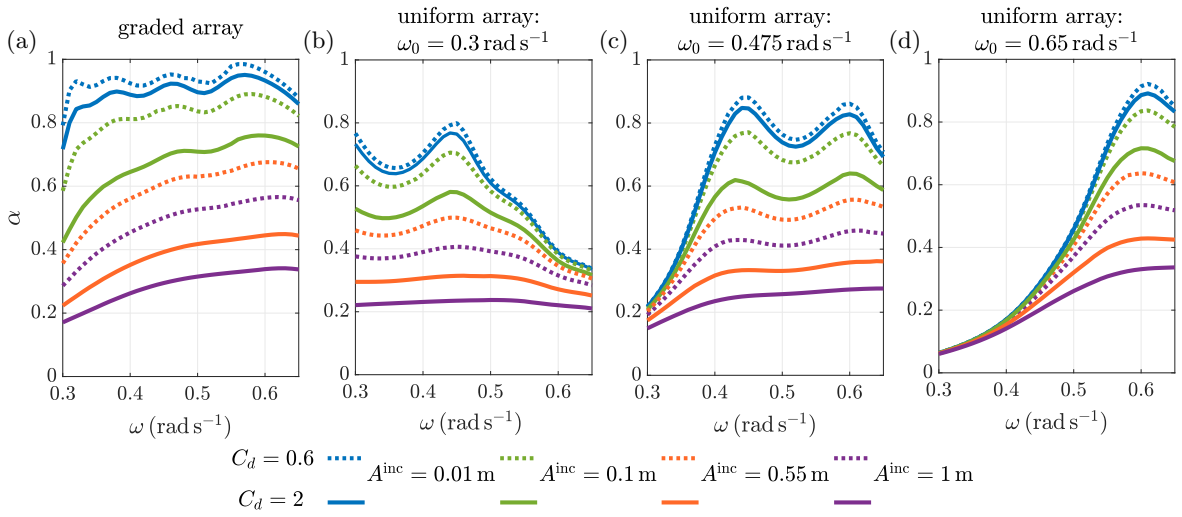

Figure 5.8: The absorption α of the (a) graded array is compared to uniform arrays tuned to (b) $\omega_0 = 0.3\,\mathrm{rad\,s^{-1}}$, (c) $\omega_0 = 0.475\,\mathrm{rad\,s^{-1}}$, and (d) $\omega_0 = 0.65\,\mathrm{rad\,s^{-1}}$ at $A^{\mathrm{inc}} = 0.01, 0.1, 0.55$, and $1\,\mathrm{m}$ when $C_d = 0.6$ (- - -) and $C_d = 2$ (——). General, α is higher and broader for the graded array at each A^{inc}, but initially declines more rapidly on $\omega \in [0.3, 0.4]\,\mathrm{rad\,s^{-1}}$ for $A^{\mathrm{inc}} \in [0.01, 0.1]\,\mathrm{m}$.

benefit from broadened responses, as the design ensures it is already sufficiently broad to cover the target interval. Resonant motions are similarly reduced in uniform arrays, but cover a smaller proportion of the target interval (non-resonant motions cover around one third of the interval, and are far less affected by drag), and the array benefits from broadened responses which helps buffer absorption losses. These differences are seen by comparing the declines in absorption over $A^{\mathrm{inc}} \in [0.01, 0.1]\,\mathrm{m}$ for $\omega \in [0.3, 0.4]\,\mathrm{rad\,s^{-1}}$ in Figures 5.8a, c and d.

To quantify the overall benefit to grading an array, the average absorptions of the graded and uniform arrays over the target frequency interval are compared in Figure 5.9 as the impact of drag increases with A^{inc}, for $C_d = 0.6$ and $C_d = 2$. Higher absorption at $C_d = 0.6$ is driven by larger WEC amplitudes. The benefit to grading an array gradually declines as the impact of drag increases, largely as a result of the disproportionate loss at low frequencies (Figure 5.8), and the broadened responses in the uniform arrays. The absorption of a uniform array tuned to $\omega_0 = 0.65\,\mathrm{rad\,s^{-1}}$ is determined solely by the stack resonance (not array resonances), and therefore remains narrower than the graded array (Figure 5.8). The ratios of the average absorption of the graded array to the uniform arrays rapidly attain a convergent-like state at both low and high C_d values, with a minimum of a 20% benefit obtained by grading.

The graded and uniform arrays experience breaching on the considered range of A^{inc} ($A^{\mathrm{inc}} \leq 1\,\mathrm{m}$). When breaching occurs, linear theory is no longer applicable, and an alternative model should be considered to cater for non-linear effects that arise. Consequently, the maximum incident wave amplitude is restricted to $A^{\mathrm{inc}} \leq 0.25\,\mathrm{m}$ when $C_d = 0.6$ ($A^{\mathrm{inc}} \leq 0.5\,\mathrm{m}$ when $C_d = 2$) to avoid breaching.

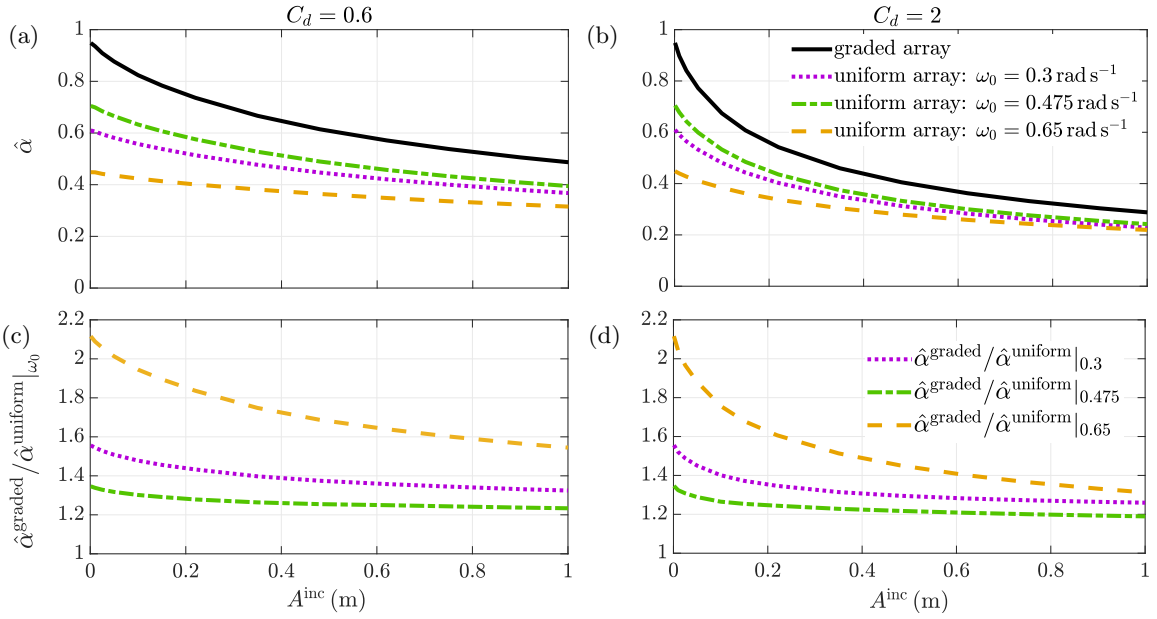

Figure 5.9: The average absorption $\hat{\alpha}$ of the graded array over the target interval $\omega \in [0.3, 0.65]\,\mathrm{rad\,s^{-1}}$ is compared to three different tunings of a uniform array when $C_d = 0.6$ in (a) and (c), and when $C_d = 2$ in (b) and (d). The relative benefit obtained by grading is illustrated in (c) and (d) using the ratio of $\hat{\alpha}$ for the respective arrays, with the grading increasing $\hat{\alpha}$ by 20–110% depending on A^{inc}.

5.4 Finite arrays

To generate practical designs for WEC-arrays, the infinite number of WECs in each stack is truncated to form a finite array. Good correspondence with the infinite, graded array is obtained with only a few WECs per row. This is illustrated in Figure 5.10 for an array of 30 WECs (PTO parameters in Table 5.1) and an incident wave amplitude of $A^{\mathrm{inc}} = 0.25\,\mathrm{m}$, when $C_d = 0.6$. The drag corrections reduce the amplified motions of WECs, located along the perimeter of the array, that arise from edge effects in the finite array. Edge effects are evident (e.g., at high frequency resonances in rows 2 and 3), but are proportionally smaller than the zero-drag model, especially at low frequencies where drag has a larger impact.

Equation (5.45) does not provide a suitable non-dimensionalised absorption for finite arrays, as $\chi \to 0$ is not generally associated with $|\zeta| \to 0$ (Evans, 1981b). Consequently, a relative capture width CW_{finite} is defined as the proportion of power in the incident waves that is captured, relative to the array width (JW_x/S) (McIver, 1994),

$$CW_{\mathrm{finite}} = \left[\frac{1}{2}\sum_{j=1}^{J} B^{j}_{\mathrm{PTO}}\,\omega^2\,|\zeta_j|^2\right] \Big/ \left[\frac{\omega}{4k_0}\left(1+\frac{2k_0h}{\sinh(2k_0h)}\right)|A^{\mathrm{inc}}|^2\,J\,W_x/S\right], \tag{5.47}$$

where S is the number of rows. Unlike Equation (5.45), CW_{finite} can exceed one, as the finite array captures energy that is incident upon its edges. The relative capture width encapsulates

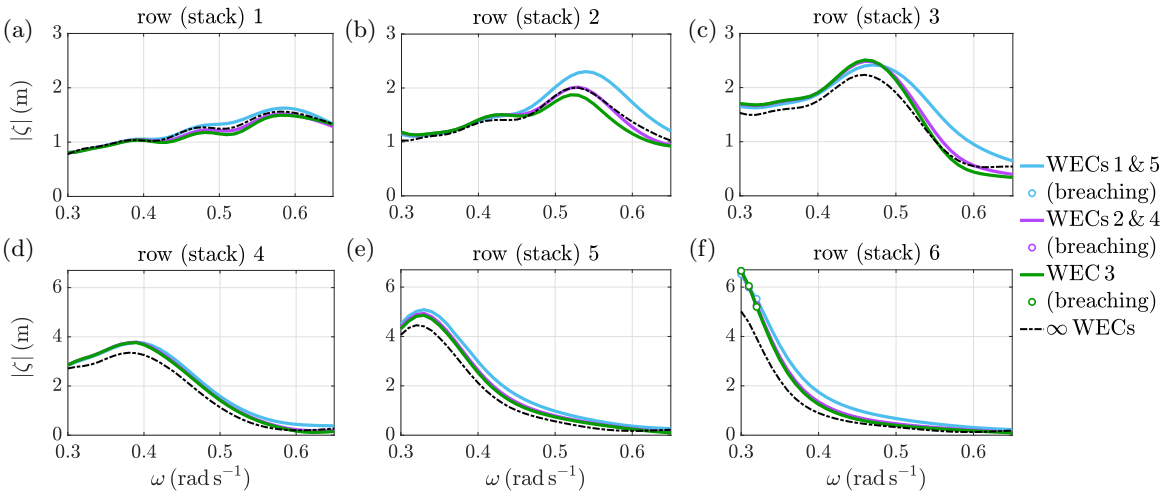

Figure 5.10: The amplitudes $|\zeta|$ (m) of the five WECs per row are shown in (a)–(f) for an incident wave with $A^{\text{inc}} = 0.25\,\text{m}$, when $C_d = 0.6$. Breaching is indicated by $\circ$, and is confined to $\omega \in [0.3, 0.32]\,\text{rad s}^{-1}$ in the sixth row. Higher $|\zeta|$ occur in the finite array, but closely resemble the behaviour of $|\zeta|$ in the infinite array (∞ WECs).

the key trends demonstrated by absorption, and the power capture of the finite array (in Figure 5.10) behaves similarly to the infinite array when $C_d = 0.6$, as shown in Figure 5.11.

As the incident wave angle decreases, increasingly many WECs in each row experience edge effects (not shown). This produces greater variation in the relative capture width, as illustrated in Figure 5.11 for three different wave directions and incident amplitudes. The individualised drag corrections disproportionately decrease the amplitudes of the low-frequency WECs, resulting in a greater decline in CW_{finite} at lower frequencies. As A^{inc} and/or C_d increases, less variation occurs (as $\chi \to 0$) as drag suppresses edge effects and amplified WEC motions to a greater extent. Generally, breaching occurs more frequently as $\chi \to 0$ due to edge effects.

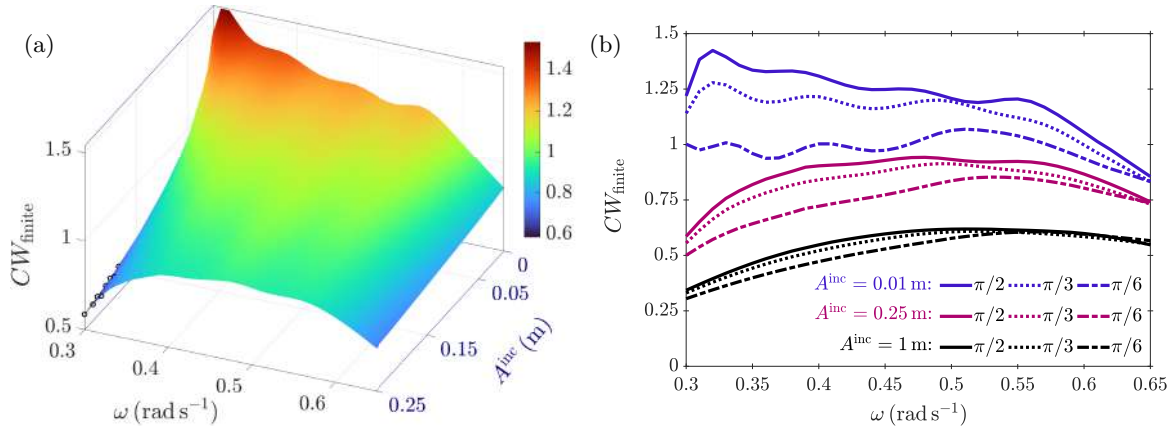

Figure 5.11: The relative capture width of the finite array CW_{finite} (a) demonstrates the same traits as α in Figure 5.6 as A^{inc} increases, when $C_d = 0.6$. Breaching events are indicated by $\circ$. As the incident wave direction decreases (b), CW_{finite} decreases, particularly at low frequencies and small incident amplitudes, where highly amplified WEC motions and edge effects are penalised by drag.

Comparisons between the relative capture widths of the graded and uniform arrays are shown in Figure 5.12. Unlike the graded array, the CW_{finite} of the uniform arrays demonstrates notable differences to the absorption of the corresponding infinite arrays (Figure 5.8). For consistency, the optimal tuning for a stack in isolation ($B_{\text{PTO}}^{\text{stack}}$) is applied to the finite uniform arrays. It is unlikely that this tuning is optimal for an array. However, $B_{\text{PTO}}^{\text{stack}}$ produces higher absorption than the optimal PTO damping for an isolated WEC ($B_{\text{PTO}}^{\text{buoy}} = b(\omega_0)$), which is commonly applied to uniform arrays in the literature (e.g., Child and Venugopal, 2010; Tokić and Yue, 2019), predominantly due to higher PTO damping (Appendix C.2).

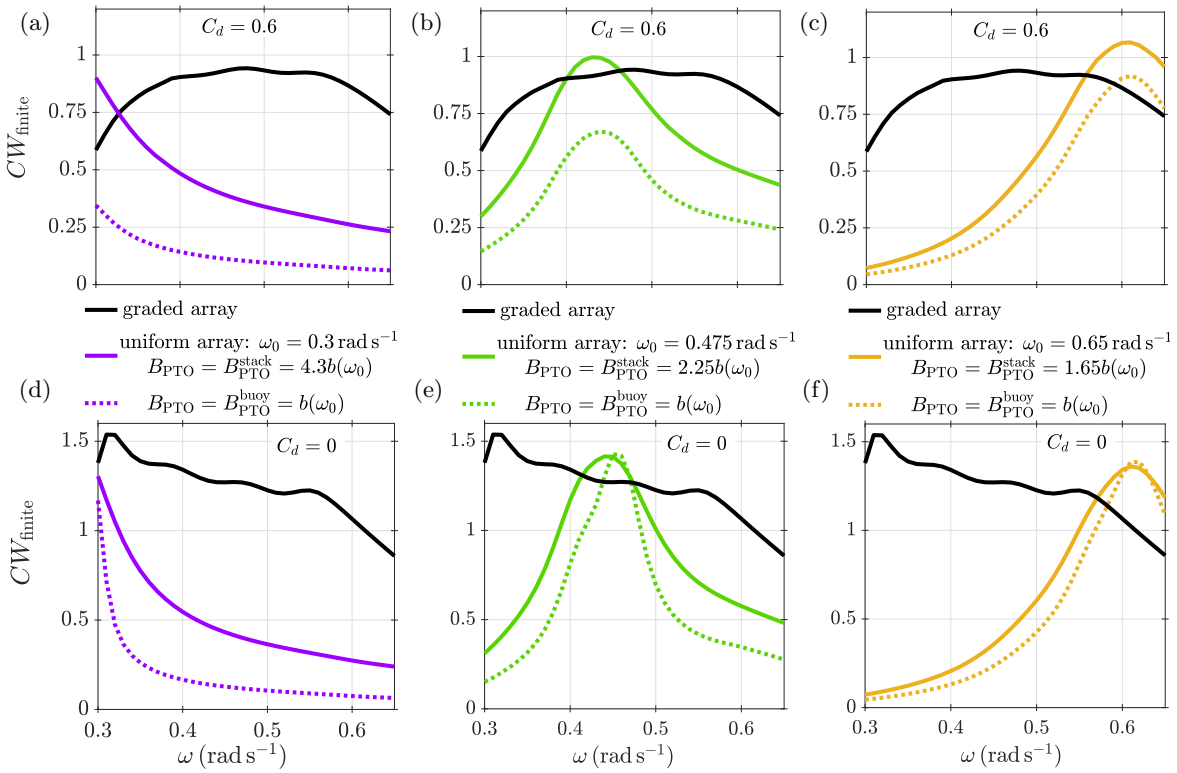

Figure 5.12: The relative capture width CW_{finite} of the finite graded array (black —) on the target interval $\omega \in [0.3, 0.65]\,\text{rad}\,\text{s}^{-1}$ is compared to uniform arrays tuned to (a) $\omega_0 = 0.3\,\text{rad}\,\text{s}^{-1}$, (b) $\omega_0 = 0.475\,\text{rad}\,\text{s}^{-1}$, and (c) $\omega_0 = 0.65\,\text{rad}\,\text{s}^{-1}$, when $C_d = 0.6$ and $A^{\text{inc}} = 0.25\,\text{m}$. The corresponding zero-drag solutions are shown in (d)–(f). The CW_{finite} of uniform arrays is depicted when the PTO damping is optimal for a stack in isolation (—; relative to the radiation damping of an isolated buoy), and when the PTO damping is optimal for a WEC in isolation (·····).

The uniform array tuned to $\omega_0 = 0.65\,\text{rad}\,\text{s}^{-1}$ behaves consistently with the corresponding infinite array (Figures 5.8d and 5.12c), aside from higher WEC motions in the finite array increasing the peak absorption. As ω_0 decreases, the finite uniform arrays increasingly deviate from the behaviour of the infinite arrays. The WEC amplitudes (not shown) are amplified so that the resonant peak in CW_{finite} exceeds that of the graded array (Figure 5.12), and display resonant motions present in the non-absorbing infinite array (as in Figure 5.4). Array

resonances are absent in the finite uniform arrays, which removes the potential for a second peak of efficient power capture (also true for zero-drag; Figures 5.12d–5.12f).

The appearance of array resonances in the finite uniform arrays depends on the number of WECs per row, and the strength with which rows reflect (Appendix C.2). For each additional WEC that is added to a row, the behaviour of the finite array better resembles the infinite array. A second peak in the relative capture width begins to emerge at ten WECs per row, but at 15 WECs per row, is still substantially smaller (approximately 20% lower; not shown) than the resonant peak, which becomes narrower and declines, reaching a comparable level to the graded array. The relative capture width of the graded array approaches the absorption of the corresponding infinite array as the number of WECs increase.

The broadband absorption generated by the rainbow absorbing, graded array outperforms the uniform arrays, and achieves higher efficiency over the majority of targeted frequencies. There is a greater benefit to grading at low incident amplitudes, as the responses of uniform arrays broaden substantially as the model becomes increasingly drag-dominated. In this regime, power capture becomes highly sensitive to the PTO damping. This is evident in Figure 5.12, where larger PTO damping broadens and raises CW_{finite} when $C_d = 0.6$ (less so at $\omega_0 = 0.65\,\text{rad}\,\text{s}^{-1}$, which experiences the least drag), compared to $C_d = 0$, where the peaks remain consistent. This behaviour is exacerbated by larger A^{inc} or $C_d = 2$ (Appendix C.2), but remains reasonable when restricting the incident amplitudes so as to prevent breaching.

5.5 Discussion and conclusions

A rainbow absorbing array of heaving buoys was shown to maintain broadband absorption when a drag correction to the WEC motions was incorporated in the model, which was otherwise based on linear theory. Amplified WEC motions were reduced as the incident wave amplitude increased, causing power capture to decline as an increasing amount of energy was dissipated by drag, but continued to support the underlying band structures responsible for broadband absorption. The average absorption over the target interval remained at least 20% higher than a uniform array. Restrictions on the incident amplitude were required to avoid breaching. The strategies transferred successfully to relatively small finite arrays, where the grading ensured broadband absorption with higher efficiency across the majority of the target interval when compared to three different tunings of a uniform array on the target interval.

The design of WECs is likely to ensure minimal drag (Guo and Ringwood, 2021), where a greater benefit can be derived by grading an array. However, breaching can become a concern due to substantially amplified motions. WECs which are stronger radiators require

lower amplitudes for high efficiency (Mei et al., 2005), so that larger WECs, and deeper draughts, are more likely to reduce breaching occurrences. Similarly, a closer within-row spacing (W_x) strengthens reflective properties. A uniform tuning will inherit the same properties (stronger reflection broadens responses), so that the benefit to grading will not necessarily improve. However, deeper draughts will narrow the resonance bandwidth (Falnes and Hals, 2012; Ruezga and Cañedo C., 2020), requiring additional rows for low transmission over a broad frequency range. Similar arguments are likely to apply to different WEC concepts.

In addition to ensuring efficient, broadband absorption over two thirds of usable ocean wave frequencies, the rainbow absorbing array lowers transmission appreciably in an appropriate parameter regime, which is generally considered to be a mark of coastal protection capability in the literature (Boodoo et al., 2025). In contrast, uniform arrays achieve low transmission at the expense of power capture for frequencies lying in bandgaps (wave shadowing inhibits power generation), while the wavefield can be amplified outside this frequency range. Optimising the grading will improve capture as the PTO parameters were determined for zero drag.

Small changes to the PTO damping can have a sizeable effect on power capture (e.g., compared to altered spacing or tuning), and given the uncertainties associated with the drag model, it is unclear whether or not this artificially inflates power. To draw concrete conclusions, it may be preferable to adopt a more complex model which captures hydrodynamic and other non-linearities, including from the PTO mechanism and mooring, which influence power capture (Folley, 2016; Wolgamot and Fitzgerald, 2015). Similarly, implementing constraints on allowable WEC motions to prevent breaching is necessary to assess the effectiveness of graded arrays at higher incident amplitudes.

In conclusion, we have shown that relatively small arrays of heaving buoys can achieve efficient, broadband absorption by grading their resonant properties using fixed PTO parameters. In general, a closer spacing between WECs and lower incident amplitudes support greater efficiency over broader frequency and directional bands. The design remains effective outside of these conditions, but the benefit gained through grading reduces as WEC motions become increasingly restricted by drag effects. However, the grading ensures efficient capture over two thirds of usable ocean wave frequencies, without dynamic tuning of the PTOs.

Chapter 6

Conclusions

Arrays of heaving buoys were designed for high efficiency power capture over broad frequency and directional bands by grading their resonant properties using attached PTO mechanisms. Linear theory and semi-analytic methods were applied to generate the rainbow absorbing design, which demonstrated efficient, broadband absorption over two thirds of usable ocean wave frequencies using fixed PTO parameters, and was robust to a drag correction. The frequency range coincides with storm swells associated with erosion, so that the properties of the array design have the potential to support coastal protection, which will enhance economic viability. The grading of arrays was shown to be a promising and robust strategy for broadband absorption, without requiring dynamic control based on short-term forecasts.

6.1 Summary of results

An understanding into the mechanisms underlying the ability to generate near-perfect, broadband absorption by grading arrays of heaving buoys was developed using a 2D model. The resonances were manipulated to create destructive interference for control over transmission, and the PTO damping was chosen to harness localised amplifications, capturing reflected wave energy. The strong reflection of 2D WECs proved effective for achieving broadband absorption with over 99% efficiency, but created strong hydrodynamic interactions between WECs that complicated the identification of appropriate PTO parameters. An analysis of the complex-valued reflection and transmission coefficients attributed the interactions to resonances from the second passband (governed by the spacing) restricting the target interval, causing closely spaced pole–zero pairs to interfere with one another and alter the resonant properties of WECs. The closer the spacing between WECs, the broader the frequency range that can be targeted.

To apply the concepts for rainbow absorption to a 3D model, infinitely many 3D WECs were periodically arranged to form (a finite number of) stacks. The spacing was chosen to ensure 2D propagation in the far field over the target interval and incident wave directions considered, and to control reflection properties for the effective manipulation of band structures. The computationally efficient formulation facilitated the development of strategies for broadband absorption, which achieved an average absorption exceeding 90% over a wide range of wave

directions, without optimisation. The PTO parameters were shown to generate rainbow absorption in finite arrays, leading to the efficient capture of directionally spread spectra with peak periods covering two thirds of usable frequencies, and outperforming uniform arrays tuned to the peak period of each incoming spectrum.

Rows of 3D WECs are weaker reflectors than 2D WECs, and allow for the relaxation of strict spatial constraints due to the absence of strong interactions between WECs and array resonances. For example, a spacing comparable to half of the WEC length was required in 2D, whereas spacings up to four times the WEC diameter remained effective in 3D. As the spacing within a row widens, more power is available to the array, but transmission rises, and the number of rows must increase to regain high efficiency. However, the WEC amplitudes increase to compensate for weaker reflection at wider spacings within a row.

The amplified WEC motions (relative to the incident wave amplitude) at resonance violate the assumptions of linear theory (WEC motions are smaller than WEC dimensions (Molin, 2023)) if not restricted to very small incident amplitudes (steepness $kA \ll 1$ (Mei et al., 2005)). The inclusion of a drag correction in the 3D model reduced amplifications around resonance as the incident amplitude increased, extending the range of incident amplitudes on which solutions remain valid, but impacted the reflection and transmission of the array. Generally, low transmission was well-maintained, with the exception of low frequencies, where sufficiently large WEC motions were not supported. However, the reflected wave energy decreased as the incident amplitude increased, which reduced the power available for capture. Consequently, the grading maintained broadband absorption over a range of wave directions, but efficiency was reduced. The grading improved efficiency by at least 20% compared to uniform arrays, in which the PTO was chosen to be optimal for a stack in isolation.

6.2 Key findings, significance and contribution

The spacing in a graded array is critical to achieving efficient, broadband absorption. To enhance the effectiveness of strategies, it is recommended that the spacing between WECs is kept as small as possible, noting that a maximum spacing will exist, beyond which the grading will lose effectiveness. The number of rows, and WECs within a row, required to produce high efficiency power capture will depend on the strength of reflection, which is determined by the resonance bandwidth of WECs and spacing within a row. The stronger the reflection, the fewer rows required for broadband absorption. The spacing between rows controls the location of Bragg resonance, and will determine whether array resonances encroach on the target interval. The grading can be extended to cover the Bragg bandgap, but power capture will drop over the frequency range associated with the array resonances. The wider the spacing, the further down the targeted interval the loss will occur.

A relatively close, or compact spacing, works to the advantage of rainbow absorption and has cost and coastal protection benefits. In particular, compact spacing is recommended on the basis of the economic cost associated with infrastructure and efficiency relative to ocean area (Engström et al., 2013; Göteman et al., 2020). To meet economic objectives, multi-row arrays that are sub-optimal for power capture, can be preferable (David et al., 2022) due to the economic cost associated with the large spacings recommended to limit destructive interactions for maximum power capture (Babarit, 2013; Teixeira-Duarte et al., 2022). Additionally, multi-row arrays and compact spacing are better at decreasing transmission, which is typically used to indicate coastal protection capability (Boodoo et al., 2025).

Strategies for broadband absorption contribute to the understanding of how to design arrays for high efficiency in dynamic ocean conditions while also serving to help protect vulnerable coastlines by reducing transmitted wave energy. Significantly, and perhaps counter-intuitively to much of the wave energy literature, the strategies demonstrate that destructive interactions generated in local bandgaps can be utilised to the overall benefit of the array by manipulating the underlying band structures through the resonant properties of WECs. There is a substantial advantage to grading arrays when the conditions on the spacing and incident amplitude can be adhered to, which perform efficiently without requiring dynamic control based on short-term forecasts across changing wave conditions.

Experimental and CFD validation of rainbow effects by non-absorbing arrays of graded resonators (Cao, Chen, Ning, Peng, Xu and Lin, 2025; Hu et al., 2025) suggest that the concepts are robust to non-linear effects. The rainbow absorption generated by an array of heaving buoys was shown to be robust to drag, which is one of the most relevant sources of non-linearity for heaving buoys in operational conditions (Giorgi and Ringwood, 2017). The reduction of WEC amplitudes by drag reduces power capture, similarly to motion constraints in the literature. However, the absorption of graded arrays remains broadband and insensitive to the wave direction, in contrast with much of the literature. Therefore, strategies to grade arrays of heaving buoys may have wider applicability, prompting further research to address limitations, experimentally validate solutions, and examine the factors that are most likely to impact efficiency.

6.3 Limitations and future work

The model assumed an idealised fluid, governed by linear potential-flow theory, to facilitate a theoretical understanding of the various facets underlying a successful grading of a WEC-array. However, non-linear effects became relevant with large, amplified WEC motions at resonance. The simplified drag correction that was incorporated to approximate these effects, is associated with much uncertainty, and requires a more complex hydrodynamic model to

ascertain whether substantial broadening of resonance bandwidths as the incident amplitude increases is physical. Notably, Morison's equation assumes that hydrodynamically transparent structures ($2L/\lambda < 0.2$) produce negligible scattering (Clauss et al., 1992). This assumption is violated by resonant WECs (with $2L/\lambda \ll 0.2$ in this study) which can significantly perturb the wavefield, as is more typical of large offshore structures ($2L/\lambda > 0.2$) where drag is usually considered to be negligible (Sarpkaya, 2010). Although Morison's drag correction is often incorporated in models based on linear radiation-diffraction theory (e.g., see Molin, 2023), the applicability to WECs (i.e., in a regime where both scattering and drag are important) is still largely under-explored. Further, restrictions on realistic PTO forces may be required to prevent PTO damping values which artificially inflate power capture when drag is included in the model. Once these limitations are addressed, the benefit to grading could be assessed by comparing optimised arrays (layouts and PTO) to optimally graded arrays.

Heaving buoys were modelled as truncated cylinders to facilitate the use of efficient, semi-analytical methods. However, realistic geometries are likely to utilise hemispherical bases for the buoys to minimise drag. Lower drag improves power capture, as localised amplifications in graded arrays are less degraded. While the number of rows and spacing can be adjusted for different resonant properties (from a different geometry) to generate an effective grading, breaching could potentially become a greater issue. Consequently, physical constraints on WEC motions are critical to investigating the performance of arrays at higher incident amplitudes, within the operational range of WECs. Similarly, mooring forces can influence power capture and should be incorporated in future models (Wolgamot and Fitzgerald, 2015). WEC concepts or geometries which increase the radiation damping so that the WEC radiates more efficiently with lower amplitudes (Mei et al., 2005) could also be investigated (e.g., Edwards et al., 2025; Edwards and Yue, 2022).

Although passive gradings were generated, the arrays retain the ability to be retuned, which opens up the possibility of combining strategies for grading with dynamic control. The underlying principles could inform geometric grading in control co-design (e.g., Ermakov et al., 2025), or be applied to smaller arrays with fewer rows, to target a narrower frequency band, while using dynamic retuning to adjust for altered wave conditions. Dynamic control would further facilitate different modes of operation. For example, the grading could be chosen to target frequencies appropriate for power capture in one mode, and be adjusted to target frequencies damaging to coastlines in a second mode, depending on the sea state.

6.3.1 Applications to coastal protection

The PTO parameters which create broadband absorption in arrays of heaving buoys, do so by minimising reflection and transmission over targeted frequencies. Consequently, the

rainbow absorbing array simultaneously addresses the goal of coastal protection. The ability to deliver both functions in a single mode of operation, depending on the targeted frequencies, departs from recent literature (e.g., Cui et al., 2024) where compromises between the two functions are suggested depending on the sea state, as maximising power does not align with coastal protection (Battisti et al., 2024). Importantly, the graded arrays address several issues highlighted by Cohen (2025) in an experimental investigation of coastal protection by WEC arrays. Namely, power capture is associated with appropriate transmission behaviour for coastal protection in graded arrays, avoiding the requirement for separate modes of operation which could instigate sediment transport, and high power capture is maintained across the frequency range, despite several rows in the array (Cohen, 2025). Further, the spacing could be selected to extend the frequency range for coastal protection using Bragg resonance.

The premise for coastal protection assumes low transmission is sufficient to predict shoreline response. However, sediment accretion requires a threshold reduction in wave height to be reached, failing which, offshore migration of sediment can occur as a result of nearshore currents generated by the array (Cohen, 2025). Changing circulation patterns induced by arrays will have nearshore implications (Cao, Shi, Zheng, Zhang and Pan, 2025; Cui et al., 2026) which are altered by the sea state, and should be analysed to understand the impact WEC arrays will have on coastal processes (Cohen, 2025). Consequently, future work should seek to model and explore the impact of arrays on coastal processes to understand the coastal protection capabilities of rainbow absorbing arrays.

6.3.2 Concluding remarks

After 50 years of research, WECs are entering a pre-commercial stage of technological readiness, as demonstrations of full-scale prototypes in operational conditions transition to pilot arrays (Arrosyid et al., 2025; IRENA and OEE, 2023; Ocean Energy Europe, 2025). Arrays capable of efficiently harnessing ocean wave energy at a commercial scale would help diversify the renewable energy mix and meet growing energy demands in conjunction with emissions targets. Strategies to grade arrays for rainbow absorption based on linear theory, deliver efficient broadband absorption that is robust to wave direction, without optimisation or dynamic control. The array properties lend themselves to the prospect of providing coastal protection to vulnerable coastlines which would enhance economic viability, with the potential for expanded functionality through dynamic control. These promising results argue for pursuing strategies to grade arrays in further investigations, with increased model complexity.

Appendix A

2D model: Single cell problem and convergence results

A.1 Scattering matrix for the single cell problem

The wavefield in cell n (subscript omitted for ease of notation) is obtained by solving separate diffraction ($^{\mathrm{d}}$) and radiation ($^{\mathrm{r}}$) sub-problems, which are combined to return the full wavefield $\phi = \phi^{\mathrm{d}} + \xi^h \phi^{\mathrm{r}}$. The unknown coefficients in the diffraction problem are determined by truncating the eigenfunction expansions at M modes and applying kinematic and dynamic boundary conditions at the interfaces between regions, namely

$$\phi_i^{\mathrm{d}} = \phi_{i+1}^{\mathrm{d}} \quad \text{and} \quad \frac{\partial \phi_i^{\mathrm{d}}}{\partial x} = \frac{\partial \phi_{i+1}^{\mathrm{d}}}{\partial x} \quad \text{at } x = \pm L \quad \text{for } i = 1, 2. \tag{A.1}$$

Multiplying by an appropriate test function and integrating over depth produces a system of equations for the unknown diffraction coefficients in terms of prescribed incident waves

$$\begin{bmatrix} \boldsymbol{a}^-{}_{\mathrm{d}} \\ \boldsymbol{b}^+{}_{\mathrm{d}} \\ \boldsymbol{\alpha}^+{}_{\mathrm{d}} \\ \boldsymbol{\alpha}^-{}_{\mathrm{d}} \end{bmatrix} = \begin{bmatrix} \boldsymbol{R}^{\mathbf{d}} & \boldsymbol{T}^{\mathbf{d}} \\ \boldsymbol{T}^{\mathbf{d}} & \boldsymbol{R}^{\mathbf{d}} \\ \boldsymbol{G}^{\mathbf{d}} & \boldsymbol{H}^{\mathbf{d}} \\ \boldsymbol{H}^{\mathbf{d}} & \boldsymbol{G}^{\mathbf{d}} \end{bmatrix} \begin{bmatrix} \boldsymbol{a}^+ \\ \boldsymbol{b}^- \end{bmatrix}. \tag{A.2}$$

The vectors $\boldsymbol{\alpha}^{\pm}{}_{\mathrm{d}}$ contain the coefficients corresponding to the potential underneath the WEC (Region 2),

$$\phi_2^{\mathrm{d}} = \alpha_0^{\mathrm{d}-} + \alpha_0^{\mathrm{d}+} x + \sum_{m=1}^{\infty} \left(\alpha_m^{\mathrm{d}+} e^{\mathrm{i}\kappa_m (x+L)} + \alpha_m^{\mathrm{d}-} e^{-\mathrm{i}\kappa_m (x-L)} \right) \frac{\cosh(\kappa_m (z+h))}{\cosh(\kappa_m (h-L))}, \tag{A.3}$$

where $\kappa_m = \mathrm{i} m\pi/(h-d)$ are purely imaginary wavenumbers. Assuming unit heave amplitude ($\xi^h = 1$), the radiation potentials in Regions 1 and 3,

$$\phi_1^{\mathrm{r}} = \sum_{m=0}^{\infty} (a_m^{\mathrm{r}-} e^{-\mathrm{i}k_m (x+L)}) \frac{\cosh(k_m (z+h))}{\cosh(k_m h)} \tag{A.4}$$

$$\phi_3^{\mathrm{r}} = \sum_{m=0}^{\infty} (b_m^{\mathrm{r}+} e^{\mathrm{i}k_n (x-L)}) \frac{\cosh(k_m (z+h))}{\cosh(k_m h)}, \tag{A.5}$$

are obtained analogously to the diffraction potential. Underneath the WEC, ϕ_2^{r} is composed of a homogeneous and particular solution which satisfies the boundary condition $\partial_z\phi = \xi^h\omega^2/g$,

$$\phi_2^{\mathrm{r}} = \alpha_0^{\mathrm{r}-} + \alpha_0^{\mathrm{r}+}x + \sum_{m=1}^{\infty}\left(\alpha_m^{\mathrm{r}+}e^{\mathrm{i}\kappa_m(x+L)} + \alpha_m^{\mathrm{r}-}e^{-\mathrm{i}\kappa_m(x-L)}\right)\zeta_m + \frac{\omega^2}{2g(h-L)}\left[(z+h)^2 - x^2\right]. \tag{A.6}$$

To determine the unknown heave amplitude (Equation (3.10)), the hydrodynamic forcing is found by integrating the pressure over the wetted surface of the body S_B, with respect to the outward pointing unit normal to the surface of the body,

$$\rho g\int_{S_B}\phi n\mathrm{d}S = \underbrace{\rho g\int_{S_B}\phi^{\mathrm{d}}n\mathrm{d}S}_{\text{excitation force}} + \underbrace{\rho g\int_{S_B}\xi^h\phi^{\mathrm{r}}n\mathrm{d}S}_{\text{radiation component}}. \tag{A.7}$$

The radiation component resulting from forced oscillations of the body is separated into real and imaginary parts in phase with the acceleration and velocity of the body, respectively, to give the added mass and radiation damping (Linton and McIver, 2001; Mei et al., 2005)

$$\left[\omega^2 a(\omega) + \mathrm{i}\omega b(\omega)\right]\xi^h = \rho g\left(\int_{S_B}\xi^h\phi^{\mathrm{r}}n\mathrm{d}S\right). \tag{A.8}$$

The excitation force F produces a vertical force at the underside of the WEC which depends on the coefficients of the incident waves, and therefore, interactions within the array. This dependence is incorporated in the initial scattering matrix of a WEC by expressing the excitation force in the radiation problem in terms of the incident amplitudes,

$$\int_{S_B}\phi^{\mathrm{d}}n\mathrm{d}S = \boldsymbol{V}^+\boldsymbol{\alpha}_{\mathbf{d}}^+ + \boldsymbol{V}^-\boldsymbol{\alpha}_{\mathbf{d}}^- \tag{A.9}$$

$$= \left[\boldsymbol{V}^+\boldsymbol{G}^{\mathbf{d}} + \boldsymbol{V}^-\boldsymbol{H}^{\mathbf{d}}\right]\boldsymbol{a}^+ + \left[\boldsymbol{V}^+\boldsymbol{H}^{\mathbf{d}} + \boldsymbol{V}^-\boldsymbol{G}^{\mathbf{d}}\right]\boldsymbol{b}^-, \tag{A.10}$$

where $\boldsymbol{V}^{\pm}$ are vectors with $M+1$ elements. From Equation (3.10), the heave amplitude is

$$\xi^h(\omega) = \left[-\omega^2\left(\mathcal{M} + a(\omega)\right) - \mathrm{i}\omega(b(\omega) + b^{\mathrm{PTO}}) + (c + c^{\mathrm{PTO}})\right]^{-1}F(\omega) \tag{A.11}$$

$$= \hat{\boldsymbol{V}}^+\boldsymbol{a}^+ + \hat{\boldsymbol{V}}^-\boldsymbol{b}^-. \tag{A.12}$$

The scattering matrix $\boldsymbol{S}$ in (3.18) for the heaving buoy is

$$\boldsymbol{S} = \boldsymbol{S}^{\mathbf{d}} + \boldsymbol{S}^{\mathbf{r}} = \begin{bmatrix}\boldsymbol{R}^{\mathbf{d}} + \boldsymbol{a}^-{}_{\mathrm{r}}\hat{\boldsymbol{V}}^+ & \boldsymbol{T}^{\mathbf{d}} + \boldsymbol{a}^-{}_{\mathrm{r}}\hat{\boldsymbol{V}}^- \\ \boldsymbol{T}^{\mathbf{d}} + \boldsymbol{b}^+{}_{\mathrm{r}}\hat{\boldsymbol{V}}^+ & \boldsymbol{R}^{\mathbf{d}} + \boldsymbol{b}^+{}_{\mathrm{r}}\hat{\boldsymbol{V}}^-\end{bmatrix}, \tag{A.13}$$

with the corresponding coefficients in Equation (3.16) given by $a_m^- = a_m^{\mathrm{d}-} + \xi^h a_m^{\mathrm{r}-}$ and $b_m^+ =$

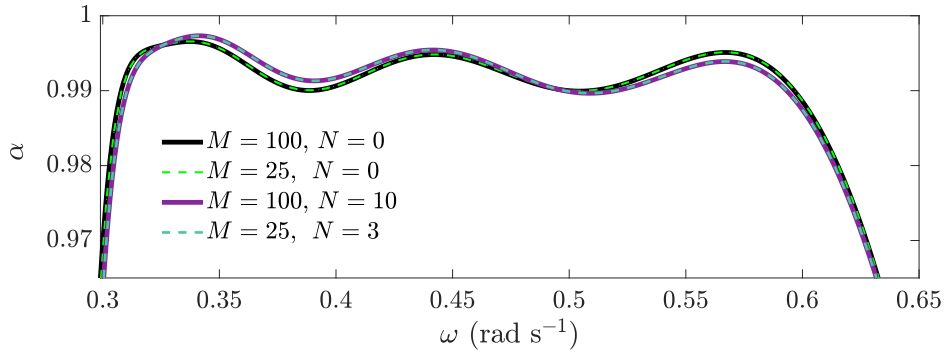

Figure A.1: The absorption of the graded array of five WECs in Table 3.2 is shown for combinations of the truncation M in the single body problem, and the number of evanescent modes N included in WEC interactions. While sufficient evanescent modes are included in the single body problem for convergence of the final solution, the wide-spacing approximation ($N = 0$) incurs a small error in the average absorption of 0.0001.

$b_m^{\mathrm{d}+} + \xi^h b_m^{\mathrm{r}+}$. The multiple scattering routine resolves the coupling between WECs, and the forces on a particular WEC can be recovered from Equation (A.10).

A.2 Convergence results

The truncation of $M = 25$ was determined based on the convergence of the WEC amplitudes and scattering coefficients in the single cell problem. Higher truncation values produce indistinguishable solutions (converged to four decimal places), as illustrated in Figure A.1 where the absorption for the array of five WECs in Table 3.2 with $M = 25$ evanescent modes is compared to the absorption when $M = 100$ evanescent modes are included. Here, N refers to the number of evanescent modes included in WEC interactions, with $N = 0$ indicating the wide-spacing approximation is applied to the array. The solution obtained when including evanescent modes ($N > 0$) in WEC interactions is overlaid to further justify the use of the wide-spacing approximation. The average absorption of the array increases from $\hat{\alpha} = 0.9900$ to $\hat{\alpha} = 0.9901$ with the inclusion of evanescent modes. Only $N = 3$ evanescent modes are required for convergence (solution is unchanged for larger truncation values, e.g., $N = 10$ with $M = 100$ in Figure A.1). The error incurred was deemed to be acceptably small so as to motivate the reduced computational effort associated with the wide-spacing approximation.

Appendix B

3D model: Solution methods and the influence of spacing

B.1 Single cell problem: Truncated cylinder

The diffraction and radiation problems are individually solved using separation of variables, subject to the respective boundary conditions (Equation (4.13)) on the wetted surface of the WEC, and are combined to return the full wavefield

$$\varphi(r,\theta,z) = \varphi^{\text{inc}}(r,\theta,z) + \varphi^{\text{diff}}(r,\theta,z) + \zeta\varphi^{\text{rad}}(r,\theta,z). \tag{B.1}$$

The fluid domain is divided into an interior ($r \leq L$) and exterior region ($r \geq L$) about the interface $r = L$, at the sides of the WEC (cylinder's radius). In the exterior region ($^{\text{E}}$),

$$\varphi^{\text{E}} = \sum_{n=0}^{\infty} Z_n(z) \sum_{\mu=-\infty}^{\infty} \left[A_{n\mu} I_\mu(\kappa_n r) + \hat{D}^{\text{diff}}_{n\mu} \frac{K_\mu(\kappa_n r)}{K_\mu(\kappa_n L)} \right] \mathrm{e}^{\mathrm{i}\mu\theta} + \zeta \sum_{n=0}^{\infty} Z_n(z) \hat{D}^{\text{rad}}_{n0} \frac{K_0(\kappa_n r)}{K_0(\kappa_n L)}, \tag{B.2}$$

where I_μ and K_μ are modified Bessel functions of the first and second kind, respectively, and of order μ, and κ_n are defined as $\kappa_n = -\mathrm{i}k_n$, $n \in \mathbb{Z} \geq 0$. The known amplitudes associated with the ambient incident wave are denoted $A_{n\mu}$. The unknown diffraction $\hat{D}^{\text{diff}}_{n\mu}$ and radiation $\hat{D}^{\text{rad}}_{n0}$ coefficients are normalised against the cylinder's sides. There is no angular dependence ($\mu = 0$) in the radiation problem, as heave radiation is symmetric. In the interior region ($^{\text{I}}$),

$$\varphi^{\text{I}} = \sum_{n=0}^{\infty} \mathcal{Z}_n(z) \sum_{\mu=-\infty}^{\infty} d^{\text{diff}}_{n\mu} \frac{I_\mu(\varkappa_n r)}{I_\mu(\varkappa_n L)} \mathrm{e}^{\mathrm{i}\mu\theta} + \zeta \left[\sum_{n=0}^{\infty} \mathcal{Z}_n(z)\, d^{\text{rad}}_{n0} \frac{I_0(\varkappa_n r)}{I_0(\varkappa_n L)} + \frac{\omega^2 \left[(z+h)^2 - r^2/2 \right]}{2g(h-L)} \right], \tag{B.3}$$

where $d^{\text{diff}}_{n\mu}$ and d^{rad}_{n0} are the unknown coefficients in the diffraction and radiation problems, respectively. The last term is the particular solution in the radiation problem, which satisfies the boundary condition (Equation 4.13b) on the WEC. The vertical eigenfunctions are given by

$$\mathcal{Z}_n(z) = \frac{\cosh(\mathrm{i}\varkappa_n(z+h))}{\cosh(\mathrm{i}\varkappa_n(h-L))} \quad \text{for} \quad \varkappa_n = \frac{n\pi}{h-L}. \tag{B.4}$$

Truncating the infinite summations at $n = N-1$ and $\mu = \pm U$ modes (sufficient for convergence), a diffraction transfer matrix $\boldsymbol{B}$ is defined such that $(\boldsymbol{D}^{\text{diff}} + \zeta \boldsymbol{D}^{\text{rad}}) = \boldsymbol{BA}$ for a given incident wave with amplitudes contained in the vector $\boldsymbol{A}$, where the elements

of $\left[\boldsymbol{D}^{\text{diff}} + \zeta \boldsymbol{D}^{\text{rad}}\right]_{n\mu} = \left(\hat{D}^{\text{diff}}_{n\mu} + \zeta \hat{D}^{\text{rad}}_{n\mu}\right)/K_\mu(\kappa_n L)$ are generated from the as yet unknown diffraction and radiation coefficients of the scattered potential,

$$\varphi^{\text{scat}} = \sum_{n=0}^{N-1} Z_n(z) \sum_{\mu=-U}^{U} \left[\hat{D}^{\text{diff}}_{n\mu} + \zeta \hat{D}^{\text{rad}}_{n\mu}\right] \frac{K_\mu(\kappa_n r)}{K_\mu(\kappa_n L)} \mathrm{e}^{\mathrm{i}\mu\theta}, \quad \text{where } \hat{D}^{\text{rad}}_{n\mu} = 0 \; \forall \; \mu \neq 0. \tag{B.5}$$

The eigenfunction expansion matching method is used to determine the unknown coefficients by enforcing continuity of pressure and horizontal velocity at the interface $r = L$ between the interior φ^{I} and exterior φ^{E} regions (Linton and McIver, 2001),

$$\varphi^{\text{E}} = \varphi^{\text{I}} \qquad \text{on } z \in (-h, -L) \tag{B.6}$$

$$\frac{\partial \varphi^{\text{E}}}{\partial r} = \begin{cases} \dfrac{\partial \varphi^{\text{I}}}{\partial r} & \text{for} \quad z \in (-h, -L), \\ 0 & \text{for} \quad z \in (-L, 0). \end{cases} \tag{B.7}$$

Systems of equations for the unknown coefficients are obtained by multiplying equations (B.6) and (B.7) by the test function $\mathcal{Z}_m$ and integrating over $z \in (-h, -L)$ and $z \in (-h, 0)$ respectively. In the diffraction problem, the resulting system of equations is given by

$$\begin{aligned} \sum_{n=0}^{N-1} \sum_{\mu=-U}^{U} \left[\mathcal{A}_{mn} d^{\text{diff}}_{n\mu} \mathrm{e}^{\mathrm{i}\mu\theta} - \mathcal{B}_{mn} \hat{D}^{\text{diff}}_{n\mu} \mathrm{e}^{\mathrm{i}\mu\theta}\right] &= \sum_{n=0}^{N-1} \sum_{\mu=-U}^{U} \mathcal{B}_{mn} A_{n\mu} I_\mu(\kappa_n L) \mathrm{e}^{\mathrm{i}\mu\theta} \\ \sum_{n=0}^{N-1} \sum_{\mu=-U}^{U} \left[\mathcal{B}_{mn} \varkappa_n d^{\text{diff}}_{n\mu} \frac{I'_\mu(\varkappa_n L)}{I_\mu(\varkappa_n L)} - \mathcal{F}_{mn} k_n \hat{D}^{\text{diff}}_{n\mu} \frac{K'_\mu(\kappa_n L)}{K_\mu(\kappa_n L)}\right] &= \sum_{n=0}^{N-1} \sum_{\mu=-U}^{U} \mathcal{F}_{mn} k_n A_{n\mu} I'_\mu(\kappa_n L), \end{aligned} \tag{B.8}$$

where the $(m, n)^{\text{th}}$ element of the $M \times N$ matrices $\mathcal{A}, \mathcal{B}$ and $\mathcal{F}$ are, respectively,

$$\mathcal{A}_{mn} = \int_{-h}^{-d} \mathcal{Z}_m \mathcal{Z}_n \mathrm{d}z, \quad \mathcal{B}_{mn} = \int_{-h}^{-d} \mathcal{Z}_m Z_n \mathrm{d}z, \text{ and } \mathcal{F}_{mn} = \int_{-h}^{0} Z_m Z_n \mathrm{d}z. \tag{B.9}$$

The diffraction transfer matrices relating the incident and scattered waves in the interior ($\boldsymbol{B}^{\text{int}}$) and exterior ($\boldsymbol{B}^{\text{diff}}$) regions, are retrieved from $[\boldsymbol{d}^{\text{diff}} \; \boldsymbol{D}^{\text{diff}}]^T = [\boldsymbol{B}^{\text{int}} \; \boldsymbol{B}^{\text{diff}}]^T [\boldsymbol{A} \; \boldsymbol{A}]^T$. For each Fourier mode μ, the $(m, n)^{\text{th}}$ term for $m, n = 1, 2, \ldots N$ is defined by

$$\boldsymbol{B}^{\text{diff}}_\mu = (B_{mn}) = \left(\frac{K'_\mu(\kappa_n L)}{K_\mu(\kappa_n L)} \mathcal{F}_{mn}\right)^{-1} \left(\frac{\varkappa_n}{k_n} \frac{I'_\mu(\varkappa_n L)}{I_\mu(\varkappa_n L)} \mathcal{B}_{mn} \left[M_1^{-1} M_2\right] - I'_\mu(\kappa_n L) \mathcal{F}_{mn}\right), \tag{B.10}$$

and $\boldsymbol{B}^{\text{int}}_\mu = (B_{mn}) = \left[M_1^{-1} M_2\right]$, where

$$M_1 = \mathcal{A}_{mn} - \mathcal{B}_{mn} \left(\frac{K'_\mu(\kappa_n L)}{K_\mu(\kappa_n L)} \mathcal{F}_{mn}\right)^{-1} \mathcal{B}_{mn} \frac{\varkappa_n}{k_n} \frac{I'_\mu(\varkappa_n L)}{I_\mu(\varkappa_n L)} \tag{B.11}$$

$$M_2 = \mathcal{B}_{mn} I_\mu(\kappa_n L) - \mathcal{B}_{mn} \left(\frac{K'_\mu(\kappa_n L)}{K_\mu(\kappa_n L)} \mathcal{F}_{mn}\right)^{-1} \mathcal{F}_{mn} I'_\mu(\kappa_n L). \tag{B.12}$$

The system of equations for the radiation problem is given by

$$\begin{aligned}\sum_{n=0}^{N-1}\mathcal{A}_{mn}d_{n0}^{\mathrm{rad}}-\sum_{n=0}^{N-1}\mathcal{B}_{mn}\hat{D}_{n0}^{\mathrm{rad}}&=F_1\\ \sum_{n=0}^{N-1}\mathcal{B}_{mn}\varkappa_n d_{n0}^{\mathrm{rad}}\frac{I_0'(\varkappa_n L)}{I_0(\varkappa_n L)}-\sum_{n=0}^{N-1}\mathcal{F}_{mn}k_n\hat{D}_{n0}^{\mathrm{rad}}\frac{K_0'(\kappa_n L)}{K_0(\kappa_n L)}&=F_2,\end{aligned}\tag{B.13}$$

where F_1 and F_2 are associated with the particular solution, and are calculated as

$$F_1=-\sum_{m=0}^{N-1}\int_{-h}^{-L}\frac{\omega^2}{2g(h-L)}\left[(z+h)^2-\frac{L^2}{2}\right]\frac{\cosh(\mathrm{i}\varkappa_m(z+h))}{\cosh(\mathrm{i}\varkappa_m(h-L))}\mathrm{d}z\tag{B.14}$$

$$F_2=\sum_{m=0}^{N-1}\int_{-h}^{0}Z_m(z)\frac{\omega^2 L}{2g(h-L)}\mathrm{d}z,\tag{B.15}$$

assuming unit heave amplitude $\zeta=1$. The heave amplitude of the WEC is calculated from Equation (4.14), given the hydrodynamic forcing on the body

$$\iint_{S_B}\varphi\, n\mathrm{d}S=\int_0^L\int_0^{2\pi}\varphi^{\mathrm{diff}}r\mathrm{d}\theta\mathrm{d}r+\int_0^L\int_0^{2\pi}\zeta\varphi^{\mathrm{rad}}r\mathrm{d}\theta\mathrm{d}r\ \text{ at }\ z=-L.\tag{B.16}$$

The radiation forcing $F^{\mathrm{rad}}=\int_0^L\int_0^{2\pi}\varphi^{\mathrm{rad}}r\,\mathrm{d}\theta\,\mathrm{d}r$ is evaluated at $z=-L$

$$\begin{aligned}\int_0^L\int_0^{2\pi}\varphi^{\mathrm{rad}}r\mathrm{d}\theta\mathrm{d}r&=\int_0^L\int_0^{2\pi}\left[\sum_n\left(d_{n0}^{\mathrm{rad}}\frac{I_0(\varkappa_n r)}{I_0(\varkappa_n L)}\right)r+\frac{\omega^2}{g}\left(\frac{r(h-L)^2}{2(h-L)}-\frac{r^3}{4(h-L)}\right)\right]\mathrm{d}\theta\mathrm{d}r\\&=2\pi\sum_n d_{n0}^{\mathrm{rad}}\frac{L}{\varkappa_n}\frac{I_1(\varkappa_n L)}{I_0(\varkappa_n L)}+2\pi\frac{\omega^2}{g}\left[\frac{L^2(h-L)^2}{4(h-L)}-\frac{L^4}{16(h-L)}\right].\end{aligned}\tag{B.17}$$

The components of F^{rad} in phase with the acceleration and velocity of the body, respectively, correspond to the added mass $a(\omega)$ and radiation damping $b(\omega)$, and are given by

$$a(\omega)=\rho g\mathrm{Re}(F^{\mathrm{rad}})/\omega^2\quad\text{and}\quad b(\omega)=\rho g\mathrm{Im}(F^{\mathrm{rad}})/\omega.\tag{B.18}$$

The excitation forcing F^{exc} results from the hydrodynamic pressure on the underside of a WEC ($z=-L$) for a given incident wave in the diffraction problem, where $\boldsymbol{d}^{\mathrm{diff}}=\boldsymbol{B}_{\mu=0}^{\mathrm{int}}\boldsymbol{A}$,

$$\begin{aligned}F^{\mathrm{exc}}=\rho g\int_0^L\int_0^{2\pi}\varphi^{\mathrm{diff}}\,r\,\mathrm{d}\theta\,\mathrm{d}r&=2\pi\rho g\sum_n d_{n0}^{\mathrm{diff}}\frac{I_1(\varkappa_n L)}{I_0(\varkappa_n L)}\frac{L}{\varkappa_n}\\&=\boldsymbol{V}\boldsymbol{d}^{\mathrm{diff}}=\left[\boldsymbol{V}\,\boldsymbol{B}_0^{\mathrm{int}}\right]\boldsymbol{A}\\&=\boldsymbol{f_e}\,\boldsymbol{A}.\end{aligned}\tag{B.19}$$

In an array, F^{exc} is determined by replacing $\boldsymbol{A}$ with the vector of amplitudes $\boldsymbol{C}$ corresponding

to the incident field which accounts for interactions within the array. The heave amplitude is expressed as a $1 \times N$ vector,

$$\boldsymbol{\zeta} = \left[-\omega^2(\mathfrak{M} + a(\omega)) - \mathrm{i}\omega\left(b(\omega) + B^j_{\mathrm{PTO}}\right) + \left(\mathfrak{C} + C^j_{\mathrm{PTO}}\right)\right]^{-1} \boldsymbol{f_e}. \tag{B.20}$$

A $N \times N$ matrix $\boldsymbol{B}^{\mathrm{rad}}$, defined for the $\mu = 0$ Fourier mode, is obtained using the $N \times 1$ vector of radiation coefficients in the exterior region

$$\boldsymbol{d}^{\mathrm{rad}}\zeta = \boldsymbol{d}^{\mathrm{rad}}\,\boldsymbol{\zeta}\boldsymbol{A} = \boldsymbol{B}^{\mathrm{rad}}\boldsymbol{A}. \tag{B.21}$$

The diffraction transfer matrix $\boldsymbol{B} = \boldsymbol{B}^{\mathrm{diff}} + \boldsymbol{B}^{\mathrm{rad}}$, where $(B^{\mathrm{rad}}_{\mu mn}) = 0\ \forall\ \mu \neq 0$, encapsulates the scattering properties of the WEC, forming a $N \times (2U+1)$-square matrix

$$\boldsymbol{B} = \begin{bmatrix} \boldsymbol{B}^{\mu}_{00} & \boldsymbol{B}^{\mu}_{01} & \dots & \boldsymbol{B}^{\mu}_{0(N-1)} \\ \boldsymbol{B}^{\mu}_{10} & \boldsymbol{B}^{\mu}_{11} & \dots & \boldsymbol{B}^{\mu}_{1(N-1)} \\ \vdots & \vdots & \ddots & \vdots \\ \boldsymbol{B}^{\mu}_{(N-1)0} & \boldsymbol{B}^{\mu}_{(N-1)1} & \dots & \boldsymbol{B}^{\mu}_{(N-1)(N-1)} \end{bmatrix}. \tag{B.22}$$

The elements of the diagonal matrix $\boldsymbol{B}^{\mu}_{mn}$ are given in Equation (B.10) when $\mu \neq 0$, with the elements in Equation (B.21) added when $\mu = 0$, such that, for $m, n = 0, 1, \dots, N-1$,

$$\boldsymbol{B}^{\mu}_{mn} = \begin{bmatrix} \boldsymbol{B}^{-U}_{mn} & 0 & \dots & 0 \\ 0 & \boldsymbol{B}^{-U+1}_{mn} & \dots & 0 \\ \vdots & \vdots & \ddots & \vdots \\ 0 & 0 & \dots & \boldsymbol{B}^{U}_{mn} \end{bmatrix}. \tag{B.23}$$

B.2 Plane-wave expansion

The velocity potential around a stack is obtained by summing the scattered wavefields of all WECs in the stack in terms of their local coordinate systems

$$\phi(x, y, z) = \varphi^{\mathrm{inc}}(r, \theta, z) + \sum_{n=0}^{\infty} Z_n(z) \sum_{j=-\infty}^{\infty} \mathcal{Q}_j \sum_{\mu=-\infty}^{\infty} D_{n\mu} K_{\mu}(\kappa_n r_j) \mathrm{e}^{\mathrm{i}\mu\theta_j}. \tag{B.24}$$

Following Peter et al. (2006), the modified Bessel functions are replaced with an integral representation to express the scattered field as a plane-wave expansion (PWE),

$$\varphi^{\mathrm{scat}}(r, \theta, z) = \sum_{n=0}^{\infty} Z_n(z) \sum_{m=-\infty}^{\infty} \mathcal{D}^{\pm}_{mn} \mathrm{e}^{\mathrm{i}k_n r \cos(\theta \mp \chi_{mn})} \quad \text{for } \pm y > L, \tag{B.25}$$

where

$$\mathcal{D}_{mn}^{\pm} = \frac{\mathrm{i}\pi}{k_n W_x} \frac{1}{\sin(\chi_{mn})} \sum_{\mu=-\infty}^{\infty} D_{n\mu} \mathrm{e}^{\pm \mathrm{i}\mu\chi_{mn}} \tag{B.26}$$

are the scattered amplitudes of the wave modes that propagate or decay in the $\pm$ y–direction. Truncating the infinite summations at $n = N_0$ and $|\mu| = U$, the scattered amplitudes are obtained from

$$\boldsymbol{D} = [\boldsymbol{I} - \boldsymbol{B}\boldsymbol{\sigma}]^{-1} \boldsymbol{B}\boldsymbol{A}, \tag{B.27}$$

where $\boldsymbol{\sigma}$ is a $N \times (2U+1)$ diagonal matrix $\boldsymbol{\sigma} = \mathrm{diag}\left[\hat{\boldsymbol{\sigma}}^0 \ \hat{\boldsymbol{\sigma}}^1 \ \ldots \hat{\boldsymbol{\sigma}}^{(N_0-1)}\right]$. The sub-matrices $\hat{\boldsymbol{\sigma}}^n$ have elements $\sigma^n_{\mu-\tau}$, as defined in Equation (4.26), such that

$$\hat{\boldsymbol{\sigma}}^n = \begin{array}{c} \mu = -U, \ldots, U \longrightarrow \\ \begin{bmatrix} \sigma^n_{-U-(-U)} & \sigma^n_{-U+1-(-U)} & \cdots & \sigma^n_{U-(-U)} \\ \sigma^n_{-U-(-U+1)} & \sigma^n_{-U+1-(-U+1)} & \cdots & \sigma^n_{U-(-U+1)} \\ \vdots & & \ddots & \vdots \\ \sigma^n_{-U-(U)} & \sigma^n_{-U+1-(U)} & \cdots & \sigma^n_{U-(U)} \end{bmatrix} \Big\downarrow \tau = -U, \ldots, U. \end{array} \tag{B.28}$$

The infinite summations in the PWE (Equation (B.25)) are truncated to $N_1 \leq N_0$ vertical modes, and $M = p + q + 1$ scattering angles (includes complex scattering angles). The $(M \times N_1)$-square reflection and transmission matrices, $\boldsymbol{R}$ and $\boldsymbol{T}$ respectively, are generated by treating the i^{th} scattering angle ($i \in [-p, q]$) and the j^{th} ($j \in [0, N_1]$) vertical mode as incident, and calculating the $(mn)^{\text{th}}$ scattered mode ($m = -p, \ldots, q$; $n = 0, \ldots, N_1$) as

$$R^{ij}_{mn} = \frac{\mathrm{i}\pi}{k_n W_x} \frac{1}{\sin(\chi_{mn})} \sum_{\mu=-U}^{U} D^{ij}_{n\mu} \mathrm{e}^{-\mathrm{i}\mu\chi_{mn}} \tag{B.29}$$

$$T^{ij}_{mn} = \delta_{jn} + \frac{\mathrm{i}\pi}{k_n W_x} \frac{1}{\sin(\chi_{mn})} \sum_{\mu=-U}^{U} D^{ij}_{n\mu} \mathrm{e}^{\mathrm{i}\mu\chi_{mn}}, \tag{B.30}$$

where $\delta_{jn} = 1$ for $n = j$, and zero otherwise. The $D^{ij}_{n\mu}$ are obtained by setting $[\boldsymbol{A}]_{n\mu} = A^{ij}_{n\mu}$ to

$$A^{ij}_{n\mu} = \begin{cases} (-1)^{\mu} \mathrm{e}^{-\mathrm{i}\mu\chi_i} & n = j, \\ 0 & n \neq j \end{cases}$$

for $n, j = 0, 1, \ldots, N_1$. The entries of the reflection matrix (analogous for $\boldsymbol{T}$) are

$$\boldsymbol{R} = \begin{bmatrix} R^{-p0}_{-p0} & R^{-p1}_{-p0} & \ldots & R^{-pN_1}_{-p0} & \ldots & R^{qN_1}_{-p0} \\ R^{-p0}_{-pN_1} & R^{-p1}_{-pN_1} & \ldots & R^{-pN_1}_{-pN_1} & \ldots & R^{qN_1}_{-pN_1} \\ \vdots & \vdots & \ddots & \vdots & \ddots & \vdots \\ R^{-p0}_{qN_1} & R^{-p1}_{qN_1} & \ldots & R^{-pN_1}_{qN_1} & \ldots & R^{qN_1}_{qN_1} \end{bmatrix}. \tag{B.31}$$

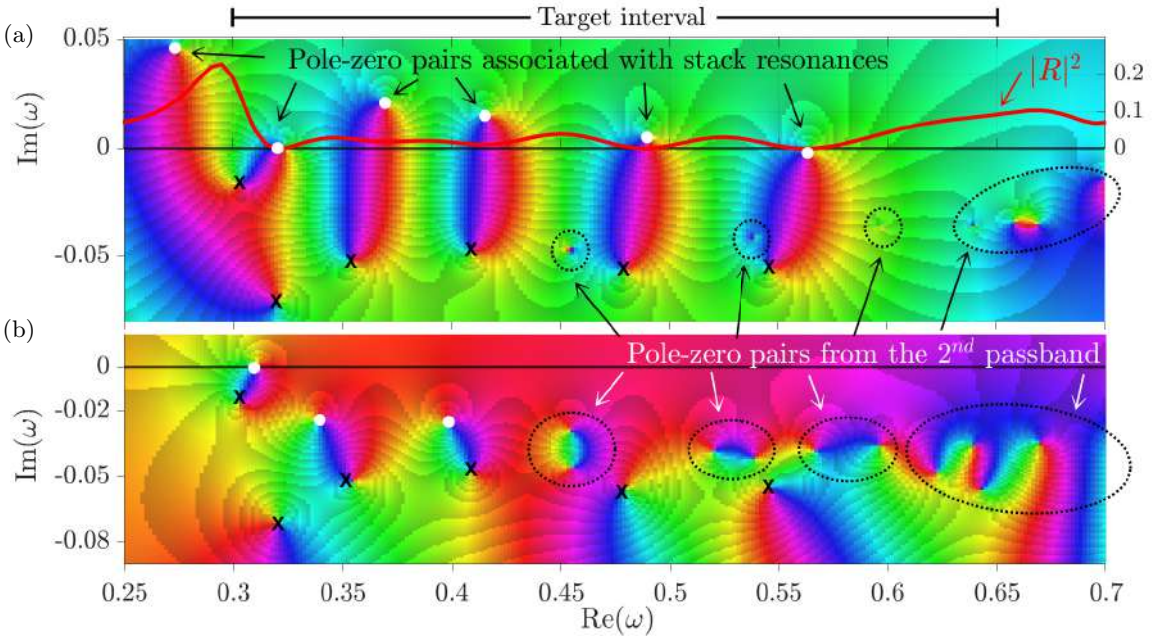

Figure B.1: Phase portraits of the (a) reflection and (b) transmission coefficients of a graded array of eight stacks with $W_x = W_y = 50\,\mathrm{m}$ are shown as a function of complex frequency. Complex resonances from the second passband are interspersed between stack resonances on the target interval. The pole–zero pairs for stacks 7 and 8 lie below the axes limits.

B.3 Maximum W_x and W_y for high efficiency

Figure B.1 shows the phase portraits of the reflection and transmission coefficients as a function of complex frequency for an array with eight stacks when $W_x = W_y = 50\,\mathrm{m}$. High absorption is maintained from $\omega = 0.3$ to $\omega = 0.6\,\mathrm{rad\,s^{-1}}$, but decreases for $\omega \geq 0.6\,\mathrm{rad\,s^{-1}}$ as resonances associated with the second passband encroach on the target interval, as a result of the chosen spacing. At $W_y = 50\,\mathrm{m}$, the Bragg bandgap is located close to the target interval, causing interactions at the upper bound (shifts the second passband down).

Additionally, $W_x = 50\,\mathrm{m}$ weakens the reflection properties of stacks, so that they are unable to shift the resonances associated with the second passband above the target interval, which become interspersed between the pole–zero pairs associated with stack resonances, and cause reflection (transmission) to rise. The number of stacks that can be tuned to the interval becomes restricted as a result, and pole–zero pairs associated with the stack resonances are pushed below the lower bound of the target interval in the complex plane.

Appendix C

3D model: Impacts of a drag correction

C.1 Infinite array: Drag coefficient

The alterations to the transmission and reflection of the graded array described in § 5.3.1 when $C_d = 2$, occur at a much slower rate as A^{inc} increases when $C_d = 0.6$, as shown in Figure C.1. Lower transmission and higher reflection are obtained in the local bandgap for the smaller drag coefficient. Once again, drag has a smaller impact on the transmission behaviour in the local bandgap than the reflection, when compared to the zero-drag model.

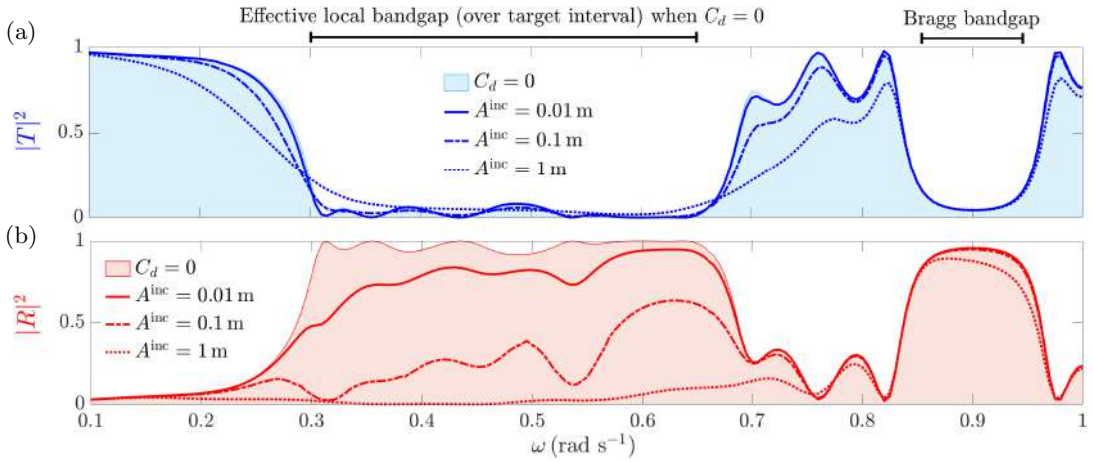

Figure C.1: The (a) transmission $|T|^2$ (blue) and (b) reflection $|R|^2$ (red) for the graded array of six stacks in Table 5.1 (when $B^s_{\text{PTO}} = 0\ \forall s$) is shown when $C_d = 0$ (shaded) and when $C_d = 0.6$ (lines), for $A^{\text{inc}} = 0.01$ (—), 0.1(- -) and 1 (····) m.

C.2 Finite array: Spacing, wave direction, and PTO

The appearance of array resonances in the finite uniform array is strongly reliant on the reflection properties of the rows of WECs, which is influenced by the spacing W_x within the row. To demonstrate this, the relative capture widths of the uniform array tuned to $\omega_0 = 0.475\,\text{rad}\,\text{s}^{-1}$, and the graded array, are shown in Figure C.2 as the wave direction changes from $\chi = \pi/2$ to $\pi/6\,\text{rad}$. The change in wave direction has the same effect as rotating the coordinate axes. The finite uniform array behaves like an infinite uniform array with $W_x = 40\,\text{m}$ and $W_y = 30\,\text{m}$ at $\chi = \pi/3\,\text{rad}$, rather than the infinite array with $W_x = 30\,\text{m}$ and $W_y = 40\,\text{m}$ at $\chi = \pi/6\,\text{rad}$. The larger within-row spacing (now $W_y = 40\,\text{m}$) weakens the

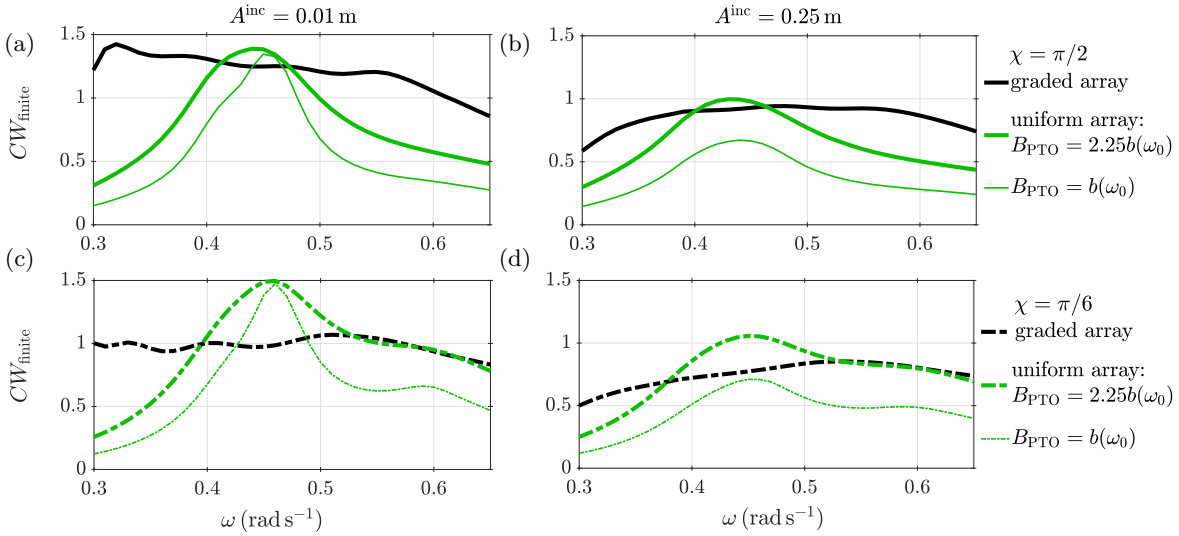

Figure C.2: The relative capture widths CW_{finite} of the graded (black) and uniform array (green) tuned to $\omega_0 = 0.475\,\text{rad}\,\text{s}^{-1}$ are compared at $A^{\text{inc}} = 0.01$ in (a) and (c), and $A^{\text{inc}} = 0.25$ in (b) and (d) for $C_d = 0.6$ (Figure 5.12b is equivalent to (b)), when $\chi = \pi/2\,\text{rad}$ (a) and (b), and when $\chi = \pi/6\,\text{rad}$ (c) and (d). The solutions at $A^{\text{inc}} = 0.01$ resemble the zero-drag model.

reflection capability of rows (Chapter 4), so that array resonances have a noticeable impact on the CW_{finite}, which develops a second, lesser peak (array resonances now result from the W_x spacing, which does not occur when $W_x = 30$ and $W_y = 40\,\text{m}$ as $\chi = \pi/6$ extends the local bandgap to cover the entire target frequency interval above resonance).

In the graded array, $\chi \to 0$ causes edge effects to become more pronounced, which amplify WEC motions, resulting in higher drag, and ultimately a lower CW_{finite} than at $\chi = \pi/2\,\text{rad}$. The rainbow absorption of the graded array is robust to wave direction, as illustrated in Figure C.3. Transmission relative to A^{inc} is comparable to the zero-drag model at $A^{\text{inc}} \leq 0.25\,\text{m}$, but rises as A^{inc} increases (entering a regime where breaching occurs), particularly at low frequencies. Increasing the number of WECs per row improves control of transmission.

The finite graded array with $C_d = 2$ closely resembles the behaviour of the infinite array. The trends in behaviour as the incident wave direction decreases are consistent with $C_d = 0.6$, but the level of absorption is decreased in the more drag-dominated regime. The benefit derived through grading an array decreases compared to a uniform tuning, as $C_d = 2$ substantially broadens the responses of the uniform arrays, as illustrated in Figure C.4 at $A^{\text{inc}} = 0.5\,\text{m}$.

The difference between $B_{\text{PTO}}^{\text{stack}}$ and $B_{\text{PTO}}^{\text{buoy}}$ accounts for over 85% of the corresponding increase in CW_{finite} for the uniform arrays at $A^{\text{inc}} = 0.5\,\text{m}$ when $C_d = 2$ (WEC amplitudes are slightly reduced at $B_{\text{PTO}}^{\text{stack}}$). In this drag-dominated regime, the PTO damping becomes, at best, commensurate with, and at worst, considerably larger than the power capture, and

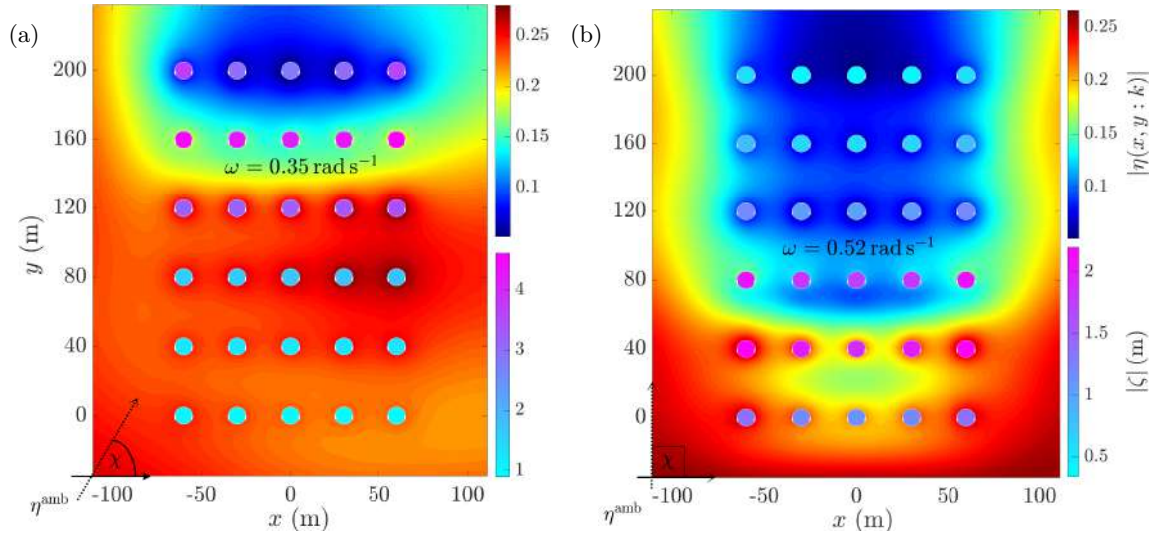

Figure C.3: The rainbow absorbing behaviour is evident from the surface elevation $|\eta|$, which is shown at (a) $\omega = 0.35$ for $\chi = \pi/3$, and (b) $\omega = 0.52$ for $\chi = \pi/2$, when $A^{\mathrm{inc}} = 0.25\,\mathrm{m}$, which slightly exceed the resonant frequencies of rows five and three, respectively. Edge effects are visible in the sixth row when $\chi = \pi/3$, and along the array edges when $\chi = \pi/2$.

overwhelmingly governs the level of absorption. Without drag, absorption is governed by a combination of the WEC amplitudes and PTO damping.

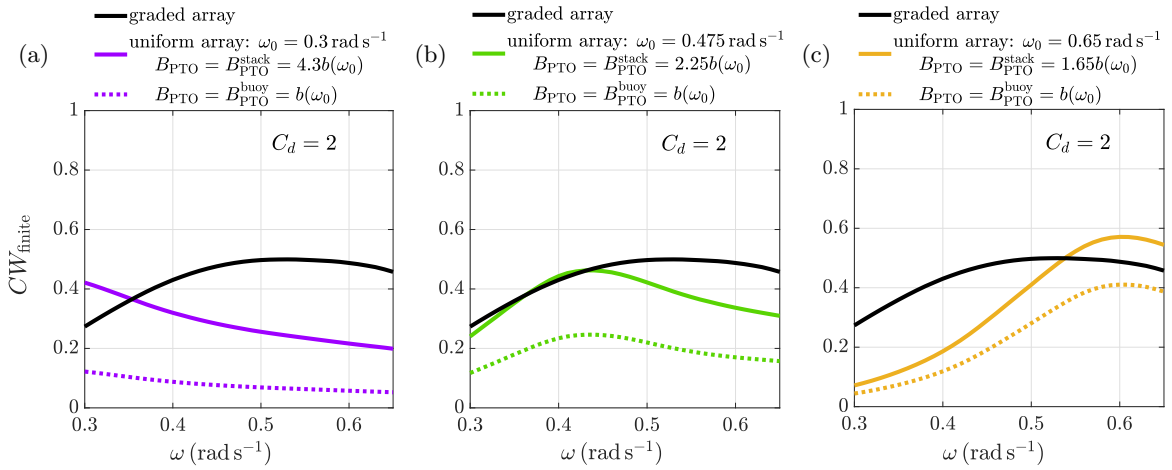

Figure C.4: The relative capture width CW_{finite} of the finite graded array (black) is compared to a uniform array tuned to (a) $\omega_0 = 0.3\,\mathrm{rad\,s^{-1}}$, (b) $\omega_0 = 0.475\,\mathrm{rad\,s^{-1}}$, and (c) $\omega_0 = 0.65\,\mathrm{rad\,s^{-1}}$ over $\omega \in [0.3, 0.65]\,\mathrm{rad\,s^{-1}}$, when $C_d = 2$ and $A^{\mathrm{inc}} = 0.5\,\mathrm{m}$.

Given the uncertainty associated with the drag correction and an appropriate drag coefficient for WECs, the model validity is arguably questionable at these values. Further, $B^{\mathrm{stack}}_{\mathrm{PTO}}$ depends on W_x and will increase as $W_x \to 0\,\mathrm{m}$, which could potentially inflate power capture. In a similar vein, Eatock Taylor et al. (2016) suspected that power estimates in regular waves were artificially compensated by large drag coefficients, which altered the PTO damping.

References

Abanades, J., Flor-Blanco, G., Flor, G. and Iglesias, G. (2018). Dual wave farms for energy production and coastal protection, *Ocean Coast. Manag.* **160**: 18–29.

Abanades, J., Greaves, D. and Iglesias, G. (2014). Coastal defence through wave farms, *Coast. Eng.* **91**: 299–307.

Abanades, J., Greaves, D. and Iglesias, G. (2015). Coastal defence using wave farms: The role of farm-to-coast distance, *Renew. Energy* **75**: 572–582.

Alday, M., Raghavan, V. and Lavidas, G. (2023). Analysis of the North Atlantic offshore energy flux from different reanalysis and hindcasts, *Proc. EWTEC* **15**.

Archer, A. J., Wolgamot, H. A., Orszaghova, J., Bennetts, L. G., Peter, M. A. and Craster, R. V. (2020). Experimental realization of broadband control of water-wave-energy amplification in chirped arrays, *Phys. Rev. Fluids* **5**(6): 062801.

Arrosyid, W. A., Sari, W. R., Waskito, K. T., Yanuar, Pria Utama, I. K. A., Binu Soesanto, Q. M., Bramantya, A. and Nugroho, B. (2025). Recent advancements in wave energy converter technologies: A comprehensive review on design and performance optimization, *Ocean Eng.* **340**: 122328.

Ashcroft, N. and Mermin, N. (1976). *Solid State Physics*, HRW International Editions, Holt, Rinehart and Winston.

Babarit, A. (2013). On the park effect in arrays of oscillating wave energy converters, *Renew. Energy* **58**: 68–78.

Babarit, A., Hals, J., Muliawan, M. J., Kurniawan, A., Moan, T. and Krokstad, J. (2012). Numerical benchmarking study of a selection of wave energy converters, *Renew. Energy* **41**: 44–63.

Bacelli, G. and Ringwood, J. (2013). Constrained control of arrays of wave energy devices, *Int. J. Mar. Energy* **3-4**: e53–e69.

Battisti, B., Giorgi, G. and Fernandez, G. V. (2024). Balancing power production and coastal protection: A bi-objective analysis of Wave Energy Converters, *Renew. Energy* **220**: 119702.

Bennetts, L. G. and Meylan, M. H. (2021). Complex resonant ice shelf vibrations, *SIAM J. Appl. Math.* **81**(4): 1483–1502.

Bennetts, L. G., Peter, M. A. and Craster, R. V. (2018). Graded resonator arrays for spatial frequency separation and amplification of water waves, *J. Fluid Mech.* **854**: R4.

Bennetts, L. G., Peter, M. A. and Craster, R. V. (2019). Low-frequency wave-energy amplification in graded two-dimensional resonator arrays, *Phil. Trans. R. Soc. A* **377**(2156): 20190104.

Bennetts, L. G. and Squire, V. A. (2009). Wave scattering by multiple rows of circular ice floes, *J. Fluid Mech.* **639**: 213–238.

Bergillos, R. J., López-Ruiz, A., Medina-López, E., Moñino, A. and Ortega-Sánchez, M. (2018). The role of wave energy converter farms on coastal protection in eroding deltas, Guadalfeo, southern Spain, *J. Clean. Prod.* **171**: 356–367.

Bergillos, R. J., Rodriguez-Delgado, C., Allen, J. and Iglesias, G. (2019a). Wave energy converter configuration in dual wave farms, *Ocean Eng.* **178**: 204–214.

Bergillos, R. J., Rodriguez-Delgado, C., Allen, J. and Iglesias, G. (2019b). Wave energy converter geometry for coastal flooding mitigation, *Sci. Total Environ.* **668**: 1232–1241.

Bergillos, R. J., Rodriguez-Delgado, C. and Iglesias, G. (2019). Wave farm impacts on coastal flooding under sea-level rise: A case study in southern Spain, *Sci. Total Environ.* **653**: 1522–1531.

Blanco, M., Villalba, I., Lafoz, M., Nájera, J., Navarro, G. and Santos-Herrán, M. (2025). Power optimization modelling as a computational tool for power take off design in wave energy converters, *Appl. Ocean Res.* **160**: 104628.

Boodoo, A., Wakeyama, T. and Cross, J. S. (2025). Wave farms for coastal protection: A systematic review of effectiveness, methodologies, and future directions, *Ocean Coast. Manag.* **269**: 107807.

Budal, K. (1977). Theory for absorption of wave power by a system of interacting bodies, *J. Ship. Res.* **21**(04): 248–254.

Calvo, L., De Padova, D., Onorato, M., Pezzutto, P. and Mossa, M. (2025). SPH modelling of wave attenuation by an array of submerged resonators and vorticity generation mechanism, *Environ. Fluid Mech.* **25**: 21.

Cao, H., Chen, L., Ning, D., Peng, C., Xu, J. and Lin, H. (2025). Broadband energy attenuation of long-period water waves by a graded array of C-shaped cylinders, *The 40th International Workshop on Water Waves and Floating Bodies*, Shanghai, China.

Cao, X., Shi, J., Zheng, J., Zhang, C. and Pan, J. (2025). Offshore wave energy converter array poses threat to coasts causing significant rip currents, *Phys. Fluids* **37**(8): 086627.

Carballo, R. and Iglesias, G. (2013). Wave farm impact based on realistic wave-WEC interaction, *Energy* **51**: 216–229.

Cenedese, M., Belloni, E. and Braghin, F. (2021). Interaction of Bragg scattering bandgaps and local resonators in mono-coupled periodic structures, *J. Appl. Phys.* **129**(12): 124501.

Chakrabarti, S. K. (ed.) (2005). *Handbook of Offshore Engineering*, Vol. 1, Elsevier.

Chaplain, G. J., Pajer, D., Ponti, J. M. D. and Craster, R. V. (2020). Delineating rainbow reflection and trapping with applications for energy harvesting, *New J. Phys.* **22**(6): 063024.

Child, B. F. M. and Venugopal, V. (2010). Optimal configurations of wave energy device arrays, *Ocean Eng.* **37**(16): 1402–1417.

Clauss, G., Lehmann, E. and Östergaard, C. (1992). *Offshore Structures*, Vol. 1, Springer.

Cleante, V. G., Brennan, M. J., Gonçalves, P. J. P. and Carneiro Jr, J. P. (2022). On the formation of a super stop-band in finite mono-coupled periodic structures using an array of vibration absorbers: Controlling parameters and physical insight, *Mech. Syst. Signal Process.* **180**: 109383.

Clemente, D., Rosa-Santos, P. and Taveira-Pinto, F. (2021). On the potential synergies and applications of wave energy converters, *Renew. Sustain. Energy Rev.* **135**: 110162.

Coe, R. G., Bacelli, G. and Forbush, D. (2021). A practical approach to wave energy modeling and control, *Renew. Sustain. Energy Rev.* **142**: 110791.

Coe, R. G., Bacelli, G., Wilson, D. G., Abdelkhalik, O., Korde, U. A. and Robinett III, R. D. (2017). A comparison of control strategies for wave energy converters, *Int. J. Mar. Energy* **20**: 45–63.

Cohen, N. (2025). *Wave Energy Converter Array Impacts on Nearshore Processes and Shoreline Realignment*, PhD thesis, University of New South Wales.

CorPower Ocean (2024). Wave energy technology. Available at: https://corpowerocean.com/wave-energy-technology/ (Accessed: 05-07-24).

Cosby, A. G., Lebakula, V., Smith, C. N., Wanik, D. W., Bergene, K., Rose, A. N., Swanson, D. and Bloom, D. E. (2024). Accelerating growth of human coastal populations at the global and continent levels: 2000–2018, *Sci. Rep.* **14**(1): 22489.

Crowley, S., Porter, R. and Evans, D. V. (2013). A submerged cylinder wave energy converter, *J. Fluid Mech.* **716**: 566–596.

Cruz, J. (ed.) (2008). *Ocean Wave Energy: Current Status and Future Perspectives*, Green Energy and Technology, Springer.

Cruz, J., Sykes, R., Siddorn, P. and Taylor, R. E. (2010). Estimating the loads and energy yield of arrays of wave energy converters under realistic seas, *IET Renew. Power Gener.* **4**(6): 488–497.

Cui, L., Sergiienko, N. Y., Cohen, N., Leontini, J. S., Cazzolato, B. S., Flocard, F. and Manasseh, R. (2026). Coastal response to wave energy converter arrays: A semi-analytical model for control of nearshore currents and beach morphology, *Renew. Energy* **263**: 125497.

Cui, L., Sergiienko, N. Y., Leontini, J. S., Cohen, N., Bennetts, L. G., Cazzolato, B., Turner, I. L., Flocard, F., Westcott, A.-R., Cheng, F. and R., M. (2024). Protecting coastlines by offshore wave farms: On optimising array configurations using a corrected far-field approximation, *Renew. Energy* **224**: 120109.

David, D. R., Kurniawan, A., Wolgamot, H., Hansen, J. E., Rijnsdorp, D. and Lowe, R. (2022). Nearshore submerged wave farm optimisation: A multi-objective approach, *Appl. Ocean Res.* **124**: 103225.

De Chowdhury, S., Bennetts, L. G. and Manasseh, R. (2023). A coupled damped harmonic oscillator model for arbitrary arrays of floating cylinders using homotopy methods, *Phys. Fluids* **35**(10): 107141.

Douglas, J. F., Gasiorek, J. M. and Swaffield, J. A. (1986). *Fluid Mechanics*, second edn, Longman Scientific & Technical.

Dupont, G., Remy, F., Kimmoun, O., Molin, B., Guenneau, S. and Enoch, S. (2017). Type of dike using C-shaped vertical cylinders, *Phys. Rev. B* **96**: 180302(R).

Eatock Taylor, R., Taylor, P. H. and Stansby, P. K. (2016). A coupled hydrodynamic–structural model of the M4 wave energy converter, *J. Fluids Struct.* **63**: 77–96.

Edwards, E. C., Whitlam, C., Chapman, J., Hughes, J., Redfearn, B., Brown, S., Draper, S., Borthwick, A. G. L., Foster, G., Yue, D. K.-P., Hann, M. and Greaves, D. (2025). The effect of device geometry on the performance of a wave energy converter, *Comms. Eng.* **4**(1): 107.

Edwards, E. C. and Yue, D. K.-P. (2022). Optimisation of the geometry of axisymmetric point-absorber wave energy converters, *J. Fluid Mech.* **933**: A1.

Elliott, S. J., Tehrani, M. G. and Langley, R. S. (2015). Nonlinear damping and quasi-linear modelling, *Phil. Trans. R. Soc. A* **373**(2051): 20140402.

Engström, J., Eriksson, M., Göteman, M., Isberg, J. and Leijon, M. (2013). Performance of large arrays of point absorbing direct-driven wave energy converters, *J. Appl. Phys.* **114**(20): 204502.

Ermakov, A. M., Ali, Z. A., Mahmoodi, K., Mason, O. and Ringwood, J. V. (2025). Optimisation of heterogeneous wave energy converter arrays: A control co-design strategy, *Renew. Energy* **244**: 122637.

Evans, D. V. (1976). A theory for wave-power absorption by oscillating bodies, *J. Fluid Mech.* **77**: 1–25.

Evans, D. V. (1981a). Maximum wave-power absorption under motion constraints, *Appl. Ocean Res.* **3**: 200–203.

Evans, D. V. (1981b). Power from water waves, *Annu. Rev. Fluid Mech.* **13**: 157–187.

Evans, D. V. and Porter, R. (2012). Wave energy extraction by coupled resonant absorbers, *Phil. Trans. R. Soc. A* **370**(1959): 315–344.

Falnes, J. (1980). Radiation impedance matrix and optimum power absorption for interaction oscillators in surface waves, *Appl. Ocean Res.* **2**(2): 75–80.

Falnes, J. (1984). Wave-power absorption by an array of attenuators oscillating with unconstrained amplitudes, *Appl. Ocean Res.* **6**(1): 16–22.

Falnes, J. (2005). *Ocean Waves and Oscillating Systems: Linear Interactions Including Wave-Energy Extraction*, Cambridge University Press.

Falnes, J. (2007). A review of wave-energy extraction, *Mar. Struct.* **20**(4): 185–201.

Falnes, J. and Budal, K. (1982). Wave-power absorption by parallel rows of interacting oscillating bodies, *Appl. Ocean Res.* **4**(4): 194–207.

Falnes, J. and Hals, J. (2012). Heaving buoys, point absorbers and arrays, *Phil. Trans. R. Soc. A* **370**(1959): 246–277.

Falnes, J. and Kurniawan, A. (2020). *Ocean Waves and Oscillating Systems: Linear Interactions Including Wave-Energy Extraction*, Vol. 8 of *Cambridge Ocean Technology Series*, 2 edn, Cambridge University Press.

Feng, Y., Huang, Z., Zhang, X. and Qiu, T. (2024). Broadband and wide-angle antireflection in silicon solar cells using atomically thin MoS2 with a gradient unit cell structure, *Sol. Energy* **284**: 113088.

Folley, M. (ed.) (2016). *Numerical Modelling of Wave Energy Converters: State-of-the-art techniques for single devices and arrays*, Academic Press.

Folley, M. and Whittaker, T. (2010). Spectral modelling of wave energy converters, *Coast. Eng.* **57**(10): 892–897.

Folley, M. and Whittaker, T. J. T. (2009). The effect of sub-optimal control and the spectral wave climate on the performance of wave energy converter arrays, *Appl. Ocean Res.* **31**(4): 260–266.

Foteinis, S. and Tsoutsos, T. (2017). Strategies to improve sustainability and offset the initial high capital expenditure of wave energy converters (WECs), *Renew. Sustain. Energy Rev.* **70**: 775–785.

Fusco, F. and Ringwood, J. V. (2010). Short-term wave forecasting for real-time control of wave energy converters, *IEEE Trans. Sustain. Energy* **1**(2): 99–106.

Gallutia, D., Fard, M. T., Soto, M. G. and He, J. (2022). Recent advances in wave energy conversion systems: From wave theory to devices and control strategies, *Ocean Eng.* **252**: 111105.

Garcia-Rosa, P. B., Bacelli, G. and Ringwood, J. V. (2015). Control-informed optimal array layout for wave farms, *IEEE Trans. Sustain. Energy* **6**(2): 575–582.

Garcia-Rosa, P. B., Torres-Olguin, R. E., Cruz, J. and D'Arco, S. (2022). A wave-to-wire model for grid integration studies of oscillating-body wave energy converters, *2022 IEEE 31st International Symposium on Industrial Electronics (ISIE)*, pp. 84–91.

Garnaud, X. and Mei, C. C. (2009). Wave-power extraction by a compact array of buoys, *J. Fluid Mech.* **635**: 389–413.

Garnaud, X. and Mei, C. C. (2010). Bragg scattering and wave-power extraction by an array of small buoys, *Proc. R. Soc. A* **466**(2113): 79–106.

George, A. and Cho, I. H. (2024). Assessment of viscous damping of a solid heave disk for motion reduction of a floating circular cylinder, *Appl. Ocean Res.* **142**: 103854.

Giassi, M. and Göteman, M. (2018). Layout design of wave energy parks by a genetic algorithm, *Ocean Eng.* **154**: 252–261.

Giorgi, G. and Ringwood, J. V. (2017). Nonlinear Froude-Krylov and viscous drag representations for wave energy converters in the computation/fidelity continuum, *Ocean Eng.* **141**: 164–175.

Gittman, R. K., Scyphers, S. B., Smith, C. S., Neylan, I. P. and Grabowski, J. H. (2016). Ecological consequences of shoreline hardening: A meta-analysis, *BioScience* **66**(9): 763–773.

Golbaz, D., Asadi, R., Amini, E., Mehdipour, H., Nasiri, M., Etaati, B., Naeeni, S. T. O., Neshat, M., Mirjalili, S. and Gandomi, A. H. (2022). Layout and design optimization of ocean wave energy converters: A scoping review of state-of-the-art canonical, hybrid, cooperative, and combinatorial optimization methods, *Energy Rep.* **8**: 15446–15479.

Gong, H., Zheng, S., Cao, F., Han, Z. and Shi, H. (2024). GWECS: An indicator to describe the energy absorption characteristics of wave energy converter arrays in real sea states, *Renew. Energy* **237**: 121483.

Göteman, M. (2022). Multiple cluster scattering with applications to wave energy park optimizations, *Appl. Ocean Res.* **125**: 103256.

Göteman, M., Engström, J., Eriksson, M. and Isberg, J. (2015). Optimizing wave energy parks with over 1000 interacting point-absorbers using an approximate analytical method, *Int. J. Mar. Energy* **10**: 113–126.

Göteman, M., Giassi, M., Engström, J. and Isberg, J. (2020). Advances and challenges in wave energy park optimization–A review, *Front. Energy Res.* **8**: 26.

Gu, H., Stansby, P., Stallard, T. and Carpintero Moreno, E. (2018). Drag, added mass and radiation damping of oscillating vertical cylindrical bodies in heave and surge in still water, *J. Fluids Struct.* **82**: 343–356.

Guo, B. and Ringwood, J. V. (2021). A review of wave energy technology from a research and commercial perspective, *IET Renew. Power Gener.* **15**(14): 3065–3090.

Guo, J., Cao, J., Xiao, Y., Shen, H. and Wen, J. (2020). Interplay of local resonances and Bragg band gaps in acoustic waveguides with periodic detuned resonators, *Phys. Lett. A* **384**(13): 126253.

Hals, J., Falnes, J. and Moan, T. (2010). Constrained optimal control of a heaving buoy wave-energy converter, *J. Offshore Mech. Arct. Eng.* **133**(011401).

Hasselmann, K., Barnett, T., Bouws, E., Carlson, H., Cartwright, D., Enke, K., Ewing, J., Gienapp, H., Hasselmann, D., Kruseman, P., Meerburg, A., Muller, P., Olbers, D., Richter, K., Sell, W. and Walden, H. (1973). Measurements of wind-wave growth and swell decay during the Joint North Sea Wave Project (JONSWAP), *Ergänzung zur Deut. Hydrogr. Z., Reihe A* **8**(12): 1–95.

He, Z., Ning, D., Gou, Y. and Mayon, R. (2022). Optimization of a wave energy converter square array based on the differential evolution algorithm, *Ocean Eng.* **262**: 112189.

Hessel, A. and Oliner, A. A. (1965). A new theory of Wood's anomalies on optical gratings, *Appl. Opt.* **4**(10): 1275–1297.

Hu, Y., Cheng, Y., Dai, S., Yuan, Z. and Incecik, A. (2025). Broadband wave conversion by a "Pan Flute"-type multi-oscillating-water-column (M-OWC) breakwater system, *Energy Convers. Manag.* **333**: 119820.

Huang, J. and Porter, R. (2024). Wave power calculation of a large periodic array of bottom-hinged paddle wave energy converters using Floquet–Bloch theory, *Appl. Ocean Res.* **150**: 104102.

IEA (2025). Global Energy Review 2025. IEA, Paris, https://www.iea.org/reports/global-energy-review-2025, Licence: CC BY 4.0.

IPCC (2019). *IPCC Special Report on the Ocean and Cryosphere in a Changing Climate*. [H.-O. Pörtner, D.C. Roberts, V. Masson-Delmotte, P. Zhai, M. Tignor, E. Poloczanska, K. Mintenbeck, A. Alegría, M. Nicolai, A. Okem, J. Petzold, B. Rama, N.M. Weyer (eds.)]. Cambridge University Press, Cambridge, UK and New York, NY, USA, p. 755. doi: 10.1017/9781009157964.007.

IPCC (2022). *Climate Change 2022: Impacts, Adaptation and Vulnerability*, Contribution of Working Group II to the Sixth Assessment Report of the Intergovernmental Panel on Climate Change, Cambridge University Press, Cambridge, UK and New York, NY, USA, p. 3056. doi: 10.1017/9781009325844.

IPCC (2023). *Climate Change 2023: Synthesis Report. Contribution of Working Groups I, II, and III to the Sixth Assessment Report of the Intergovernmental Panel on Climate Change*, p. 184. [Core Writing Team, H. Lee and J. Romero (eds.)]. IPCC, Geneva, Switzerland.

IRENA (2020). *Innovation Outlook: Ocean Energy Technologies*, International Renewable Energy Agency, Abu Dhabi.

IRENA (2025). *Renewable power generation costs in 2024*. International Renewable Energy Agency, Abu Dhabi.

IRENA and OEE (2023). *Scaling up Investments in Ocean Energy Technologies*. International Renewable Energy Agency, Abu Dhabi.

Jiménez, N., Romero-García, V., Pagneux, V. and Groby, J.-P. (2017a). Quasiperfect absorption by subwavelength acoustic panels in transmission using accumulation of resonances due to slow sound, *Phys. Rev. B* **95**(1): 014205.

Jiménez, N., Romero-García, V., Pagneux, V. and Groby, J.-P. (2017b). Rainbow-trapping absorbers: Broadband, perfect and asymmetric sound absorption by subwavelength panels for transmission problems, *Sci. Rep.* **7**.

Jin, H., Zhang, H., Zheng, S., Lu, Y., Xu, D. and Greaves, D. (2024). Dual-purpose wave farm with nonlinear stiffness mechanism for energy extraction and wave attenuation, *Phys. Fluids* **36**(9): 097126.

Jin, H., Zhang, H., Zheng, S. and Xu, D. (2024). Characteristics of a two-dimensional periodic wave energy converter array, *Renew. Energy* **222**: 119834.

Journée, J. M. J. and Massie, W. W. (2001). *Offshore Hydromechanics*, 1st edn, Delft University of Technology.

Kagemoto, H. and Yue, D. K. P. (1986). Interactions among multiple three-dimensional bodies in water waves: an exact algebraic method, *J. Fluid Mech.* **166**: 189–209.

Kaneko, S., Nakamura, T., Inada, F., Kato, M., Ishihara, K., Nishihara, T. and Langthjem, M. A. (eds) (2014). *Flow-Induced Vibrations: Classifications and Lessons from Practical Experiences*, second edn, Academic Press.

Konispoliatis, D. N. and Mavrakos, S. A. (2020). Wave power absorption by arrays of wave energy converters in front of a vertical breakwater: A theoretical study, *Energies* **13**(8): 1985.

Korde, U. A. and Ringwood, J. (2016). *Hydrodynamic Control of Wave Energy Devices*, Cambridge University Press.

Kurniawan, A. and Zhang, X. (2018). Application of a negative stiffness mechanism on pitching wave energy devices, *Proceedings of the 5th Offshore Energy and Storage Symposium*, Ningbo, China.

Lei, W., Chen, J., Shao, Y. and Yu, X. (2023). CFD-assisted linearized frequency-domain analysis of motion and structural loads for floating structures with damping plates, *Ocean Eng.* **281**: 114924.

Li, G., Weiss, G., Mueller, M., Townley, S. and Belmont, M. R. (2012). Wave energy converter control by wave prediction and dynamic programming, *Renew. Energy* **48**: 392–403.

Li, H., Shi, X., Kong, W., Kong, L., Hu, Y., Wu, X., Pan, H., Zhang, Z., Pan, Y. and Yan, J. (2025). Advanced wave energy conversion technologies for sustainable and smart sea: A comprehensive review, *Renew. Energy* **238**: 121980.

Li, S., Chen, T., Wang, X., Li, Y. and Chen, W. (2016). Expansion of lower-frequency locally resonant band gaps using a double-sided stubbed composite phononic crystals plate with composite stubs, *Phys. Lett. A.* **380**(25): 2167–2172.

Linton, C. (1998). The Green's Function for the two-dimensional Helmholtz equation in periodic domains, *J. Eng. Math.* **33**(4): 377–401.

Linton, C. (2011). Water waves over arrays of horizontal cylinders: Band gaps and Bragg resonance, *J. Fluid Mech.* **670**: 504–526.

Linton, C. and McIver, P. (2001). *Handbook of Mathematical Techniques for Wave/Structure Interactions*, CRC Press.

Liu, H., Farhat, M., Bagci, H., Guenneau, S. and Wu, Y. (2025). Broadband water wave reflector with customisable frequency range enabled by floating metaplates, *J. Fluid Mech.* **1020**: A50.

Liu, J., Meucci, A., Liu, Q., Babanin, A. V., Ierodiaconou, D., Xu, X. and Young, I. R. (2023). A high-resolution wave energy assessment of south-east Australia based on a 40-year hindcast, *Renew. Energy* **215**: 118943.

Lorenzo, M., Pezzutto, P., De Lillo, F., Ventrella, F. M., De Vita, F., Bosia, F. and Onorato, M. (2023). Attenuating surface gravity waves with an array of submerged resonators: An experimental study, *J. Fluid Mech.* **973**: A16.

Mahmoodi, K., Fard, H. R. and Böling, J. (2025). Long-term climate change effects on power performance of wave energy converters: A case study, *Energy* **326**: 136101.

Martin, P. A. (2006). *Multiple Scattering: Interaction of Time-Harmonic Waves with N Obstacles*, Vol. 107 of *Encyclopedia of Mathematics and its Applications*, Cambridge University Press.

Mazzaretto, O. M., Menéndez, M. and Lobeto, H. (2022). A global evaluation of the JONSWAP spectra suitability on coastal areas, *Ocean Eng.* **266**: 112756.

McGuinness, J. P. L. and Thomas, G. (2017). The constrained optimisation of small linear arrays of heaving point absorbers. Part I: The influence of spacing, *Int. J. Mar. Energy* **20**: 33–44.

McIver, P. (1985). Scattering of water waves by two surface-piercing vertical barriers, *IMA J. Appl. Math.* **35**(3): 339–355.

McIver, P. (1994). Some hydrodynamic aspects of arrays of wave-energy devices, *Appl. Ocean Res.* **16**(2): 61–69.

McIver, P. (2000). Water-wave propagation through an infinite array of cylindrical structures, *J. Fluid Mech.* **424**: 101–125.

McIver, P. (2002). Wave interaction with arrays of structures, *Appl. Ocean Res.* **24**(3): 121–126.

Mei, C. C., Stiassnie, M. and Yue, D. K.-P. (2005). *Theory and Applications of Ocean Surface Waves: Part 1: Linear Aspects*, Vol. 23 of *Advanced Series on Ocean Engineering*, World Scientific Publishing Co. Pte. Ltd.

Mendoza, E., Silva, R., Zanuttigh, B., Angelelli, E., Lykke Andersen, T., Martinelli, L., Nørgaard, J. Q. H. and Ruol, P. (2014). Beach response to wave energy converter farms acting as coastal defence, *Coast. Eng.* **87**: 97–111.

Mérigaud, A., Thiria, B., Godoy-Diana, R. and Perret, G. (2024). Modelling the far-field effect of drag-induced dissipation in wave–structure interaction: A numerical and experimental study, *J. Fluid Mech.* **987**: A24.

Meylan, M. H. and Fitzgerald, C. (2018). Computation of long lived resonant modes and the poles of the S-matrix in water wave scattering, *J. Fluids and Struct.* **76**: 153–165.

Michele, S., Sammarco, P. and d'Errico, M. (2018). Weakly nonlinear theory for oscillating wave surge converters in a channel, *J. Fluid Mech.* **834**: 55–91.

Molin, B. (2023). *Offshore Structure Hydrodynamics*, Cambridge Ocean Technology Series, Cambridge University Press.

Morison, J., Johnson, J. and Schaaf, S. (1950). The force exerted by surface waves on piles, *J. Pet. Technol.* **2**(05): 149–154.

Mortlock, T. R., Goodwin, I. D., McAneney, J. K. and Roche, K. (2017). The June 2016 Australian East Coast low: Importance of wave direction for coastal erosion assessment, *Water* **9**(2): 121.

Mulholland, L. S. and Heckl, M. A. (1994). Multi-directional sound wave propagation through a tube bundle, *J. Sound Vib.* **176**(3): 377–398.

Newman, J. N. (1975). Interaction of waves with two-dimensional obstacles: A relation between the radiation and scattering problems, *J. Fluid Mech.* **71**(2): 273–282.

Ning, D. and Ding, B. (eds) (2022). *Modelling and Optimization of Wave Energy Converters*, CRC Press.

Noad, I. F. and Porter, R. (2015). Optimisation of arrays of flap-type oscillating wave surge converters, *Appl. Ocean Res.* **50**: 237–253.

Ocean Energy Europe (2025). Ocean energy stats & trends 2024, *Technical report*, Ocean Energy Europe. Available at: https://www.oceanenergy-europe.eu/wp-content/uploads/2025/04/Ocean-Energy-Stats-Trends-2024.pdf (Accessed: 10-11-25).

Ozkan, C., Mayo, T. and Passeri, D. L. (2022). The potential of wave energy conversion to mitigate coastal erosion from hurricanes, *J. Mar. Sci. Eng.* **10**(2): 143.

Palm, J., Eskilsson, C., Paredes, G. M. and Bergdahl, L. (2016). Coupled mooring analysis for floating wave energy converters using CFD: Formulation and validation, *Int. J. Mar. Energy* **16**: 83–99.

Peña-Sanchez, Y., García-Violini, D., Penalba, M., Zarketa-Astigarraga, A., Ferri, F., Nava, V. and Ringwood, J. V. (2024). Control co-design for wave energy farms: Optimisation of array layout and mooring configuration in a realistic wave climate, *Renew. Energy* **227**: 120506.

Pecher, A. and Kofoed, J. (eds) (2017). *Handbook of Ocean Wave Energy*, Vol. 7 of *Ocean Engineering & Oceanography*, Springer International Publishing.

Penalba, M., Giorgi, G. and Ringwood, J. V. (2017). Mathematical modelling of wave energy converters: A review of nonlinear approaches, *Renew. Sustain. Energy Rev.* **78**: 1188–1207.

Penalba, M., Touzón, I., Lopez-Mendia, J. and Nava, V. (2017). A numerical study on the hydrodynamic impact of device slenderness and array size in wave energy farms in realistic wave climates, *Ocean Eng.* **142**: 224–232.

Peter, M. A. and Meylan, M. H. (2010). Water-wave scattering by vast fields of bodies, *SIAM J. Appl. Math.* **70**(5): 1567–1586.

Peter, M. A., Meylan, M. H. and Linton, C. M. (2006). Water-wave scattering by a periodic array of arbitrary bodies, *J. Fluid Mech.* **548**: 237–256.

Petit, R. (ed.) (1980). *Electromagnetic Theory of Gratings*, Vol. 22 of *Topics in Current Physics*, Springer.

Porter, R. (2021). Modelling and design of a perfectly-absorbing wave energy converter, *Appl. Ocean Res.* **113**: 102724.

Porter, R. and Porter, D. (2003). Scattered and free waves over periodic beds, *J. Fluid Mech.* **483**: 129–163.

Porter, R., Zheng, S. and Greaves, D. (2021). Extending limits for wave power absorption by axisymmetric devices, *J. Fluid Mech.* **924**: A39.

Qu, M., Shen, L., Zeng, Z., Yang, B., Zhong, H., Yang, X. and Lu, X. (2025). Prolonged wind droughts in a warming climate threaten global wind power security, *Nat. Clim. Change* **15**(8): 842–849.

Raghavan, L. and Phani, A. S. (2013). Local resonance bandgaps in periodic media: Theory and experiment, *J. Acoust. Soc. Am.* **134**(3): 1950–1959.

Renzi, E. and Dias, F. (2012). Resonant behaviour of an oscillating wave energy converter in a channel, *J. Fluid Mech.* **701**: 482–510.

Ringwood, J. V. (2025). Control co-design for wave energy systems, *Appl. Ocean Res.* **158**: 104514.

Ringwood, J. V., Zhan, S. and Faedo, N. (2023). Empowering wave energy with control technology: Possibilities and pitfalls, *Annu. Rev. Control* **55**: 18–44.

Rodriguez-Delgado, C., Bergillos, R. J. and Iglesias, G. (2019). Dual wave farms and coastline dynamics: The role of inter-device spacing, *Sci. Total Environ.* **646**: 1241–1252.

Romero-García, V., Picó, R., Cebrecos, A., Sánchez-Morcillo, V. J. and Staliunas, K. (2013). Enhancement of sound in chirped sonic crystals, *Appl. Phys. Lett.* **102**(9): 091906.

Romero-García, V., Theocharis, G., Richoux, O., Merkel, A., Tournat, V. and Pagneux, V. (2016). Perfect and broadband acoustic absorption by critically coupled sub-wavelength resonators, *Sci. Rep.* **6**(1): 19519.

Romero-García, V., Theocharis, G., Richoux, O. and Pagneux, V. (2016). Use of complex frequency plane to design broadband and sub-wavelength absorbers, *J. Acoust. Soc. Am.* **139**(6): 3395–3403.

Ruezga, A. and Cañedo C., J. M. (2020). Buoy analysis in a point-absorber wave energy converter, *IEEE J. Ocean. Eng.* **45**(2): 472–479.

Ryoo, H., Yong Lee, K. and Jeon, W. (2024). Broadband sound absorption using hybrid resonators with embedded necks and micro-perforations in parallel, *Mech. Syst. Signal Process.* **211**: 111205.

Said, H. A. and Ringwood, J. V. (2021). Grid integration aspects of wave energy—Overview and perspectives, *IET Renew. Power Gener.* **15**(14): 3045–3064.

Sarpkaya, T. (2010). *Wave Forces on Offshore Structures*, Cambridge University Press.

Satymov, R., Bogdanov, D., Dadashi, M., Lavidas, G. and Breyer, C. (2024). Techno-economic assessment of global and regional wave energy resource potentials and profiles in hourly resolution, *Appl. Energy* **364**: 123119.

Schmitt, P. and Elsäßer, B. (2017). The application of Froude scaling to model tests of Oscillating Wave Surge Converters, *Ocean Eng.* **141**: 108–115.

Schubert, B. W., Robertson, W. S. P., Cazzolato, B. S., Sergiienko, N. Y. and Ghayesh, M. H. (2022). Nonlinear stiffness enhancement of submerged wave energy device in high fidelity model, *Ocean Eng.* **254**: 111295.

Sergiienko, N., Cazzolato, B., Ding, B., Hardy, P. and Arjomandi, M. (2017). Performance comparison of the floating and fully submerged quasi-point absorber wave energy converters, *Renew. Energy* **108**: 425–437.

Sharp, C. and DuPont, B. (2018). Wave energy converter array optimization: A genetic algorithm approach and minimum separation distance study, *Ocean Eng.* **163**: 148–156.

Sheng, P., Zhang, X. X., Liu, Z. and Chan, C. T. (2003). Locally resonant sonic materials, *Phys. B: Condens. Matter* **338**(1): 201–205.

Sheng, W. (2019). Wave energy conversion and hydrodynamics modelling technologies: A review, *Renew. Sustain. Energy Rev.* **109**: 482–498.

Sheng, W., Alcorn, R. and Lewis, T. (2014). Physical modelling of wave energy converters, *Ocean Eng.* **84**: 29–36.

Sheng, W. and Lewis, A. (2016). Power takeoff optimization for maximizing energy conversion of wave-activated bodies, *IEEE J. Ocean. Eng.* **41**(3): 529–540.

Simon, M. J. (1982). Multiple scattering in arrays of axisymmetric wave-energy devices. Part 1. A matrix method using a plane-wave approximation, *J. Fluid Mech.* **120**: 1–25.

Soliman, S. E., Barlou, M., Tsakmakidis, K. L. and Wong, Z. J. (2025). Rainbow trapping for advanced wave control, *Adv. Phys.: X* **10**(1): 2517551.

Stansby, P., Carpintero Moreno, E., Stallard, T. and Maggi, A. (2015). Three-float broad-band resonant line absorber with surge for wave energy conversion, *Renew. Energy* **78**: 132–140.

Tang, X.-L., Zhang, X.-Q., Ma, T.-X., Kim, M. and Wang, Y.-S. (2025). Topological rainbow trapping and broadband piezoelectric energy harvesting of acoustic waves in gradient phononic crystals with coupled interfaces, *Appl. Acoust.* **233**: 110630.

Teillant, B., Costello, R., Weber, J. and Ringwood, J. (2012). Productivity and economic assessment of wave energy projects through operational simulations, *Renew. Energy* **48**: 220–230.

Teixeira-Duarte, F., Clemente, D., Giannini, G., Rosa-Santos, P. and Taveira-Pinto, F. (2022). Review on layout optimization strategies of offshore parks for wave energy converters, *Renew. Sustain. Energy Rev.* **163**: 112513.

Todalshaug, J. H. (2013). Practical limits to the power that can be captured from ocean waves by oscillating bodies, *Int. J. Mar. Energy* **3–4**: e70–e81.

Todalshaug, J. H., Ásgeirsson, G. S., Hjálmarsson, E., Maillet, J., Möller, P., Pires, P., Guérinel, M. and Lopes, M. (2016). Tank testing of an inherently phase-controlled wave energy converter, *Int. J. Mar. Energy* **15**: 68–84.

Tokić, G. and Yue, D. K. P. (2019). Hydrodynamics of periodic wave energy converter arrays, *J. Fluid Mech.* **862**: 34–74.

Tokić, G. and Yue, D. K. P. (2021). Hydrodynamics of large wave energy converter arrays with random configuration variations, *J. Fluid Mech.* **923**: R1.

Tokić, G. and Yue, D. K. P. (2023). Axisymmetric reflectors in wave energy converter arrays: Harnessing scattering to increase energy extraction, *Phys. Fluids* **35**(6): 067120.

Tom, N. and Yeung, R. W. (2013). Performance enhancements and validations of a generic ocean-wave energy extractor, *J. Offshore Mech. Arct. Eng.* **135**(041101).

Tsakmakidis, K. L., Boardman, A. D. and Hess, O. (2007). 'Trapped rainbow' storage of light in metamaterials, *Nature* **450**(7168): 397–401.

Twersky, V. (1962). On scattering of waves by the infinite grating of circular cylinders, *IRE Trans. Antennas Propag.* **10**(6): 737–765.

Veurink, M. G., Weaver, W. W., Robinett, R. D., Wilson, D. G., Matthews, R. C., Michelen, C. and Dallman, A. R. (2023). Impact of wave forecasting accuracy on design and power predictions of a wec array, *2023 IEEE Energy Conversion Congress and Exposition (ECCE)*, pp. 399–404.

Wang, L., Engström, J., Göteman, M. and Isberg, J. (2015). Constrained optimal control of a point absorber wave energy converter with linear generator, *J. Renew. Sustain. Energy* **7**(4): 043127.

Wegert, E. (2012). *Visual Complex Functions: An Introduction with Phase Portraits*, Springer.

Westcott, A.-R., Bennetts, L. G., Sergiienko, N. Y. and Cazzolato, B. S. (2024). Broadband near-perfect capture of water wave energy by an array of heaving buoy wave energy converters, *J. Fluid Mech.* **998**: A5.

Westcott, A.-R., Bennetts, L. G., Sergiienko, N. Y., Cazzolato, B. S. and Peter, M. A. (2025). Broadband absorption of wave energy by graded arrays of heaving buoys in 3D, *The 40th International Workshop on Water Waves and Floating Bodies*, Shanghai, China.

Wilcox, C. H. (1984). *Scattering Theory for Diffraction Gratings*, Vol. 46 of *Applied Mathematical Sciences*, Springer.

Wilks, B., Meylan, M. H., Montiel, F., Balasooriya, D. S., Jauhar, T., Blair, A., Wheeler, C. and Chalup, S. (2025). Layout and device parameter optimisation of a wave energy park in a broadband sea, *The 40th International Workshop on Water Waves and Floating Bodies*, Shanghai, China.

Wilks, B., Montiel, F., Bennetts, L. G. and Wakes, S. (2024). Water wave interactions with surface-piercing vertical barriers in a rectangular tank: Connections with Bloch waves and quasimodes. arXiv 2404.06743 [Preprint]. Available from: https://doi.org/10.48550/arXiv.2404.06743.

Wilks, B., Montiel, F. and Wakes, S. (2022). Rainbow reflection and broadband energy absorption of water waves by graded arrays of vertical barriers, *J. Fluid Mech.* **941**: A26.

Windt, C., Davidson, J. and Ringwood, J. V. (2021). Numerical analysis of the hydrodynamic scaling effects for the Wavestar wave energy converter, *J. Fluids Struct.* **105**: 103328.

Wolgamot, H. A. and Fitzgerald, C. J. (2015). Nonlinear hydrodynamic and real fluid effects on wave energy converters, *Proc. Inst. Mech. Eng. A: J. Power Energy* **229**(7): 772–794.

Wolgamot, H. A., Taylor, P. H. and Eatock Taylor, R. (2012). The interaction factor and directionality in wave energy arrays, *Ocean Eng.* **47**: 65–73.

Xie, J.-J., Ye, Q. and Liu, H.-W. (2025). Rainbow reflection of linear long waves excited by a finite graded array of trapezoidal bars, *Appl. Ocean Res.* **156**: 104472.

Xu, J., Chen, L., Ning, D. and Zhao, M. (2023). Resonance of water waves propagating over a uniform and a graded line array of rectified submerged cosinoidal bars, *Appl. Ocean Res.* **134**: 103531.

Xu, J., Ning, D.-Z. and Chen, L.-F. (2024). Rainbow trapping within graded array of C-shaped cylinders, *The 39th International Workshop on Water Waves and Floating Bodies*, St Andrews, Scotland.

Yeung, R. W. and Jiang, Y. (2014). Shape effects on viscous damping and motion of heaving cylinders, *J. Offshore Mech. Arct. Eng.* **136**(041801).

Yiew, L. J., Bennetts, L. G., Meylan, M. H., French, B. J. and Thomas, G. A. (2016). Hydrodynamic responses of a thin floating disk to regular waves, *Ocean Model.* **97**: 52–64.

Zanuttigh, B., Nicholls, R., Vanderlinden, J. P., Burcharth, H. F. and Thompson, R. C. (eds) (2015). *Coastal Risk Management in a Changing Climate*, Butterworth-Heinemann.

Zhang, H., Jin, H., Zheng, S. and Xu, D. (2024). Resonant periodic structures for strong attenuation of surface water wave, *J. Appl. Phys.* **135**(1): 014702.

Zhao, X., Li, F., Zhou, J., Geng, J., Zou, Q. and Qin, D. (2023). Theoretical investigation of hydrodynamic performance of multi-resonant OWC breakwater array, *Appl. Ocean Res.* **141**: 103756.

Zhong, Q. and Yeung, R. W. (2022). On optimal energy-extraction performance of arrays of wave-energy converters, with full consideration of wave and multi-body interactions, *Ocean Eng.* **250**: 110863.

Zhou, Z. and Song, Z. (2025). Three-dimensional viscous study on rainbow trapping of water waves within graded cylindrical arrays, *Phys. Fluids* **37**(8): 087197.